The Dissertation Committee for Hema Chandra Prakash Movva
certifies that this is the approved version of the following dissertation:

Magnetotransport Studies of Tungsten Diselenide Holes

Committee:

Emanuel Tutuc, Co-Supervisor

Sanjay K. Banerjee, Co-Supervisor

Leonard F. Register

Edward T. Yu

Deji Akinwande

Alexander A. Demkov

Magnetotransport Studies of Tungsten Diselenide Holes

by

Hema Chandra Prakash Movva

DISSERTATION

Presented to the Faculty of the Graduate School of

The University of Texas at Austin

in Partial Fulfillment

of the Requirements

for the Degree of

DOCTOR OF PHILOSOPHY

THE UNIVERSITY OF TEXAS AT AUSTIN

August 2018

Acknowledgments

Although this dissertation bears only my name, it contains indispensable contributions from collaborators, colleagues, and mentors, without whose inputs it would not have come to fruition. I am, and will always be deeply indebted to them.

I would like to offer my sincerest thanks to Babak Fallahazad for showing me the ropes on everything from measurements to data analysis, for tackling the first hurdles in magnetotransport experiments of tungsten diselenide, and methodically taming them down before handing over to me. Thank you for being a great mentor and role model. I would also like to extend my sincere gratitude to Timothy Lovorn and Prof. Allan MacDonald for their crucial theoretical support in interpreting the experimental data of Chapter 5.

I have received immeasurable assistance from many colleagues in carrying out the experiments discussed here. I am grateful for my partnership with Kyounghwan Kim, who had immediate solutions to all device fabrication obstacles, never hesitated to help, and was pivotal in developing the transfer technique which was the core enabler for assembling all the samples investigated in this dissertation. I would like to thank Stefano Larentis for his invaluable camaraderie during our Magnet Lab trips, and for many stimulating discussions on measurements and data analysis. I owe many thanks to Sangwoo Kang for teaching me his special exfoliation technique, and many other clever tips and tricks for device fabrication. I am thankful to Amritesh Rai for his companionship, and helping with inventory and lab upkeep. I would like to thank Will Burg for meticulously wire-bonding samples, even on short notice.

I would also like to acknowledge help from Tanmoy Pramanik on simulations, and from Rik Dey on condensed matter theory discussions. I am indebted to Michael Ramón and Chris Corbet for their invaluable mentoring during my first few years of research. I am very grateful to Anupam Roy, Tanuj Trivedi, Praveenkumar Pasupathy, Atresh Sanne, Sushant Sonde, and Dharmendar Reddy for many fruitful discussions on research and science.

I would also like to thank all the other members, past and present, of the Tutuc and Banerjee groups, who have directly or indirectly contributed to the work in this dissertation. I would like to acknowledge Seyoung Kim, En-Shao Liu, Micah Points, Jiamin Xue, David Dillen, Kayoung Lee, Feng Wen, Yimeng Wang, Fahmida Ferdousi, Mustafa Jamil, Jiwon Chang, Aparna Gupta, Domingo Ferrer, Priyamvada Jadaun, Yujia Zhai, Emmanuel Onyegam, Sayan Saha, Sk. Fahad Chowdhury, Tarik Akyol, Urmimala Roy, Dax Crum,

Samaresh Guchhait, Jason Mantey, Rudresh Ghosh, Donghyi Koh, William Hsu, Andreas Hsieh, Connor McClellan, Nima Asoudegi, Sarmita Majumder, Omar Mohammed, Jaehyun Ahn, Harry Chou, Sungkyu Kwon, and Sayema Chowdhury.

I am very grateful to the large peer group and amazing company, past and present, at the Microelectronics Research Center (MRC), working on numerous interesting problems, who have provided plenty of food for thought from their unique research experiences. I would like to acknowledge Michael Rodder, Karun Vijayraghavan, Milo Holt, Daniel Fine, Xuehao Mou, Amithraj Valsaraj, Nitin Prasad, Xian Wu, Donghwan Kim, David Choi, Mir Mohammad Sadeghi, Fei Zhou, Seungyong Jung, Yingnan Liu, Feng Lu, Aiting Jiang, Kristen Parrish, Maruthi Yogeesh, Saungeun Park, Li Tao, Joonseok Kim, Avinash Nayak, Md. Hasibul Alam, Jongho Lee, Ankit Sharma, Myungsoo Kim, Wei Li, Di Wu, Weinan Zhu, Rohit Yadav, Leander Schulz, Yang Zhang, Xiaohui Lin, Nima Dabidian, Nihal Arju, Emily Walker, Deepyanti Taneja, Ying-Chen Chen, Yao-Feng Chang, and David Cayll.

I would like to wholeheartedly thank the MRC staff, Ricardo Garcia, Jesse James, Bill Ostler, Johnny Johnson, Joyce Kokes, Gerlinde Sehne, Kenneth Ziegler, Robert Stephens, Rick Gomez, Darren Robins, and James Hitzfelder, for keeping the cleanroom process equipment and MRC facilities in order, and always being available for help. Special thanks to Jean Toll and Christine Wood for helping with everything administrative.

I would also like to thank the scientists and staff at the National High Magnetic Field Laboratory, David Graf, Alexey Suslov, Jan Jaroszynski, Scott Hannahs, Tim Murphy, Juhyun Park, Scott Maier, and Bobby Pullum, for their invaluable help in facilitating the high magnetic field measurements discussed in this dissertation.

I am extremely grateful to Prof. Jack Lee for generously providing access to his group's probe station for setting-up the transfer apparatus. Many thanks to the folks at HQ Graphene for synthesizing high-quality tungsten diselenide crystals, and Takashi Taniguchi and Kenji Watanabe for kindly providing pristine hexagonal boron nitride crystals, both of which were core ingredients in the devices studied in this dissertation. I would like to acknowledge support from the SouthWest Academy of Nanoelectronics and overall research directions from Luigi Colombo.

I should also acknowledge technical discussions with Xiao Li, Andor Kormányos, Prof. Kin Fai Mak, Prof. Fan Zhang, and Prof. Qian Niu, which helped clarify several experimental findings of this dissertation.

I am very grateful to the professors whom I have taken classes with, whose pedagogy helped me immensely in carrying out the research presented here, Prof. Emanuel Tutuc, Prof. Frank Register, Prof. Alexander Demkov, Prof. Edward Yu, Prof. Jack Lee, Prof. Dean Neikirk, Prof. Arno Bohm, Prof. James Chelikowsky, and Prof. Deji Akinwande.

Lastly, and most importantly, I would like to express my heartfelt gratitude to my research co-supervisors, Prof. Emanuel Tutuc and Prof. Sanjay Banerjee, for giving me the opportunity to work under their tutelage, and without whom none of this would have been possible. Thank you for making my Ph.D. study an extremely enriching experience. I could not have asked for better advisors.

Thank you, Dr. Banerjee, for supporting me throughout the past eight years, for letting me overstay my welcome, for giving me the fullest freedom to work in my own way, for always being available to talk, and for your boundless patience. Thank you for providing unlimited resources, and for heading a diverse research group with an assortment of research projects, where there was never a dearth of learning.

Thank you, Dr. Tutuc, for taking me under your wing, for introducing me to a whole new world of physics, for patiently walking me through the entire research cycle, and for your immeasurable research guidance which formed the backbone of all the findings in this dissertation. Thank you for teaching me the significance of attention to detail, the value of persistence, and the importance of scientific rigor. Thank you for showing me how to be truly appreciative of the challenges and thrills of research.

Hema Chandra Prakash Movva
Austin, Texas, USA
August 2018

Magnetotransport Studies of Tungsten Diselenide Holes

Hema Chandra Prakash Movva, Ph.D.
The University of Texas at Austin, 2018

Co-Supervisors: Emanuel Tutuc
Sanjay K. Banerjee

This dissertation describes the electronic transport properties of holes in tungsten diselenide (WSe_2), a prototypical transition metal dichalcogenide (TMD) material, probed using low-temperature magnetotransport measurements, and facilitated by a device structure with platinum (Pt) bottom-contacts and hexagonal boron nitride (h-BN) encapsulation.

The discovery of graphene has stimulated an intense interest in exploration of materials with stable two-dimensional allotropes, TMDs being one of them. Of the myriad variety of TMDs, sulfides and selenides of molybdenum and tungsten have garnered great attention on account of their semiconducting nature. A major roadblock to investigation of TMDs' electronic transport properties has been the poor quality of electrical contacts.

The top-gated device structure with Pt bottom-electrodes presented in this dissertation ensures Ohmic hole contacts to WSe_2 down to a temperature of 0.3 K and permits low-temperature magnetotransport measurements. Encapsulating WSe_2 in h-BN preserves its intrinsic quality, resulting in high hole mobilities at low-temperatures, and thereby enabling observation of Shubnikov–de Haas (SdH) oscillations and quantum Hall states (QHS) in perpendicular magnetic fields. Analysis of the SdH oscillations in monolayer and bilayer WSe_2 reveals two-fold degenerate Landau levels and a hole effective mass of $0.45m_e$; m_e is the free electron mass. Bilayer data also show carrier localization in the two layers signifying weak interlayer coupling, and negative compressibility of holes in the bottom layer. The QHS data reveal interesting transitions between even and odd filling factors as the hole density is tuned, which can be explained by a Zeeman-to-cyclotron energy ratio that changes as a function of density due to strong electron-electron interactions. Tilted magnetic field measurements reveal that the holes reside in the K valleys, as evinced by their spins which are locked perpendicular to the WSe_2 plane.

In trilayer WSe_2, holes are found to populate two subbands with different effective masses, $0.5m_e$ and $1.2m_e$, associated with the K and Γ valleys, respectively. At a fixed total hole density, the K and Γ occupations are tunable via an applied transverse electric field, an observation which can be explained in terms of an electric field dependent bandstructure.

Table of Contents

List of Tables

List of Figures

Chapter 1

Introduction

At low-temperatures, and when subject to a strong perpendicular magnetic field, two-dimensional electron systems (2DESs) display a wealth of fascinating electronic phenomena, a notable example of which is the integer quantum Hall effect [1]. Even in the absence of a magnetic field, when disorder is sufficiently low, carriers in a 2DES are expected to display interesting correlated quantum electronic phases such as the Wigner crystal [2]. In addition to hosting several such interesting electronic phenomena, 2DESs are a powerful platform to study the electronic transport properties of materials.

Traditionally studied 2DESs [3] are based on semiconductors such as gallium arsenide (GaAs), aluminum arsenide (AlAs), silicon (Si), etc., which are synthesized using molecular beam epitaxy (MBE) growth techniques. Improving the quality of the materials hosting the 2DESs has been at the forefront of 2DES research, aimed at reducing disorder, and expanding the horizon of accessible quantum electronic phases. A second direction of research has been the exploration of new 2DES host material systems such as graphene [4], topological insulators [5], oxide interfaces [6], etc., each with their own unique properties and differences with traditional semiconductor 2DESs.

A pioneering discovery in the search for alternate 2DES host materials was the isolation of graphene [7], a monolayer of carbon atoms arranged in a honeycomb lattice. Graphene 2DESs have played host to a plethora of exotic electronic phenomena, and have triggered an intense interest in exploration of other materials with stable two-dimensional (2D) allotropes, notable examples of which are transition metal dichalcogenides (TMDs) [8], black phosphorus [9], indium selenide [10], etc.

Transition metal dichalcogenides can be synthesized down to a monolayer thickness, similar to graphene, and occur in myriad chemical compositions, among which, sulfides and selenides of molybdenum and tungsten have garnered great attention on account of their semiconducting nature. This dissertation describes the electronic transport properties of holes in tungsten diselenide (WSe_2), a prototypical TMD material, probed using low-temperature magnetotransport measurements. The following sections of this chapter present an overview of 2DESs, electron-electron interaction effects in 2DESs, and a review of the basic material properties of TMDs.

1.1 Two-Dimensional Electron Systems

Restricting the electron motion in a solid to two spatial dimensions provides a versatile platform to study their many interesting phases. At high-temperatures, and in the absence of interactions, where Boltzmann statistics prevail, electrons or holes in a 2DES can be treated as a gas. At low-temperatures, and in the limit of low-disorder, they can be treated as a liquid, referred to as a Fermi liquid, where electron-electron interaction effects play a significant role in determining the 2DES's electronic properties [11]. When Coulomb interactions become sufficiently strong, electrons or holes can also condense into a lattice, effectively behaving as a solid, known as a Wigner crystal [2].

Furthermore, application of a magnetic field provides an extra knob to increase the strength of interactions in a 2DES, and access interesting phases such as the integer and fractional quantum Hall liquids [1, 12] and magnetically induced Wigner crystals [13, 14, 15]. Uncovering these fascinating phases of electrons has been a topic of intense interest, being investigated in several material systems. Two-dimensional electron systems have been the vehicle of choice for a majority of these experiments, thanks to the ability to fabricate these systems with reduced disorder, and the ability to tune the electron or hole densities in order to access the multitude of electronic phases they can potentially host [3].

Figure 1.1 shows schematic representations of three different structures used to realize 2DESs. Figure 1.1(a) shows a metal-oxide-semiconductor field-effect transistor (MOSFET) structure where charge carriers are accumulated at the interface of a host semiconductor, e.g., Si, with an insulator, e.g., silicon dioxide (SiO_2) by field-effect from a metal gate. One of the major drawback of Si MOSFETs is the roughness at the Si–SiO_2 interface due to the amorphous nature of SiO_2 which causes disorder in the 2DES [16].

The heterostructure 2DES of Fig. 1.1(b) solves this problem by inducing the 2DES at the interface of a host semiconductor e.g., GaAs, and an epitaxially grown barrier layer, e.g., aluminum gallium arsenide (AlGaAs), by a dopant layer, e.g., Si, away from the 2DES interface. Adding metal gates further allows tuning of the 2DES density. This system has a smoother interface since both the barrier and host semiconductors are crystalline, and results in a 2DES with reduced disorder.

Figure 1.1(c) shows the schematic of a 2DES hosted by a layered semiconductor monolayer. The 2DESs hosted by layered semiconductors differ in several ways from traditional 2DESs based on Si or GaAs. The 2DES in a layered semiconductor monolayer is truly 2D, unlike in traditional 2DESs which are only quasi-2D due to a finite width ($5 - 50$ nm) in the third dimension [4]. The absence of surface dangling bonds in layered semiconductors is expected to reduce extrinsic disorder from the interface, and result in higher quality 2DESs, limited only by the intrinsic material properties.

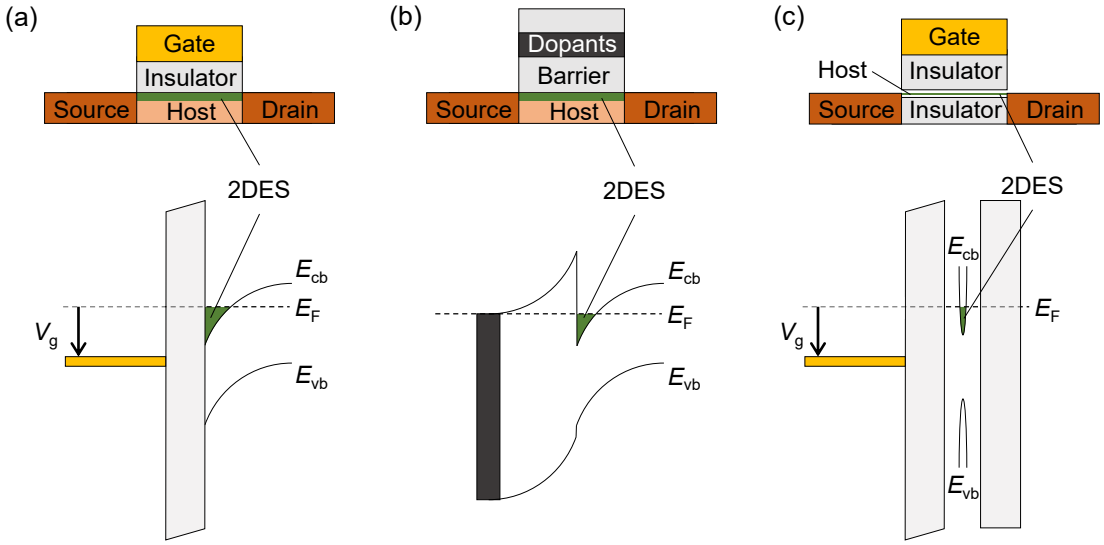

Figure 1.1: (a) A 2DES at the interface of an insulator and a host semiconductor, induced through field-effect from a metal gate. (b) A 2DES at the interface between two semiconductors, induced by a dopant layer in the barrier semiconductor. (c) A 2DES in a layered semiconductor monolayer, induced through field-effect from a metal gate. E_{cb} and E_{vb} denote the conduction and valence band edges, respectively, E_F the Fermi level, and V_g the gate voltage. Adapted, in part, from Ref. [4].

Thanks to the lack of surface dangling bonds, layered semiconductors do not have any fundamental material constraints on the substrate and superstrate insulators which encapsulate them. Therefore, in principle, it is possible to choose a low dielectric constant encapsulant which can enhance the strength of electron-electron interactions in the 2DES, and facilitate observation of novel correlated electronic phenomena [17]. The following section describes why a low dielectric constant is favorable for enhanced electron-electron interactions.

1.1.1 Electron-Electron Interactions in 2DESs

The Hamiltonian for a free electron in vacuum is given by

$$\hat{H} = \frac{\hat{\mathbf{p}}^2}{2m_e} \tag{1.1}$$

where $\hat{\mathbf{p}}$ is the canonical momentum operator and m_e is the electron mass. When an electron moves in a 2DES, it experiences Coulomb forces from the positively charged atomic nuclei which influence its motion. This effect can be approximated by treating the electron as a

quasiparticle having an effective mass (m^*) different from m_e. The Hamiltonian in this case is referred to as the effective mass Hamiltonian, and is given by[1]

$$\hat{H} = \frac{\hat{\mathbf{p}}^2}{2m^*} \tag{1.2}$$

Practical 2DESs, however, have many electrons which can also interact with each other, an effect which is neglected by the effective mass Hamiltonian of Eq. 1.2. Coulomb interactions between electrons can be incorporated into the Hamiltonian as follows

$$\hat{H} = \sum_i \frac{\hat{\mathbf{p}}_i^2}{2m^*} + \sum_{i<j} \frac{e^2}{4\pi\epsilon} \frac{1}{|\mathbf{r}_i - \mathbf{r}_j|} \tag{1.3}$$

where the indices i, j denote the number of electrons in the system, $\mathbf{r}$ denotes the individual electron position, e is the electron charge, and ϵ is the dielectric constant of the medium surrounding the 2DES. The second term in Eq. 1.3 denotes the Coulomb interactions between all pairs of electrons residing in the 2DES. The average distance between electrons in a 2DES, $\langle \mathbf{r} \rangle$, is given by $1/\sqrt{\pi n}$, where n is the areal density of electrons. The average Coulomb energy per electron due to interactions with other electrons in the 2DES, $\mathcal{E}_\mathrm{C}$, can therefore be written as

$$\mathcal{E}_\mathrm{C} = \frac{e^2}{4\pi\epsilon\langle \mathbf{r} \rangle} = \frac{e^2}{4\pi\epsilon}\sqrt{\pi n} \tag{1.4}$$

The kinetic energy per electron at the Fermi level, also called the Fermi energy, $\mathcal{E}_\mathrm{F}$, is given by[2]

$$\mathcal{E}_\mathrm{F} = \frac{n\pi\hbar^2}{m^*} \tag{1.5}$$

using a 2D density of states, $m^*/\pi\hbar^2$; $\hbar$ is the reduced Planck constant. It is instructive to evaluate the ratio of the Coulomb energy to the kinetic energy to judge the strength of electron-electron interactions, as follows

$$r_s = \frac{\mathcal{E}_\mathrm{C}}{\mathcal{E}_\mathrm{F}} = \frac{m^* e^2}{4\pi\epsilon\hbar^2\sqrt{\pi n}} = \frac{1}{a_\mathrm{B}^*\sqrt{\pi n}} \tag{1.6}$$

where $a_\mathrm{B}^* = 4\pi\epsilon\hbar^2/m^* e^2$ is the effective Bohr radius, i.e., the Bohr radius in a medium with an electron effective mass of m^* and a dielectric constant of ϵ. The interaction parameter,

[1] For simplicity, it is assumed that the quasiparticle resides in the conduction band of a 2DES with a parabolic energy dispersion.

[2] It is assumed that the temperature (T) is sufficiently low, i.e., $k_\mathrm{B}T \ll \mathcal{E}_\mathrm{F}$; k_B is the Boltzmann constant.

r_s, is larger at lower densities, i.e., when the electrons are further apart from each other. Furthermore, interaction effects are expected to be stronger in 2DESs with small a_B^* values, i.e., large effective masses and media with low dielectric constants.

In essence, interaction effects dominate under the following set of conditions: (i) at low carrier densities, where the Coulomb interaction energy of the particles makes up a majority of their total energy [Eq. 1.6], (ii) for heavy carriers, which, by virtue of having a smaller Fermi (kinetic) energy [Eq. 1.5], are therefore, subject to increased Coulomb interactions from adjacent carriers, and (iii) a low dielectric constant of the medium surrounding the 2DES, which increases the Coulomb interactions by virtue of reduced electrostatic screening [Eq. 1.4] between adjacent carriers.

One of the primary directions of research in 2DESs has therefore been to explore novel material systems which possess heavy carriers, and which can be embedded in low dielectric constant surroundings. Examples of 2DESs with heavy carriers include holes in GaAs [3], electrons in AlAs [18], and electrons at polar oxide interfaces [6]. The lower limit of densities below which interaction effects are no longer manifested is determined by the amount of disorder in the 2DES, which causes strong localization of charge carriers and a consequent insulating behavior [19].

The ground state of a 2DES in the absence of magnetic field is therefore determined by the relative strength of disorder and interactions. Figure 1.2 shows a possible ground state phase diagram of a 2DES as a function of carrier density ($\propto 1/r_s^2$) and disorder [20]. In the limit of high-disorder, the ground state is an Anderson insulator, where the carriers are localized and the 2DES becomes insulating [19]. However, when the disorder is sufficiently small, interaction effects become significant and can lead to correlated ground states.

In the weakly interacting regime, i.e., high densities and small r_s values, carriers in a 2DES behave like a paramagnetic Fermi liquid, characterized by an interaction-renormalized spin susceptibility. In the limit of strong interactions, i.e., low densities and large r_s values, the electrons are expected to form a Wigner crystal, possessing both spatial and spin order [17]. Numerical calculations employing quantum Monte Carlo (QMC) algorithms predict a Wigner crystal to form when $r_s \gtrapprox 35$ [21]. For intermediate r_s values, i.e., $26 \lessapprox r_s \lessapprox 35$, QMC calculations predict a ferromagnetic Fermi liquid as the ground state. Experimentally, r_s values larger than 35 have been reported in 2DESs, e.g., GaAs 2D holes [22, 23]; however, evidence for the Wigner crystal phase from these studies was inconclusive [24].

To date, there exists no compelling experimental evidence of the Wigner crystal and ferromagnetic Fermi liquid phases in a 2DES in zero magnetic field. Of the multitude of alternate 2DES host materials, the appeal of TMDs for exploring such correlated quantum

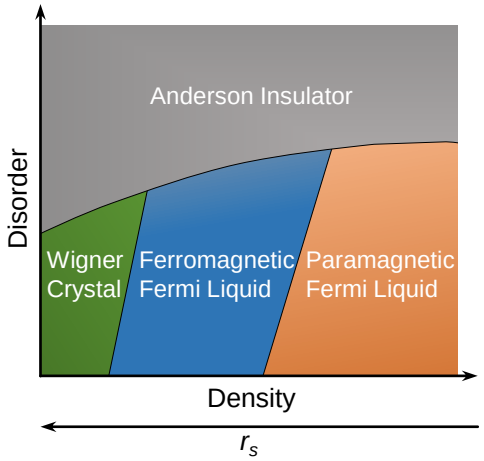

Figure 1.2: Possible ground state phase diagram of a 2DES in zero magnetic field. The phase transitions at zero disorder are substantiated by QMC calculations [21], but the exact phase diagram and specifics of the transitions in the presence of disorder are unknown. Adapted from Ref. [20].

electronic phases can be attributed to their intrinsic 2D nature, and more importantly, to their large effective mass carriers, the details of which are discussed in the following section.

1.2 Transition Metal Dichalcogenides

Transition metal dichalcogenides are layered materials with the chemical formula MX_2, where M is a transition metal and X is a chalcogen. They occur in myriad chemical compositions thanks to the large assortment of transition metals, and can be isolated down to a monolayer using the same techniques used to synthesize graphene. One of the earliest studied TMDs was molybdenite, the mineral form of molybdenum disulfide (MoS_2), which was found to occur in hexagonal crystals and show easy cleavage, similar to graphite [25].

The physical and electrical properties of bulk TMDs were studied extensively in the last century, thanks to interest in their use as solid lubricants and photovoltaics, among others [26, 27, & references therein]. The recent wave of resurgence is motivated by the ability to synthesize them in monolayer and few-layer forms which possess properties very different from their bulk counterparts [28], and the ability to engineer complex heterostructures by stacking several different TMDs and other layered semiconductors on top of each other [29].

The TMD crystal structure consists of X–M–X atomic trilayers, in which an M atom layer is enclosed within two X atom layers. The individual MX_2 layers are stacked on top of each other through weak interlayer van der Waals (vdW) bonding, which allows

cleavage along the interlayer planes. The specific geometry of the X–M–X bonding and stacking sequence of the MX_2 layers leads to various allotropic forms, of which, the trigonal prismatic form, also known as the $2H$ polytype is pertinent to this dissertation.

The sulfides and selenides of molybdenum and tungsten in the $2H$ phase possess sizable ($1 - 2$ eV) bandgaps, and have received the most attention on account of their semiconducting nature. Figure 1.3 shows schematic representations of the $2H$-TMD crystal lattice along the in-plane and out-of-plane directions. The M atoms have a trigonal prismatic coordination with respect to the X atoms within a layer, and the M atoms of one MX_2 layer reside on top of the X atoms of the next layer, and vice versa. Each MX_2 layer forms a 2D honeycomb lattice when viewed from the out-of-plane direction. The spacing between layers is $6 - 7$ Å and the M–X bond length $2.4 - 2.5$ Å [27].

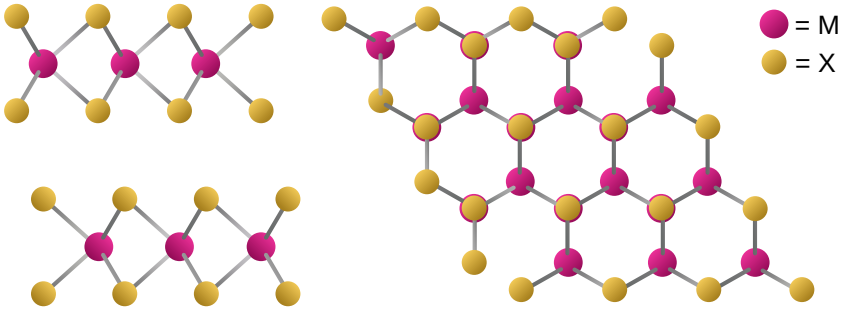

Figure 1.3: Schematic representations of the $2H$-TMD [MX_2] crystal lattice viewed along the in-plane (left) and out-of-plane (right) directions.

Figure 1.4(a) shows the first Brillouin zone of the bulk $2H$-TMD lattice along with its high-symmetry points and Fig. 1.4(b) shows the schematic bandstructure of bulk $2H$-WSe_2. Bulk $2H$-WSe_2 possesses an indirect electronic bandgap of ≈ 1.2 eV at room temperature [30] with the valence band maximum at the Brillouin zone center, Γ, and the conduction band minimum at 55% of the $\Gamma - K$ distance [31]. Noteworthy, there also exists a valence band maximum at K, close in energy, but lower than the maximum at Γ. A second noteworthy feature, which is of significance when thinned down to a monolayer, is the splitting of both the conduction and valence bands at K due to effects of spin–orbit interaction arising from the tungsten d-orbitals.

An interesting characteristic of the TMD electronic bandstructure is the changes it undergoes when the TMD thickness is reduced to a monolayer.[3] First, the Brillouin

[3]All references to TMD(s) and WSe_2 in this dissertation pertain only to the $2H$ polytypes. The $2H$ prefix is often omitted for brevity.

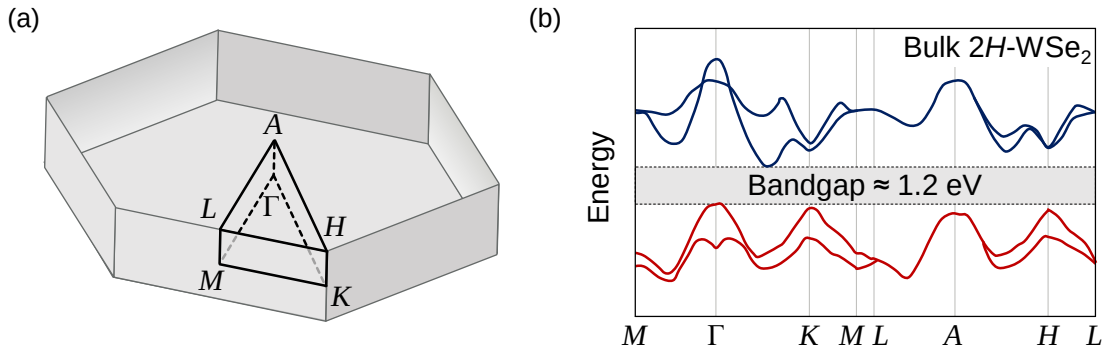

Figure 1.4: (a) Schematic of the first Brillouin zone of bulk 2H-TMDs. The high-symmetry points are labeled. (b) Bandstructure of bulk 2H-WSe_2 showing the two lowest conduction bands and the two highest valence bands. Adapted from Ref. [31].

zone collapses into a 2D hexagon as shown in Fig. 1.5. Second, there is a loss of inversion symmetry in the monolayer lattice due to the trigonal prismatic coordination of the chalcogen atoms with the metal atom within a layer.[4] A consequence of inversion symmetry breaking and the strong spin–orbit interaction present in the material is a breaking of the spin-degeneracy of the valence and conduction bands along the $\Gamma - K$ direction [32]. This is reminiscent of the spin–orbit interaction-induced band splitting at the K points in bulk WSe_2, but with the addition of inversion symmetry breaking in the monolayer, results in the electron-spin being coupled to each of the two valence bands at the K and K' points, i.e., spin-↑ in the upper valence band and and spin-↓ in the lower valence band at K, and vice versa at K' [33], as shown in Fig. 1.5.

Another interesting feature of the monolayer TMDs' bandstructure is the locations of the conduction and valence band extrema, which now occur at the K and K' points of the Brillouin zone [Fig. 1.5]. Monolayer TMDs are therefore direct bandgap semiconductors with peculiar spin-valley locked band extrema.[5] Figure 1.6(a) shows the room temperature photoluminescence (PL) spectra of monolayer molybdenum diselenide ($MoSe_2$), WSe_2, MoS_2, and tungsten disulfide (WS_2), each of which show sharp peaks at values characteristic of each material's direct bandgap.[6]

[4]Inversion symmetry is broken in all odd number-of-layers TMD films and preserved in even number-of-layers films.

[5]The conduction bands also possess spin-valley locking, but with a much smaller spin-splitting due to the lower magnitude of spin–orbit interaction in the conduction band [32].

[6]The peak positions are indicative of the optical bandgap which is different from the electronic bandgap due to a large exciton binding energy in TMDs [34].

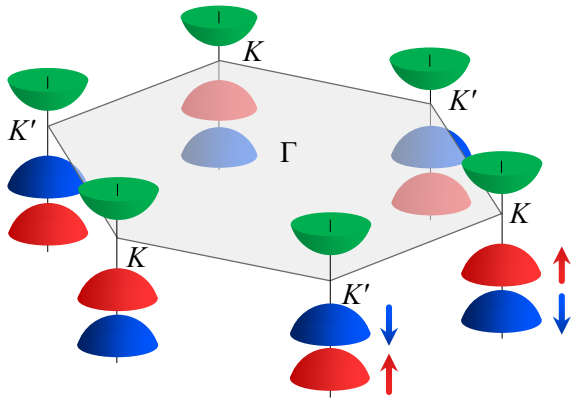

Figure 1.5: Schematic of the monolayer 2H-TMD Brillouin zone and bandstructure at the K and K' points. Adapted from Ref. [33].

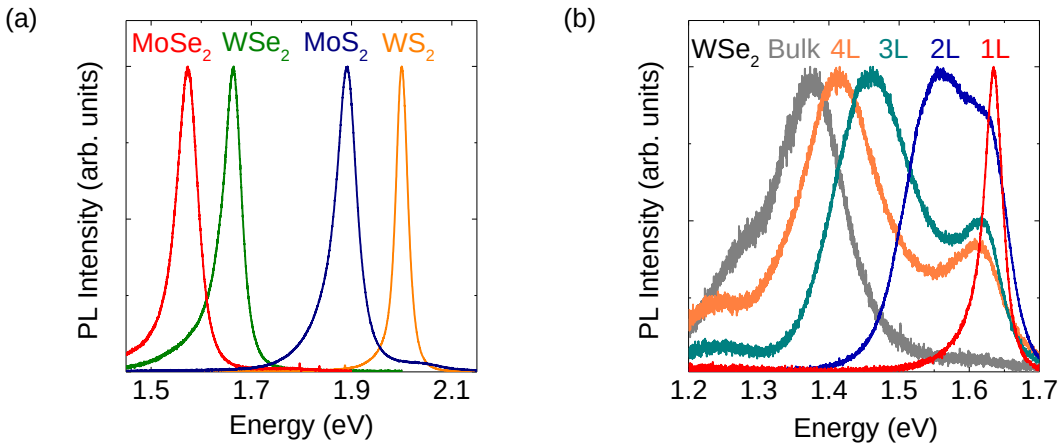

Figure 1.6: (a) PL spectra of exfoliated monolayer $MoSe_2$, WSe_2, MoS_2, and WS_2. (b) PL spectra of WSe_2 as a function of number-of-layers. Bulk WSe_2 is more than ten-layers thick. The spectra were obtained using 532 nm wavelength excitation at room temperature.

The variation of the TMDs' bandstructure between the monolayer and bulk limits is not sudden, but happens gradually with varying layer number. For example, Fig. 1.6(b) shows the PL spectra of WSe_2 for different number-of-layers from one to four, and bulk WSe_2, where the peak positions and shapes are indicative of their bandstructures. While the monolayer spectrum shows a single sharp peak, the spectra shapes get more complex and the peak positions shift to lower energies, i.e., lower bandgaps with increasing number-of-layers. This variation stems from the layer-number-dependent bandstructure of WSe_2 [35], and other TMDs, where optical transitions from multiple valleys contribute to the PL

spectra.

From the standpoint of 2DESs, an appealing feature of TMDs is their large effective mass carriers. Table 1.1 summarizes the effective masses for electrons (m_e^*) and holes (m_h^*) at the K valley extrema for monolayers of MoS_2, $MoSe_2$, WS_2, and WSe_2, calculated using density functional theory (DFT) calculations [36]. The heavy carriers in TMDs are expected to amplify electron-electron interaction effects even at relatively large carrier densities.

Table 1.1: Calculated carrier effective masses in select TMD monolayers from Ref. [36].

	Electron (m_e^*/m_e)	Hole (m_h^*/m_e)
MoS_2	0.56	0.64
$MoSe_2$	0.62	0.72
WS_2	0.33	0.43
WSe_2	0.35	0.46

A vital ingredient in fabricating TMD based 2DESs is an appropriate dielectric medium with a sufficiently low dielectric constant to enhance electron-electron interactions, while more importantly providing dielectric integrity, and clean interfaces in order to reduce extrinsic disorder. Hexagonal boron nitride (h-BN) is a layered material with a honeycomb lattice similar to graphene, and has been the dielectric of choice for high-quality graphene 2DESs [37], thanks to its atomically flat surface free of dangling bonds. The moderately low effective dielectric constants along the in-plane ($\kappa^{\perp}_{h\text{-BN}} = 6.9$) and out-of-plane ($\kappa^{||}_{h\text{-BN}} = 3.0$) directions [38, Appendix C], a bandgap of 6.0 eV [39], and a high dielectric breakdown strength of 1.0 V/nm [40] make h-BN the dielectric of choice for integration with TMDs.

Another avenue of research where TMDs have attracted considerable attention is in the field of semiconductor devices, e.g., field-effect transistors (FETs). The ever increasing complexity in continued scaling of semiconductor devices [41, 42] has prompted an intense interest in alternate materials and device concepts [43, 44]. Layered semiconductors such as TMDs are expected to offer several advantages over conventional three-dimensional (3D) semiconductors such as Si, thanks to the possibility of obtaining devices with ultrathin bodies down to the monolayer limit and atomically sharp interfaces [45].

A prerequisite for high-quality semiconductor devices, and also for electrical transport characterization of 2DESs is the existence of low-resistance Ohmic electrical contacts. The large bandgaps of TMDs make it non-trivial to create low-resistance Ohmic contacts, especially at low-temperatures. The moderate charge carrier mobilities, and lack of low-temperature-compatible electrical contacts have prevented systematic electrical transport

experiments in TMDs. The work presented in this dissertation started with a goal to develop Ohmic contacts to the valence band of WSe_2, and having found a reliable contact strategy, evolved into a study of the magnetotransport properties of holes in WSe_2.

1.3 Dissertation Outline

Chapter 2 outlines the challenges in making Ohmic contacts to TMDs, and discusses a device strategy employing platinum bottom-contacts and an *h*-BN top-gate dielectric to achieve Ohmic hole contacts to WSe_2. The contacts stay Ohmic down to a temperature of 2 K, where the hole mobilities approach 4000 cm^2/Vs in three/four-layer WSe_2. Temperature-dependent mobility measurements indicate phonon scattering at high-temperatures and Coulomb scattering, or defects at low-temperatures to be the dominant mobility limiting mechanisms affecting hole transport.

Chapter 3 begins with an overview of the classical and quantum Hall effects in 2DESs and continues to discuss magnetotransport measurements of holes in monolayer and bilayer WSe_2 Hall bar devices, which display Shubnikov–de Haas (SdH) oscillations and quantum Hall states (QHS) in high perpendicular magnetic fields. A Fourier analysis of the SdH oscillations reveals two-fold degenerate Landau levels (LLs) and a hole effective mass of $0.45m_e$ in both monolayer and bilayer WSe_2. The bilayer data also show carrier localization in the two constituent layers, signifying weak interlayer coupling and negative compressibility of holes in the bottom layer.

Chapter 4 continues with a discussion of the quantum Hall states in monolayer and bilayer WSe_2. The QHS reveal interesting transitions between even and odd filling factors as the hole density is tuned, which can be explained by a Zeeman-to-cyclotron energy ratio that changes as a function of density due to strong electron-electron interactions. Tilted magnetic field measurements reveal that the hole-spin is locked perpendicular to the WSe_2 plane, indicating that the holes reside in the K valleys in both monolayer and bilayer WSe_2.

Chapter 5 discusses magnetotransport measurements in trilayer WSe_2 which reveal holes populating two subbands with different effective masses, $0.5m_e$ and $1.2m_e$, associated with the K and Γ valleys, respectively. At a fixed total hole density, the K and Γ occupations can be tuned by an applied electric field, with Γ and K being the lowest energy states at low and high electric fields, respectively. *Ab initio* calculations support these findings and explain the shift of the valence band maxima with increasing electric field.

Chapter 6 summarizes the findings of the dissertation, and discusses the appeal of TMDs in comparison to other 2DES host materials for exploring novel quantum electronic phenomena. Finally, possible directions for future work are discussed.

Appendix A lists the WSe_2 samples whose data is presented in this dissertation, and Appendix B describes the fabrication techniques used to assemble them. Appendix C describes the measurement of the out-of-plane effective dielectric constant of the *h*-BN top-gate dielectrics used in the WSe_2 samples. Appendix D lists the symbols and Appendix E the acronyms used in this dissertation.

Chapter 2

High-Mobility Holes in WSe_2 Field-Effect Transistors

The most commonly used device for electrical characterization of TMDs is a field-effect transistor (FET). Properties such as the TMD carrier type and mobility can be easily obtained from measurements of the FET current as a function of the gate-bias [47, 48, 49]. More extensive low-temperature magnetotransport measurements are also performed using multiterminal FETs. A prerequisite for any kind of electrical measurements is the existence of electrical contacts which can inject carriers reliably into the TMD channel. However, the 2D nature of TMDs and their large bandgaps make it non-trivial to create low-resistance Ohmic contacts. Most commonly used metal contacts form large Schottky barriers at the metal–TMD interface in the absence of reliable TMD doping techniques, and drastically diminish drive currents, thereby preventing meaningful electrical measurements.

Since the recent revival of interest in TMDs as FET channel materials, much research has been devoted to obtaining low-resistance electrical contacts to TMDs [50, 51]. The first section of this chapter presents an overview of the contact Schottky barrier problem and techniques from literature to create low-resistance Ohmic hole contacts to WSe_2. The later sections discuss the feasibility of using platinum (Pt) electrodes as hole contacts to WSe_2 and the subsequent electrical characterization of Pt-contacted WSe_2 FETs.

By using a device design with the Pt contacts underneath the WSe_2, and an *h*-BN top-gate dielectric, top-gated FETs were realized with hole contacts that stay Ohmic down to cryogenic temperatures. The three/four-layer thick WSe_2 FETs show high ON/OFF current ratios $> 10^7$, hole field-effect mobilities of 140 cm^2/Vs at room temperature which increase up to 4000 cm^2/Vs at 2 K. The output characteristics exhibit current saturation and interesting negative differential resistance characteristics. Temperature-dependent transport measurements reveal a metal–insulator transition. The mobility shows a strong temperature dependence at high-temperatures, indicative of phonon scattering dominated transport, and saturates at low-temperatures, possibly limited by Coulomb scattering or defects.

Portions of this chapter have been published as Ref. [46]: H. C. P. Movva, A. Rai, S. Kang, K. Kim, B. Fallahazad, T. Taniguchi, K. Watanabe, E. Tutuc, and S. K. Banerjee, "High-Mobility Holes in Dual-Gated WSe_2 Field-Effect Transistors," *ACS Nano*, vol. 9, no. 10, p. 10402, 2015. The dissertator, H. C. P. Movva, fabricated and characterized the WSe_2 samples, and contributed to data analysis and writing the paper.

2.1 Transition Metal Dichalcogenide Field-Effect Transistors

Figure 2.1(a) shows the schematic cross section of a typical back-gated TMD FET with metal top-contacts. A degenerately doped Si substrate is used as a gate and a thermally grown SiO_2 layer (typically 300 nm thick) on top as the gate dielectric. Electrical contacts to the TMD are made by metal electrodes deposited on top of the TMD layer. Typical two-terminal field-effect measurements involve applying a drain bias (V_D), while grounding the source terminal ($V_S = 0$) and monitoring the drain current (I_D) as a function of the back-gate bias (V_{BG}).

In the absence of chemical bonding at the metal–TMD interface, i.e., metal contacts which do not affect the TMD bandstructure, the alignment of the metal Fermi level to the TMD bands is determined by the difference between the metal and TMD workfunctions. Figure 2.1(b) shows representative band diagrams of a TMD FET at $V_D = 0$ for the three possible regimes of operation at $V_{BG} < 0$, $= 0$, or > 0. It is assumed that the Fermi level (E_F) of the metal and TMD align at $V_{BG} = 0$ and that E_F is slightly above mid-gap between the TMD conduction (E_{cb}) and valence (E_{vb}) bands. There usually exist Schottky barriers at the metal–TMD interface for most metal–TMD combinations and therefore, most TMD FETs are Schottky FETs.

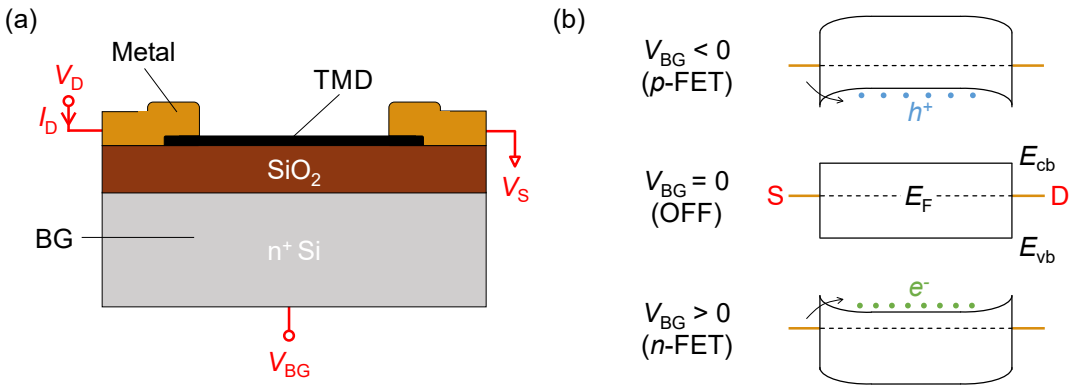

Figure 2.1: (a) Schematic cross section of a back-gated TMD FET with metal top-contacts. The biasing scheme is shown in red. (b) Representative band diagrams of a TMD FET at $V_D = 0$ for the three possible regimes of operation at $V_{BG} < 0$, $= 0$, or > 0. The location of E_F is assumed to be slightly above mid-gap between E_{cb} and E_{vb}. The arrows indicate injection of holes (electrons) into the valence (conduction) band of the TMD for $V_{BG} < 0$ (> 0).

At $V_{BG} = 0$, the FET is in the OFF state since the TMD channel is close to intrinsic, and depleted of both electrons and holes. On applying a non-zero V_D, the Schottky barriers obstruct injection of electrons and holes from the metal into the TMD conduction and

valence bands, respectively. When $V_{BG} < 0$, the TMD bands are displaced upwards in energy and the channel accumulates holes with a density proportional to $|V_{BG}|$. The valence band Schottky barrier width also narrows and holes can be injected from the metal contact into the TMD valence band for non-zero V_D, resulting in an I_D which increases with $|V_{BG}|$, the signature of a *p*-FET. Similarly, when $V_{BG} > 0$, the channel accumulates electrons and the resulting I_D vs V_{BG} shows an *n*-FET behavior. Most TMD FETs are therefore expected to show ambipolar characteristics.

To date, MoS_2 has received the most attention as an FET channel material among all TMDs, with the devices exhibiting predominantly *n*-type behavior [52, 53], in contrast to what is predicted by the simple model of Fig. 2.1(b). The departure is due to Fermi level pinning which can markedly affect the Schottky barrier heights [54], and consequently, in the case of MoS_2, severely reduce injection of holes into the channel [50, 55]. The exact nature of Fermi level pinning depends on the chemistry at the metal–TMD interface.

Ambipolar characteristics have been observed more readily in WSe_2 FETs, where the issue of Fermi level pinning is less severe [47, 56, 57]. The high-propensity of chalcogen vacancies in sulfide TMDs tends to pin the Fermi level close to the conduction band edge, creating a large Schottky barrier to the valence band, thereby suppressing hole injection [58]. Figure 2.2(a) shows ambipolar I_D vs V_{BG} for a few-layer WSe_2 FET on a 300 nm SiO_2/Si substrate contacted using nickel (Ni) electrodes. While the data show considerable *p*-type conduction, the higher I_D values for $V_{BG} = 60$ V compared to -60 V indicate alignment of the Ni Fermi level slightly closer to the conduction band edge, similar to the representative band diagrams of Fig. 2.1(b), and also determined from recent experiments [59]. The hysteresis between the forward and reverse sweeps is due to charge-trapping at the WSe_2–SiO_2 interface [60].

Selective injection of holes has proven to be a more arduous problem for TMDs. In light of its less severe Fermi level pinning, the TMD that has attracted most attention for *p*-FETs is WSe_2, with early reports of bulk WSe_2 FETs showing hole mobilities approaching 500 cm^2/Vs [47]. Subsequently, monolayer WSe_2 FETs have also been demonstrated using high workfunction palladium (Pd) contacts [61]. Figure 2.2(b) shows I_D vs V_{BG} for a monolayer WSe_2 FET on a 300 nm SiO_2/Si substrate contacted using Pd electrodes, which displays a predominantly *p*-type behavior.

However, in the absence of considerable Fermi level pinning, the Schottky barrier heights to both the WSe_2 conduction and valence bands tend to be high due to its large bandgap, resulting in large contact resistances and low drive currents as shown by Fig. 2.2 data, a problem which worsens at low-temperatures. Considerable research effort has been devoted to addressing the problem of creating low-resistance Ohmic contacts to WSe_2, and all TMDs in general [50] in order to probe their intrinsic electronic transport properties.

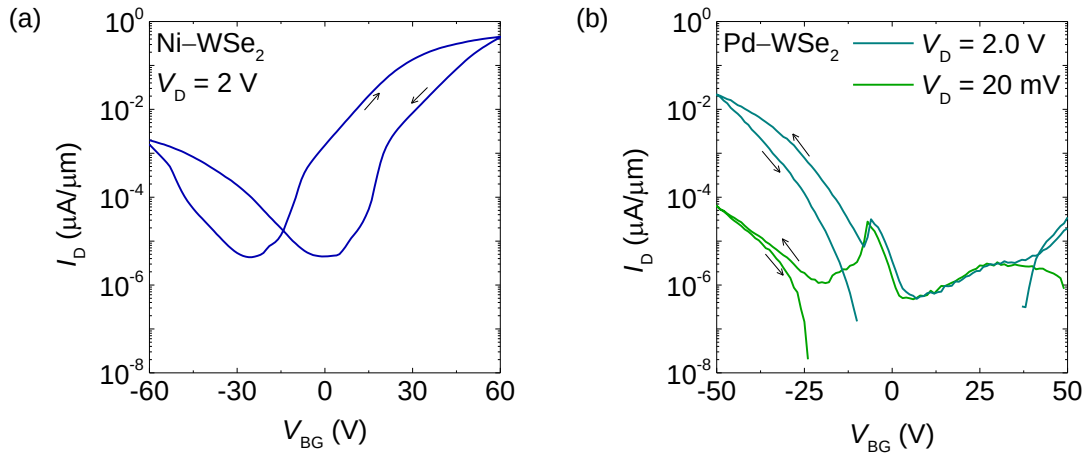

Figure 2.2: (a) I_D vs V_{BG} for a few-layer WSe_2 FET with Ni top-contacts. (b) I_D vs V_{BG} for a monolayer WSe_2 FET with Pd top-contacts. The back-gate dielectric is 300 nm of SiO_2.

2.1.1 Electrical Contacts to the Valence Band of WSe_2

The most commonly used contact metal for WSe_2 p-FETs in literature is Pd, motivated by its relatively high workfunction, $\phi_{Pd} \approx 5.5$ eV [62]. In the absence of Fermi level pinning, the Fermi level of Pd is intuitively expected to lie below the valence band edge of few-layer WSe_2 with an electron affinity, $\chi_{WSe_2} \approx 4.1$ eV, and a bandgap, $E_g \approx 1.3$ eV [60], i.e., $\phi_{Pd} \gtrsim \chi_{WSe_2} + E_g$, resulting in low-resistance contacts to the valence band. Experimental data however suggest a considerable valence band Schottky barrier height (Φ_{SB}) up to 0.38 eV for Pd contacts to few-layer WSe_2 [57]. The variance is due to inevitable chemical bonding between the metal and TMD orbitals which modifies their original energy levels, and results in a Schottky barrier height which is very different from the intuitively expected value [54, 63].

In essence, experimental Schottky barrier heights and thus, the nature of contacts are rarely in agreement with the intuitive picture. Further, the higher bandgap of monolayer WSe_2 ($E_g \approx 2.2$ eV) [64, 65] is expected to result in a an even larger Schottky barrier height, as suggested by the moderate I_D values of Fig. 2.2(b) data. Several interesting contact strategies have been attempted in literature to address the problem of hole contacts to WSe_2 such as surface transfer doping [61] and ionic liquid doping [66] of the source and drain access regions, ionic liquid doped graphene [67, 68] and high-workfunction 2D materials [69, 70, 71] as contacts, sub-stoichiometric hole injecting oxide layers between the contact metal and WSe_2 [72, 73], and plasma-etched contact regions [74], among others. Table 2.1 summarizes some of these contact strategies.

Table 2.1: Survey of electrical contact strategies employed for WSe_2 p-FETs.[a] The approximate (indicated by "∼") contact resistance values are extracted assuming the two-terminal channel resistance is dominated by the contact resistance. All contact resistance values are at room temperature.

Ref.	Layers	Contact material	Contact resistance	Comment
[61]	1	NO_2-doped p^+-WSe_2	~ 50 k$\Omega\cdot\mu$m	Air-unstable
[66]	1	Ionic liquid doped p^+-WSe_2	10 k$\Omega\cdot\mu$m	Ion-gel on top
[67]	4 – 12	Ionic liquid doped p^+-graphene	2 k$\Omega\cdot\mu$m	h-BN encapsulated
[68]	3		~ 10 k$\Omega\cdot\mu$m	
[69]	5	Few-layer Nb-doped p^+-WSe_2	~ 0.3 k$\Omega\cdot\mu$m	h-BN encapsulated
[70]	8	Few-layer $NbSe_2$	~ 50 k$\Omega\cdot\mu$m	h-BN encapsulated
[71]	Few		540 k$\Omega\cdot\mu$m	$\Phi_{SB} = 50$ meV
[72]	> 40	Pd on MoO_x	~ 1 M$\Omega\cdot\mu$m	$\Phi_{SB} = 0.29$ eV
[73]	3	Ti/Au on WO_x overlayer	66 k$\Omega\cdot\mu$m	$\Phi_{SB} = 0.24$ eV
[74]	5 – 8	Pd on O_2 plasma treated WSe_2	5 k$\Omega\cdot\mu$m	h-BN encapsulated

[a] Nitrogen dioxide (NO_2) is a p-type surface transfer dopant [61] and niobium (Nb) a p-type substitutional dopant for WSe_2 [69]. $2H$ niobium diselenide ($NbSe_2$) is a metallic TMD whose Fermi level lies below the valence band edge of WSe_2 [70]. Sub-stoichiometric molybdenum trioxide (MoO_x, $x < 3$) [72] and tungsten trioxide (WO_x, $x < 3$) [73] are high-workfunction hole injecting layers. Titanium (Ti)/ gold (Au) electrodes on a WO_x overlayer result in p-type contacts to WSe_2. An oxygen (O_2) plasma partially etches and modifies the WSe_2 surface [74].

While improving hole injection, these techniques have limitations, such as poor environmental stability, restrictions on the WSe_2 thickness, increased impurities in proximity of the WSe_2 channel which increase disorder, thereby reducing the carrier mobility, and sizable Schottky barrier heights which affect low-temperature performance. Probing the intrinsic transport properties of WSe_2 requires the channel to be free of unwanted charged impurities and extraneous disorder which can degrade the carrier mobility. Trapped charges at the WSe_2–SiO_2 interface which cause hysteresis in Fig. 2.2 data are one such example of extrinsic disorder which also severely deteriorate mobilities.

Therefore, in addition to reliable electrical contacts, a clean dielectric environment is essential to eliminate debilitating contributions from extrinsic factors to electronic transport in TMDs. Hexagonal boron nitride has been shown to be a desirable dielectric in view of its ultraflat surface free of dangling bonds, thereby helping preserve the intrinsic transport properties of TMDs [37, 75].

The following sections discuss the suitability of Pt as a contact metal to the valence band of WSe_2 and subsequent electrical measurements of Pt contacted WSe_2 FETs. Three/four-layer WSe_2 flakes were chosen initially in light of their smaller bandgaps compared to monolayer WSe_2.

2.2 WSe_2 FETs with Pt Bottom-Contacts

The high workfunction ($\phi_{Pt} \approx 6.0$ eV) of Pt [76, 77] places its Fermi level below the valence band edge of few-layer WSe_2 ($\chi_{WSe_2} + E_g \approx 5.5$ eV) [60]. In the zeroth order approximation, this band alignment is intuitively expected to result in Ohmic p-type contacts. However, direct deposition of Pt on WSe_2 as a top-contact is impractical due to its poor adhesion. While this problem is usually addressed by depositing a thin adhesion layer of chromium (Cr) or Ti prior to Pt deposition, it would reduce the effective metal workfunction at the contact interface and defeat the purpose of using Pt in the first place.

A way to circumvent this problem is to place the Pt contacts underneath the WSe_2 flake. The Pt electrodes can be deposited with an appropriate adhesion layer at the bottom without affecting the top surface workfunction. Placing WSe_2 on top of the Pt electrodes would contact the pristine Pt top surface, whose high-workfunction would still be preserved. Furthermore, Pt being a noble metal is immune to oxidation and contamination which keeps the top-surface clean. Figure 2.3(a) shows the schematic cross section of a dual-gated WSe_2 FET with Pt bottom-contacts along with its biasing scheme, and Fig. 2.3(b) shows the optical micrograph of LD55, a typical three/four-layer WSe_2 FET sample.

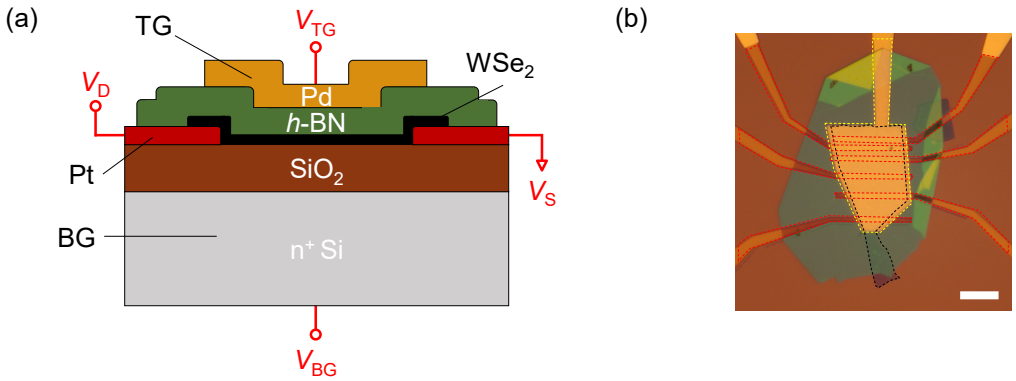

Figure 2.3: (a) Schematic cross section of a dual-gated WSe_2 FET with Pt contacts underneath the WSe_2, an h-BN top-gate dielectric, and a Pd top-gate. The biasing scheme is shown in red. (b) Optical micrograph of LD55, a typical WSe_2 FET. The top-gate, Pt contacts, and WSe_2 flake are outlined by yellow, red, and black dashed lines, respectively. The scale bar is 10 μm.

The FETs were fabricated using exfoliated flakes obtained from bulk WSe_2 and h-BN crystals. First, three/four-layer WSe_2 and 10 – 30 nm thick h-BN flakes were exfoliated on independent SiO_2/Si substrates. On a separate substrate, thin Cr/Pt (2 nm/ 10 nm) electrodes were patterned using a combination of electron-beam lithography (EBL), electron-beam metal evaporation (EBME), and lift-off. Multiple electrodes were patterned to enable four-point measurements to eliminate contact resistance effects and extract the intrinsic properties of the WSe_2 channel. Using a custom micromanipulator–microscope setup and a silicone stamp spin-coated with a heat-release polymer [78, 79], the h-BN and WSe_2 flakes were "picked-up" sequentially and the resulting h-BN/WSe_2 stack subsequently aligned with and "placed" onto the Cr/Pt electrodes. Finally, a local Pd top-gate, and metal bond pads were patterned using EBL, EBME, and lift-off. A more detailed discussion on the "pick and place" technique and other fabrication steps is presented in Appendix B. Three different three/four-layer WSe_2 FETs, LD39, LD55, and LD56 were investigated in this study, all with consistent results. Appendix A provides the samples' details.

The effectiveness of the Pt bottom-contacts was evaluated by performing electrical measurements using the biasing scheme shown in Fig. 2.3(a). Electrical measurements were conducted using a semiconductor parameter analyzer (Agilent B1500A) in a vacuum probe station (Lakeshore FWPX). Figure 2.4(a) shows I_D vs V_{TG} at various V_D values, and $V_{BG} = 0$ V at room temperature in a four-layer WSe_2 FET, LD56, with a channel length, $L = 6$ μm, and width, $W = 12$ μm. At the lowest $V_D = 1$ mV, the FET shows predominant p-type conduction and negligible n-type conduction. With every decade of increase in V_D, the p-type I_D increases by a decade, whereas the n-type I_D increases nonlinearly. This behavior hints at Ohmic and Schottky nature of the Pt bottom-contacts to the valence and conduction bands of WSe_2, respectively.

The emerging ambipolar characteristics in Fig. 2.4 are similar to the data of Fig. 2.2 with conventional top-contacts, and are due to emanant injection of electrons into the WSe_2 conduction band at large V_D values. Negligible conduction near $V_{TG} = 0$ V indicates the intrinsic nature of WSe_2, and evidence of clear subthreshold and insulating regimes, along with a large p-type ON/OFF current ratio $> 10^7$ at $V_D = 1$ V signify no unintentional doping. Negligible hysteresis signifies minimal charge-trapping, and therefore, clean interfaces in the device and absence of trapping centers in the WSe_2.

The contrasting p-type and n-type behavior of the contacts is apparent in the low-bias I_D vs V_D data for $V_{TG} \leq 0$ V and $V_{TG} \geq 0$ V shown in Figs. 2.4(b) and 2.4(c), respectively. A salient difference is the p-type I_D vs V_D being linear and nearly three orders of magnitude larger than the nonlinear and asymmetric n-type I_D vs V_D, indicative of a large Schottky barrier for Pt contacts to the conduction band. These data suggest that the Pt bottom-contacts are indeed favorable for injecting holes into the valence band of WSe_2. Recent

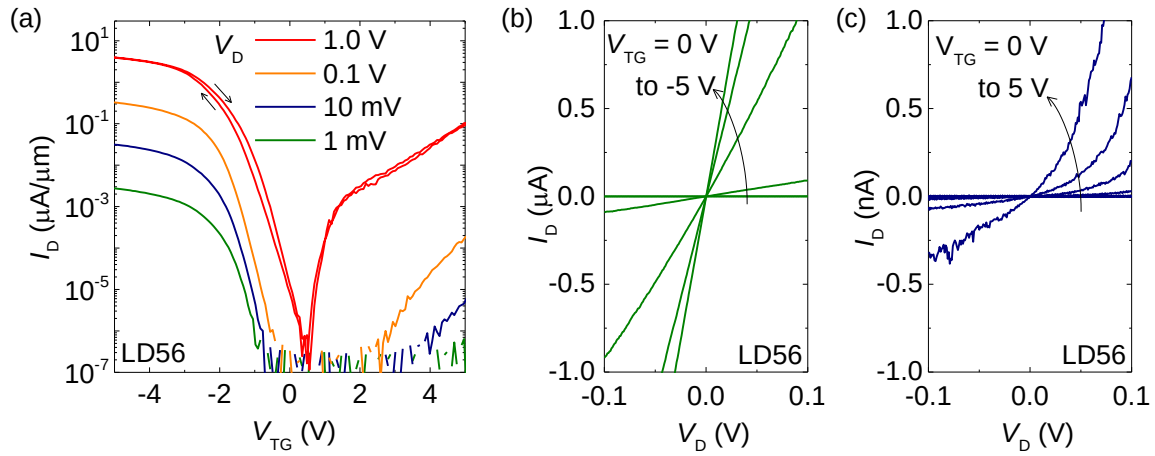

Figure 2.4: (a) I_D vs V_{TG} at various V_D values and at room temperature in a four-layer WSe_2 FET, LD56, with a channel length $L = 6$ μm show p-type conduction at V_D as low as 1 mV. (b) The corresponding low-bias I_D vs V_D for various V_{TG} values from 0 V to −5 V in steps of −1 V show Ohmic p-type contacts. (c) The low-bias I_D vs V_D for V_{TG} between 0 V and 5 V in 1 V increments are symptomatic of Schottky contacts. The measurements are at $V_{BG} = 0$ V.

DFT calculations predict the Schottky barrier between Pt and the valence band of WSe_2 to vanish and result in Ohmic p-type contacts, thanks to effective hybridization between the Pt d-orbitals and the WSe_2 valence band states [80]. Lower workfunction metals such as indium and silver would intuitively be preferable as n-type contacts [81].

2.3 Field-Effect Mobility and Contact Resistance

Multiterminal four-point measurements were used to extract the intrinsic hole mobilities and contact resistances of the WSe_2 FETs. Figure 2.5(a) shows the two-point conductance (G_{2pt}) and four-point, intrinsic conductance (G_{4pt}) vs V_{TG} in LD56 at room temperature. While $G_{2pt} = I_D/V_D$ is measured as the conductance between an adjacent pair of contacts, $G_{4pt} = I_D/\Delta V$ is measured using the voltage difference (ΔV) measured between the same two contacts when biasing an outer pair of contacts.

The difference between G_{2pt} and G_{4pt} is due to a substantial voltage drop across the contacts which reduces the effective drain voltage on the WSe_2 channel, thereby reducing G_{2pt}. The field-effect mobility (μ_{FE}) can be calculated using

$$\mu_{FE} = \frac{1}{C_{TG}} \frac{L}{W} \frac{dG}{dV_{TG}} \tag{2.1}$$

where C_{TG} is the top-gate capacitance, and $G = G_{2pt}$ yields the two-point field-effect

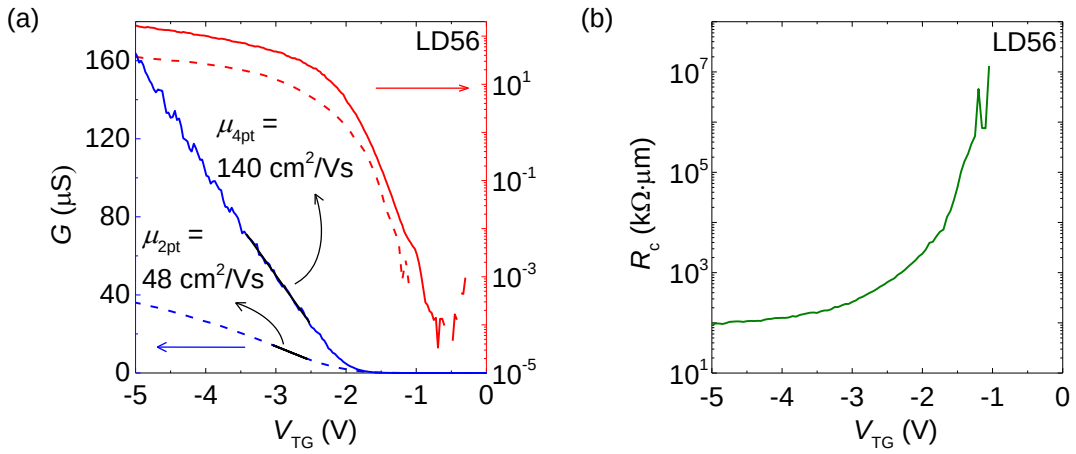

Figure 2.5: (a) Two-point (dashed lines) and four-point (solid lines) G vs V_{TG} in linear (left axis, blue) and log (right axis, red) scales in LD56 at room temperature. The black lines show linear fits which yield μ_{2pt} = 48 cm^2/Vs and μ_{4pt} = 140 cm^2/Vs. (b) R_c vs V_{TG} extracted from panel (a) data show strong V_{TG}-modulation of R_c. The measurements are at V_{BG} = 0 V.

mobility (μ_{2pt}) and $G = G_{4pt}$ yields the four-point, intrinsic field-effect mobility (μ_{4pt}). For LD56 which has a top-gate h-BN thickness of 18 nm, and using the h-BN out-of-plane effective dielectric constant of 3.0,[1] C_{TG} = 150 nF/cm^2. Using Eq. 2.1 for the G vs V_{TG} data of Fig. 2.5(a) gives μ_{2pt} = 48 cm^2/Vs and μ_{4pt} = 140 cm^2/Vs. The intrinsic field-effect mobility of 140 cm^2/Vs for holes in WSe_2 compares favorably with prior reports from literature [66, 67, 68]. The considerably lower μ_{2pt} value compared to μ_{4pt} is due to the detrimental effect of contact resistance on G_{2pt}.

The specific contact resistance (R_c) can be determined from the difference of the two-point and four-point resistances as

$$R_c = \frac{W}{2}\left(\frac{1}{G_{2pt}} - \frac{1}{G_{4pt}}\right) \tag{2.2}$$

where it is assumed that the source and drain contact resistances are equal. Figure 2.5(b) shows R_c vs V_{TG} extracted from Fig. 2.5(a) data. The contact resistance shows a strong V_{TG} dependence, reducing with increasing $|V_{TG}|$, and asymptotically approaching 100 kΩ·μm at $V_{TG} = -5$ V. The contact resistance trend mirrors the inverse of the channel conductance trend and is due to modulation of the WSe_2 contact regions' resistance by the top-gate.

[1]The out-of-plane effective dielectric constant of h-BN is extracted using capacitance values measured from magnetotransport measurements in WSe_2 Hall bar samples, and is discussed in Appendix C.

Variation of contact resistance with gate-bias is not observed in traditional MOSFETs due to their highly doped source and drain regions [82]. However, if they are undoped, as in typical TMD FETs, the gate can electrostatically modulate the contact regions, and in turn, the contact resistance.

The data of Fig. 2.5 underline the importance of four-point measurements in extracting the intrinsic transport properties of TMDs. Two-point mobility measurements severely underestimate the channel mobility, especially in TMD FETs, where the contact resistances are typically larger than the channel resistance.

2.4 Effect of Dual-Gating and Output Characteristics

The back-gate provides a second knob to tune the carrier density in the WSe_2 channel, and therefore the FET characteristics. Figure 2.6(a) shows G_{2pt} vs V_{BG} at various values of V_{TG} and Fig. 2.6(b) shows G_{2pt} vs V_{TG} at various values of V_{BG} in LD56, measured at room temperature. While Fig. 2.6(a) data show a large modulation of the ON state conductance with varying V_{TG}, the ON state conductance in Fig. 2.6(b) remains relatively unchanged with varying V_{BG}. The stark difference in the FET response to varying V_{TG} and V_{BG} can be understood by examining the electrostatics in the device.

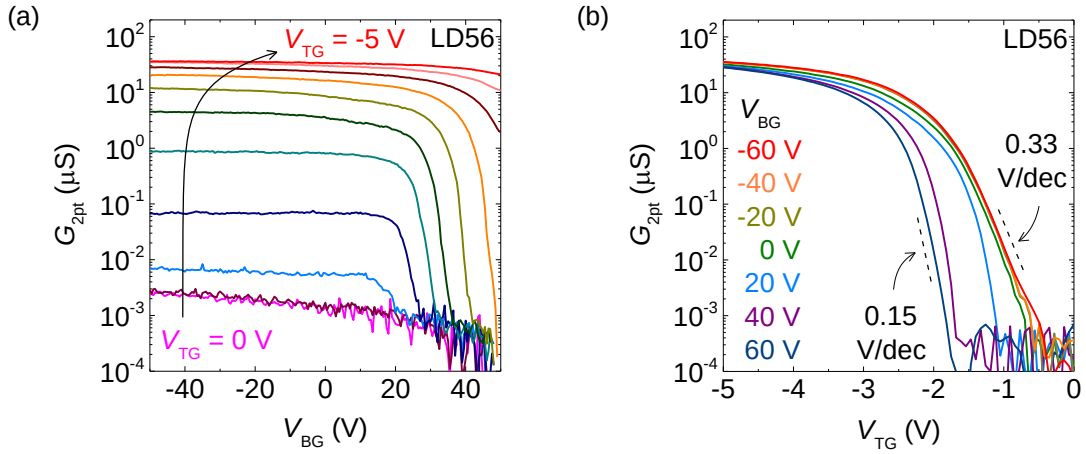

Figure 2.6: (a) G_{2pt} vs V_{BG} at V_{TG} values varying from 0 V to −5 V in steps of −0.5 V in LD56. (b) G_{2pt} vs V_{TG} at various V_{BG} values in LD56. The dashed lines indicate the regions where the SS values are evaluated. The data are at room temperature.

Figure 2.7(a) shows a schematic of the electrostatic field-lines from the top- and back-gate in a WSe_2 FET with bottom-contacts. While the top-gate can modulate the WSe_2 regions both in the channel and on top of the contacts, the back-gate can only modulate the

WSe_2 channel, but not the contact regions due to screening by the contacts. Back-gated transfer characteristics are therefore contact resistance limited, especially at low $|V_{TG}|$.

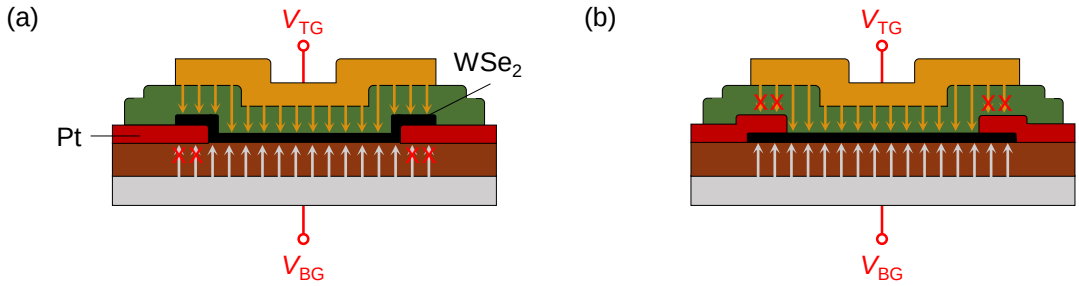

Figure 2.7: (a) Schematic of the electrostatic field-lines from the top- and back-gate in a WSe_2 FET with bottom-contacts. (b) Schematic of the electrostatic field-lines in an FET with conventional top-contacts. The field-lines marked by red crosses indicate that they are screened by the contacts.

When $V_{TG} = 0$ V in Fig. 2.6(a), the contact regions are highly resistive, and inhibit current flow through the channel, resulting in a low G_{2pt} irrespective of the V_{BG} value. As V_{TG} is progressively made more negative, the contact resistance decreases, and in turn, G_{2pt} increases in the ON state. The G_{2pt} saturation is due to the contact resistance dominating the total channel resistance. Since the contact resistance can be modulated much more effectively by V_{TG}, G_{2pt} in the ON state is more sensitive to V_{TG} than V_{BG}. The shift in V_{BG} at the onset of saturation with varying V_{TG} values is due to the effect of dual-gating of the channel. A more negative V_{TG} accumulates additional holes in the channel which then requires a more positive V_{BG} to deplete.

The weak dependence of the ON state G_{2pt} with varying V_{BG} values in Fig. 2.6(b) is due to the dominant contact resistance in this regime which is determined only by V_{TG}. A noteworthy feature in Fig. 2.6(b) data is the subthreshold swing (SS) which shows evidently different slopes when $V_{BG} \leq 0$ V and > 0 V. For $V_{BG} \leq 0$ V, the channel accumulates holes at $V_{TG} = 0$ V, and the SS $\simeq 0.33$ V/dec is determined by the rate at which the contacts turn ON. In contrast, for $V_{BG} > 0$ V, the channel is populated with electrons at $V_{TG} = 0$ V, analogous to a conventional p-MOSFET with a nominally n-type channel. The SS $\simeq 0.15$ V/dec is consequently dictated by thermionic emission over the barrier between the contacts and the channel, and is therefore lower.

The data of Fig. 2.6(a) are closely similar to the transfer characteristics of conventional WSe_2 FETs with top-contacts, but with the roles of the top- and back-gates reversed [61, 68]. Figure 2.7(b) shows a schematic of the electrostatic field-lines in a conventional TMD FET where the top-gate has no electrostatic access to the contact regions, analogous to the back-gate in Fig. 2.7(a). The back-gate in the bottom-contacted WSe_2 FETs can

be used as a knob to tune the FET characteristics by modulating only the channel density without significantly affecting the contact resistance.

Figure 2.8 shows I_D vs V_D at various V_{TG} and V_{BG} values in LD56 at room temperature. First, there is a clear evidence of current saturation at large negative V_D for all V_{TG} and V_{BG} values. The maximum drive current of ~ 5 μA/μm obtained at $V_{TG} = -5$ V is comparable to values reported for WSe_2 p-FETs with chemically doped source and drain contacts [61]. A second interesting feature is the negative differential resistance (NDR) behavior prior to the onset of current saturation. Third, there is considerable hysteresis between the forward and reverse sweeps near the NDR region. Both the NDR and hysteresis amplitudes are correlated and decrease with increasing V_{BG} from -40 V to 40 V and also decrease with decreasing $|V_{TG}|$ values.

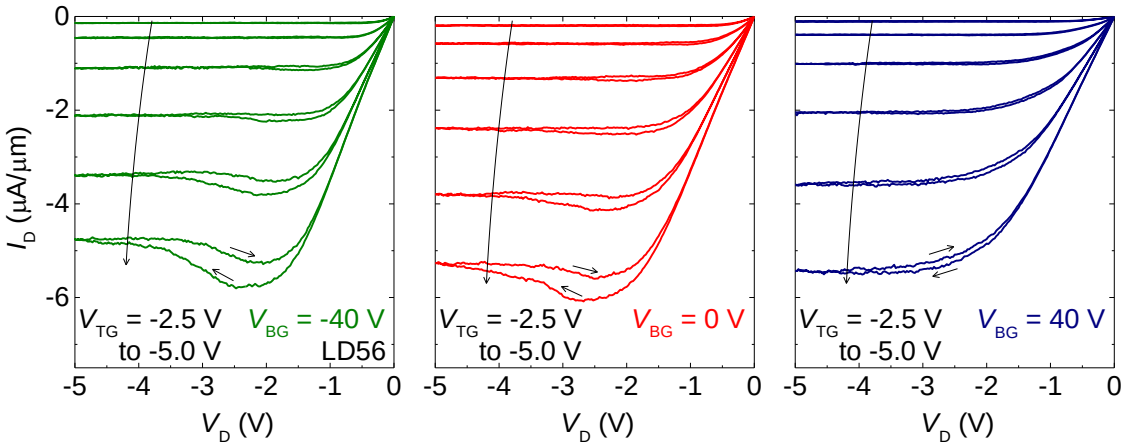

Figure 2.8: I_D vs V_D at various V_{TG} values from -2.5 V to -5.0 V in steps of -0.5 V and at different V_{BG} values of -40 V (left panel), 0 V (center panel), and 40 V (right panel), at room temperature, in LD56.

The NDR behavior that is commonly observed in FETs with III–V channel materials is due to a transferred electron mechanism, referred to as the Gunn effect [82]. At high lateral electric fields, electrons get transferred to a lower mobility satellite valley which results in a reduction of the current and thus an NDR characteristic. Prior reports of NDR in MoS_2 FETs have also been attributed to a transferred electron mechanism between satellite valleys and/or a self-heating effect [83]. The peculiar V_{BG} dependence of the NDR in LD56, a four-layer WSe_2 FET suggests that the vertical carrier distribution among the WSe_2 layers plays a key role.

Application of V_{BG} changes the position of the charge centroid in the WSe_2, with negative (positive) V_{BG} shifting the holes closer to (further away from) the SiO_2 substrate.

A real space transfer between the high-mobility top layer closer to the *h*-BN and the low-mobility bottom layer closer to the SiO_2 substrate could lead to an NDR behavior. The hysteresis dependence on V_{BG} is further suggestive of hot carrier trapping at the WSe_2–SiO_2 interface [60] which increases (decreases) when the carriers are closer to (further away from) the SiO_2 substrate. The persistent NDR in both the forward and reverse sweeps suggests that a transferred electron mechanism could be at play, in view of the close energy proximity between the valence band Γ and *K* valleys in four-layer WSe_2 [35].[2] However, the hysteresis makes it difficult to unambiguously draw this conclusion.

2.5 Temperature-Dependence and Metal–Insulator Transition

To evaluate the performance of the Pt contacts at low-temperatures, the WSe_2 FETs were cooled in a Physical Properties Measurement System (PPMS) down to a temperature, $T = 2$ K. Figure 2.9(a) shows the low-bias I_D vs V_D at various values of V_{TG} at $T = 2$ K in a trilayer WSe_2 FET, LD39. While I_D vs V_D at low $|V_{TG}|$ show a slight nonlinearity, the data are linear at large $|V_{TG}|$, where the contact regions are populated with holes, indicating that the Ohmic nature of the Pt contacts is retained down to $T = 2$ K.

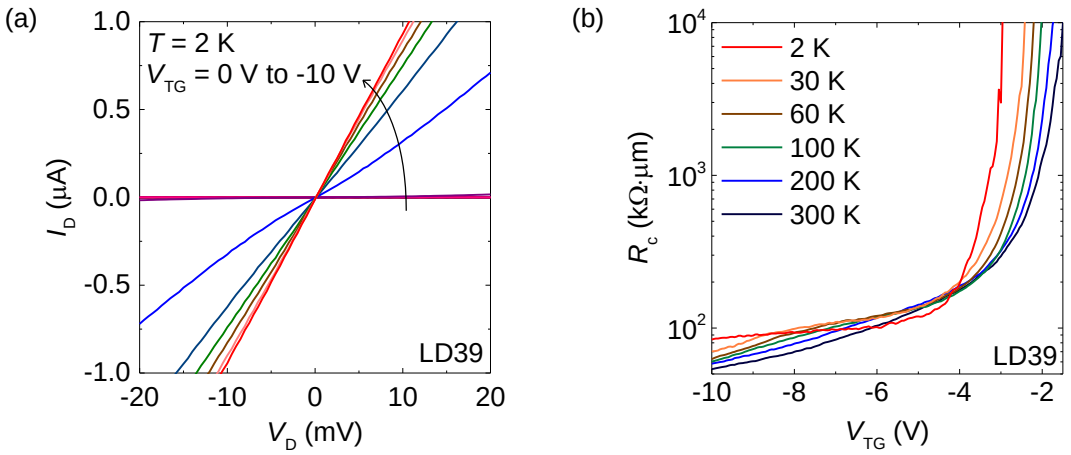

Figure 2.9: (a) Low-bias I_D vs V_D at various V_{TG} values from 0 V to −10 V in steps of −1 V at $T = 2$ K in a trilayer WSe_2 FET, LD39. (b) R_c vs V_{TG} at various temperatures in LD39. The measurements are at $V_{BG} = 0$ V.

[2]Chapter 5 discusses valley populations in trilayer WSe_2 where holes are found to populate both the Γ and *K* valleys depending on the transverse electric field. The *K* valley holes reside closer to, and the Γ holes further away from the top-gate. Varying V_{BG} changes the electric field and therefore the relative Γ and *K* valley populations, conceivably explaining the V_{BG} dependence of the NDR characteristics.

The Ohmic Pt contacts permit four-point measurements in order to extract the channel conductivity and contact resistances. Figure 2.9(b) shows R_c vs V_{TG} at various T values in LD39 calculated using Eq. 2.2. The data show a relatively unvarying R_c vs V_{TG} for $V_{TG} < -4$ V over the entire temperature range, indicating the absence of a noticeable Schottky barrier for the Pt contacts to the valence band of WSe_2, and substantiating the theoretical predictions of Ref. [80]. In contrast, contacts with a sizable Schottky barrier show a drastic increase of the contact resistance with decreasing temperature [82].

Temperature-dependent measurements of the channel conductivity, $G_\square = G_{4pt} \times L/W$, were performed using small excitation current, low-frequency (9 – 13 Hz) lock-in techniques in order to minimize self-heating, especially at low-temperatures. The linear I_D vs V_D enabled such measurements at an excitation current as low as $I = 10$ nA. Figure 2.10(a) shows $G_\square$ vs V_{TG} as a function of varying temperature in LD39.

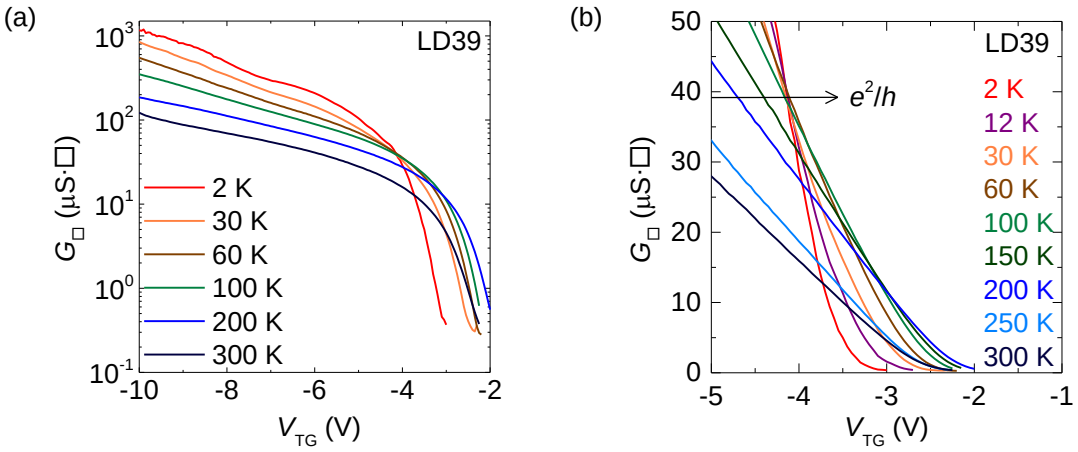

Figure 2.10: (a) $G_\square$ vs V_{TG} at various temperatures in LD39. (b) Close up of panel (a) data near the crossover at $G_c = 39\ \mu S \simeq e^2/h$. The measurements are at $V_{BG} = 0$ V.

Two distinct regimes are evident in the temperature dependence of $G_\square$; for $V_{TG} < -4$ V, $G_\square$ increases monotonically with decreasing temperature, and for $V_{TG} > -4$ V, $G_\square$ does not follow a monotonic trend. The crossover between these two regimes suggests a metal–insulator transition (MIT), consistent with previous observations for a variety of 2D electron, and hole systems, including TMDs [66, 67, 84, 85]. Figure 2.10(b) shows a close-up of the MIT crossover occurring at a conductivity, $G_c = 39\ \mu S \simeq e^2/h$; e is the electron charge and h is the Planck constant. To better understand the nature of the metal–insulator transition in WSe_2, the results are discussed using the theoretical framework developed to explain the phenomenon in a large set of 2D electron and hole systems [86, 87].

According to the scaling theory of localization [19], all non-interacting 2DESs exhibit an insulating ground state in the limit of zero-temperature due to the inevitable presence of disorder which leads to localization of charge carriers. However, at high carrier densities, and in samples with reduced disorder, the localization length can exceed the sample size. In this weakly localized state, the 2DES can exhibit an apparent metallic behavior, explained in terms of the temperature-dependent screening of fixed charged impurities. For high sample disorder, or at low carrier densities, the system becomes strongly localized, and the temperature-dependence of conductivity displays the expected insulating behavior. This crossover from a metallic weakly localized regime at high carrier densities to an insulating strongly localized regime at low carrier densities has been used to explain the MIT in 2D semiconductors [84, 86].

To evaluate if the MIT in WSe_2 is indeed caused by a similar crossover, the following density-dependent temperature scales are examined [86]: the Fermi temperature (T_F) which represents the Fermi energy of the holes, the Bloch–Grüneisen temperature (T_{BG}) which defines the phonon temperature scale, and the Dingle temperature (T_D) which represents the temperature scale associated with disorder.

$$k_B T_F = \mathcal{E}_F = \frac{\hbar^2 k_F^2}{2m^*} = \frac{\hbar^2 \pi p_c}{m^*} \tag{2.3}$$

$$k_B T_{BG} = 2\hbar k_F v_{ph} = 2\hbar v_{ph}\sqrt{2\pi p_c} \tag{2.4}$$

$$k_B T_D = \Gamma_D = \frac{\hbar}{2}\left(\frac{e}{m^*\mu}\right) \tag{2.5}$$

Here, $\mathcal{E}_F$ is the Fermi energy, $k_F = \sqrt{2\pi p_c}$ is the Fermi wavevector, p_c is the carrier density at crossover, m^* is the hole effective mass, v_{ph} is the phonon velocity, Γ_D is the impurity-scattering induced level broadening determined by μ, the hole mobility, k_B is the Boltzmann constant, and $\hbar$ is the reduced Planck constant. A degeneracy factor of two is used to relate k_F and p_c, $m^* = 1.2m_e$, where m_e is the free electron mass, and $v_{ph} = 3.3 \times 10^3$ m/s is the phonon velocity in WSe_2 [88].[3]

An unambiguous evidence of a weak localization mediated metallic phase requires $T_D < T_F < T_{BG}$ at the crossover point. The latter condition, $T_F < T_{BG}$ is necessary to rule out

[3]Chapter 5 data on holes in trilayer WSe_2 reveal a degeneracy of two for both the K (two valleys with spin-valley locking) and Γ (one valley with two spins) valleys. The effective mass, $m^* = 1.2m_e$ is chosen based on the assumption that the holes reside in the Γ valley at the MIT crossover point.

contribution from phonon scattering which can also lead to an apparent metallic behavior for $T > T_{BG}$. The earlier condition, $T_D < T_F$ is required to ensure that disorder is sufficiently weak, in the absence of which a metallic behavior would not be observed in the first place. From Fig. 2.10 data, the crossover density is estimated to be $p_c = 3.7 \times 10^{12}$ cm^{-2}, which yields $T_F = 86$ K and $T_{BG} = 24$ K.[4] Since $T_F > T_{BG}$, the metallic behavior in Fig. 2.10 could likely be due to phonon scattering. For acoustic phonon scattering at $T > T_{BG}$, $G_\square$ is expected to follow a $\sim T^{-1}$ law, resulting in an apparent metallic behavior [89].

The insulating phase, on the other hand, is the expected behavior for a 2DES. While a strong localization effect at low carrier densities results in an insulating behavior, an alternate semiclassical percolation model can also explain this phenomenon [87, 90]. Density inhomogeneities induced by disorder are believed to block conductive paths in the channel at low carrier densities, leading to an insulating state due to percolation of carriers between the potential fluctuations. The similar values of $G_c = O(e^2/h)$ expected for both the localization, and percolation mechanisms make it difficult to choose one to explain the insulating phase in the WSe_2 devices, as is the case for other 2DESs [86].

The apparent metallic behavior mediated by phonon scattering is closely similar to observations made in Si MOSFETs in the 1970s [16, 91]. A strong-to-weak localization driven MIT requires $T_F < T_{BG}$, which places an upper limit on the crossover density, $p_c < 3.0 \times 10^{11}$ cm^{-2} for WSe_2 holes in the Γ valley. Additionally, $T_D < T_F$ also places a lower limit on the mobility at crossover, $\mu_c > 800$ cm^2/Vs. For comparison, $\mu_c = 65$ cm^2/Vs for Fig. 2.10 data at $T = 2$ K. Observation of a weak localization driven metallic behavior therefore requires samples with mobilities higher by at least a factor of $10 - 15$.

2.6 Hole Mobilities in WSe_2

To determine the scattering mechanisms limiting hole transport in WSe_2, the mobility was studied as a function of temperature. Figure 2.11(a) shows the four-point field-effect mobility extracted in the metallic regime, μ_{FE} vs T for three WSe_2 FET devices. All three devices show a modest μ_{FE} of around 140 cm^2/Vs at room temperature, which then increases rapidly with decreasing temperature. The mobility variation in the high temperature regime for $T > 100$ K follows a power-law dependence, $\mu_{FE} \propto T^{-\gamma}$, where the exponent γ varies between $0.8 - 1.2$ for the three devices. Below a certain critical temperature (T_c),

[4] In the absence of a direct density measurement, e.g., through the Hall effect, $p_c = C_{TG}(V_c - V_T)/e$ is used to estimate p_c; V_c is the top-gate voltage at the crossover point and V_T is the threshold voltage which is assumed to be 0, based on Chapter 3 data.

the mobility saturates to an upper limit and stays nearly constant with further reduction of temperature.

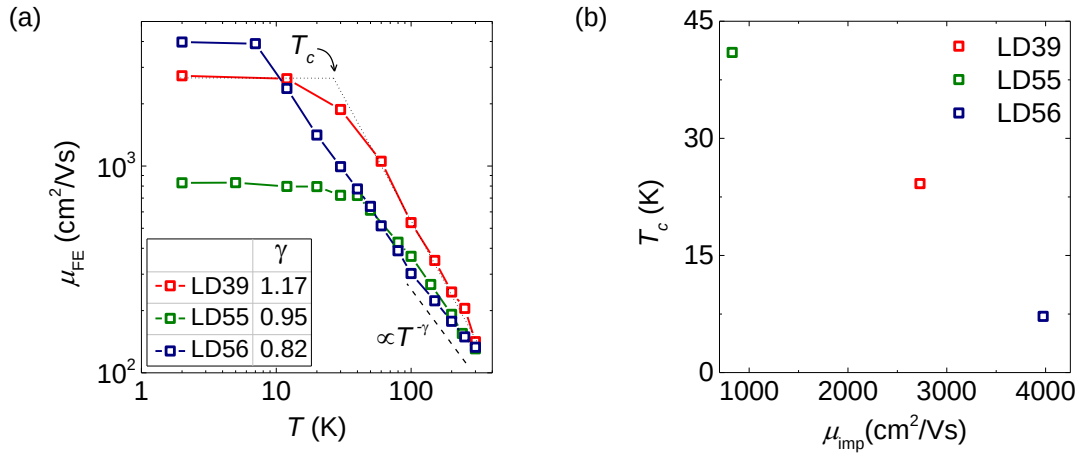

Figure 2.11: (a) μ_{FE} vs T for three different WSe_2 FET devices. The dashed line for $T > 100$ K indicates a $\propto T^{-\gamma}$ power-law trend expected for mobility dominated by phonon scattering. The inset table shows the γ values extracted for the three devices. The dotted lines for LD39 data mark its T_c value. (b) T_c vs μ_{imp} for the three devices of panel (a).

Phonon scattering is the dominant mobility limiting mechanism at high-temperatures, leading to a $\mu \propto T^{-\gamma}$ trend, where the exponent γ depends on the specifics of the phonon scattering mechanisms at play. Acoustic phonon scattering is expected to result in $\gamma = 1$, whereas $\gamma > 1$ is a signature of optical phonon scattering [89, 92]. The values of γ closer to 1 in the WSe_2 devices suggest that acoustic phonon scattering is the mobility limiting factor for $T > 100$ K.

At low-temperatures, μ_{FE} saturates to an upper limit (μ_{imp}), likely limited by Coulomb scattering or defects [89, 93]. A T_c value can be assigned to each of the μ_{FE} vs T data of Fig. 2.11(a) by linearly extrapolating the two temperature dependence regimes of μ_{FE}, shown for LD39 data as an example. Figure 2.11(b) shows T_c vs μ_{imp} for the three devices of Fig. 2.11(a). There is considerable variability in μ_{imp} between samples, $\mu_{imp} \in 800 - 4000$ cm^2/Vs, varying inversely with $T_c \in 40 - 7$ K. The T_c value can be an indicator of sample quality, with cleaner samples transitioning to an impurity scattering dominated mobility regime at lower temperatures [93]. It is to be noted that μ_{imp} does not seem to depend on γ.

2.6.1 Hall Mobilities in Monolayer and Bilayer WSe_2

An alternate measure of the carrier mobility is via Hall measurements, which allow independent measurement of the carrier density and mobility, referred to as the Hall mobility (μ_{Hall}). Measurements of the Hall mobility require multiterminal Hall bar devices in order to measure the transverse Hall voltage in a perpendicular magnetic field, from which the Hall mobility and carrier density can be determined.[5] Figure 2.12(a) shows μ_{Hall} vs T measured in h-BN encapsulated WSe_2 Hall bar samples, monolayer WSe_2-08 and bilayer WSe_2-09, at a hole density, $p = 8.0 \times 10^{12}$ cm^{-2}. Using h-BN as the substrate in addition to the top-gate dielectric reduces charged impurity scattering from the SiO_2 substrate and yields higher quality samples [37].

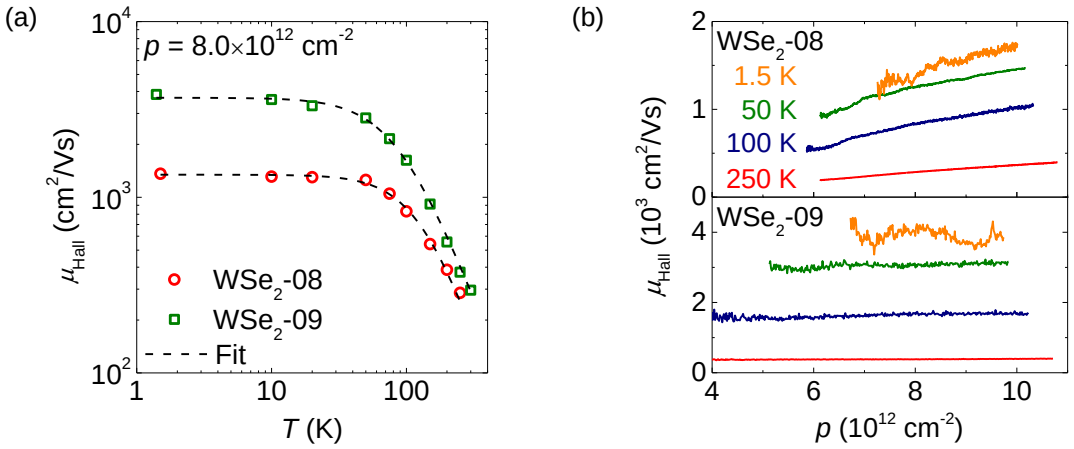

Figure 2.12: (a) μ_{Hall} vs T at $p = 8.0 \times 10^{12}$ cm^{-2} in monolayer WSe_2-08 and bilayer WSe_2-09 Hall bar samples. The dashed lines show fits to Eq. 2.6. (b) μ_{Hall} vs p at various T values in WSe_2-08 (top panel) and WSe_2-09 (bottom panel).

Both the monolayer and bilayer data of Fig. 2.12(a) show a behavior very similar to the three/four-layer WSe_2 data of Fig. 2.11(a), with a steep μ_{Hall} increase with reducing temperature for $T > 100$ K, indicative of phonon scattering limited mobility, and a saturation and relative insensitivity of μ_{Hall} to temperature for $T < 50$ K, indicative of impurity scattering limited mobility. Figure 2.12(b) shows μ_{Hall} vs p at various temperatures in WSe_2-08 and WSe_2-09. At a given temperature in monolayer WSe_2-08, μ_{Hall} increases with increasing density due to increased screening of charged impurities at higher densities. The data of bilayer WSe_2-09 show a weaker variation of μ_{Hall} vs p, presumably due to

[5] Section 3.1.1 discusses the classical Hall effect, and measurement of the Hall mobility and carrier density in a 2DES.

stronger screening of charged impurities by the bottom unpopulated WSe_2 layer,[6] rendering the effect of screening by an increased density of holes relatively less important [4].

The individual contributions of the phonon scattering limited mobility and charged impurity scattering limited mobility to the total hole mobility can be summed up using Matthiessen's rule as

$$\frac{1}{\mu} = \frac{1}{\mu_{\text{imp}}} + \frac{1}{\mu_{\text{ph}}} = \frac{1}{\mu_{\text{imp}}} + \frac{1}{\eta T^{-\gamma}} \tag{2.6}$$

where μ_{imp} is the charged impurity scattering limited mobility contribution and $\mu_{\text{ph}} = \eta T^{-\gamma}$ is the phonon scattering limited mobility contribution; η is a proportionality constant. The dashed lines in Fig. 2.12(a) are fits of the mobility data to Eq. 2.6 which yield $\gamma = 1.92$ and $\mu_{\text{imp}} = 1340$ cm^2/Vs for monolayer WSe_2-08, and $\gamma = 1.88$ and $\mu_{\text{imp}} = 3680$ cm^2/Vs for bilayer WSe_2-09. Figures 2.13(a) and 2.13(b) summarize γ and μ_{imp} vs p, respectively, obtained by fitting Eq. 2.6 to the μ_{Hall} vs T data at various p values in two monolayer WSe_2 Hall bar samples, WSe_2-06 and WSe_2-08, and two bilayer WSe_2 Hall bar samples, WSe_2-07 and WSe_2-09. The γ values show very little variation with density.

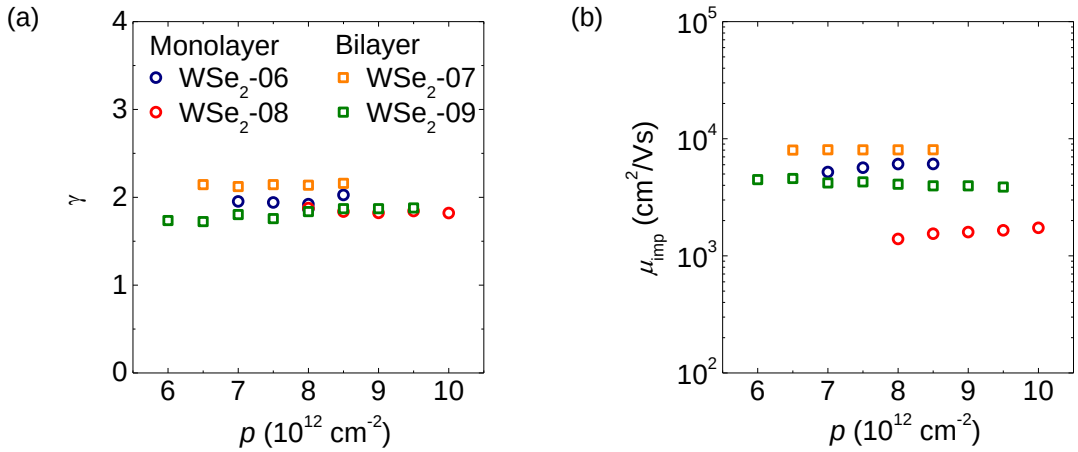

Figure 2.13: (a) γ vs p for two monolayer and two bilayer WSe_2 Hall bar samples. (b) μ_{imp} vs p for the samples of panel (a).

Notably, the γ values in h-BN encapsulated monolayer and bilayer WSe_2 samples are higher; $\gamma \simeq 2$, suggestive of optical phonon scattering being the dominant mobility limiting mechanism [89], compared to the acoustic phonon scattering limited γ values ~ 1 in the three/four-layer WSe_2 samples of Fig. 2.11(a). The difference can be attributed to the dissimilar dielectric environments, each with its own distinct phonon modes which

[6]Chapter 3 data show that holes in bilayer WSe_2 for $V_{\text{BG}} > 0$ V populate only the top WSe_2 layer.

determine γ through extrinsic phonon scattering mechanisms [93]. For comparison, h-BN encapsulated MoS_2 samples [75] show values of $\gamma \simeq 2$ in contrast to $\gamma < 2$ for MoS_2 samples on SiO_2/Si substrates [84, 85].

The μ_{imp} values of Fig. 2.13(b) show considerable variation between samples similar to the three/four-layer WSe_2 data of Fig. 2.11, likely due to variations in the WSe_2 flake quality, and do not seem to depend on γ.

2.7 Summary

In summary, the top-gated device design with Pt bottom-electrodes presented in this chapter provides Ohmic hole contacts to the valence band of WSe_2 down to cryogenic temperatures. The high hole mobilities at low-temperatures underline the high intrinsic material quality of WSe_2, thereby enabling more extensive magnetotransport measurements, which are the subject of the remainder of this dissertation.

The bottom-contact strategy is not unique to Pt–WSe_2, but is also applicable to other TMDs with an appropriate choice of electrode metal. For instance, Pd bottom-electrodes result in Ohmic electron contacts to $MoSe_2$ [94] and Au bottom-electrodes result in Ohmic electron contacts to MoS_2 [95] down to cryogenic temperatures.

Chapter 3

Shubnikov–de Haas Oscillations of Holes in Monolayer and Bilayer WSe_2

Low-temperature magnetotransport is a powerful probe of the electron physics in a material. Several key electronic transport properties of semiconductors such as the carrier type, valley-degeneracy, carrier effective mass, etc., and spin–orbit and electron-electron interaction effects have traditionally been probed using magnetotransport measurements [16]. The 2D or quasi-2D inversion or accumulation layers at a semiconductor–insulator interface or a semiconductor heterojunction have been the most commonly used vehicles for such studies with a majority of the seminal experiments being performed in 2DESs based on Si and GaAs, thanks to their high carrier mobilities [1, 12, 97, 98]. More recently, magnetotransport measurements of graphene 2DESs have yielded invaluable insights into the rich physics at play in the 2D limit [99, 100, 101, 102].

Exploring the electron physics in TMDs at low-temperatures and high magnetic fields has proven arduous because of moderate mobilities and high-resistance electrical contacts. In view of the results of Chapter 2, the high hole mobilities combined with the ease of electrical access to the valence band facilitate a study of hole magnetotransport in WSe_2, which will be the focus of this chapter.

The first section of this chapter presents an overview of the classical Hall effect, the quantum Hall effect, and techniques to analyze Shubnikov–de Haas (SdH) oscillations aimed at investigation of the electron transport properties of a 2DES. The subsequent sections discuss measurement results and analyses of SdH oscillations of holes in dual-gated monolayer and bilayer WSe_2 Hall bar devices. The data reveal a two-fold Landau level degeneracy and a hole effective mass of $m^* = 0.45m_e$ in both monolayer and bilayer WSe_2; m_e is the free electron mass. The bilayer data also reveal carrier localization in the two constituent layers and negative compressibility of holes in the bottom layer.

Portions of this chapter have been published as Ref. [96]: B. Fallahazad, H. C. P. Movva, K. Kim, S. Larentis, T. Taniguchi, K. Watanabe, S. K. Banerjee, and E. Tutuc, "Shubnikov–de Haas Oscillations of High-Mobility Holes in Monolayer and Bilayer WSe_2: Landau Level Degeneracy, Effective Mass, and Negative Compressibility," *Phys. Rev. Lett.*, vol. 116, no. 8, p. 086601, 2016. The dissertator, H. C. P. Movva, fabricated the WSe_2 samples, and contributed to characterization, data analysis, and writing the paper.

3.1 Electrical Transport in a Magnetic Field

A magnetic field provides a knob to tune the motion of charge carriers in a material, which manifests as changes in its measurable properties, e.g., resistance. The special case of a magnetic field applied perpendicular to the direction of charge flow produces the classical and quantum Hall effects, which are discussed in the following sections.

3.1.1 Classical Hall Effect

The classical Hall effect is named after Edwin H. Hall who discovered that a current through a thin foil sample in the presence of a perpendicular magnetic field produces a voltage drop in the direction transverse to the direction of current flow [103]. This voltage, called the Hall voltage (V_{H}) was found to be proportional to the strength of the magnetic field (B) and the current (I). Figure 3.1 shows a schematic of the classical Hall effect.

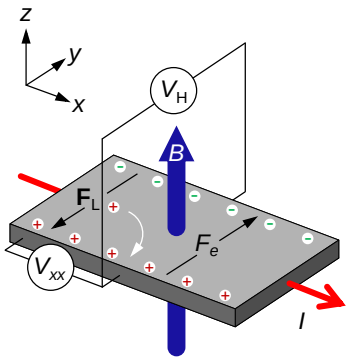

Figure 3.1: Schematic of the classical Hall effect. Charge carriers in a current carrying conductor experience a Lorentz force on application of a magnetic field perpendicular to the direction of current flow. This results in charge build-up in the direction normal to both the applied magnetic and electric fields, thereby causing a voltage difference across the transverse edges known as the Hall voltage.

The appearance of a non-zero Hall voltage can be attributed to the Lorentz force which states that a charged particle moving in a magnetic field experiences a force given by

$$\mathbf{F}_{\mathrm{L}} = e\,(\mathbf{v} \times \mathbf{B}) \tag{3.1}$$

where $\mathbf{F}_{\mathrm{L}}$ is the Lorentz force, e is the particle charge (positive for holes and negative for electrons), $\mathbf{v}$ is the particle velocity defined by the current flow, i.e., the drift velocity ($|\mathbf{v}| = v_d$), and $\mathbf{B}$ is the magnetic field vector. The Lorentz force causes the particles to drift in the transverse direction, resulting in charge build-up on one side of the sample. This

charge imbalance in turn creates an electric field, giving rise to an electrostatic force which opposes the Lorentz force, given by

$$F_e = \frac{eV_{\mathrm{H}}}{W} \tag{3.2}$$

where W is the width of the sample.

For equilibrium to be established, the two forces must be equal in magnitude, i.e., $F_{\mathrm{e}} = |\mathbf{F}_{\mathrm{L}}|$, which gives

$$\frac{eV_{\mathrm{H}}}{W} = ev_dB \tag{3.3}$$

where $B = |\mathbf{B}|$. The current flowing through the sample is given by

$$I = Nev_dA \tag{3.4}$$

where N is the particle density per unit volume and A is the cross sectional area through with the current flows, i.e., $A = Wt$, where t is the sample thickness. Eliminating v_d from Eq. 3.3 and Eq. 3.4 gives the full relationship between the Hall voltage, current, and magnetic field as

$$V_{\mathrm{H}} = \frac{IB}{Nte} \tag{3.5}$$

For commonly measured thin samples such as 2DESs, the areal density as opposed to the volume density is a more informative quantity. Therefore, defining the sheet (areal) charge density as $n = Nt$ transforms Eq. 3.5 to

$$V_{\mathrm{H}} = \frac{IB}{ne} \tag{3.6}$$

Transport in the longitudinal direction, i.e., in the direction of current flow is unaffected by the magnetic field. The longitudinal resistance (R_{xx}) can therefore be defined as

$$R_{xx} = \frac{V_{xx}}{I} \tag{3.7}$$

where V_{xx} is the voltage drop across the sample along the current flow direction (x). While there is no current flow along the transverse direction, it is instructive to define a transverse resistance (R_{xy}), also referred to as the Hall resistance using the Hall voltage as

$$R_{xy} = \frac{V_{\mathrm{H}}}{I} = \frac{B}{ne} \tag{3.8}$$

Equation 3.8 reveals that the Hall resistance is independent of the sample size and geometry, but depends only on the applied magnetic field, the sheet charge density, and

the polarity of the charge particles. When the applied magnetic field is a known quantity, the charge density of the 2DES can therefore be determined from the slope of the Hall resistance vs magnetic field as

$$n = \frac{1}{e}\left(\frac{dR_{xy}}{dB}\right)^{-1} \tag{3.9}$$

The classical Hall effect therefore provides a direct measurement of the charge density of a 2DES. With the charge density known, the Hall mobility (μ_{Hall}) of the charge carriers can be calculated from the longitudinal resistance and the specifics of the sample geometry as

$$\mu_{\text{Hall}} = \frac{N_{\square}}{neR_{xx}} \tag{3.10}$$

where $N_{\square} = L/W$ is the number of squares and L is the distance between the voltage probes used to measure the longitudinal resistance.

The analysis presented in this section is purely classical and breaks down when quantum effects come into picture, especially at low-temperatures and in strong magnetic fields. The following section provides a quantum mechanical treatment of the same system which more accurately describes the transport phenomena under such conditions.

3.1.2 Quantum Hall Effect

The first indication of the role of quantum phenomena in magnetotransport at low-temperatures and in strong magnetic fields was reported in 1930 by Lev V. Shubnikov and Wander J. de Haas, who observed oscillations in the longitudinal resistance of bismuth crystals as a function of the magnetic field as shown in Fig. 3.2(a) [104]. An even more striking manifestation of quantum effects was discovered in 1980 by Klaus von Klitzing in a high mobility Si 2DES. The Hall resistance was found to display plateaux accompanied by vanishing longitudinal resistance at high magnetic fields as shown in Fig. 3.2(b) [1], a phenomenon which is now referred to as the quantum Hall effect. The Hall resistance at the plateaux was found to be exactly quantized at values

$$R_{xy} = \frac{1}{i}\frac{h}{e^2} \tag{3.11}$$

where i is an integer and h is the Planck constant. Both the Shubnikov–de Haas oscillations and quantum Hall effect can be understood by considering the quantum effects on electron motion in a magnetic field.

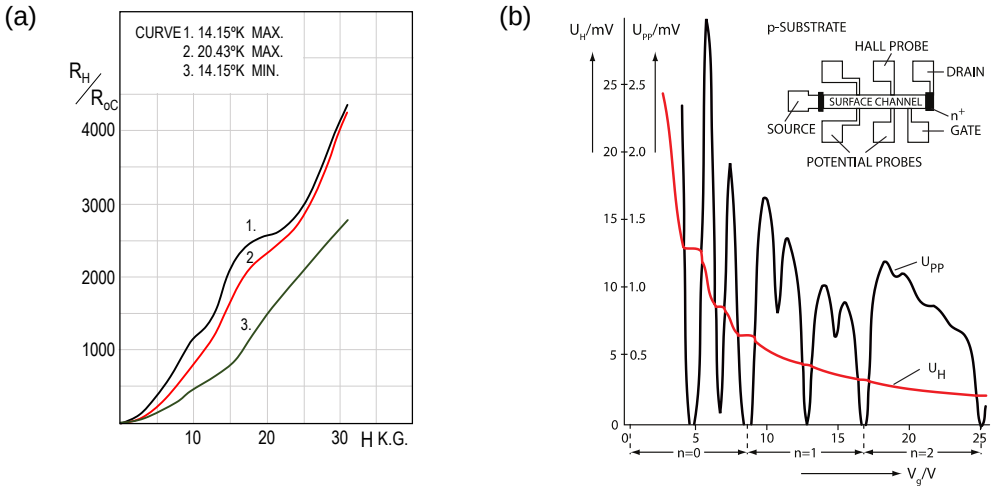

Figure 3.2: (a) Plot from Shubnikov and de Haas' observation of oscillatory features in the longitudinal resistance of bismuth as a function of magnetic field. Adapted from Ref. [104]. (b) Plot from von Klitzing's discovery of the quantum Hall effect in a Si 2DES. Adapted from Refs. [1, 105].

The Hamiltonian describing the motion of spin-less, non-interacting, massive electrons in the xy-plane in a 2DES in the presence of a magnetic field can be written as

$$\hat{H} = \frac{1}{2m^*}\left(\hat{\mathbf{p}} + e\hat{\mathbf{A}}\right)^2 \tag{3.12}$$

where m^* is the effective mass of electrons in the material hosting the 2DES, $\hat{\mathbf{p}}$ is the canonical momentum operator, and $\hat{\mathbf{A}}$ is the magnetic vector potential which is related to the magnetic field by

$$\mathbf{B} = \nabla \times \hat{\mathbf{A}} \tag{3.13}$$

In the special case of a perpendicular magnetic field, i.e., $\mathbf{B} = (0, 0, B)$ and choosing the Landau gauge for the magnetic vector potential, i.e., $\hat{\mathbf{A}} = (0, B\hat{x}, 0)$, Eq. 3.12 can be written as

$$\hat{H} = \frac{\hat{p_x}^2}{2m^*} + \frac{1}{2m^*}\left(\hat{p_y} + eB\hat{x}\right)^2 \tag{3.14}$$

The Schrödinger equation can consequently be written as

$$\hat{H}\psi(x, y) = \frac{\hbar^2}{2m^*}\left[-\nabla_x^2 + \left(\frac{1}{i}\nabla_y + \frac{eBx}{\hbar}\right)^2\right]\psi(x, y) = \mathcal{E}\psi(x, y) \tag{3.15}$$

where ψ is the wavefunction, $\mathcal{E}$ is the eigenenergy, and $\hbar$ is the reduced Planck constant. Since the Hamiltonian does not depend on y, the wavefunction can be separated into a plane

wave of y and an unknown function of x as

$$\psi(x, y) = \phi(x)e^{ik_y y} \tag{3.16}$$

where k_y is the wavevector of the plane wave. Substituting Eq. 3.16 in Eq. 3.15 gives

$$\left[-\frac{\hbar^2}{2m^*}\nabla_x^2 + \frac{1}{2}m^*\omega_c^2\,(x + x_0)^2\right]\phi(x) = \mathcal{E}\phi(x) \tag{3.17}$$

where the cyclotron frequency, ω_c, is defined as $\omega_c = eB/m^*$, and the guiding center, x_0, as $x_0 = \hbar k_y/eB = l_B^2 k_y$, where $l_B = \sqrt{\hbar/eB}$ is the magnetic length, or the characteristic size of an electron orbit.

Equation 3.17 is the equation of motion for a one-dimensional harmonic oscillator centered at $-x_0$, whose energy eigenvalues are of the form

$$E_{n_{\mathrm{LL}}} = \hbar\omega_c\left(n_{\mathrm{LL}} + \frac{1}{2}\right) \tag{3.18}$$

where $n_{\mathrm{LL}} = 0, 1, 2, \ldots$ is referred to as the Landau level index and the discrete energies $E_{n_{\mathrm{LL}}}$ are known as the Landau levels, named after Lev Landau who first solved this problem. The quantization of the electron energy into discrete levels is called Landau quantization.

Therefore, electron wavefunctions in the xy-plane subject to a magnetic field applied in the z-direction are described by the wavevector k_y and the discrete Landau level index n_{LL}. Since the energy depends only on n_{LL}, each Landau level is degenerate over k_y or the guiding center x_0. Figure 3.3(a) shows a schematic of the quantum Hall effect where the carriers in the interior of the sample are shown to execute circular orbits at several different x_0. A prerequisite for the observation of the quantum Hall effect is that the carriers be able to execute a full cyclotron orbit before being scattered. This places a lower bound on the scattering lifetime, τ_q, as $\tau_q > 1/\omega_c$, or equivalently, $\mu_q > 1/B$, where the quantum mobility $\mu_q = e\tau_q/m^*$. Therefore, high-mobility samples, or equivalently, high magnetic fields are needed to observe the quantum Hall effect.

It can be shown that the Landau level degeneracy is $L_x L_y/2\pi l_B^2$, where L_x and L_y are the sample dimensions in the x- and y-directions, respectively. Consequently, the Landau level degeneracy per unit area can be written as $1/2\pi l_B^2$. Therefore, the density of states (DOS) in a Landau level is given by

$$n_{\mathrm{DOS}} = \frac{eB}{h} \tag{3.19}$$

where the spin-degeneracy has not been included. There would be an extra factor of two for a spin-degenerate system.

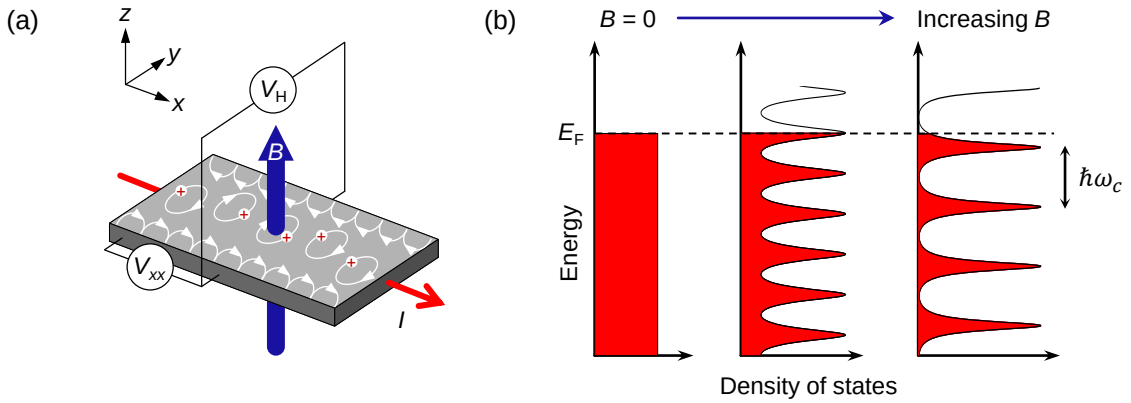

Figure 3.3: (a) Schematic of the quantum Hall effect. Carriers (shown here as positively charged holes) execute cyclotron motion around guiding centers in the interior of the sample. The current is carried by carriers at the edges executing skipping orbits. (b) Evolution of the density of states with magnetic field for a spin-degenerate 2DES with disorder broadening. Starting with a constant density of states at $B = 0$, the density of states evolve into Landau levels with increasing degeneracy and spacing ($= \hbar\omega_c$) as the magnetic field increases. The Fermi level is indicated by E_F.

The effect of Landau quantization on the density of states of a 2DES is shown in Fig. 3.3(b). The 2D density of states, which is constant in the absence of a magnetic field collapses into a series of highly degenerate δ-functions corresponding to the Landau levels in the presence of a magnetic field [Eq. 3.18]. However, in real samples with disorder, the δ-functions are broadened into Lorentzian lineshapes, as shown in Fig. 3.3(b). With increasing magnetic field, the spacing between consecutive Landau levels as well as the degeneracy of each Landau level increases, so that more electrons are required to fill an individual Landau level.

At a given magnetic field and 2DES carrier density, the number of filled Landau levels is called the filling factor and is given by

$$\nu = \frac{n}{n_{\mathrm{DOS}}} = \frac{nh}{eB} \tag{3.20}$$

There exist special cases when an integer number of Landau levels are exactly filled, i.e., the Fermi level, E_F, lies in the gap between two consecutive Landau levels. Due to the Pauli exclusion principle, electrons in the filled states cannot scatter into other filled states of the lower Landau levels. They also cannot scatter into empty states of the higher unoccupied Landau levels, provided the temperature (T) is low, i.e., $k_B T \ll \hbar\omega_c$; k_B is the Boltzmann constant. Consequently, all scattering events are suppressed, and transport is dissipationless, with the longitudinal resistance going to zero. For the Hall resistance,

substituting Eq. 3.20 into the classical Hall resistance equation, $R_{xy} = B/ne$ [Eq. 3.8] gives

$$R_{xy} = \frac{1}{\nu}\frac{h}{e^2} \tag{3.21}$$

which is exactly the quantized resistance value of Eq. 3.11.

While the quantized Hall resistance and zero longitudinal resistance are met only at exact fillings in this framework, i.e., unique values of the magnetic field, experimentally, the Hall resistance displays plateaux and the longitudinal resistance is zero over a wide range of magnetic field values around exact fillings. This can be explained by taking into account the semiclassical localization of electrons due to the inevitable impurities that are responsible for the Landau level broadening [106]. Figure 3.4 shows two scenarios corresponding to non-integer fillings, and the corresponding Hall and longitudinal resistance behavior.

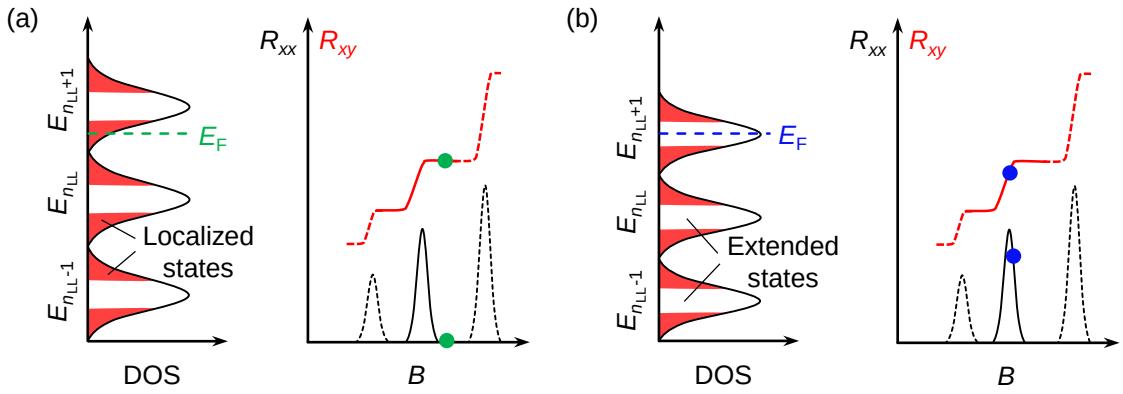

Figure 3.4: (a) Energy vs density of states for disorder broadened Landau levels. The Fermi level lies in the tails of a disorder broadened Landau level, localized in the sample interior and not affecting the global transport properties. The Hall resistance remains quantized and the longitudinal resistance remains zero. (b) When the Fermi level lies near the center of a Landau level, the electrons can scatter among the extended edge states that are responsible for conduction. This causes a non-zero longitudinal resistance and a transition between Hall resistance plateaux.

The broadened Landau levels are comprised of two types of states, namely localized states that occupy the tails and extended states that occupy the middle of the Landau levels, as shown in Fig. 3.4. The localized states result from the impurities in the sample which create potential variations and trap electrons in tight orbits. These electrons do not affect the global transport properties because they are not probed by the sample contacts at the edges. When the Fermi level lies in a localized state, current is carried by edge states [Fig. 3.3(a)] which are dissipationless, thereby resulting in zero longitudinal resistance and quantized Hall resistance [Fig. 3.4(a)]. The extended states on the other hand reside at the

edges of the sample and are responsible for current conduction. When the Fermi levels lies in an extended state, there can be scattering among the edge states which causes a non-zero longitudinal resistance and a transition between Hall resistance plateaux [Fig. 3.4(b)].

The effects of electron-spin have thus far been ignored in the analysis presented here. Accounting for the interaction of electron-spin with the magnetic field, Eq. 3.18 becomes

$$E_{n_{\mathrm{LL}}} = \hbar\omega_c \left(n_{\mathrm{LL}} + \frac{1}{2}\right) \pm \frac{1}{2} g \mu_{\mathrm{B}} B \tag{3.22}$$

where g is the electron Landé g-factor, μ_{B} is the Bohr magneton, and the plus (+) and minus (−) signs correspond to the spin-↓ and spin-↑ states of the electron, respectively. Equation 3.22 states that each Landau level is further split into two energy levels separated by the Zeeman energy, $E_{\mathrm{Z}} = g\mu_{\mathrm{B}}B$. In the absence of Zeeman splitting, Landau levels occur in pairs,[1] but at high magnetic fields when the Zeeman energy is larger than the disorder and thermal broadening, the Landau levels are spin-resolved.

A key requirement for the observation of the quantum Hall effect is that the Landau level energy gaps are well-resolved and larger than both the disorder and thermal broadening. This is satisfied at high magnetic fields and low-temperatures in high-mobility samples. However, at lower magnetic fields, where the Landau levels are not completely separated from each other, the density of states becomes a continuous periodic function of $1/B$, as shown in Fig. 3.5(a). The periodicity in the density of states at the Fermi level as a function of varying magnetic field is reflected in the longitudinal resistance as SdH oscillations. Several key transport characteristics of a 2DES can be extracted from its SdH oscillations.

3.1.3 Analysis of SdH Oscillations

The oscillatory part of the longitudinal resistance (ΔR_{xx}), i.e., only the SdH oscillations without the background for a single-subband spin-degenerate 2DES can be expressed using the simplified Lifschitz–Kosevich formula [107, 108] as

$$\Delta R_{xx} = R_0 \frac{\xi}{\sinh \xi} \exp\left(-\frac{\pi}{\omega_c \tau_q}\right) \cos\left(\frac{2\pi E_{\mathrm{F}}}{\hbar\omega_c} - \pi\right) \tag{3.23}$$

where R_0 is the zero-field resistance and the parameter ξ is given by

$$\xi = \frac{2\pi^2 k_{\mathrm{B}} T}{\hbar\omega_c} \tag{3.24}$$

[1] Transition metal dichalcogenide monolayers are an exception. In the absence of Zeeman splitting, the zeroth Landau level of semiconducting TMD monolayers is non-degenerate. This topic is discussed in more detail in Section 4.1.

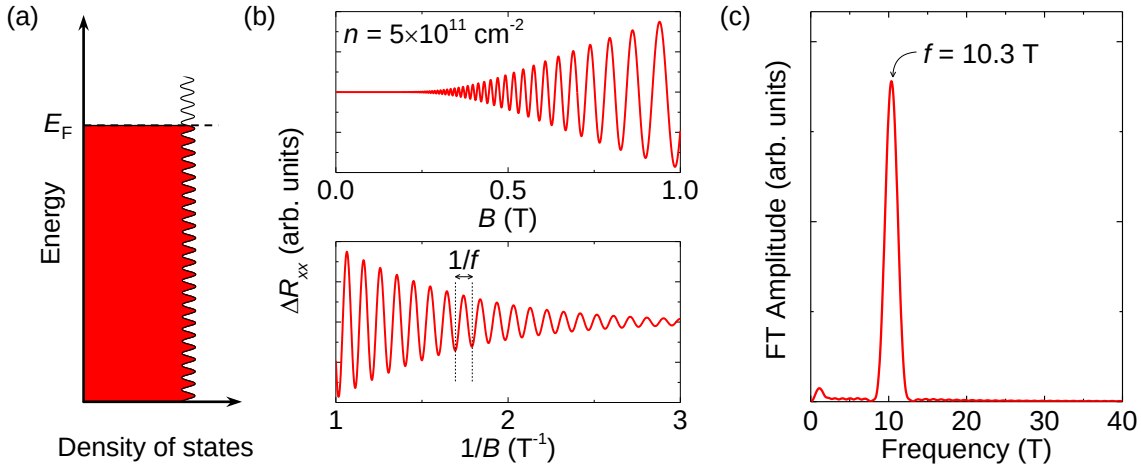

Figure 3.5: (a) Schematic of the periodic density of states of a 2DES in a low magnetic field. (b) Calculated SdH oscillations for a GaAs 2DES with a density of 5×10^{11} cm^{-2}, $\tau_q = 1.9$ ps, and $T = 1.5$ K [top panel] and the corresponding ΔR_{xx} vs $1/B$ plot showing oscillations periodic in $1/B$ [bottom panel]. (c) Fourier transform spectrum of the ΔR_{xx} vs $1/B$ data shows a single peak at $f = 10.3$ T.

The salient feature of Eq. 3.23 is the oscillatory cosine term periodic in $1/B$. Therefore, plotting ΔR_{xx} vs $1/B$ yields oscillations with a characteristic frequency, f, which is related to the 2DES density by

$$n = \frac{2e}{h} f \tag{3.25}$$

Figure 3.5(b) shows example SdH ΔR_{xx} vs B calculated for GaAs 2D electrons [$n = 5 \times 10^{11}$ cm^{-2}, $\tau_q = 1.9$ ps, $T = 1.5$ K] using Eq. 3.23 and the corresponding ΔR_{xx} vs $1/B$ oscillations which are periodic with a period $1/f$. A commonly used technique to extract the frequency is to perform a Fourier transform (FT) of the ΔR_{xx} vs $1/B$ data and examine the FT amplitude spectrum. Fig. 3.5(c) shows the FT spectrum of the ΔR_{xx} vs $1/B$ data of Fig. 3.5(b). There is one characteristic peak at $f = 10.3$ T, which yields a 2DES density, $n = 5 \times 10^{11}$ cm^{-2}, using Eq. 3.25.

Equation 3.25 is valid for the case of a spin-degenerate 2DES with a valley-degeneracy of one, but can readily be modified to include the spin (D_s) and valley (D_v) degeneracies as $n = D_v D_s \times (e/h) \times f$. The frequency of SdH oscillations therefore provides a direct measure of the 2DES density when the valley-degeneracy is known, or more interestingly, can be used to discern the unknown valley-degeneracy of a 2DES by comparing the frequency of SdH oscillations with the density extracted from the classical Hall effect.

There can be scenarios where the Fourier transforms of SdH oscillations show

multiple peaks in their amplitude spectra. Figure 3.6(a) shows an example of SdH oscillations calculated for GaAs 2D electrons, similar to Fig. 3.5, but taking Zeeman splitting into account. The ΔR_{xx} vs B data show the characteristic spin-splitting of the oscillations at high magnetic fields. The corresponding FT spectrum shows two peaks at frequencies $f = 10.3$ T and its second harmonic, $2f$. The degeneracy used to convert the SdH frequency to a density can seem to vary between 2 or 1 depending on the choice of f or $2f$. This uncertainty can be reconciled by noting that the $2f$ peak is due to spin-splitting of carriers associated with the f peak, and both peaks with an appropriate choice of degeneracy value give the same density.

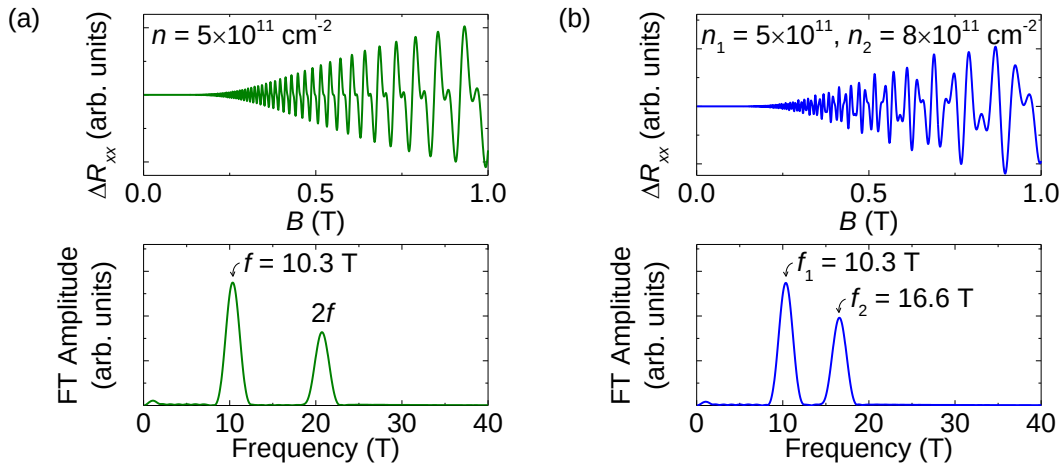

Figure 3.6: (a) Calculated SdH oscillations for a GaAs 2DES with a density of 5×10^{11} cm^{-2} accounting for Zeeman splitting [top panel] and the corresponding FT spectrum which shows two peaks at frequencies $f = 10.3$ T and $2f$ [bottom panel]. (b) Calculated SdH oscillations for a GaAs 2DES with two different subbands with densities $n_1 = 5 \times 10^{11}$ cm^{-2} and $n_2 = 8 \times 10^{11}$ cm^{-2} [top panel]. The associated FT spectrum shows two peaks at frequencies $f_1 = 10.3$ T corresponding to n_1 and $f_2 = 16.6$ T corresponding to n_2 [bottom panel].

Another example is shown in Fig. 3.6(b), which shows SdH oscillations calculated for a GaAs 2DES with two subbands of densities $n_1 = 5 \times 10^{11}$ cm^{-2} and $n_2 = 8 \times 10^{11}$ cm^{-2}. The ΔR_{xx} vs B data show a characteristic beating pattern indicative of underlying oscillations with two different frequencies. The two frequencies can be readily distinguished by inspecting the FT spectrum, which shows two peaks at $f_1 = 10.3$ T corresponding to n_1 and $f_2 = 16.6$ T corresponding to n_2. The presence of two different subbands in the 2DES can be recognized this way. Further, electrostatic gating can be used to tune the 2DES density and provide an extra knob to discern the valley-degeneracies of each subband by comparing the peak frequencies with the total density.

It is to be noted that the SdH oscillations and the corresponding FT spectra of Figs. 3.5 and 3.6 are calculated using the simplified model of Eq. 3.23 and do not capture all experimental features. In reality, there may be mixing of the oscillations, resulting in higher harmonics and/or peaks at sums and differences of the component peak frequencies.

Another main transport metric that can be extracted from the SdH oscillations is the effective mass of carriers in the 2DES. Increasing the temperature decreases the SdH oscillations' amplitude due to smearing of the density of states oscillations at the Fermi level because of thermal broadening. The parameter ξ [Eq. 3.24], which appears in Eq. 3.23 determines the temperature dependence of the SdH oscillations' amplitude via the Dingle factor, $\xi/\sinh\xi$ [109, 110]. At a fixed magnetic field, fitting ΔR_{xx} vs T to the Dingle factor yields the effective mass.

Figure 3.7(a) shows the calculated SdH oscillations for a GaAs 2DES with a density $n = 5 \times 10^{11}$ cm^{-2} and effective mass $m^* = 0.067m_e$ at various temperatures between $T = 1.5$ K to 4.0 K, which shows the oscillation amplitude decreasing with increasing temperature. Figure 3.7(b) shows the extracted ΔR_{xx} values vs T at the ΔR_{xx} maximum at $B = 0.86$ T. A Dingle factor fit yields the effective mass as $m^* = 0.067m_e$. The same analysis can be repeated at different locations of ΔR_{xx} maxima or minima to generate m^* values at different values of magnetic field. A more thorough way of extracting the effective mass, especially when the SdH oscillations have a background, and/or when multiple subbands are present in the FT spectrum is to filter the relevant FT peaks, followed by an inverse Fourier transform, and subsequent extraction, and Dingle factor fitting of ΔR_{xx} vs T.

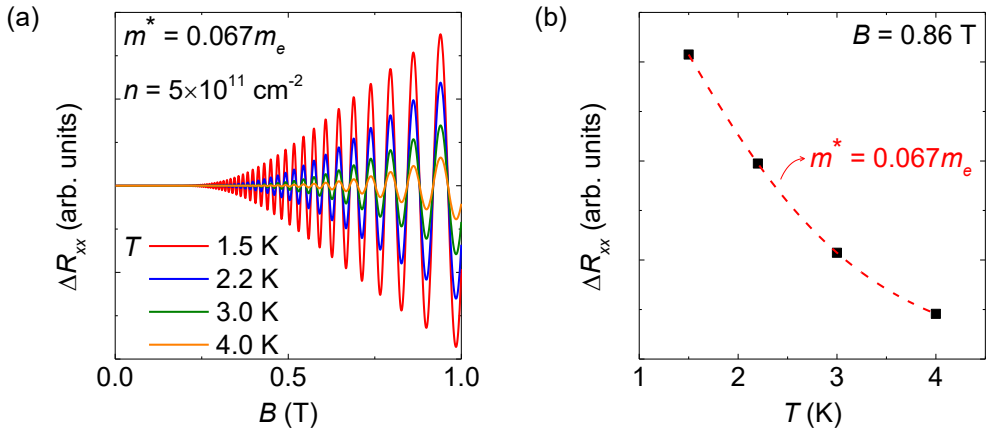

Figure 3.7: (a) Calculated SdH oscillations for a GaAs 2DES with a density of 5×10^{11} cm^{-2} and $m^* = 0.067m_e$ as the temperature is varied from 1.5 K to 4.0 K. (b) Variation of ΔR_{xx} vs T at the ΔR_{xx} maximum at $B = 0.86$ T [squares] and the corresponding Dingle factor fit [dashed line] which yields an effective mass, $m^* = 0.067m_e$.

Apart from the 2DES density, degeneracy, subband populations, and effective mass, the SdH oscillations can also be used to map out the Fermi surface of a material by determining the periods of oscillations for various applied magnetic field directions. This is one of the common techniques used in Fermiology, the study of Fermi surfaces.

3.2 Monolayer and Bilayer WSe_2 Hall Bar Samples

The high hole mobilities of WSe_2 as discussed in Chapter 2 make it feasible to perform magnetotransport measurements in the quantum Hall regime within the range of magnetic fields accessible with a typical superconducting magnet. Given the versatility of SdH oscillations in uncovering the transport properties of a 2DES, the following sections of this chapter discuss measurements and analyses of SdH oscillations in monolayer and bilayer WSe_2 Hall bar devices. Monolayer and bilayer WSe_2 were specifically chosen instead of thicker WSe_2 in light of their simpler bandstructures.

To further reduce surface roughness and charged impurity scattering in the channel compared to the samples of Chapter 2, the WSe_2 samples used for this study were encapsulated in *h*-BN and the Pt bottom-contacts were patterned in a Hall bar geometry to enable simultaneous measurement of R_{xx} and R_{xy}. Four WSe_2 samples, two monolayers, LD71 and LD103, and two bilayers, LD63 and LD99B were investigated in this study, all with consistent results. The samples' details are listed in Appendix A. The data presented in Secs. 3.2–3.5 are from monolayer LD103 and bilayer LD99B.

Figure 3.8(a) shows the schematic cross section of a dual-gated *h*-BN encapsulated WSe_2 device and Fig. 3.8(b) shows the optical micrograph of bilayer LD99B, a typical WSe_2 Hall bar device, along with the magnetotransport measurement configuration. The samples were fabricated using the same "pick and place" technique [79] of Chapter 2 with the only addition of a bottom *h*-BN flake as the substrate. The monolayer and bilayer WSe_2 flakes were chosen to match the size and shape of the prepatterned Pt contacts as closely as possible, and the Pd top-gate was patterned to entirely cover the WSe_2 flake. The detailed fabrication process flow and techniques are described in Appendix B.

The samples were cooled in a variable temperature insert coupled to a 14 T superconducting magnet in an Oxford ^{4}He cryostat. Preliminary DC electrical measurements were conducted using a semiconductor parameter analyzer (Agilent 4156C). Figure 3.9(a) shows the two-point transfer characteristics, I_D vs V_{TG} for bilayer LD99B at room temperature (RT) and 1.5 K. The apparent shift in the threshold voltage is similar to the devices of Chapter 2 and can be attributed to high-resistance contacts at low $|V_{TG}|$, especially at low-temperatures. Figure 3.9(b) shows the corresponding four-point resistance, R_{4pt} vs V_{TG}

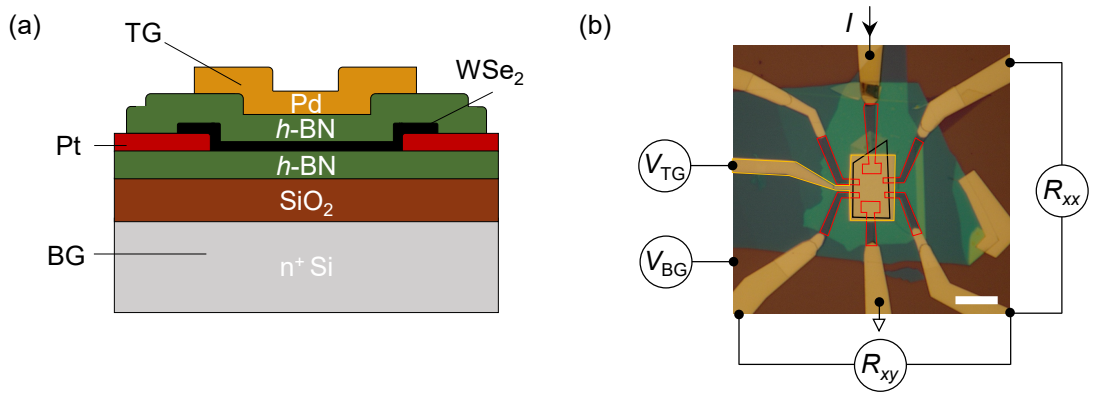

Figure 3.8: (a) Schematic cross section of a dual-gated *h*-BN encapsulated WSe_2 device. (b) Optical micrograph of LD99B, a typical WSe_2 Hall bar sample, along with the measurement configuration. The top-gate, Pt contacts, and WSe_2 flake are outlined by yellow, red, and black lines, respectively. The scale bar is 10 μm.

which decreases with decreasing temperature, indicative of increased mobility at 1.5 K. The noise in the 1.5 K R_{4pt} data at low $|V_{TG}|$ values are due to high-resistance contacts which inhibit reliable measurement of R_{4pt} in this regime.

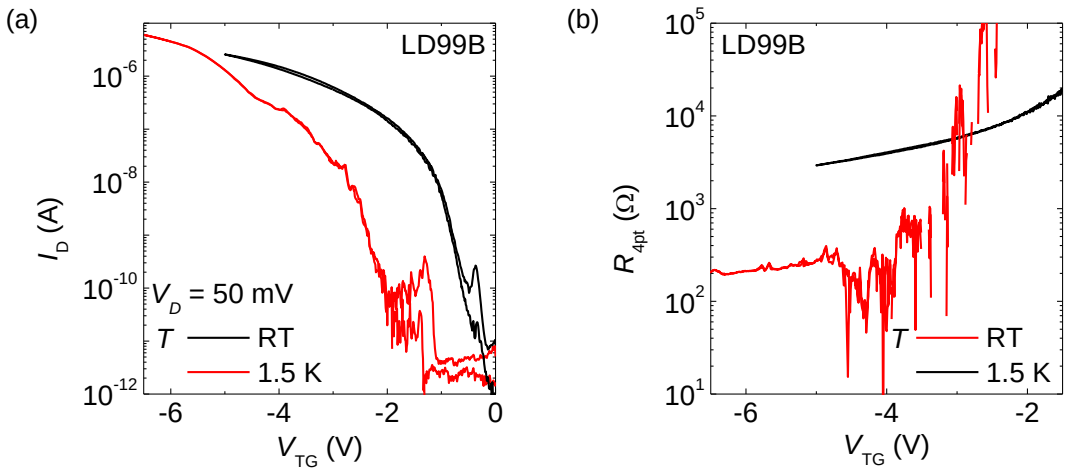

Figure 3.9: (a) I_D vs V_{TG} in bilayer LD99B shows an apparent threshold voltage shift when the sample is cooled from RT to $T = 1.5$ K. (b) The corresponding R_{4pt} vs V_{TG} shows a decrease of R_{4pt} with decreasing temperature, indicative of higher mobility at 1.5 K. The noise in the 1.5 K data at low $|V_{TG}|$ values stems from an increased contact resistance. Data for this particular sample were collected only for V_{TG} values $\lesssim -5$ V, where the noise is absent.

The devices were subsequently characterized in perpendicular magnetic fields up

to $B = 14$ T using small-signal excitation current, $I = 10$ nA, low-frequency ($9 - 13$ Hz) lock-in techniques, keeping in mind the useful range of V_{TG} required for reliable R_{xx} and R_{xy} measurements. Typical measurements involved magnetic field sweeps (≤ 0.3 T/minute) at a fixed top-gate and back-gate bias, i.e., a fixed hole density, p.

Examples of R_{xx} and R_{xy} vs B at $T = 1.6$ K and a fixed hole density for monolayer WSe_2 LD103 [$V_{TG} = -6$ V; $V_{BG} = 0$ V] and bilayer WSe_2 LD99B [$V_{TG} = -6.25$ V; $V_{BG} = 0$ V] are shown in Figs. 3.10(a) and 3.10(b), respectively. Both the plots show well-defined SdH oscillations starting at $B \simeq 4 - 5$ T, indicative of their high hole mobilities. The oscillatory features in R_{xy} at high B-fields stem from mixing with R_{xx}, in part due to the irregularly shaped WSe_2 flake shape and the resultant departure from an ideal Hall bar geometry. Some of these effects can be corrected for by anti-symmetrizing the R_{xy} data collected in positive and negative B-fields, i.e., $R_{xy} = (R_{xy,B+} - R_{xy,B-})/2$. The hole Hall densities were extracted from the low-field slope of the anti-symmetrized R_{xy} vs B data using Eq. 3.9.

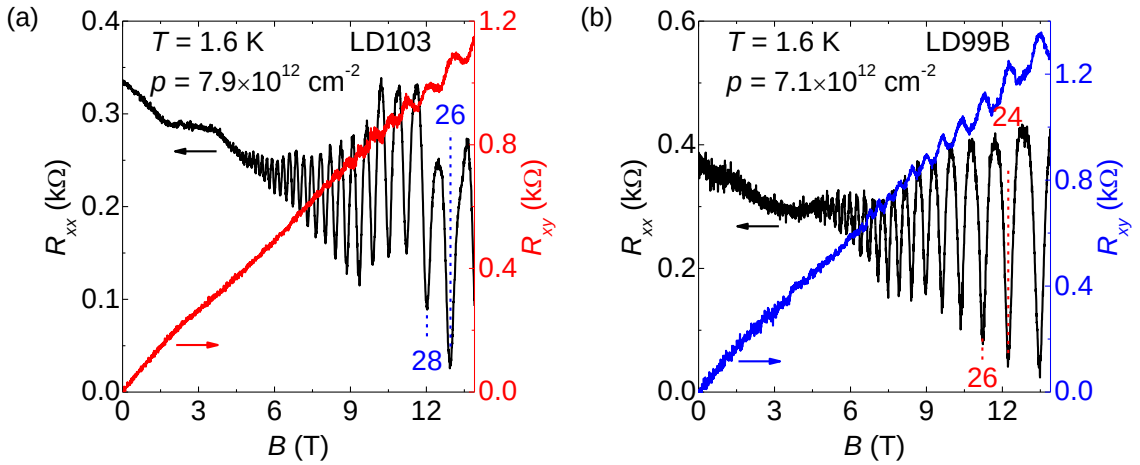

Figure 3.10: (a) R_{xx} and R_{xy} vs B for monolayer WSe_2 LD103 at $V_{TG} = -6$ V, $V_{BG} = 0$ V, and $T = 1.6$ K where $p = 7.9 \times 10^{12}$ cm^{-2}; the two lowest filling factors at $\nu = 26$ and 28 are indicated. (b) R_{xx} and R_{xy} vs B for bilayer WSe_2 LD99B at $V_{TG} = -6.25$ V, $V_{BG} = 0$ V, and $T = 1.6$ K where $p = 7.1 \times 10^{12}$ cm^{-2}. The two filling factors at $\nu = 24$ and 26 are indicated.

To ascertain the Landau level degeneracy of the WSe_2 holes, the filling factors at the R_{xx} minima can be extracted using Eq. 3.20 as $\nu = ph/eB$. The filling factors for both monolayer and bilayer WSe_2 are found to be even, hinting at a two-fold Landau level degeneracy for holes in monolayer and bilayer WSe_2. A different approach to analyze the Landau level degeneracies is through an FT analysis of the SdH data and is discussed in the next section.

3.3 Fourier Analysis of Monolayer WSe_2 SdH Oscillations

Thanks to knobs in the form of electrostatic gates, the WSe_2 SdH oscillations can be analyzed as a function of varying hole densities, and their Landau level degeneracies can be determined by comparing the SdH oscillations' frequencies with hole densities determined from Hall measurements. Figure 3.11(a) shows a set of R_{xx} vs B data for monolayer WSe_2 LD103 at different V_{TG} values, $V_{BG} = 0$ V, and $T = 1.6$ K. The SdH oscillations respond to V_{TG}, i.e., the hole density, as expected.

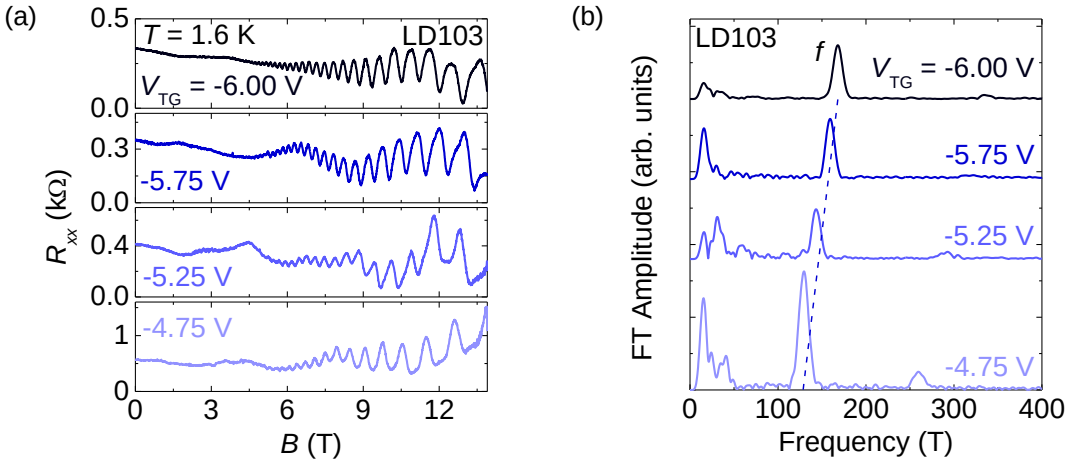

Figure 3.11: (a) R_{xx} vs B for monolayer WSe_2 LD103 at different V_{TG} values, $V_{BG} = 0$ V, and $T = 1.6$ K. (b) FT amplitude vs frequency corresponding to the R_{xx} vs $1/B$ data of panel (a); the traces are shifted for clarity. The dashed line tracks the peak at frequency f and is a guide to the eye.

In contrast to the simplified model of Eq. 3.23 and Fig. 3.5, the WSe_2 SdH oscillations of Fig. 3.11(a) are added onto on a background magnetoresistance which needs to be removed before performing the Fourier transform. First, a third order polynomial was subtracted from the R_{xx} vs $1/B$ data in order to remove the slowly (in comparison to the SdH oscillations' period) varying background and center the oscillations around zero. The data were then multiplied by a Hamming window to reduce artifacts associated with a finite $1/B$ range before finally applying a fast Fourier transform algorithm. Figure 3.11(b) shows the FT amplitude spectra of the R_{xx} vs $1/B$ data of Fig. 3.11(a) calculated this way.

The FT data for all V_{TG} show a principal peak at a frequency f, along with a small peak at its second harmonic, $2f$, due to spin-splitting at high B-fields. The peaks near zero-frequency are Fourier transform artifacts due to the residual background. Both the f and $2f$ peaks increase in frequency with increasing $|V_{TG}|$, i.e., with increasing density. The presence of a single principal peak in the FT data signals the population of a single

WSe_2 subband, most likely the upper valence band. This finding is consistent with the large (> 0.4 eV) spin–orbit induced splitting of the valence band of WSe_2 [32].

The FT peak frequencies of Fig. 3.11(b) can be converted into a density using Eq. 3.25 with the appropriate degeneracy factor. In light of Fig. 3.10(a) data which suggest a two-fold degeneracy, the FT density can be tentatively calculated as $p = (2e/h) \times f$ and compared with the Hall density values. Figure 3.12 shows p vs V_{TG} calculated from the FT data and from Hall measurements. The close agreement between the two density values confirms the assignment of a Landau level degeneracy of two in monolayer WSe_2, consistent with the coupled spin-valley degrees of freedom in TMD monolayers [33].

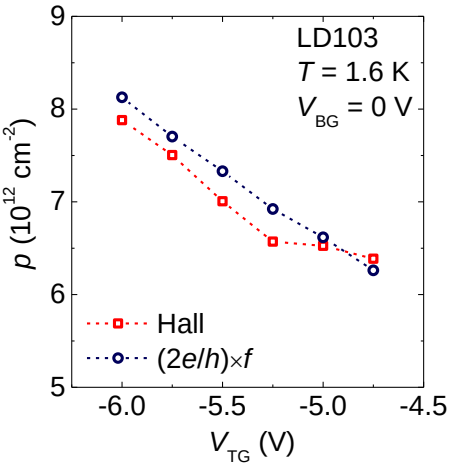

Figure 3.12: p vs V_{TG} calculated from Hall measurements and the FT frequency, $p = (2e/h) \times f$ for monolayer WSe_2 LD103. The close match between the two density values corroborates the two-fold Landau level degeneracy in monolayer WSe_2.

A noteworthy observation that can be made from Fig. 3.12 data is that extrapolating the measured p vs V_{TG} data to $p = 0$ yields an onset of the valence band population at $V_{TG} \simeq 0$ V, implying that the WSe_2 flakes are close to intrinsic at low-temperatures. The experimentally accessible range of densities however has a lower bound, predominantly limited by disorder close to the band edge, and/or high-resistance contacts at low $|V_{TG}|$ values.

3.4 Fourier Analysis of Bilayer WSe_2 SdH Oscillations

A similar analysis can be carried out for bilayer WSe_2 to determine its Landau level degeneracy and subband populations. Figure 3.13(a) shows a set of R_{xx} vs B for bilayer

WSe_2 LD99B at different V_{BG} values, fixed $V_{TG} = -6.5$ V, and $T = 1.6$ K. All the traces show SdH oscillations markedly dependent on V_{BG}, along with a beating pattern at negative V_{BG} values. Figure 3.13(b) shows the corresponding FT spectra of the R_{xx} vs $1/B$ data of Fig. 3.13(a).

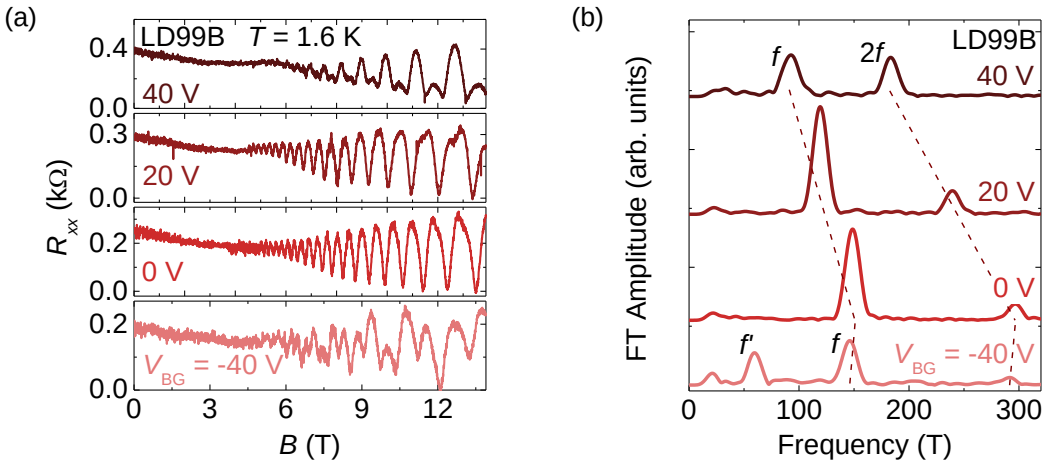

Figure 3.13: (a) R_{xx} vs B for bilayer WSe_2 LD99B at different V_{BG} values, $V_{TG} = -6.5$ V, and $T = 1.6$ K. (b) FT amplitude vs frequency corresponding to the R_{xx} vs $1/B$ data of panel (a); the traces are shifted for clarity. At negative V_{BG}, an additional peak, f', emerges and the peak at f no longer responds to V_{BG}. The dashed lines are a guide to the eye.

Similar to monolayer WSe_2, the FT spectra at positive V_{BG} values shows a principal peak at f and its second harmonic at $2f$. For positive V_{BG}, both the f and $2f$ peaks' frequencies increases with reducing V_{BG}, i.e., with increasing density. However, at $V_{BG} = -40$ V, the FT data show an additional peak at a lower frequency, f', consistent with the corresponding R_{xx} vs B beating pattern. Concomitantly, the f and $2f$ peaks also shift to a slightly lower frequency compared to their values at $V_{BG} = 0$ V. The f' peak and its corresponding R_{xx} vs B beating pattern are absent in monolayer WSe_2 and suggest an origin unique to the bilayer WSe_2 system, possibly a second subband being populated.

To investigate the origin of the f' peak, a second set of R_{xx} vs B data at a different value of $V_{TG} = -5.75$ V were collected and their corresponding FT spectra computed. Figure 3.14(a) summarizes the f and f' frequency values vs V_{BG} for the two datasets. There are several noteworthy features in Fig. 3.14(a) data. First, both the f and f' peak frequencies depend linearly on V_{BG}, albeit in different regimes. While f responds to positive V_{BG} values, f' responds to negative V_{BG} values. Second, the emergence of the f' peak at negative V_{BG} coincides with the f peak frequency becoming weakly dependent on V_{BG}. Third, at a fixed V_{BG} the f peak frequency increases with $|V_{TG}|$, suggesting that f responds to the carrier

density induced by the top-gate. When present, the f' peak frequency is insensitive to V_{TG}, but depends linearly on V_{BG}, suggesting that f' responds to the carrier density induced by the back-gate.

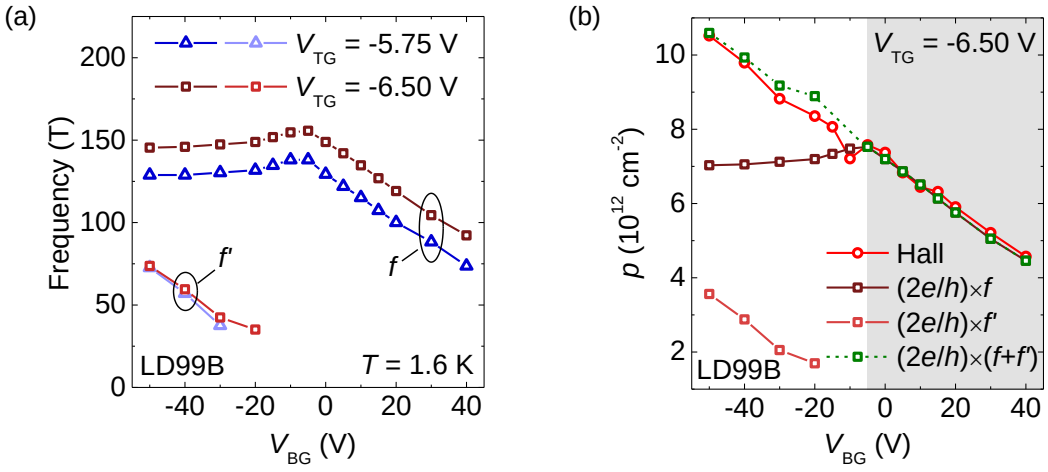

Figure 3.14: (a) FT peaks frequencies f and f' vs V_{BG} for bilayer WSe_2 LD99B at $V_{TG} = -5.75$ V and -6.50 V. (b) p vs V_{BG} corresponding to the $V_{TG} = -6.50$ V FT data of panel (a) and from Hall measurements. The f peak corresponds to holes in the top layer and f' to holes in the bottom layer of bilayer WSe_2. The total FT density $p = (2e/h) \times (f + f')$ matches closely with the Hall density. The shaded area indicates the region where the bottom layer is depopulated.

The combined dependence of the f and f' peaks on V_{BG} and V_{TG} suggest the following interpretation for their origin. The peak f is determined by the hole density in the top layer of bilayer WSe_2 and the peak f' by the hole density in the bottom layer of bilayer WSe_2. For positive V_{BG} values, the bottom layer is fully depleted, while the top layer is populated by the applied V_{TG}. Consequently, only the f peak appears in this regime. Further, since the top layer can be depleted by both V_{TG} and positive V_{BG}, the f peak responds to both V_{TG} and positive V_{BG} values. A negative V_{BG}, on the other hand, populates the bottom layer with holes. The f' peak therefore appears in this regime. When both the layers are populated, the f and f' peaks respond largely to V_{TG} and V_{BG}, respectively, and are insensitive to the opposite gate due to screening.

To verify this interpretation, Fig. 3.14(b) shows a comparison of p vs V_{BG} determined from Hall measurements and from the FT data, assuming a two-fold Landau level degeneracy for both peaks. The Hall density matches closely with the FT density, $p = (2e/h) \times (f + f')$, justifying the interpretation that f and f' are determined by the top and bottom layer densities, respectively, and also proves the two-fold Landau level degeneracy assignment for both the top and bottom layer subbands of bilayer WSe_2. Resolving individual layer

densities in bilayer WSe_2 indicates that the layers are weakly coupled, and can effectively be treated as two monolayers of WSe_2. This behavior in bilayer WSe_2 is similar to the layer density dependence on gate-bias in GaAs double quantum wells separated by a tunneling barrier [111].

Another interesting feature of Fig. 3.14 data is that the frequency f, and therefore the top layer density decreases with increasing total density when V_{BG} is negative, i.e., when the bottom layer is populated. This behavior is a consequence of negative compressibility of holes in the bottom WSe_2 layer as a result of electron-electron interactions. The decrease of the top layer density can be explained as follows. At equilibrium, the Fermi level has to be the same in both the layers. This necessitates the top layer density, which is a proxy for its Fermi level, to track the bottom layer Fermi level [112]. If negative compressibility in the bottom layer causes its Fermi level to decrease with increasing density, the top layer density consequently mirrors this decrease. Similar observations of negative compressibility have been made for 2DESs in GaAs [113], metal oxide heterojunctions [114], and even TMDs such as MoS_2 [112], and bulk WSe_2 [115].

3.5 Effective Mass of Holes in Monolayer and Bilayer WSe_2

This section discusses the temperature-dependence of the SdH oscillations in monolayer and bilayer WSe_2 in order to extract their hole effective masses. Figure 3.15(a) shows R_{xx} vs B for monolayer WSe_2 LD103 at $p = 7.9 \times 10^{12}$ cm^{-2}, and at temperatures ranging between $T = 1.6$ K and 7.0 K. The SdH oscillations' amplitude decreases with increasing temperature as expected.

Given the non-zero background in the data, a Fourier analysis was performed to more accurately extract the corresponding ΔR_{xx} vs T data. Figure 3.15(b) shows the FT spectra of the R_{xx} vs $1/B$ data of Fig. 3.15(a). A band-pass filter centered at the peak of interest at f [shaded region in Fig. 3.15(b)] was then applied and an inverse Fourier transform performed to yield the ΔR_{xx} vs $1/B$ data at different temperature values, as shown in Fig. 3.15(c). At a fixed B-field, the ΔR_{xx} vs T data was fitted to the Dingle factor, $\xi/\sinh\xi$, where $\xi = 2\pi^2 k_B T/\hbar\omega_c$ [Eq. 3.24] to obtain m^* at that particular value of B [inset of Fig. 3.15(c)]. Figure 3.15(d) summarizes the extracted values of m^*/m_e vs B. The value of m^* is $0.45m_e$, and is insensitive to the B-field.

Figure 3.16 shows a similar set of data for bilayer LD99B at $p = 9.8 \times 10^{12}$ cm^{-2} [$V_{TG} = -6.50$ V, $V_{BG} = -40$ V], chosen specifically in order to populate both the bilayer subbands. Figure 3.16(a) show the R_{xx} vs B data and Fig. 3.16(b) the corresponding FT amplitude vs frequency of the R_{xx} vs $1/B$ data. The FT spectra show two principal peaks

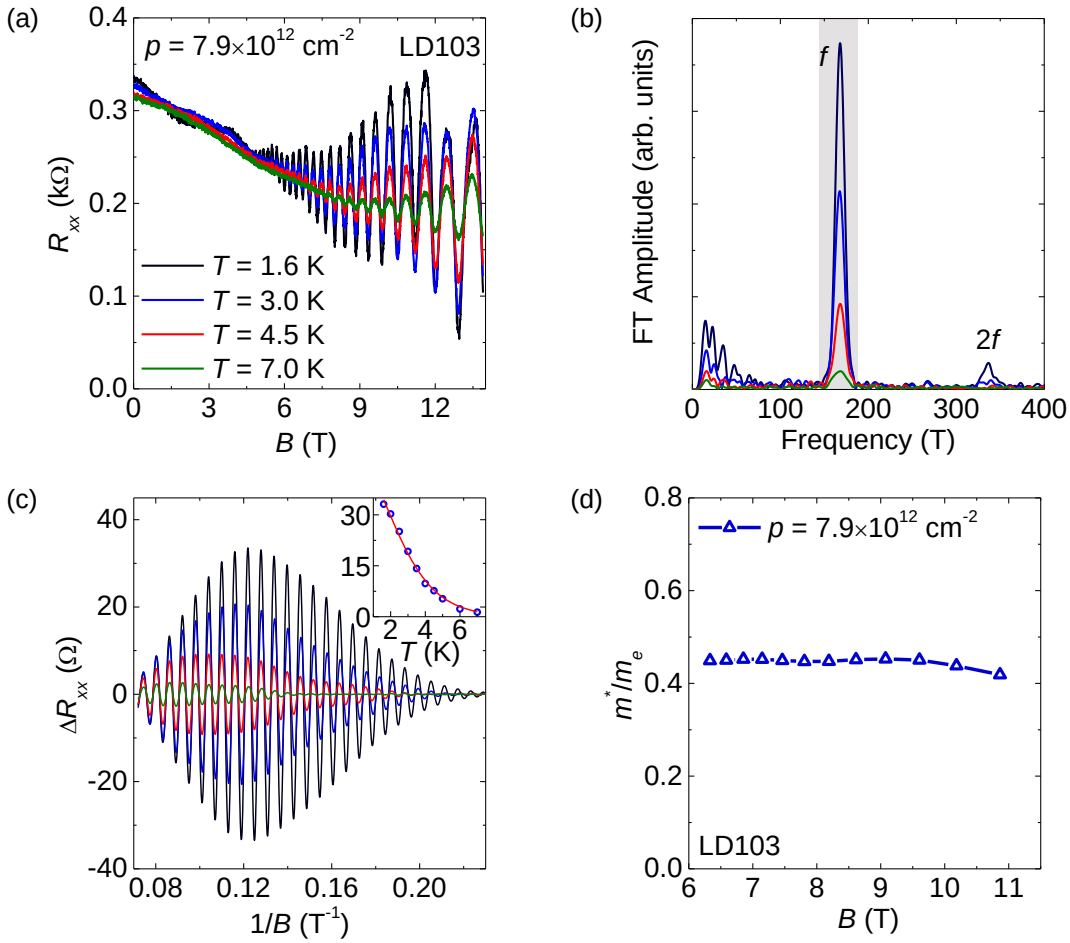

Figure 3.15: (a) R_{xx} vs B for monolayer WSe_2 LD103 at $p = 7.9 \times 10^{12}$ cm^{-2}, and varying temperature. (b) FT amplitude vs frequency of the R_{xx} vs $1/B$ data of panel (a). (c) ΔR_{xx} vs $1/B$ calculated from the inverse FT of panel (b) data after isolating the peak f, shown by the shaded region in panel (b). Inset: Dingle factor fit (line) to the ΔR_{xx} vs T data extracted at $B = 7.8$ T (symbols). (d) Summary of m^*/m_e vs B yields an $m^* = 0.45m_e$, nearly independent of B.

labeled f (top layer subband) and f' (bottom layer subband). Similar to the monolayer case, band-pass filters were centered at each individual peak and their inverse Fourier transforms computed. The ΔR_{xx} contributions of each peak can be deconvoluted this way to calculate the effective mass associated with each peak (subband). Figure 3.16(c) shows the ΔR_{xx} vs $1/B$ data obtained from the inverse Fourier transform of the filtered f' peak. Finally, performing Dingle factor fits for ΔR_{xx} vs T obtained from both the f and f' peaks yields their corresponding m^*/m_e values, as summarized in Fig. 3.16(d). Both the top and bottom layer subbands have the same $m^* = 0.45m_e$, in agreement with Fig. 3.15(d) for monolayer

WSe_2.

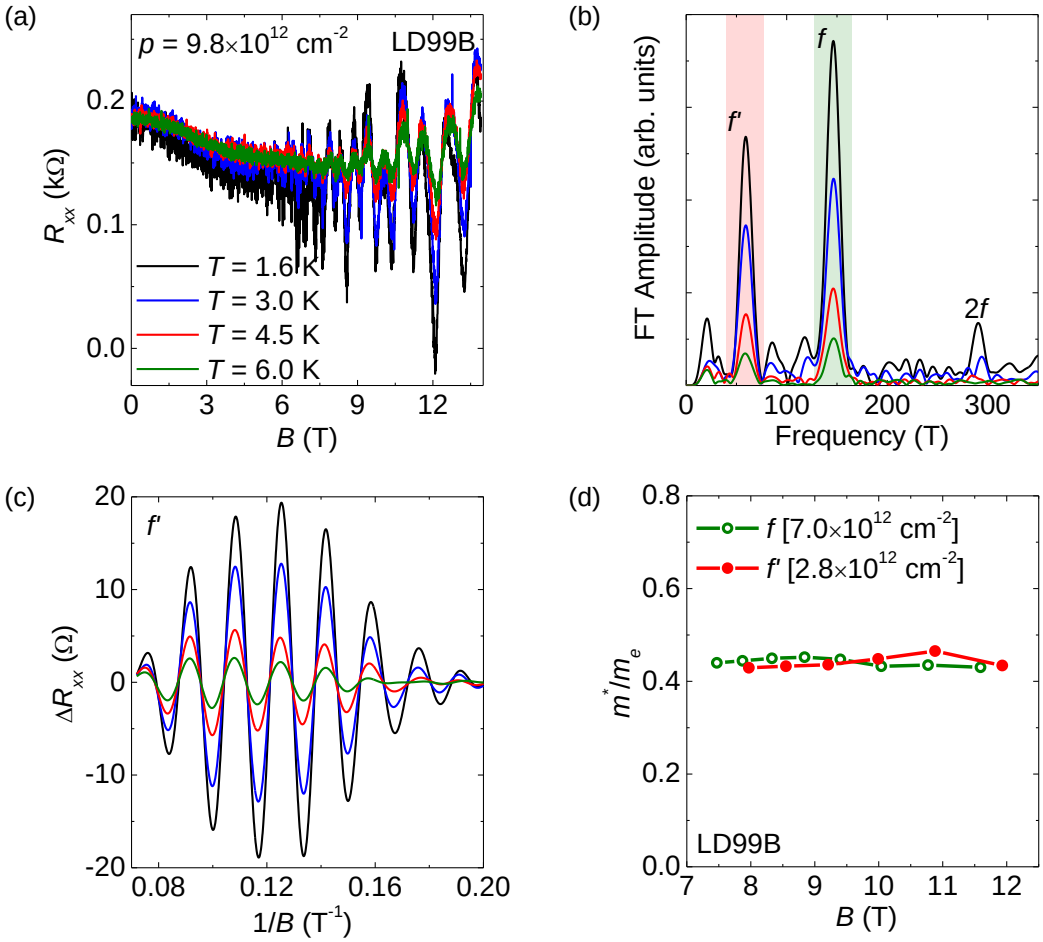

Figure 3.16: (a) R_{xx} vs B for bilayer WSe_2 LD99B measured at $p = 9.8 \times 10^{12}$ cm^{-2}, and varying temperature. (b) FT amplitude vs frequency corresponding to the R_{xx} vs $1/B$ data of panel (a). The peaks f and f' are independently filtered [shaded regions] and their corresponding inverse Fourier transforms computed. (c) ΔR_{xx} vs $1/B$ of the inverse Fourier transform corresponding to peak f' of panel (b) data. (d) Summary of m^*/m_e vs B yields an $m^* = 0.45m_e$ for both the peaks (subbands) of bilayer WSe_2.

The fact that the m^* values associated with the two bilayer subbands are close, and similar to that of monolayer WSe_2 further confirms that the two subbands correspond to the two layers of bilayer WSe_2. Reported theoretical m^*/m_e values for the upper valence band in monolayer WSe_2 include 0.33 [116], 0.34 [117], 0.36 [118, 119], 0.43 [120], 0.46 [36], and 0.51 [88]. Recent Landau level spectroscopy measurements of monolayer WSe_2 holes report an $m^* = 0.5m_e$ [121].

3.6 Density-Dependence of Hole Effective Mass

The effective mass in semiconductors, to first order, depends only on the parabolicity of the bands and is expected to be independent of the carrier density. However, in the presence of electron-electron interaction effects, especially at low-densities, the effective mass has been reported to vary as a function of density. For instance, the effective mass has been reported to increase with decreasing density in Si [122], GaAs [123], and AlAs [124] 2D electrons, but also to decrease with decreasing density in GaAs [125] and spin-polarized AlAs [126] 2D electrons.

To investigate the effect of interactions on the hole effective mass in WSe_2, the SdH oscillations' temperature-dependence was studied as a function of varying density. Figure 3.17 shows the extracted m^*/m_e vs B data at various density values from $p = 1.4$ to 7.6×10^{12} cm^{-2} for a bilayer WSe_2 sample, LD163. The gate-bias values were chosen such that only the top layer is populated with holes, rendering the bilayer equivalent to a monolayer in this regime. The value of $m^* \simeq 0.45m_e$ and is nearly independent of the density. These data suggest that interaction effects have a negligible impact on the effective mass of WSe_2 in the range of density values probed here.

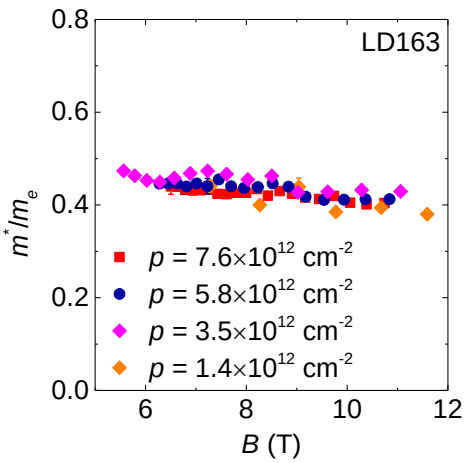

Figure 3.17: Summary of m^*/m_e vs B measured at various hole densities in bilayer LD163, where only the top layer subband is occupied. The m^* values are nearly independent of density in the range of densities probed.

3.7 Interlayer Coupling in Bilayer WSe_2

The tunability of individual layer densities hints at a weak interlayer coupling between the constituent layers of bilayer WSe_2. This is in contrast to Bernal stacked bilayer

graphene, where the strong interlayer coupling ($\simeq 0.4$ eV) alters its bandstructure compared to monolayer graphene, and prevents independent tuning of layer densities. An experimental measurement of the interlayer coupling in bilayer WSe_2 can be made by balancing the top and bottom layer densities, and measuring the subband splitting at the anti-crossing of the f and f' peaks [127].

Figure 3.18(a) shows the FT spectra and Fig. 3.18(b) the associated p vs V_{BG} data for bilayer WSe_2 LD201, corresponding to a set of R_{xx} vs B data measured at fixed $V_{TG} = -7.5$ V and varying $V_{BG} = -8.0$ to 3.0 V. The data show two peaks, f and f', for $V_{BG} \leq -2.0$ V, characteristic of two populated subbands in bilayer WSe_2. Similar to Fig. 3.14 data, the f' peak frequency increases, while the f peak frequency remains relatively unchanged with increasing $|V_{BG}|$ in this regime. Interestingly, the two peaks merge into one at $V_{BG} = -7.0$ V, before splitting again at $V_{BG} = -8.0$ V. The merging of the two peaks is indicative of equal hole densities in the two subbands, up to a resolution limit determined by the FT peak width, and places an upper bound on the interlayer coupling [127].

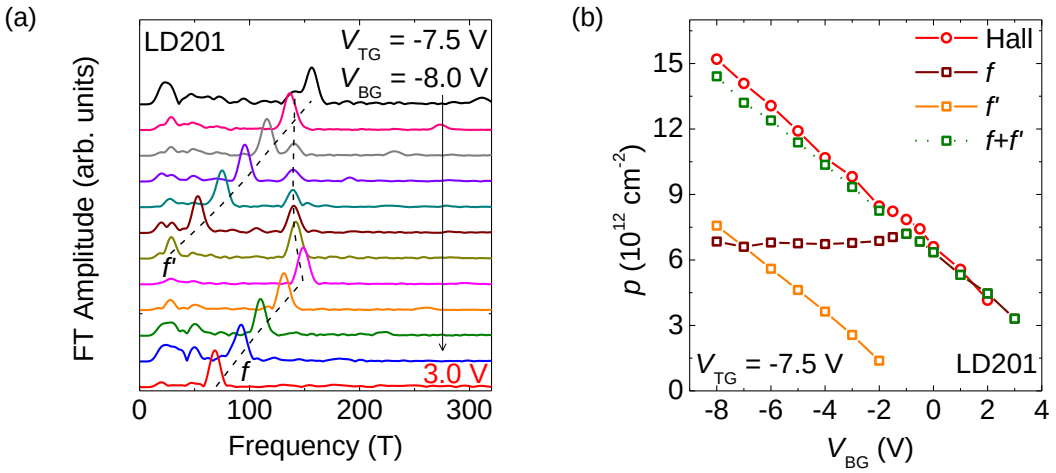

Figure 3.18: (a) FT amplitude vs frequency corresponding to the R_{xx} vs B data for bilayer WSe_2 LD201 at a fixed $V_{TG} = -7.5$ V and varying V_{BG} values from -8.0 V to 3.0 V, in steps of 1 V. The spectra are shifted for clarity. The dashed lines are a guide to the eye and track the f and f' peaks. The f and f' peaks merge into one peak at $V_{BG} = -7$ V. (b) p vs V_{BG} corresponding to the FT data of panel (a) and from Hall measurements.

The FT peak width at $V_{BG} = -7.0$ V of 13 T corresponds to a density difference between the two subbands not greater than 0.63×10^{12} cm^{-2}. Using a density of states, $m^*/\pi\hbar^2 = 1.88 \times 10^{14}$ cm^{-2}eV^{-1}, this yields a maximum subband separation of 3.4 meV, a value much smaller than theoretical estimates. Theoretical estimates of the interlayer coupling in bilayer WSe_2 range from 60 meV [120] to 67 meV [128].

3.8 Summary

In summary, magnetotransport measurements in monolayer and bilayer WSe_2 reveal well-defined SdH oscillations, a bona fide signature of high-mobility holes in WSe_2. Fourier analyses of the SdH oscillations evince important electronic transport properties such as two-fold degenerate Landau levels, and a hole effective mass of $m^* = 0.45m_e$ in both monolayer and bilayer WSe_2. The bilayer data also reveal carrier localization in the two constituent layers, signifying a weak interlayer coupling for holes in the K and K' valleys. Bilayer WSe_2 is therefore closely similar to monolayer WSe_2 for non-negative back-gate biases, i.e., when the bottom layer is unpopulated. When populated, holes in the bottom layer of bilayer WSe_2 show evidence of negative compressibility, as a result of electron-electron interactions, stemming from their large effective mass.

Interaction effects are expected to be a strong function of the carrier density, and can be probed by a systematic density-dependence of the quantum Hall states. A more detailed study of the quantum Hall effect in high magnetic fields would also give insights into the Landau level degeneracies, their splittings, and the contribution of the spin and valley Zeeman energies. The measurements and findings of this chapter lay the foundation for more extensive measurements in higher magnetic fields, and over a wider range of densities, which are the focus of the next chapter.

Chapter 4

Density-Dependent Quantum Hall States and Zeeman Splitting in Monolayer and Bilayer WSe_2

The strong spin–orbit coupling and broken inversion symmetry in $2H$-TMD monolayers leads to coupled spin and valley degrees of freedom [33], resulting in two-fold degenerate Landau levels in low magnetic fields. In contrast, graphene 2DESs display four-fold spin-valley degenerate Landau levels in low magnetic fields which evolve into more interesting broken-symmetry quantum Hall states at low-densities and in high magnetic fields, driven by electron-electron interactions and Zeeman splitting [130, 131, 132].

A question to ask is what happens to the WSe_2 quantum Hall states at low-densities and in high magnetic fields. The Zeeman effect is expected to be strong in TMDs due to the large magnetic moment of the d-orbitals which make up the conduction and valence band states in the K and K' valleys [33]. Magneto-optical measurements of TMD monolayers have reported accordingly large exciton g-factors from luminescence shifts in magnetic fields [133, 134, 135, 136, 137, 138]. The exciton g-factor, however, could be different from the g-factor of either electrons or holes, and may not capture interaction effects that are expected to be strong in TMDs. Traditionally, magnetotransport has been used to determine the effective g-factor (g^*) and interaction effects in several 2DESs [124, 139, 140], hindered thus far in TMDs due to poor electrical contacts and mobilities.

In continuation to Chapter 3, this chapter focuses on magnetotransport in monolayer and bilayer WSe_2 in the quantum Hall regime. The quantum Hall states (QHS) reveal interesting transitions between predominantly even and predominantly odd filling factors as the hole density is tuned, which can be explained by a Zeeman-to-cyclotron energy ratio that changes as a function of density due to strong electron-electron interactions. Further, tilted magnetic field measurements reveal that the QHS are insensitive to the in-plane magnetic field, implying that the hole-spin is locked perpendicular to the WSe_2 plane.

Portions of this chapter have been published as Ref. [129]: H. C. P. Movva, B. Fallahazad, K. Kim, S. Larentis, T. Taniguchi, K. Watanabe, S. K. Banerjee, and E. Tutuc, "Density-Dependent Quantum Hall States and Zeeman Splitting in Monolayer and Bilayer WSe_2," *Phys. Rev. Lett.*, vol. 118, no. 24, p. 247701, 2017. The dissertator, H. C. P. Movva, contributed to the WSe_2 sample fabrication, characterization, data analysis, and writing the paper.

4.1 Quantum Hall Effect in Monolayer TMDs

The analysis of the quantum Hall effect in Sec. 3.1.2 was carried out for carriers in a parabolic band, without taking into account material specific details such as the lattice symmetries, spin–orbit coupling, and their associated effects on the electronic bandstructure. A more accurate picture of the quantum Hall effect in TMDs in general, and WSe_2 in particular, can be obtained by considering such details as follows.

Two salient features of $2H$-TMD monolayers which distinguish them from graphene, and which are responsible for their interesting electronic bandstructure are the breaking of inversion symmetry, and strong spin–orbit coupling due to the heavy metal atoms [32, 33]. The $\mathbf{k} \cdot \mathbf{p}$ Hamiltonian describing the bandstructure of $2H$-TMD monolayers in the vicinity of the K and K' points of the hexagonal Brillouin zone is similar to that of graphene, but with an energy difference between the two sublattices due to inversion symmetry breaking, and is given by [116]

$$\mathcal{H} = v_{\mathrm{F}}(p_x \tau \sigma_x + p_y \sigma_y) + \Delta \sigma_z - \lambda \tau s \sigma_z + \lambda \tau s \tag{4.1}$$

where $v_{\mathrm{F}} = a t_h/\hbar$ is the Fermi velocity; a is the in-plane lattice constant, t_h is the effective hopping integral, $\boldsymbol{p}$ is the momentum operator, $\boldsymbol{\sigma}$ denote the Pauli matrices, $\tau = \pm 1$ is the valley index (+1 for K and −1 for K'), $s = \pm 1$ denotes the electron spin-↑ and spin-↓, Δ is a measure of the energy gap, and λ is a measure of the spin-splitting in the valence band caused by spin–orbit coupling.[1]

Solving the Hamiltonian yields the energy dispersions as

$$E_{\pm} = \lambda \tau s \pm \sqrt{v_{\mathrm{F}}{}^2 p^2 + (\Delta - \lambda \tau s)^2} \tag{4.2}$$

where ± stand for the conduction and valence bands, respectively. Figure 4.1(a) shows the bandstructure of monolayer WSe_2 in the vicinity of the K and K' points calculated using Eq. 4.2 and parameters from Ref. [33]. The upper and lower valence band maxima correspond to $\tau s = 1$ and $\tau s = -1$, respectively. In other words, the spin (s) and valley (τ) degrees of freedom are coupled at the K and K' points.[2]

In the presence of a perpendicular magnetic field, the Hamiltonian of Eq. 4.1 can be modified to include the magnetic vector potential ($\boldsymbol{A}$) by replacing $\boldsymbol{p}$ with $\boldsymbol{p} + e\boldsymbol{A}/c$; c is the speed of light. To focus on the influence of the inversion asymmetry and spin–orbit

[1] The notations for Δ and λ in Ref. [116] are the same as in Ref. [33] scaled by a factor of 1/2.

[2] The conduction band states are also spin-valley locked, but more advanced models are needed to accurately reproduce the conduction band splitting, for instance Refs. [141, 142].

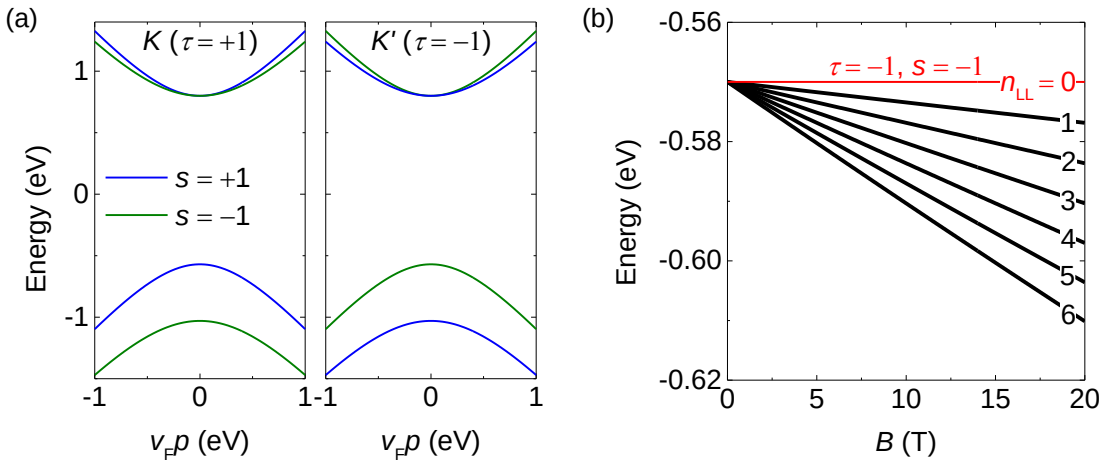

Figure 4.1: (a) Bandstructure of monolayer WSe_2 near the K and K' points calculated using Eq. 4.2 and parameters from Ref. [33]. (b) The corresponding Landau level spectrum of the upper valence band calculated using Eq. 4.3. The $n_{LL} = 0$ Landau level is non-degenerate and $n_{LL} > 0$ Landau levels are two-fold degenerate. Adapted from Ref. [116].

coupling, Zeeman coupling and interaction effects are neglected, and Eq. 4.1 solved to obtain the Landau level spectrum at K and K' as [116]

$$E_{n_{LL},\pm} = \lambda\tau s \pm \sqrt{n_{LL}\hbar^2\omega_c^2 + (\Delta - \lambda\tau s)^2} \tag{4.3}$$

where $\omega_c = \sqrt{2}v_F/l_B$ is the cyclotron frequency; $l_B = \sqrt{\hbar/eB}$, and n_{LL} is the Landau level index. The four $n_{LL} = 0$ Landau levels are broken into a two-fold spin-degenerate conduction band $n_{LL} = 0$ Landau level at the K valley, and two spin-split upper and lower valence band $n_{LL} = 0$ Landau levels at K' [116]. Figure 4.1(b) shows the Landau level spectrum of the upper valence band where the $n_{LL} = 0$ Landau level is non-degenerate and resides in the K' valley (spin-$\downarrow$ state) and $n_{LL} > 0$ Landau levels are two-fold degenerate, consisting of one spin-$\uparrow$ state from one valley and one spin-$\downarrow$ state from the other valley. Therefore, quantum Hall states are expected at odd filling factors, i.e., $\nu = 1, 3, 5, \ldots$ when only the upper valence band is populated.

However, the data of Fig. 3.10 show even filling factors, in apparent disagreement with this picture. This can be explained by considering the Zeeman contribution to the Landau level energies. Expanding Eq. 4.3 at low $n_{LL}B$, and defining an effective mass $m^* = (\Delta - \lambda)/v_F^2$ and the upper valence band energy $\Delta_V = -\Delta + 2\lambda$ yields the Landau level spectrum for the upper valence band in the absence of Zeeman splitting as

$$E_{n_{LL},V} = \Delta_V - n_{LL}\hbar\omega_c \tag{4.4}$$

where $\omega_c = eB/m^*$ is the usual cyclotron frequency. Adding the spin and valley Zeeman contributions gives

$$E^{\tau s}_{n_{\mathrm{LL}},V} = \Delta_V - n_{\mathrm{LL}}\hbar\omega_c + \frac{s}{2}g_s\mu_{\mathrm{B}}B + \frac{\tau}{2}g_v\mu_{\mathrm{B}}B \tag{4.5}$$

where g_s and g_v are the spin and valley g-factors, respectively, $\tau = s = \pm 1$ for the upper valence band, and μ_{B} is the Bohr magneton. Theoretically, $g_s = 2$ and $|g_v| = g_d + 2\alpha$, where the first term, g_d, stems from the d-orbital magnetic moment, and the second, $\alpha = m_e/m^*$, is associated with the valley Berry phase [143]. Comparing the Zeeman contributions in Eq. 4.5 with Eq. 3.22, an effective g-factor (g^*) can be defined tentatively[3] as $g^* = g_s + g_v$, which in turn determines the Zeeman splitting in WSe_2 as $E_{\mathrm{Z}} = g^*\mu_{\mathrm{B}}B$.

Given the large m^* of holes in WSe_2, the Zeeman contribution can substantially alter the Landau level spectrum. For instance, certain values of the Zeeman energy can bring into alignment the non-degenerate $n_{\mathrm{LL}} = 0$ Landau level with the spin-↑ state of the $n_{\mathrm{LL}} = 1$ Landau level, and so on, transforming the filling factors to $\nu = 2, 4, 6, \ldots$ The following sections discuss magnetotransport measurements in monolayer and bilayer WSe_2 aimed towards revealing the role of Zeeman splitting on the Landau level spectrum, and in turn, determining the effective g-factor of holes in WSe_2.

4.2 Quantum Hall Effect in Monolayer and Bilayer WSe_2

Achieving low filling factors in magnetotransport requires access to low carrier densities and high magnetic fields. Compared to an Si/SiO_2 back-gate, a local metal back-gate with an h-BN dielectric allows more effective depletion of the WSe_2 channel, and permits access to lower hole densities. Further, a metal back-gate has also been shown to screen charged impurities from the SiO_2 substrate, yielding higher quality samples with lower disorder [144].

Figure 4.2(a) shows the schematic cross section of an h-BN encapsulated WSe_2 device with local top- and back-gates, and Fig. 4.2(b) the optical micrograph of bilayer LD123, a typical WSe_2 Hall bar sample of this structure. The local back-gated samples were fabricated following the same steps as in Chapters 2 and 3, but with the addition of a local metal back-gate underneath the bottom h-BN substrate. The detailed fabrication process and techniques are described in Appendix B and the samples' details in Appendix A.

[3] The effective g-factor is a more complicated function of the material bandstructure and electron-electron interaction effects. A more detailed description is provided in Sec. 4.6.1.

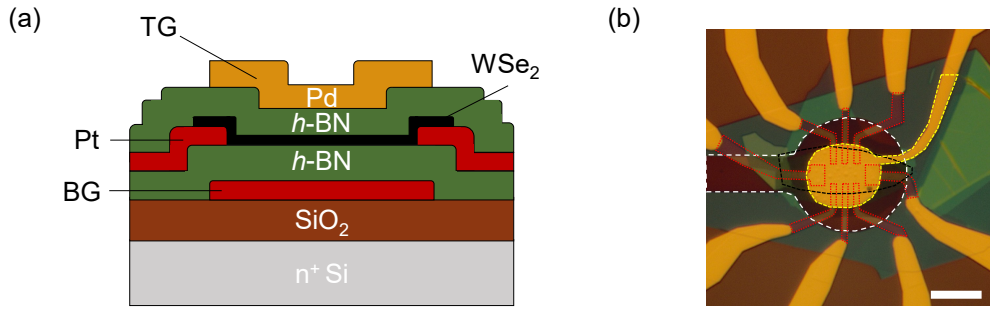

Figure 4.2: (a) Schematic cross section of an h-BN encapsulated WSe_2 device with a metal local back-gate. (b) Optical micrograph of LD123, a typical local back-gated WSe_2 Hall bar sample. The top-gate, Pt contacts, WSe_2 flake, and back-gate are outlined by yellow, red, black, and white dashed lines, respectively. The scale bar is 10 μm.

In order to access magnetic fields higher than 14 T, the samples were cooled in a variable temperature insert coupled to a 35 T resistive magnet at the National High Magnetic Field Laboratory in Tallahassee, Florida. Magnetotransport was probed using standard small-signal excitation current, $I = 10$ nA, low-frequency (9 – 13 Hz) lock-in techniques, similar to Chapter 3. At a fixed hole density, the magnetic field was swept at 1 T/minute, and the R_{xx} and R_{xy} data recorded as a function of B. Examples of R_{xx} and R_{xy} vs B at $T = 1.5$ K and at a fixed hole density $p = 4.6 \times 10^{12}$ cm^{-2} for monolayer WSe_2 LD108 [$V_{TG} = -8.5$ V, $V_{BG} = 4.0$ V] and at $p = 1.6 \times 10^{12}$ cm^{-2} for bilayer WSe_2 LD123 [$V_{TG} = -5.8$ V, $V_{BG} = 6.8$ V] are shown in Figs. 4.3(a) and 4.3(b), respectively. It is noteworthy that these density values are lower than the typical densities attainable in samples with Si/SiO_2 back-gates.

Both the monolayer and bilayer R_{xx} vs B data show well-defined SdH oscillations starting at $B \simeq 5$ T. At high B-fields, the R_{xx} minima evolve towards zero resistance, accompanied by plateaux in R_{xy}, signifying developing QHS. The filling factors, $\nu = ph/eB$, corresponding to the R_{xx} minima are marked along with the expected quantized values of R_{xy} at $h/\nu e^2$. The filling factors of Figs. 4.3(a) and 4.3(b) are found to be predominantly odd in the low B-field regime, in stark contrast to the low B-field R_{xx} vs B data of Fig. 3.10 which show even filling factors. Furthermore, the data of Fig. 4.3(b) show QHS at consecutive integral filling factors ($\nu = 2, 3, 4, \ldots$) for $B > 10$ T, signifying a lifting of the two-fold Landau level degeneracy.

While odd filling factors are expected for TMDs in the absence of Zeeman splitting [116, 145], it contrasts and brings into question the observation of even filling factors in Chapter 3 data. To investigate the origin of this difference, magnetotransport measurements

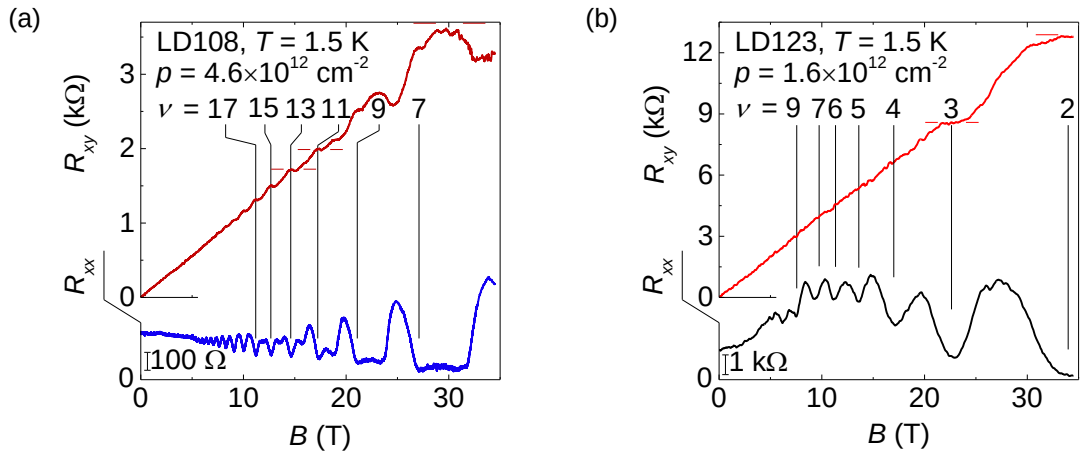

Figure 4.3: (a) R_{xx} and R_{xy} vs B for monolayer WSe_2 LD108 measured at T = 1.5 K and $p = 4.6 \times 10^{12}$ cm^{-2}. (b) R_{xx} and R_{xy} vs B for bilayer WSe_2 LD123 measured at T = 1.5 K and $p = 1.6 \times 10^{12}$ cm^{-2}. The filling factors, ν, corresponding to the R_{xx} minima are labeled, along with quantized R_{xy} plateaux, when present.

were performed as a function of varying density in both monolayer and bilayer WSe_2. All the bilayer data presented in this chapter are for gate-biases where only the top layer subband is populated, and are therefore closely similar to monolayer data, albeit with a dissimilar dielectric environment.[4] For the subsequent discussion, the term "QHS sequence" is used to denote the sequence of the QHS filling factors in the low B-field regime, such that the Landau level degeneracy is not fully lifted.

4.3 Density-Dependent Quantum Hall States Sequence

Figures 4.4(a) and 4.4(b) show R_{xx} and R_{xy} vs B measured in bilayer WSe_2 LD123 at two other density values, $p = 3.9 \times 10^{12}$ cm^{-2} and $p = 5.3 \times 10^{12}$ cm^{-2}, respectively. While the data at $p = 3.9 \times 10^{12}$ cm^{-2} show an odd QHS sequence, the QHS sequence is even at $p = 5.3 \times 10^{12}$ cm^{-2}. This is also apparent in the high B-field data based on the stronger R_{xx} minima at the filling factors marked in Fig. 4.4, in comparison to their adjacent weaker minima which arise from spin-splitting at high B-fields. Alternation of the QHS sequence between even and odd filling factors depending on the density hints at a systematic density-dependence of the QHS sequence.

[4]While a monolayer has only h-BN as the bottom dielectric, a bilayer biased to populate only the top layer has an unpopulated WSe_2 bottom layer which alters the dielectric environment of holes in the top layer.

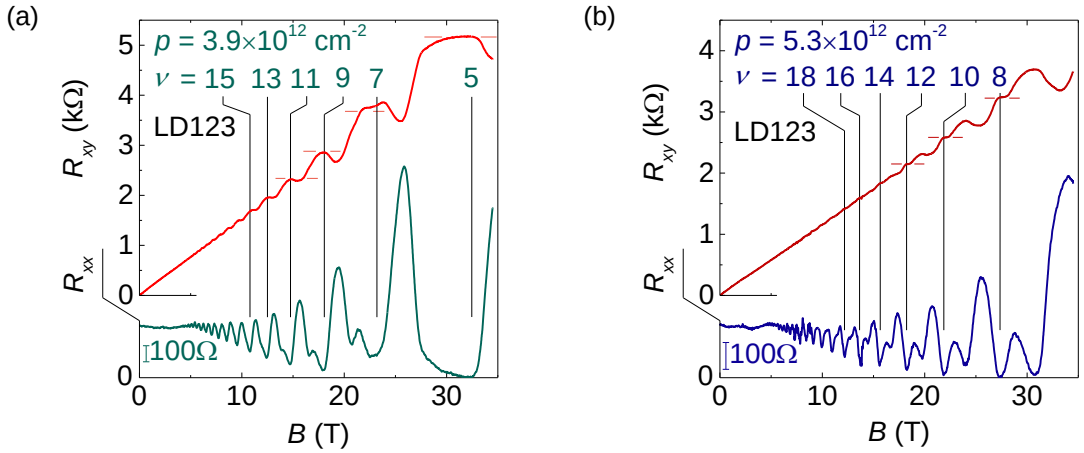

Figure 4.4: (a) R_{xx} and R_{xy} vs B for bilayer WSe_2 LD123 at $p = 3.9 \times 10^{12}$ cm^{-2} show QHS at predominantly odd filling factors. (b) R_{xx} and R_{xy} vs B for the same bilayer LD123 at a different density $p = 5.3 \times 10^{12}$ cm^{-2} show QHS at predominantly even filling factors.

Figure 4.5(a) shows R_{xx} vs ν for bilayer WSe_2 LD123 at various density values from $p = 6.1 \times 10^{12}$ cm^{-2} to 2.4×10^{12} cm^{-2}. The data at $p = 6.1 \times 10^{12}$ cm^{-2} show strong R_{xx} minima at even filling factors, and weakly developing minima at odd filling factors for $\nu < 16$, hence an even QHS sequence. As the density is reduced to 4.4×10^{12} cm^{-2}, the minima at odd filling factors get stronger and become equal in strength to the minima at even filling factors. The QHS sequence at this density cannot be unambiguously classified as even or odd. Further reduction of the density to 3.9×10^{12} cm^{-2} makes the odd filling factors stronger than the even filling factors, rendering the QHS sequence odd. The odd QHS sequence is retained down to $p = 2.9 \times 10^{12}$ cm^{-2} and upon further reducing the density to 2.4×10^{12} cm^{-2}, the QHS sequence reverts to even. Figure 4.5(b) shows a similar set of data for monolayer WSe_2 LD108, where the QHS sequence is even at $p = 9.7 \times 10^{12}$ cm^{-2}, becomes odd at $p = 4.6 \times 10^{12}$ cm^{-2}, and is back to even at $p = 3.3 \times 10^{12}$ cm^{-2}.

This unusual density-dependence of the QHS sequence suggests an interesting interplay of the Landau level Zeeman splitting and the cyclotron energy. As discussed in Sec. 4.1, in the absence of Zeeman splitting, the Landau levels of the upper valence band in monolayer WSe_2 are $E_{n_{LL}} = -n_{LL}\hbar\omega_c$, with a non-degenerate $n_{LL} = 0$ Landau level and two-fold, spin-valley degenerate $n_{LL} > 0$ Landau levels. Consequently, as shown in Fig. 4.6(a), an odd QHS sequence is expected when there is no Zeeman splitting. However, if the Landau level spin-degeneracy is lifted through a Zeeman splitting, $E_Z = g^*\mu_B B$, comparable to the cyclotron energy, $E_c = \hbar\omega_c$, the QHS sequence can change. For instance, Fig. 4.6(b) shows the Landau level spectrum when $E_Z \approx E_c$, in which case the QHS se-

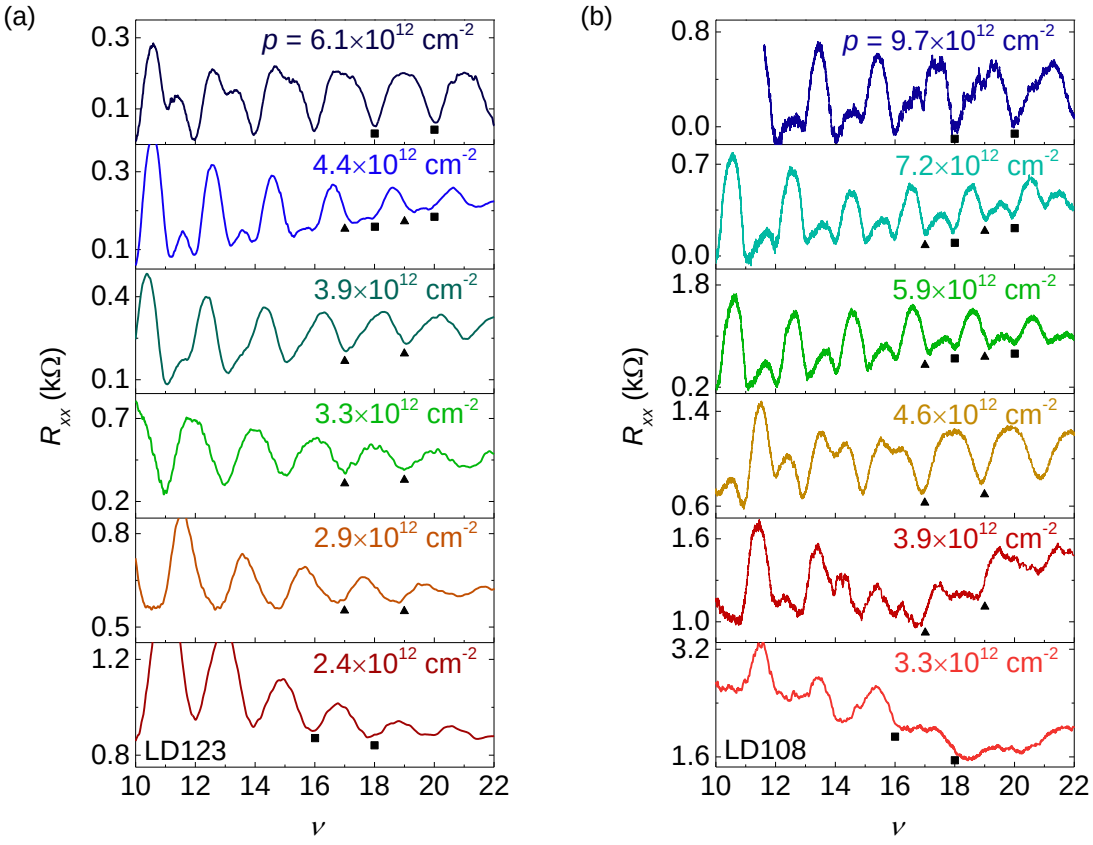

Figure 4.5: (a) R_{xx} vs ν for bilayer WSe_2 LD123 as a function of varying density show the transition of the QHS sequence from even at $p = 6.1 \times 10^{12}$ cm^{-2} to odd at $p = 3.3 \times 10^{12}$ cm^{-2}, and back to even at $p = 2.4 \times 10^{12}$ cm^{-2}. (b) R_{xx} vs ν for monolayer WSe_2 LD108 as a function of density show similar QHS sequence transitions, albeit over a different density range. Representative even and odd QHS R_{xx} minima are marked by ■ and ▲ symbols, respectively.

quence is expected to be even. If the Zeeman splitting is even larger, for instance, twice the cyclotron energy, $E_Z \approx 2E_c$, the QHS sequence can revert to odd [Fig. 4.6(c)]. Finally, in the case when the Zeeman splitting is in-between, say, $E_Z \approx 1.5E_c$, the Landau levels are fully spin-resolved and the QHS sequence cannot be assigned as even or odd.

Two important observations can be made by employing this argument to the QHS sequence transitions of Fig. 4.5. First, the presence of an odd or even QHS sequence at a fixed density which does not change with the magnetic field implies that the E_Z/E_c ratio, and therefore g^*, also do not change with the magnetic field. Second, the QHS transitions as a function of density suggest that the E_Z/E_c ratio, and therefore g^*, vary as a function of density, likely because electron-electron interactions associated with the large effective

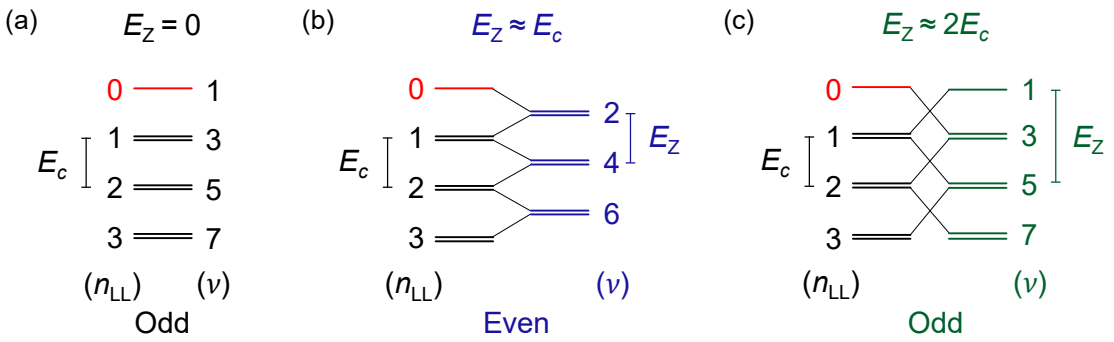

Figure 4.6: (a) Schematic of the upper valence band Landau levels in monolayer WSe_2 in the absence of Zeeman splitting, which is expected to result in an odd QHS sequence. (b) An even QHS sequence is expected if the Zeeman splitting is approximately equal to the cyclotron energy, and (c) an odd QHS sequence if the Zeeman splitting is double the cyclotron energy.

mass of holes in WSe_2 leads to an enhancement of g^* as the density is reduced.

4.4 Tilted Magnetic Field Measurements

Measurements in magnetic fields tilted at an angle from the normal of the 2DES plane have been traditionally used to probe the Zeeman splitting in 2DESs [98]. While the cyclotron energy depends only on the perpendicular component of the magnetic field ($B_\perp$), the Zeeman splitting varies with the total field, B. Therefore, tilting the sample with respect to the magnetic field direction changes the Zeeman-to-cyclotron energy ratio, and consequently, the relative strengths of successive spin-resolved R_{xx} minima. Certain "coincidence" tilt angles can be reached where E_Z/E_c attains integer values, yielding successive R_{xx} minima of equal strength. The value of Zeeman splitting can be discerned from these coincidence angles [98], and their evolution with carrier density.

Figure 4.7(a) shows R_{xx} vs $B_\perp$ for monolayer WSe_2 LD108 at $p = 4.6 \times 10^{12}$ cm^{-2} and at several tilt angles, θ. The R_{xx} data at $\theta = 0°$ show an odd QHS sequence, which remains unchanged for all values of θ up to 77°. Figure 4.7(b) shows a similar set of R_{xx} vs $B_\perp$ data for bilayer WSe_2 LD123 at $p = 3.5 \times 10^{12}$ cm^{-2}, where the QHS sequence is also found to be insensitive to the tilt angle. These observations suggest that the Zeeman splitting does not depend on the parallel component of the magnetic field ($B_{||}$) in both monolayer and bilayer WSe_2. The insensitivity of the monolayer and bilayer WSe_2 R_{xx} data to the tilt angle is in stark contrast to the vast majority of 2DESs based on Si [98], GaAs [140], black phosphorus [146], and even bulk WSe_2 [147], which show significant tilt angle dependence of R_{xx}.

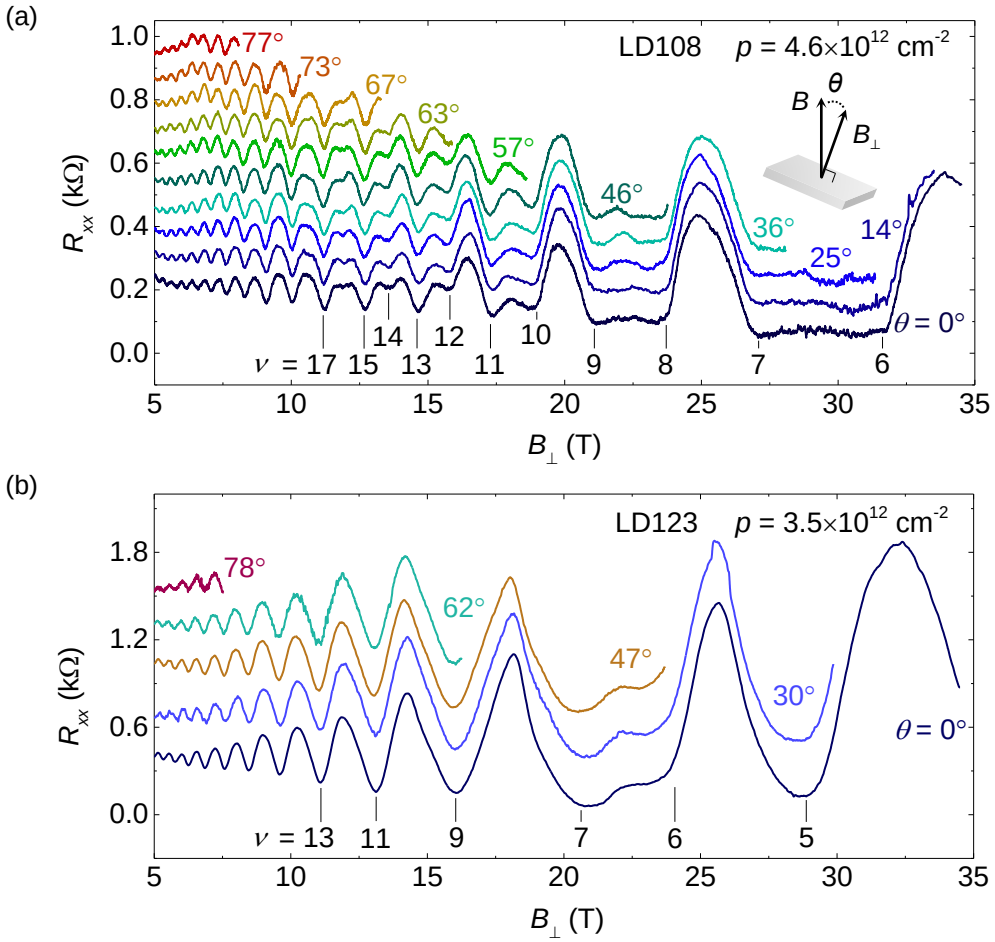

Figure 4.7: (a) R_{xx} vs $B_\perp$ for monolayer WSe_2 LD108 at $p = 4.6\times10^{12}$ cm^{-2} and varying values of tilt angle, θ. The QHS sequence is insensitive to θ. Inset: Schematic of the sample orientation with respect to the magnetic field. (b) R_{xx} vs $B_\perp$ for bilayer WSe_2 LD123 at $p = 3.5\times10^{12}$ cm^{-2} and varying θ shows a similar insensitivity of the QHS sequence to θ. The traces are offset for clarity in panels (a) and (b).

A second technique used to determine the Zeeman splitting is the magnetoresistance measured as a function of the magnetic field applied parallel to the 2DES plane. An in-plane magnetic field leads to a spin-polarization of the 2DES, which reaches unity when the Zeeman energy is equal to the Fermi energy. Experimentally, R_{xx} vs $B_{||}$ shows a positive magnetoresistance, along with a saturation or a marked kink at the magnetic field corresponding to full spin-polarization [124, 140, 148, 149].

Figures 4.8(a) and 4.8(b) show R_{xx} vs $B_{||}$ for monolayer WSe_2 LD108 corresponding to Fig. 4.7(a), and bilayer WSe_2 LD123 corresponding to Fig. 4.7(b), respectively. Surpris-

ingly, yet consistent with Fig. 4.7 data, both the R_{xx} data of Fig. 4.8 remain constant over the entire range of $B_{||}$ from 0 to 35 T, validating the insensitivity of the Zeeman splitting to $B_{||}$. This implies that the Zeeman splitting depends only on $B_{\perp}$, i.e., $E_Z = g^* \mu_B B_{\perp}$, via a density-dependent g^*.

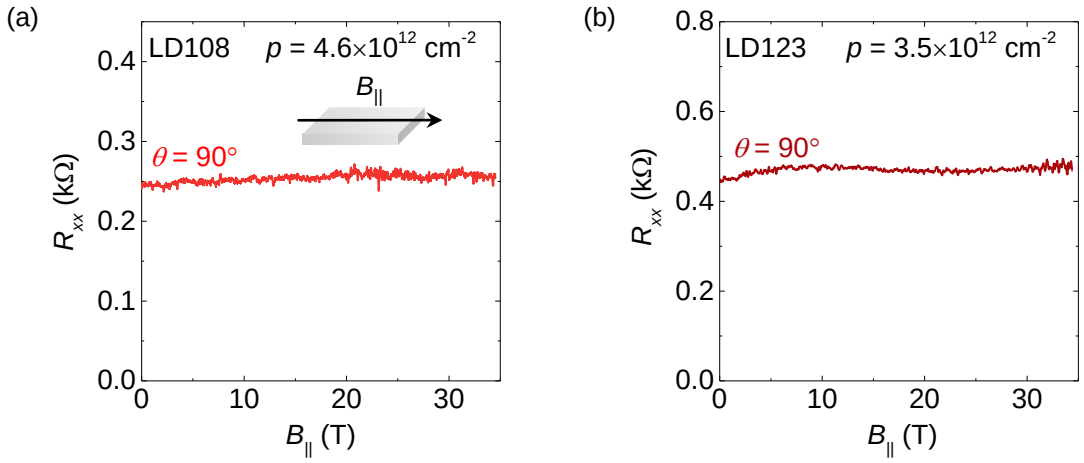

Figure 4.8: (a) R_{xx} vs $B_{||}$ for monolayer WSe_2 LD108 at $p = 4.6 \times 10^{12}$ cm^{-2} corresponding to the $\theta = 90°$ case of Fig. 4.7(a). The R_{xx} remains unchanged over the entire magnetic field range. Inset: Schematic of the sample orientation with respect to the magnetic field. (b) R_{xx} vs $B_{||}$ for bilayer WSe_2 LD123 at $p = 3.5 \times 10^{12}$ cm^{-2} also shows an unchanged R_{xx} from $B_{||} = 0$ to 35 T.

The insensitivity of E_Z to $B_{||}$ indicates that the hole-spin in both monolayer and bilayer WSe_2 at the K and K' points is locked in a direction perpendicular to the 2D plane. This spin-locking is a direct consequence of the strong spin–orbit coupling, and mirror symmetry in monolayer WSe_2 which decouples the spin-↑ and spin-↓ components away from the Brillouin zone center [32, 33]. Due to the crystal electric field ($\vec{\epsilon}_c$) being restricted to the 2D plane thanks to mirror symmetry, the spin–orbit interaction manifests itself as an effective magnetic field, $\vec{B}_{SO}(\mathbf{k}) \propto \vec{\epsilon}_c \times \mathbf{k}$ directed along the z-direction. Furthermore, the large $|\mathbf{k}|$ value at the K and K' points makes $\vec{B}_{SO}$ correspondingly large and opposite in sign at K and K', which locks the hole-spin perpendicular to the 2D plane and in opposite directions at K and K' [150].

Optical experiments on monolayer WSe_2 have also shown a similar insensitivity of the Zeeman splitting to $B_{||}$ [135]. The spin–orbit interaction-induced spin-locking is also responsible for the high in-plane upper critical fields in the "Ising" superconductors based on TMDs such as $NbSe_2$ [150] and MoS_2 [151]. It is to be noted that spin-locking perpendicular to the WSe_2 plane renders the tilted magnetic field technique ineffective for determination of the Zeeman splitting in monolayer and bilayer WSe_2.

4.5 Transverse Electric Field Dependence of the QHS Sequence

In light of Fig. 4.5 data which suggest a density-dependent g^*, an important question is whether the g^* variation is determined by the density, or by the applied transverse electric field (E), which depends on the applied gate-biases and can change concomitantly with the density. In the presence of broken inversion symmetry and strong spin–orbit coupling, the spin-splitting in the valence band can be tuned by the transverse electric field, mediated by the Rashba effect [152, 153]. Varying the carrier density, and concurrently, the electric field, can alter the g^* in such 2DESs, for instance in 2D electrons in indium gallium arsenide/indium aluminum arsenide (InGaAs/InAlAs) [154] and 2D holes in GaAs [155, 156].

To probe the impact of the electric field on the QHS sequence, measurements were performed by varying $E = |C_{TG}V_{TG} - C_{BG}V_{BG}|/2\epsilon_0$, where C_{TG} and C_{BG} are the top-gate and back-gate capacitances, respectively, and ϵ_0 is the vacuum permittivity. Figure 4.9(a) and 4.9(b) show R_{xx} vs ν for bilayer WSe_2 LD123 at $p = 3.5\times10^{12}$ cm^{-2} and $p = 2.4\times10^{12}$ cm^{-2}, respectively, and at different values of E.

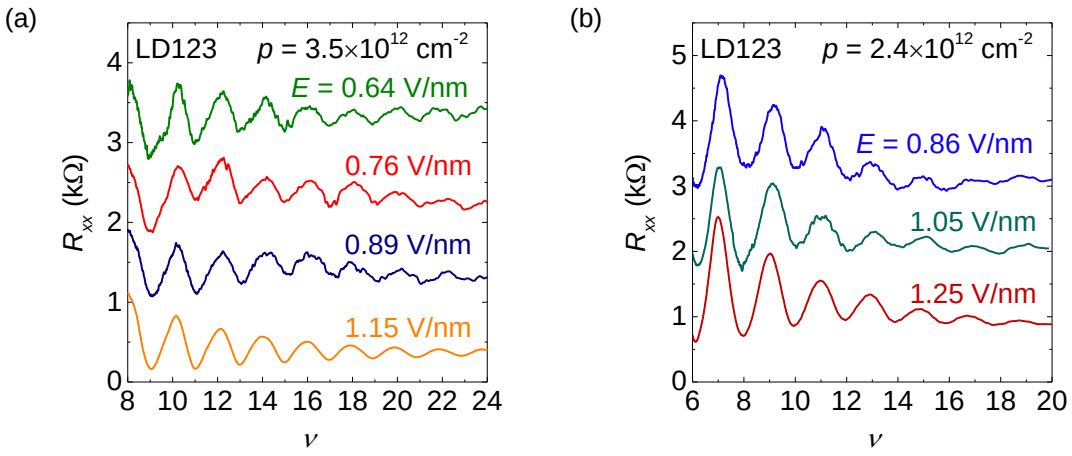

Figure 4.9: (a) R_{xx} vs ν at $p = 3.5\times10^{12}$ cm^{-2} and varying transverse E-field values for bilayer WSe_2 LD123 show an E-field-independent odd QHS sequence. (b) R_{xx} vs ν for the same bilayer LD123 at $p = 2.4\times10^{12}$ cm^{-2} show an even QHS sequence which also does not change with E-field. The traces are offset for clarity in panels (a) and (b).

The QHS sequence does not change over the range of electric field values from 0.64 – 1.15 V/nm at $p = 3.5\times10^{12}$ cm^{-2} and 0.86 – 1.25 V/nm at $p = 2.4\times10^{12}$ cm^{-2}. By comparison, the electric field changes from 0.92 – 1.11 V/nm in Fig. 4.5(a), concomitantly with the density change from 6.1×10^{12} cm^{-2} to 3.9×10^{12} cm^{-2}, a range in which the QHS sequence changes from even to odd. Measurable Rashba splitting was observed in bulk

WSe_2 only at densities $\sim 10^{14}$ cm^{-2}, and likely does not play a role in the range of densities probed here [153]. Based on these observations, the effect of the electric field on g^*, and in turn, on the QHS sequence can be ruled out.

4.6 Zeeman Splitting in Monolayer and Bilayer WSe_2

The QHS sequence transitions are therefore attributed to a change in the Zeeman-to-cyclotron energy ratio only as a function of density. Figure 4.10(a) and 4.10(b) show a summary of the QHS sequence as a function of density for four different monolayer and four different bilayer WSe_2 samples, respectively. The data points are grouped into an even or odd QHS sequence over a range of density values, suggesting a systematic density-dependence of the Zeeman energy.

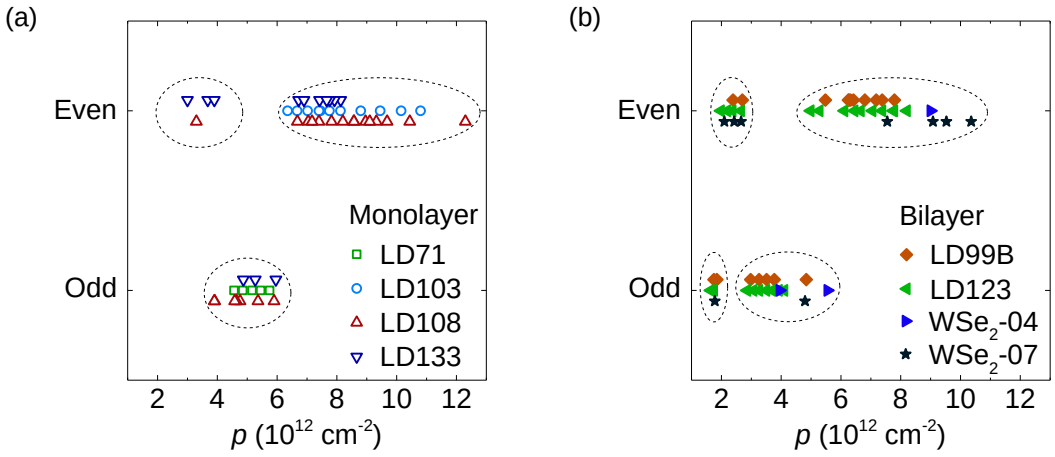

Figure 4.10: (a) Summary of the QHS sequence vs p for four different monolayer WSe_2 samples. (b) QHS sequence vs p for four different bilayer WSe_2 samples. The dotted lines group the data points belonging to the same QHS sequence in a given density range. Symbols within a group are vertically offset for clarity in panels (a) and (b).

The data of Fig. 4.10 can be analyzed within the framework of Fig. 4.6, i.e., $E_Z \approx E_c$ yields an even QHS sequence, and $E_Z \approx 2E_c$ yields an odd QHS sequence. Generalized further, $|E_Z|/E_c \in [2k - 1/2, 2k + 1/2]$ yields an odd QHS sequence, and $|E_Z|/E_c \in [2k + 1/2, 2k + 3/2]$ yields an even QHS sequence; k is an integer. Each of the groups of Fig. 4.10 can therefore be assigned an $|E_Z|$ within a $[-E_c/2, E_c/2]$ window. Starting with $|E_Z| = E_Z^0$ at the highest value of density probed, and assuming the Zeeman splitting increases with reducing density because of interactions, $|E_Z|$ is increased by E_c at every

QHS sequence transition as the density is decreased. Figure 4.11 shows the data of Fig. 4.10 converted into an $|E_Z|$ vs p variation in this manner.

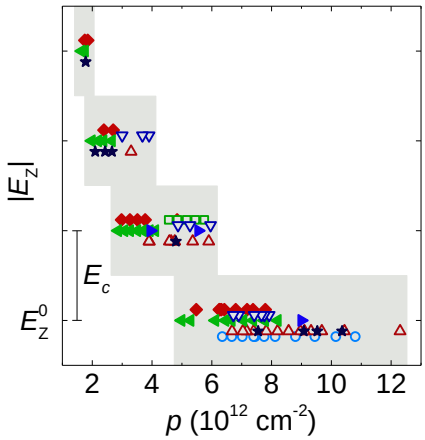

Figure 4.11: Data from Fig. 4.10 converted to an $|E_Z|$ vs p variation assuming an $|E_Z|$ increment of E_c for every QHS sequence transition in the direction of decreasing density, starting at $|E_Z| = E_Z^0$ at the highest density probed. The shaded regions correspond to a $\pm E_c/2$ error bar. Symbols within a group are vertically offset for clarity.

4.6.1 Interaction-Enhancement of the g-factor

In the absence of electron-electron interactions, the g-factor for electrons or holes in a material is determined by its bandstructure, and referred to as the band g-factor (g_b). The band g-factor is usually different from the bare electron g-factor (≈ 2). For instance, $g_b = -0.44$ for GaAs and $g_b = 1.52$ for AlAs electrons [157]. Exchange interactions can enhance g_b to a value g^*, which increases with decreasing density, an observation reported for several 2DESs in Si [139, 148], GaAs [140], and AlAs [124].

Interaction-enhancement of g^* with reducing density can be understood as follows. As the density of a 2DES is lowered, the Coulomb energy of the system starts to dominates over its kinetic (Fermi) energy. Below a critical density, the many-body exchange and correlation energies are expected to drive the system towards a ferromagnetic ground state, as shown in Fig. 1.2 [17]. Above this critical density, the electron/hole-spins tend to align more easily so that they would spatially stay farther apart from each other, thereby minimizing the 2DES Coulomb energy. This manifests as an enhancement of the 2DES spin susceptibility, χ, given by [140]

$$\chi = \frac{p_\uparrow - p_\downarrow}{B} = \frac{g^* \mu_B \mathrm{D}(E)}{2} \tag{4.6}$$

where $p_\uparrow$ and $p_\downarrow$ are the densities of the spin-↑ and spin-↓ holes (or electrons), respectively, and $\mathrm{D}(E) = m^*/\pi\hbar^2$ is the 2D density of states. Therefore, Eq. 4.6 can be written as

$$\chi = \frac{g^* m^* \mu_\mathrm{B}}{2\pi\hbar^2} \tag{4.7}$$

The interaction enhancement of the spin susceptibility is usually specified by the ratio χ/χ_0, where χ_0 is the Pauli susceptibility in the absence of interactions determined by the band g-factor and band effective mass (m_b), so that

$$\frac{\chi}{\chi_0} = \frac{g^* m^*}{g_b m_b} \tag{4.8}$$

In the case of monolayer and bilayer WSe_2 where the effective mass shows very little dependence on the density [Sec. 3.6], i.e., $m^* = m_b$, Eq. 4.8 becomes $\chi/\chi_0 = g^*/g_b$. Therefore, interactions cause an enhancement of g^* over g_b with reducing density.

The interaction strength is gauged by the dimensionless interaction parameter (r_s) which is the interelectron spacing measured in units of the effective Bohr radius (a^*_B), or equivalently, the ratio of the Coulomb energy to the kinetic energy [Eq. 1.6], given by

$$r_s = \frac{1}{a^*_\mathrm{B}\sqrt{\pi p}} \tag{4.9}$$

where $a^*_\mathrm{B} = a_\mathrm{B}(\kappa m_e/m^*)$, $a_\mathrm{B} = 4\pi\epsilon_0\hbar^2/m_e e^2$ is the Bohr radius, m_e is the free electron mass, and κ is the effective dielectric constant of the medium surrounding the 2DES.

Theoretically, the spin susceptibility of an interacting 2DES can be calculated by adding the many-body exchange and correlation energies to the single particle energy and studying the spin-polarization in the 2DES induced by a weak applied in-plane magnetic field [158]. Of the several approaches to include the many-body effects, the quantum Monte Carlo (QMC) technique of Attaccalite *et al.* [21] reproduces the spin susceptibility enhancement in 2DESs reasonably well [124, 140, 159].

Figure 4.12 shows χ/χ_0 vs r_s calculated using the QMC formulation of Ref. [21]. In the limit of $r_s \to 0$, i.e., in the high density limit where interaction effects are negligible, $\chi/\chi_0 \to 1$. With decreasing density, i.e., increasing r_s, the 2DES spin susceptibility is enhanced over its Pauli susceptibility value. The QMC calculation predicts the transition to the ferromagnetic ground state at $r_s \simeq 26$ [21].

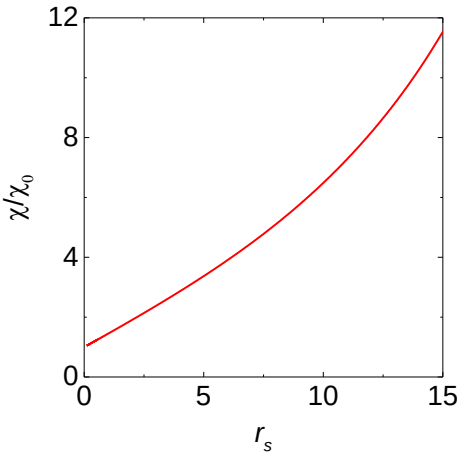

Figure 4.12: χ/χ_0 vs r_s for a 2DES calculated using the quantum Monte Carlo formulation of Ref. [21] shows an enhancement of the spin susceptibility with increasing r_s, i.e., reducing density.

4.6.2 Density-Dependent g-factor in Monolayer and Bilayer WSe_2

The $|E_Z|$ vs p data of Fig. 4.11 can therefore be converted to $|g^*|$ vs r_s in order to assess the effect of interactions in monolayer and bilayer WSe_2. The value of $E_Z^0 = g_0^* \mu_B B$ is addressed first; g_0^* is the effective g-factor at the highest density probed. The observation of an even QHS sequence at the highest density probed implies that $E_Z^0 = (2k+1)E_c$, or equivalently, $g_0^* = 4.44(2k+1)$, using $m^* = 0.45m_e$; k is an integer. Recent magneto-reflectance measurements that resolve the Landau level spectrum report a $g_b = 8.5$ for monolayer WSe_2 holes [160]. To account for the uncertainty in E_Z^0, two scenarios of g_0^* corresponding to $k = 1$ ($E_Z^0 = 3E_c$), and $k = 2$ ($E_Z^0 = 5E_c$) are considered. The $k = 0$ case is ruled out based on the reported g_b value [160]. The E_c-step increments of $|E_Z|$ between groups are equivalent to a $|g^*|$ increment of $\Delta g^* = 2m_e/m^* = 4.44$. Within this framework, Figs. 4.13(a) and 4.13(b) show $|g^*|$ vs r_s for monolayer and bilayer WSe_2, respectively. Because of the difference in dielectric environment, slightly different κ values were used to convert p into r_s for monolayer and bilayer WSe_2.[5]

For comparison, Fig. 4.13 shows the g_b value of Ref. [160] multiplied by the QMC spin susceptibility enhancement [21] which matches well with $|g^*|$ determined using $E_Z^0 = 5E_c$ for both monolayer and bilayer WSe_2. More recent Landau level spectroscopy

[5]For a 2DES with an asymmetric dielectric environment, $\kappa(t,b) = [(\kappa_t^{||}\kappa_t^{\perp})^{1/2} + (\kappa_b^{||}\kappa_b^{\perp})^{1/2}]/2$; $\kappa_{t(b)}^{||/\perp}$ are the top (bottom) medium effective dielectric constants. For monolayer WSe_2, $\kappa = \kappa(h\text{-BN}, h\text{-BN})$. For bilayer WSe_2, $\kappa = [\kappa(h\text{-BN}, h\text{-BN}) + \kappa(h\text{-BN}, WSe_2)]/2$. The values of $\kappa_{h\text{-BN}}^{||} = 3.0$ [Appendix C], $\kappa_{h\text{-BN}}^{\perp} = 6.9$ [38], $\kappa_{WSe_2}^{||} = 7.2$ [60], and $\kappa_{WSe_2}^{\perp} = 14$ [161].

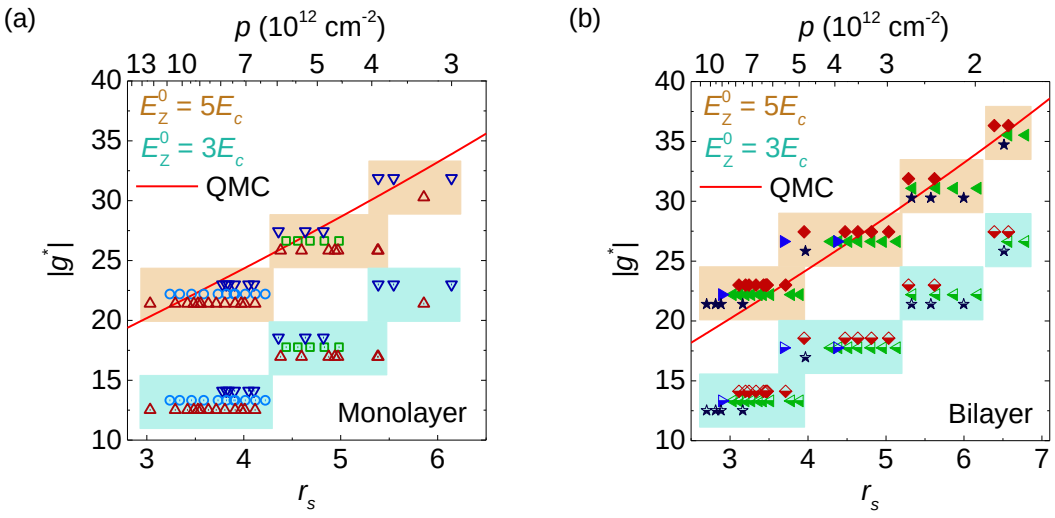

Figure 4.13: (a) Monolayer and (b) Bilayer WSe_2 $|g^*|$ vs r_s (bottom axis) or p (top axis) for $E_Z^0 = 5E_c$ (open, solid symbols), $E_Z^0 = 3E_c$ (dotted, half-filled symbols), and the QMC calculation for $g_b = 8.5$ (line). The symbols within a group are vertically offset for clarity. The shaded regions correspond to a $\pm\Delta g^*/2$ error bar in panels (a) and (b).

measurements of monolayer WSe_2 show a similar enhancement of the valence band Zeeman energy with reducing density [121].

In light of the unique Landau level spectrum of monolayer WSe_2, one question to ask is if the QMC calculation, which was developed for a one-valley system with two-fold degenerate Landau levels, is applicable to the WSe_2 system with two valleys and an unpaired zeroth Landau level. For instance, while multivalley 2DESs based on AlAs [162, 163] and Si [139, 148] have shown spin susceptibility enhancements, there are differences with the one-valley picture [159, 164]. Furthermore, there also exist studies of the Landau level spectrum of monolayer TMDs treated in an alternate framework, where all the Landau levels are two-fold degenerate [142, 165, 166]. It is therefore instructive to re-analyze the data of Fig. 4.13 in this framework.

The valley Zeeman contribution in the Landau level spectrum of Eq. 4.5 can be written as

$$E_{Z,v} = \frac{\tau}{2} g_v \mu_B B = \frac{\tau}{2} g_d \mu_B B + \frac{\tau}{2} \hbar\omega_c \tag{4.10}$$

where the Berry phase contribution, $(\tau/2)\hbar\omega_c$, can be combined with the cyclotron Landau level energies, $-n_{LL}\hbar\omega_c$, to obtain

$$E^{\tau s}_{n_{LL},V} = \Delta_V - \left(n_{LL} - \frac{\tau}{2}\right)\hbar\omega_c + \frac{s}{2} g_s \mu_B B + \frac{\tau}{2} g_d \mu_B B \tag{4.11}$$

Now, in the absence of the Zeeman terms in Eq. 4.11, i.e., $g_s = g_d = 0$, the Landau levels transform to two-fold degenerate for all values of $n_{\mathrm{LL}} = 0, 1, 2, \ldots$ as shown in Fig. 4.14. In essence, the difference between Eq. 4.5 [Fig. 4.14(a)] and Eq. 4.11[Fig. 4.14(b)] is the inclusion or exclusion of the valley dependent Berry phase contribution in the definition of the Zeeman energy [142].

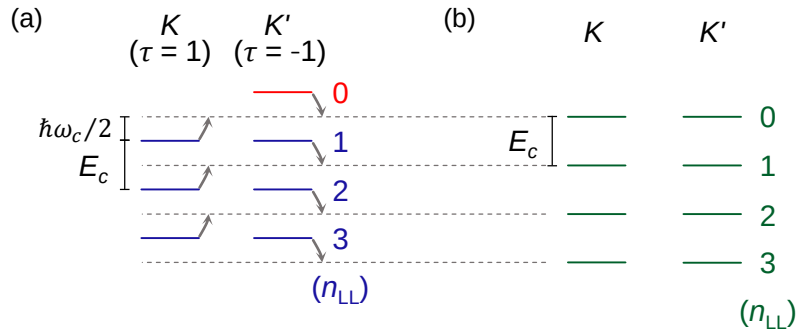

Figure 4.14: (a) Landau level spectrum given by Eq. 4.5 with a non-degenerate $n_{\mathrm{LL}} = 0$ Landau level in the absence of Zeeman splitting. (b) Landau level spectrum given by Eq. 4.11, where all the Landau levels are two-fold spin-valley degenerate in the absence of Zeeman splitting. The Landau levels of (a) shifted by $(\tau/2)\hbar\omega_c$ [indicated by gray arrows] yield the Landau levels of (b).

In the picture with all the Landau levels two-fold degenerate, the QHS sequence in the absence of Zeeman splitting would be even, and a Zeeman-to-cyclotron energy ratio of an even or odd integer would yield an even or odd QHS sequence, respectively. Applied to the $|E_{\mathrm{Z}}|$ vs p data of Fig. 4.11, it merely offsets the value of E_{Z}^0 by E_c, or equivalently, offsets the effective g-factor by $2m_e/m^* = 4.44$. Figure 4.15(a) and 4.15(b) show $|g^*|$ vs r_s for monolayer and bilayer WSe_2, respectively, in this picture.

The g^* vs r_s data of Fig. 4.15 fit well to the QMC spin susceptibility calculation assuming a band g-factor of $g_b = 6.8$. It it to be noted that the choice of the non-degenerate or two-fold degenerate zeroth Landau level picture is purely a notational convention and would yield different values of the g-factors accordingly. Whether the Zeeman energy with or without inclusion of the Berry phase component is interaction-enhanced remains an open question. Given the hole-spins are locked along the z-direction, and do not respond to an in-plane magnetic field in WSe_2, there is no way to decouple the Zeeman and cyclotron contributions in order to resolve this ambivalence.

Furthermore, the band g-factor value for holes in WSe_2 remains to be established. Table 4.1 lists the reported g-factor values for WSe_2 holes from literature. While there seems to be reasonable consensus between the data presented here and the experimentally

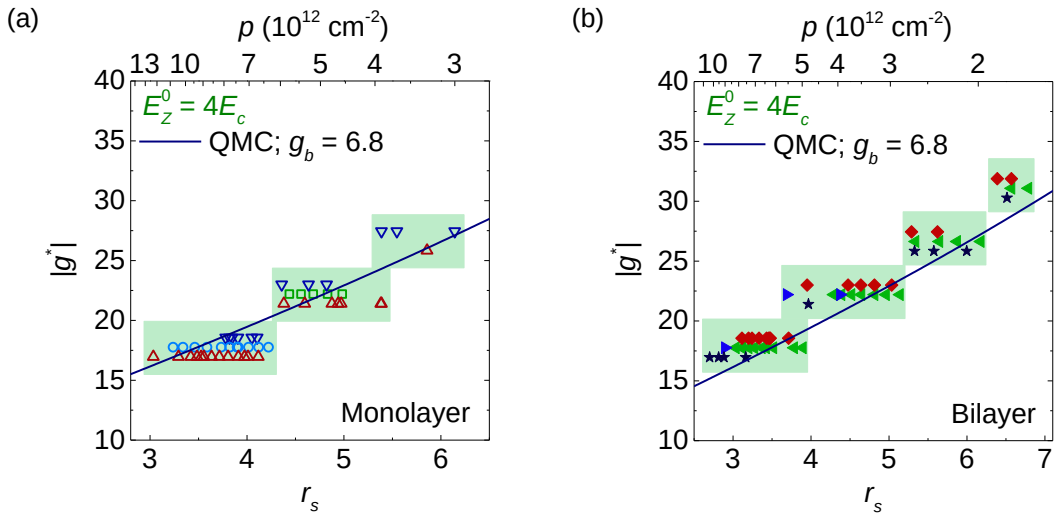

Figure 4.15: (a) Monolayer and (b) Bilayer WSe_2 $|g^*|$ vs r_s (bottom axis) or p (top axis) for the model with all Landau levels being two-fold degenerate and $E_Z^0 = 4E_c$ fit well with the QMC calculation assuming $g_b = 6.8$ (line). The symbols within a group are vertically offset for clarity. The shaded regions correspond to a $\pm\Delta g^*/2$ error bar in panels (a) and (b).

determined g-factor values from Ref. [121], estimates from calculations vary between reports.

Table 4.1: Survey of hole effective g-factor values in monolayer WSe_2 from literature.

Ref.	Experiment/ Calculation	Technique	g-factor	Comment
[160]	Experiment	Magneto-optical	8.5	Band g-factor
[121]	Experiment	LL spectroscopy	$20-24$	Over a density range of $p = 5 - 2.5 \times 10^{12}$ cm^{-2}; two-fold $n = 0$ LL
[165]	Calculation	DFT GW[a]	-2.38 0.55	Two-fold $n = 0$ LL
[166]	Calculation	DFT DFT+GW	5.64 4.08	Two-fold $n = 0$ LL

[a]The GW approximation is one of many techniques to account for many-body correlation effects in the DFT calculation of the bandstructure.

It is noteworthy that the relatively large $m^* = 0.45m_0$ for holes in WSe_2 leads to

moderately large r_s values, and potentially strong interaction effects even at high carrier densities. An order of magnitude improvement in mobility by comparison to the present values would allow access to r_s values in the $20 - 30$ range, which make WSe_2 a promising platform for exploring correlated phenomena [17, 21].

4.7 Summary

In summary, the quantum Hall states sequence of holes in monolayer and bilayer WSe_2 undergo transitions between predominantly odd and even filling factors as the hole density is varied. These transitions stem from an interplay between the cyclotron energy and a density-dependent Zeeman splitting, which is a direct manifestation of the strong electron-electron interactions in WSe_2. The extracted density-dependent, interaction-enhanced, effective g-factor closely matches the expected trend based on quantum Monte Carlo calculations, corroborating the role of interactions in WSe_2.

Also interestingly, the quantum Hall states are insensitive to an in-plane magnetic field, indicating that the hole-spin is locked perpendicular to the WSe_2 plane in both monolayer and bilayer WSe_2, confirming that the holes reside in the K and K' valleys.

Chapter 5

Tunable $\Gamma - K$ Valley Populations in Trilayer WSe_2

Monolayer $2H$-TMDs possess band extrema at the time-reversed partner K and K' Brillouin zone corners with a finite energy gap between dipole coupled conduction and valence bands [33]. Beyond the monolayer limit, the TMD bandstructure becomes more complicated, for instance, evinced by their complex layer number dependent photoluminescence (PL) spectra [168, 169, Fig. 1.6(b)]. The low quantum yield and convoluted exciton features make it difficult to draw conclusions from optical measurements of few-layer TMDs in contrast to monolayers, which show a more straightforward optical response. While angle-resolved photoemission spectroscopy (ARPES) measurements provide a direct probe of the bandstructure, there are limitations on the spatial and energy resolutions [170, 171]. In essence, the locations of the band extrema in few layer TMDs, and their dependence on externally controllable parameters like transverse electric fields (E), have remained open questions for the vast majority of TMDs.

A transverse electric field has been shown to alter the bandstructure in several 2DESs. Notable examples include the Rashba effect in structural inversion asymmetric 2DESs, which yields an E-field-dependent spin-splitting [154, 155], and an E-field-tunable bandgap in bilayer graphene as a result of electric field induced inversion symmetry breaking [172, 173]. More recently, electric field tunable bandstructures have been theoretically investigated in TMDs [174] and have also been reported in WSe_2 [153] and MoS_2 [175, 176].

This chapter addresses the valence band maxima in trilayer WSe_2 and their response to an applied transverse electric field. Magnetotransport measurements reveal holes populating two subbands with different effective masses, $0.5m_e$ and $1.2m_e$, associated with the K and Γ valleys, respectively; m_e is the free electron mass. At a fixed total hole density, the K and Γ occupations can be tuned by an applied electric field, with Γ being the lowest energy state at low electric field and K being the lowest energy state at high electric field. *Ab initio*

Portions of this chapter have been published as Ref. [167]: H. C. P. Movva, T. Lovorn, B. Fallahazad, S. Larentis, K. Kim, T. Taniguchi, K. Watanabe, S. K. Banerjee, A. H. MacDonald, and E. Tutuc, "Tunable $\Gamma - K$ Valley Populations in Hole-Doped Trilayer WSe_2," *Phys. Rev. Lett.*, vol. 120, no. 10, p. 107703, 2018. The dissertator, H. C. P. Movva, fabricated and characterized the WSe_2 samples, and contributed to data analysis and writing the paper.

calculations support these findings and explain the shift of the valence band maxima, and the consequent transfer of holes from Γ to K with increasing electric field.

5.1 Locations of Valence Band Maxima in WSe_2

Theoretical calculations predict [35, 177, 178, 179, 180] and experimental results unambiguously confirm [129, 147, 170, 171] that the valence band maxima of monolayer and bulk WSe_2 are located at the K and Γ points of the Brillouin zone, respectively. Magnetotransport studies on monolayer [Chapter 4] and bulk [147] WSe_2 corroborate this fact as evidenced by measurements in tilted magnetic fields, which reveal the spin is locked perpendicular to the WSe_2 plane for K valley holes, while Γ valley holes couple to an in-plane magnetic field. There is however, large variation in literature reports on the valence band maxima locations in few-layer WSe_2, and the number-of-layers where the valence band maximum shifts from K to Γ. Figure 5.1 shows the variation of the energy gap between the valence band K and Γ valleys ($E_K - E_\Gamma$) as a function of WSe_2 number-of-layers compiled from literature, where the transition from K to Γ is reported to occur at either bilayer or trilayer WSe_2.

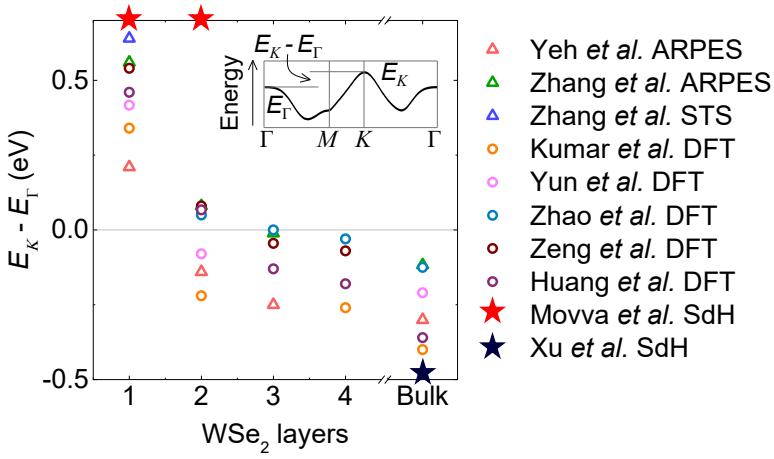

Figure 5.1: Summary of the reported valence band maxima $E_K - E_\Gamma$ values vs WSe_2 number-of-layers from literature. The inset shows a schematic of the upper valence band in monolayer WSe_2. The measured values are from Yeh *et al.* [170], Zhang *et al.* [171] using ARPES, and Zhang *et al.* [64] using scanning tunneling spectroscopy (STS). The calculated values are from Kumar *et al.* [177], Yun *et al.* [178], Zhao *et al.* [35], Zeng *et al.* [179], and Huang *et al.* [180] using DFT. The stars only indicate K valley holes probed by Movva *et al.* [129] in monolayer and bilayer WSe_2, and Γ valley holes probed by Xu *et al.* [147] in bulk WSe_2 by SdH oscillations measurements and do not correspond to specific $E_K - E_\Gamma$ values. Bulk WSe_2 is more than five-layers thick.

Tilted magnetic field measurements from Chapter 4 indicate that holes in bilayer WSe_2 reside in the K valleys. It is therefore worthwhile to study trilayer WSe_2 to examine its valence band maxima locations. The precise k-space locations of the band extrema have a strong bearing on the electron physics. For instance, when carriers reside in the K and K' valleys, their opposite Berry curvatures allow manipulation of the valley pseudospin degree of freedom [33, 181, 182], an effect which is expected to be absent for carriers in the Γ valley. The following sections discuss magnetotransport measurements in trilayer WSe_2 aimed towards uncovering its valence bandstructure.

5.2 Magnetotransport in Trilayer WSe_2

The h-BN encapsulated trilayer WSe_2 Hall bar samples used in this study were fabricated similar to the samples of Chapter 3, using Pt bottom-contacts and either Si/SiO_2, Pt metal, or graphite back-gates. The trilayer WSe_2 flakes were exfoliated from bulk $2H$-WSe_2 crystals and unambiguously identified thanks to their unique PL spectra [Fig. 1.6(b)] and distinct optical contrast. The detailed fabrication process flow and techniques are described in Appendix B. Figure 5.2(a) shows the room temperature PL spectrum of trilayer $2H$-WSe_2 which shows distinct peaks at 1.45 eV corresponding to the indirect gap transition, and 1.60 eV corresponding to the direct gap transition [169].

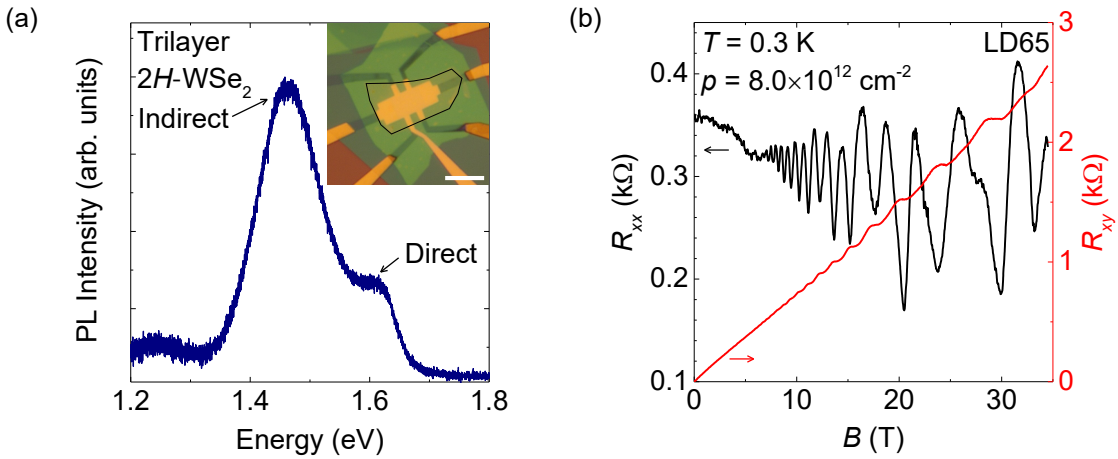

Figure 5.2: (a) Room temperature PL spectrum of trilayer $2H$-WSe_2 obtained using 532 nm wavelength excitation. The peaks corresponding to the direct and indirect gap transitions are labeled. Inset: Optical micrograph of an h-BN encapsulated, dual-gated trilayer WSe_2 Hall bar sample LD65. The black line marks the contour of the WSe_2 flake. The scale bar is 10 μm. (b) R_{xx} and R_{xy} vs B for trilayer WSe_2 LD65 measured at $T = 0.3$ K and at $p = 8.0 \times 10^{12}$ cm^{-2}.

The inset of Fig. 5.2(a) shows the optical micrograph of LD65, a typical h-BN encapsulated, dual-gated trilayer WSe_2 Hall bar sample with an Si/SiO_2 back-gate. The samples were probed in perpendicular magnetic fields in both the 14 T superconducting and 35 T resistive magnets, and down to $T = 0.3$ K in a pumped ^{3}He insert, or $T = 1.5$ K in a variable temperature insert. Magnetotransport measurements were conducted using standard small-signal excitation current, $I = 10$ nA, low-frequency ($9 - 13$ Hz) lock-in techniques. Four trilayer WSe_2 samples, LD65, LD187, LD189, and LD205 were investigated in this study, all with consistent results. The samples' details are provided in Appendix A. The data presented in Secs. 5.2–5.5 are from LD65 and LD189.

Figure 5.2(b) shows R_{xx} and R_{xy} vs B for trilayer WSe_2 LD65 at $V_{TG} = -8.5$ V and $V_{BG} = 0$ V. The hole Hall density is $p = 8.0 \times 10^{12}$ cm^{-2}. The R_{xx} data show well-defined SdH oscillations accompanied by emergence of QHS plateaux in R_{xy} coincident with the R_{xx} minima at high B-fields. Unlike holes in monolayer and bilayer WSe_2 at $V_{BG} = 0$ V which show one fundamental SdH oscillation frequency, i.e., one populated subband [Secs. 3.3–3.4], the trilayer data of Fig. 5.2(b) show a beating pattern, suggestive of hole population in multiple subbands.

5.3 Gate-Dependence of SdH Oscillations

To investigate the origin of the SdH oscillations' beating pattern, magnetotransport measurements were performed as a function of V_{TG} and V_{BG}. Figure 5.3(a) shows R_{xx} vs B measured in a second trilayer WSe_2 sample, LD189, at different V_{TG} values, $V_{BG} = 0$ V, and $T = 1.5$ K. Figure 5.3(b) shows the FT amplitude vs frequency corresponding to the R_{xx} vs $1/B$ data of Fig. 5.3(a).

The FT spectra show two principal peaks which vary markedly in their response to V_{TG}. While the low-frequency peak increases in frequency with $|V_{TG}|$, the high-frequency peak position is nearly independent of V_{TG}. The existence of two principal FT peaks is indicative of holes at the Fermi level in two distinct subbands. Further, the dependence of the two peaks on V_{TG} suggests that the two subbands have very different spatial confinement, with the lower frequency peak localized in closer proximity to the top-gate.

Figure 5.4(a) shows a similar set of R_{xx} vs B data in the same sample, LD189, measured at different V_{BG} values, $V_{TG} = -12$ V, and $T = 1.5$ K, and Fig. 5.4(b) the FT amplitude vs frequency of the corresponding R_{xx} vs $1/B$ data.

The FT data consist of one or two characteristic peak(s) depending on the value of V_{BG}. When $V_{BG} \leq 0$ V, the FT data show two peaks similar to Fig. 5.3(b) data. However, the low-frequency peak increases in frequency and the high-frequency peak decreases in

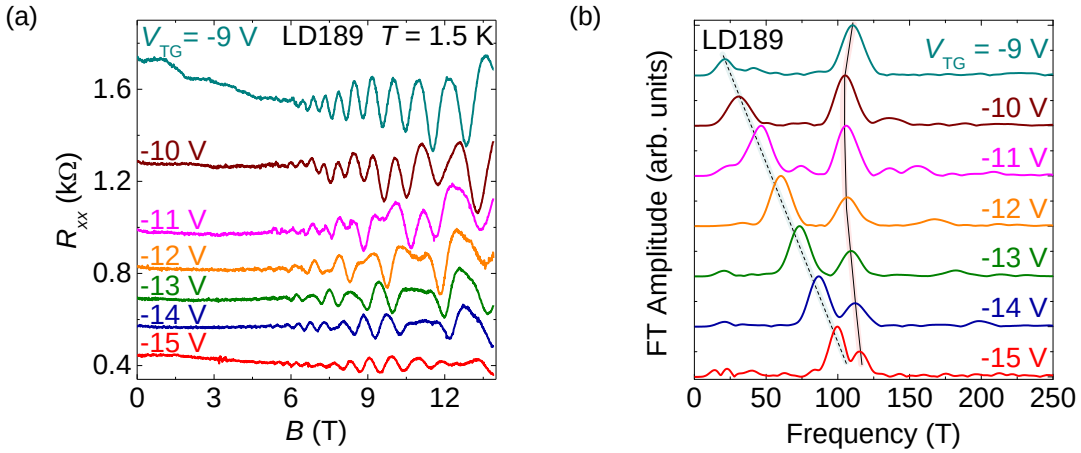

Figure 5.3: (a) R_{xx} vs B at various V_{TG} values, $V_{\mathrm{BG}} = 0$ V, and $T = 1.5$ K for trilayer WSe_2 LD189. (b) FT amplitude vs frequency corresponding to the R_{xx} vs $1/B$ data of panel (a). The solid and dashed lines are a guide to the eye and track the high- and low-frequency peaks, respectively. The traces are offset for clarity in panels (a) and (b).

frequency with increasing V_{BG}. The two peaks merge into one broad peak at $V_{\mathrm{BG}} = 1$ V and cannot be individually resolved. For 1 V $\leq V_{\mathrm{BG}} \leq 4$ V, the resulting sole peak increases in frequency with increasing V_{BG}. When $V_{\mathrm{BG}} \geq 4$ V, this peak reverses its trend and starts decreasing in frequency with increasing V_{BG}. This unusual V_{BG} dependence suggests depopulation of one subband with increasing V_{BG}.

5.4 Effective Masses of Holes in Trilayer WSe_2 Subbands

To further investigate the nature of the two subbands, temperature-dependent measurements were performed to extract the subband effective masses. Figure 5.5(a) shows R_{xx} vs B for LD189 at $V_{\mathrm{TG}} = -12$ V, $V_{\mathrm{BG}} = 0$ V, and at various T values, and Fig. 5.5(b) the corresponding FT data.

The FT amplitudes of the two peaks show a distinct temperature-dependence with the high-frequency peak decaying more rapidly with temperature compared to the low-frequency peak. This observation is indicative of different effective masses for holes in the two subbands. The individual subband effective masses were extracted in a similar way as described in Sec. 3.5. First, the FT peak of interest was isolated by applying a band-pass filter centered at its peak and an inverse Fourier transform performed. A Dingle factor fit was performed to each peak's inverse FT oscillation amplitude, ΔR_{xx} vs T at a fixed B-field, $\Delta R_{xx} \propto \xi/\sinh\xi$, where $\xi = 2\pi^2 k_B T/\hbar\omega_c$ and $\omega_c = eB/m^*$. The inset of Fig. 5.5(b) shows

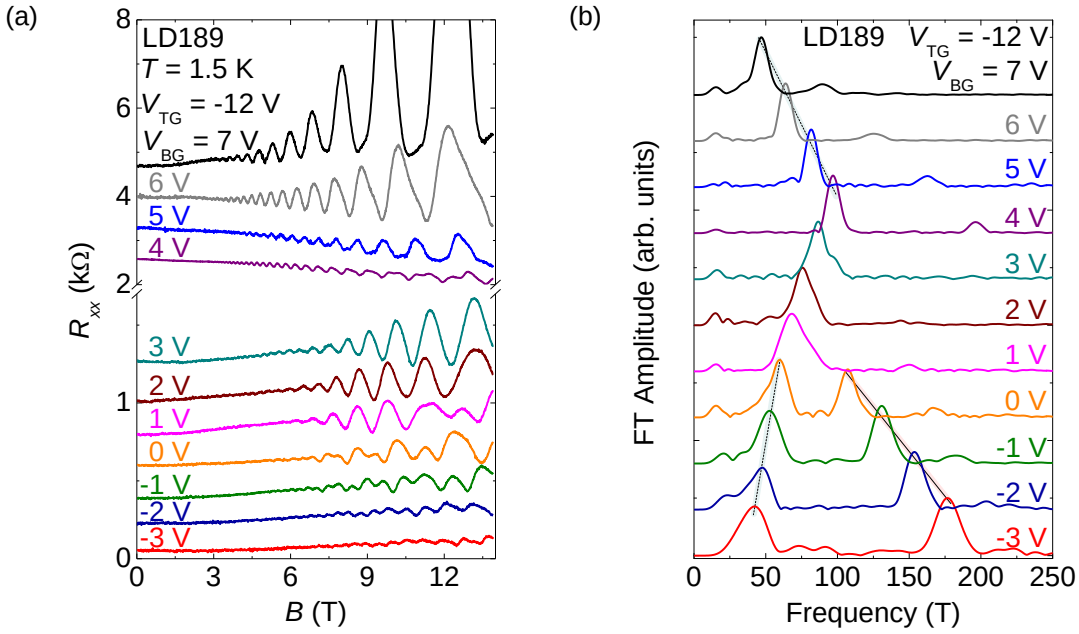

Figure 5.4: (a) R_{xx} vs B at various V_{BG} values, $V_{\mathrm{TG}} = -12$ V, and $T = 1.5$ K for trilayer WSe_2 LD189. (b) FT amplitude vs frequency corresponding to the R_{xx} vs $1/B$ data of panel (a). The solid and dashed lines are a guide to the eye and track the high- and low- (or sole) frequency peaks, respectively, when they can be individually discerned. The traces are offset for clarity in panels (a) and (b).

example Dingle factor fits to the low- and high-frequency peaks' ΔR_{xx} vs T data at a fixed $B = 8.5$ T.

A similar set of measurements were performed at a different density where the FT data show only one principal peak. Figure 5.5(c) shows R_{xx} vs B for LD189 at $V_{\mathrm{TG}} = -12$ V, $V_{\mathrm{BG}} = 6$ V, and at various T values, and Fig. 5.5(d) the corresponding FT data. The effective mass corresponding to the sole FT peak subband is extracted by performing similar Dingle factor fits [Fig. 5.5(d) inset].

Figure 5.6 summarizes the extracted m^* vs B from Fig. 5.5 data. At $V_{\mathrm{TG}} = -12$ V, $V_{\mathrm{BG}} = 0$ V, where $p = 8.0 \times 10^{12}$ cm^{-2}, holes associated with the high-frequency peak have $m^* = 1.2m_e$ and holes associated with the low-frequency peak have $m^* = 0.5m_e$. The lower m^* matches closely with $m^* = 0.45m_e$ measured for K valley holes in monolayer and bilayer WSe_2 [Chapter 3]. The heavy m^* on the other hand is closer to $m^* = 0.89m_e$ measured for Γ valley holes in few-layer WSe_2 [147]. The light holes in trilayer WSe_2 are therefore assigned to the K valley and the heavy holes to the Γ valley. At $V_{\mathrm{TG}} = -12$ V, $V_{\mathrm{BG}} = 6$ V, where $p = 3.0 \times 10^{12}$ cm^{-2}, the holes associated with the sole FT peak have

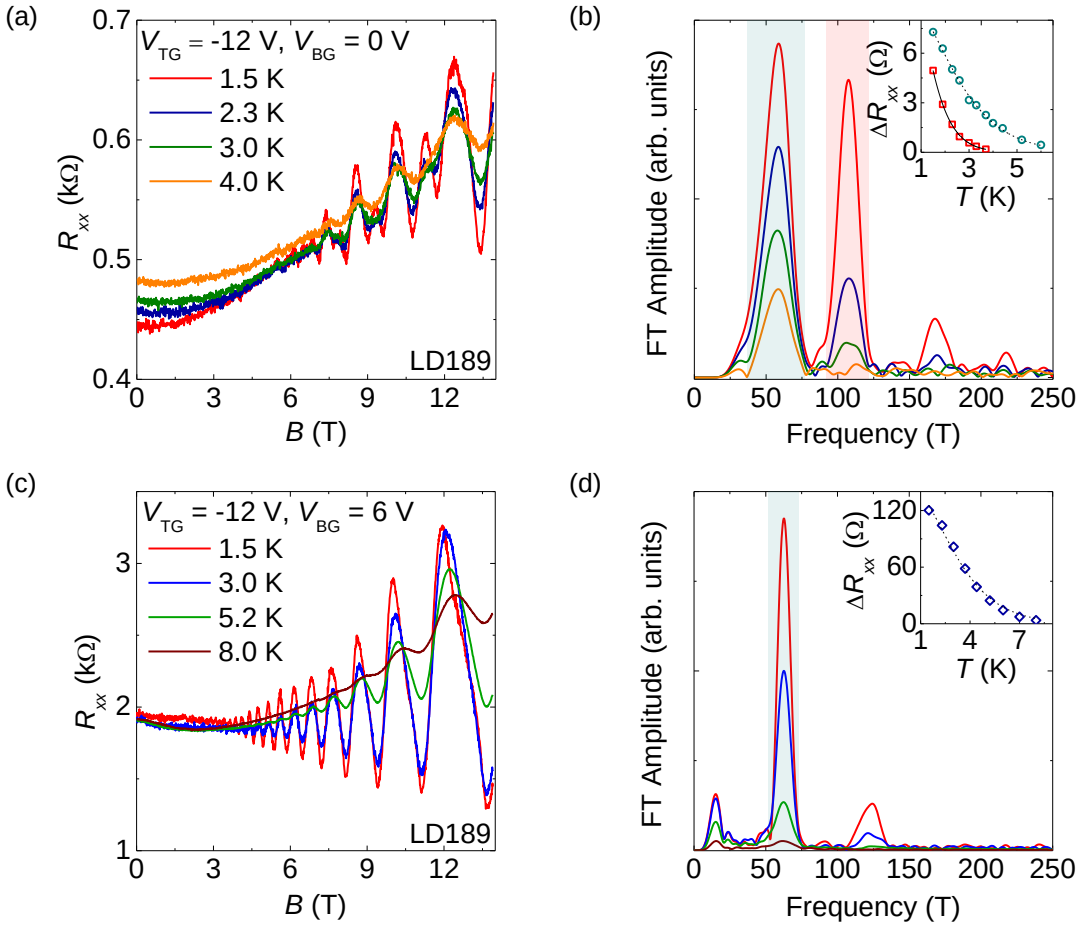

Figure 5.5: (a) R_{xx} vs B at $V_{\rm TG} = -12$ V, $V_{\rm BG} = 0$ V, and at different T values for trilayer LD189. (b) FT amplitude vs frequency of the R_{xx} vs $1/B$ data of panel (a). Inset: ΔR_{xx} vs T at $B = 8.5$ T calculated from the inverse FT of panel (b) data, using band-pass filters (shaded bands). The dashed (solid) line shows the Dingle factor fit to the low- (high-) frequency peak's ΔR_{xx} vs T data. (c) R_{xx} vs B in the same trilayer LD189 at $V_{\rm TG} = -12$ V, $V_{\rm BG} = 6$ V, and at different T values. (d) FT amplitude vs frequency of the R_{xx} vs $1/B$ data of panel (c). Inset: ΔR_{xx} vs T at $B = 8.7$ T calculated from the inverse FT of panel (d) data, using a band-pass filter around the sole peak (shaded band).

$m^* = 0.5m_e$, implying that they all reside in the K valley.

To substantiate this interpretation, the density values determined from Hall measurements can be compared with the density values associated with the FT peaks frequency (f), $p = D_{\rm LL} \times e/h \times f$, where $D_{\rm LL}$ is the Landau level degeneracy of the subband associated with f. Figure 5.7(a) shows p vs $V_{\rm TG}$ and Fig. 5.7(b) shows p vs $V_{\rm BG}$ determined from Hall measurements, along with the individual Γ and K valley densities, and their sum ($\Gamma + K$)

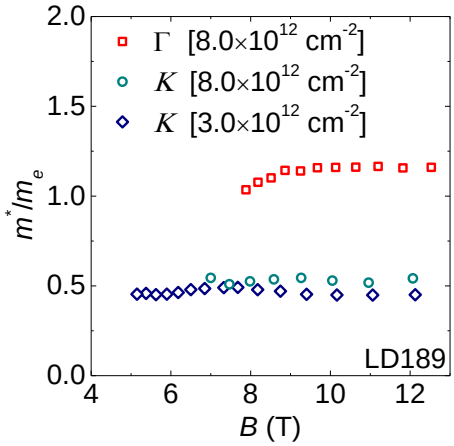

Figure 5.6: m^*/m_e vs B in LD189 for the two subbands at $V_{\mathrm{TG}} = -12$ V, $V_{\mathrm{BG}} = 0$ V, where $p = 8.0 \times 10^{12}$ cm^{-2} and for the sole subband resolved at $V_{\mathrm{TG}} = -12$ V, $V_{\mathrm{BG}} = 6$ V, where $p = 3.0 \times 10^{12}$ cm^{-2}. The light holes with $m^* = 0.5m_e$ belong to the K valley and the heavy holes with $m^* = 1.2m_e$ to the Γ valley.

determined from the two FT peaks of Fig. 5.3(b) and Fig. 5.4(b) data, respectively, using $D_{\mathrm{LL}} = 2$ for both the Γ and K valleys. In the range 1 V $\leq V_{\mathrm{BG}} <$ 4 V in Fig. 5.7(b), the component peak frequencies cannot be individually resolved, and are therefore omitted.

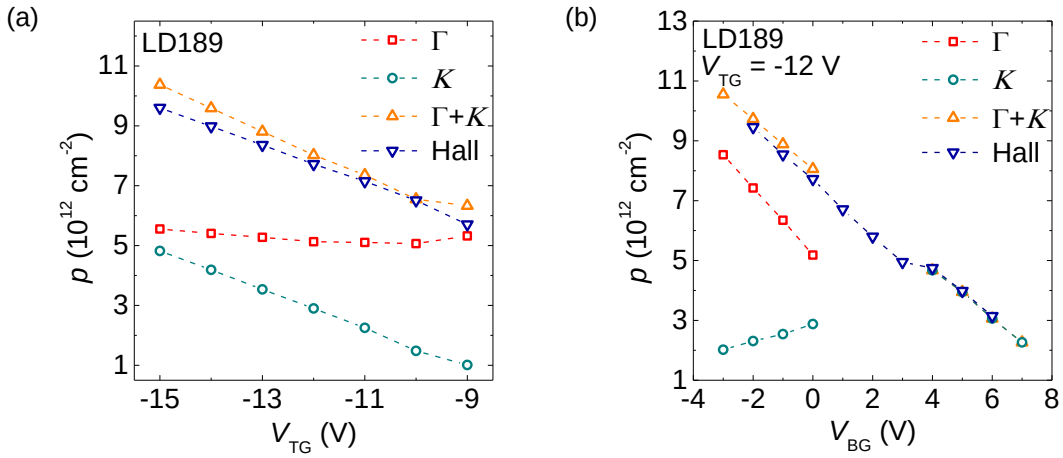

Figure 5.7: (a) p vs V_{TG} associated with the individual FT peaks of Fig. 5.3(b) data (Γ, K), their sum ($\Gamma + K$), and Hall measurements. (b) p vs V_{BG} associated with the individual FT peaks of Fig. 5.4(b) data (Γ, K), their sum ($\Gamma + K$), and Hall measurements. Only data points where the component peak frequencies can be clearly resolved are shown.

The close match between the Hall and $\Gamma + K$ density values validates the valley desig-

nation. The $D_{\mathrm{LL}} = 2$ Landau level degeneracy is consistent with the expected degeneracies for holes in the Γ [147] and K [Chapter 3] valleys of WSe_2.

5.5 Electric Field Dependence of SdH Oscillations

To assess the impact of the transverse electric field on the Γ and K valley densities, magnetotransport measurements were performed as a function of varying transverse electric field, $E = |C_{\mathrm{TG}}V_{\mathrm{TG}} - C_{\mathrm{BG}}V_{\mathrm{BG}}|/2\epsilon_0$ at constant total density; C_{TG} and C_{BG} are the top- and back-gate capacitances, respectively, and ϵ_0 is the vacuum permittivity. Figure 5.8(a) shows R_{xx} vs B in trilayer WSe_2 LD189 at various E values, constant $p = 8.0 \times 10^{12}$ cm^{-2}, and $T = 1.5$ K. The R_{xx} SdH oscillations' beating pattern changes with the E-field, suggesting an electric field dependence of the relative valley occupations.

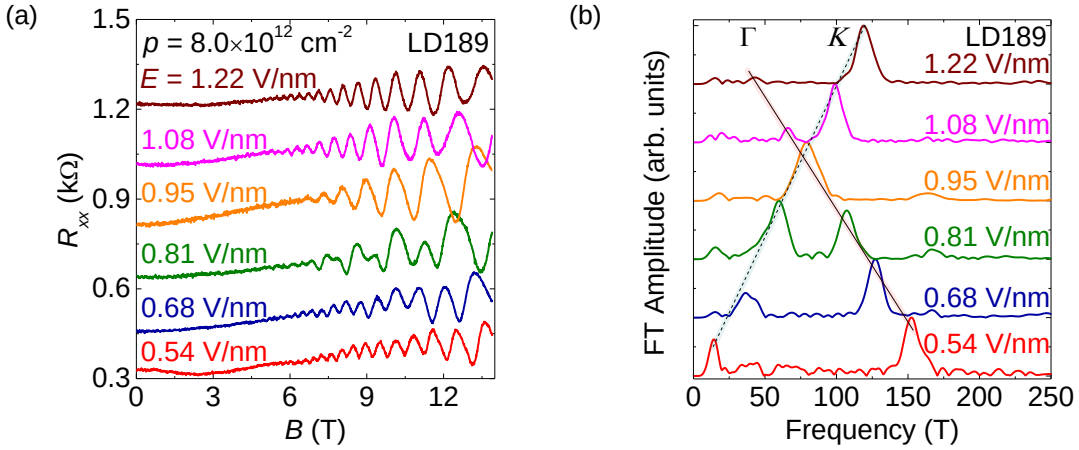

Figure 5.8: (a) R_{xx} vs B at various E values in LD189 at $p = 8.0 \times 10^{12}$ cm^{-2}, and $T = 1.5$ K. (b) FT amplitude vs frequency corresponding to the R_{xx} vs $1/B$ data of panel (a). The Γ and K peak frequencies decrease and increase with increasing electric field, respectively. The traces are shifted for clarity in panels (a) and (b). The solid and dashed lines are a guide to the eye.

Figure 5.8(b) shows the FT amplitude vs frequency associated with the R_{xx} vs $1/B$ data of Fig. 5.8(a). The Γ and K peak frequencies, and their corresponding densities decrease and increase with increasing electric field, respectively. The individual Γ, K valley contributions to the total density, p vs E are summarized in Fig. 5.9(a).

At low-values of the electric field, a majority of the holes reside in the Γ valley and progressively get transferred to the K valley with increasing electric field. The relative occupancies of the Γ and K valleys at fixed total density vary linearly with the electric field over the range probed. A similar set of data at a different fixed total density, $p =$

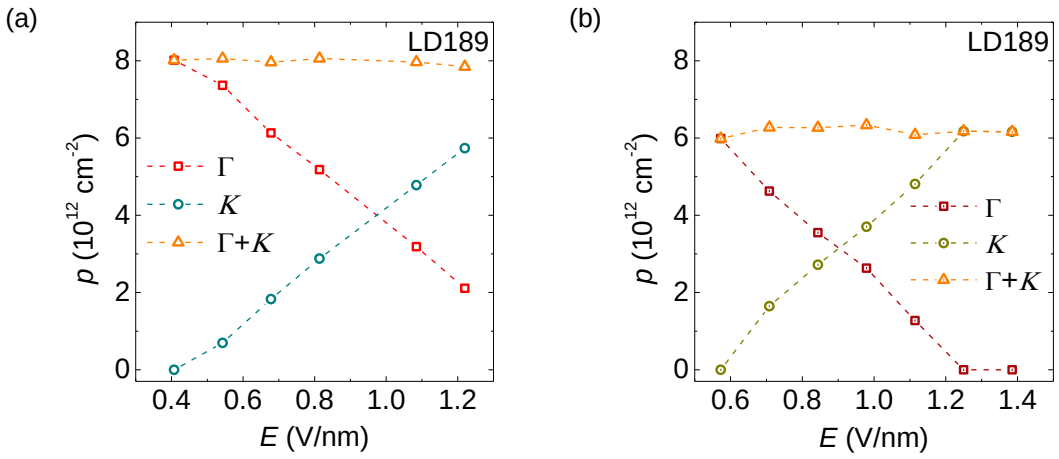

Figure 5.9: (a) p vs E corresponding to Fig. 5.8(b) FT data associated with the Γ and K valleys show a linear decrease (increase) of the Γ (K) valley density with increasing electric field. The sum (Γ + K) is $p = 8.0 \times 10^{12}$ cm^{-2}. The two peaks overlap at $E = 0.95$ V/nm. (b) p vs E for the Γ and K subbands at a different fixed total density of 6.1×10^{12} cm^{-2} show a similar variation of the subband densities with varying E. Beyond $E = 1.25$ V/nm, all the holes reside in the K valley.

6.1×10^{12} cm^{-2} in trilayer WSe_2 LD189 are shown in Fig. 5.9(b). The Γ and K densities vary linearly with the electric field up to $E = 1.25$ V/nm, beyond which all the holes reside in the K valley. These observations demonstrate that the $\Gamma - K$ splitting in the valence band of trilayer WSe_2 is electric field dependent.

5.6 *Ab Initio* Calculations of the Bandstructure

Ab initio calculations were performed to understand the origin of the electric field dependent $\Gamma - K$ splitting in trilayer $2H$-WSe_2. Figure 5.10(a) shows the bandstructure of trilayer WSe_2 computed using fully-relativistic density functional theory calculations under the local-density approximation [183], using the Quantum Espresso distribution [184]. The full dataset of calculations is available in Ref. [185].

In the absence of a transverse electric field, the valence band maximum is at Γ with a $\Gamma - K$ valley-splitting of $\simeq 55$ meV. On application of a transverse electric field, the valence band maximum at the K point responds much more strongly to the E-field than the valence band maximum at Γ. A small electric field is sufficient to induce substantial localization of the three high energy K subbands in the individual WSe_2 layers, leading to a threefold splitting of these states. Figure 5.10(b) shows a close-up of the valence band maxima splitting at K, which increases nearly linearly with E. Tracking the difference between the

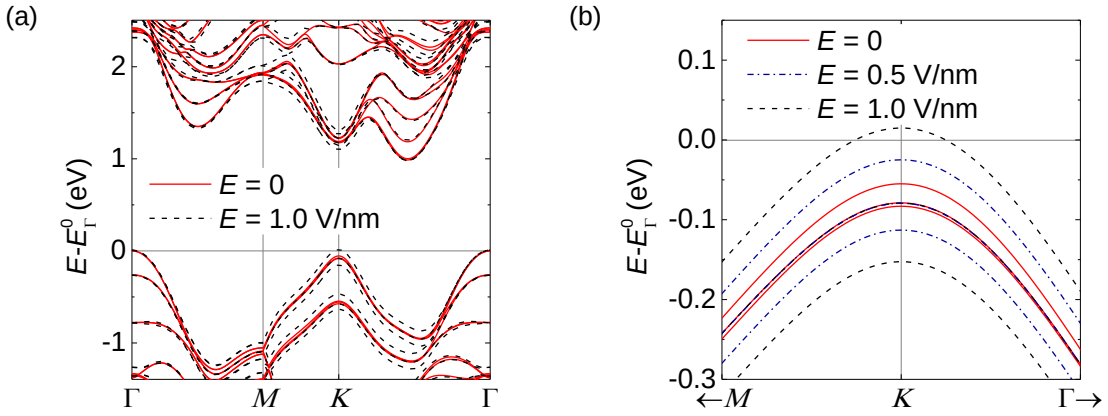

Figure 5.10: (a) Bandstructure of trilayer $2H$-WSe_2 with and without an applied transverse electric field. Energies are given relative to the valence band maximum at Γ at $E = 0$ (E^0_Γ). (b) A zoomed-in view of the valence band maximum at K, showing an approximately linear shift with electric field. Reproduced from Ref. [167].

valence band maxima $E_\Gamma - E_K$, the highest energy valence band is found to shift from Γ to K for $E \gtrapprox 0.9$ V/nm as shown by the red squares in Fig. 5.11(a).

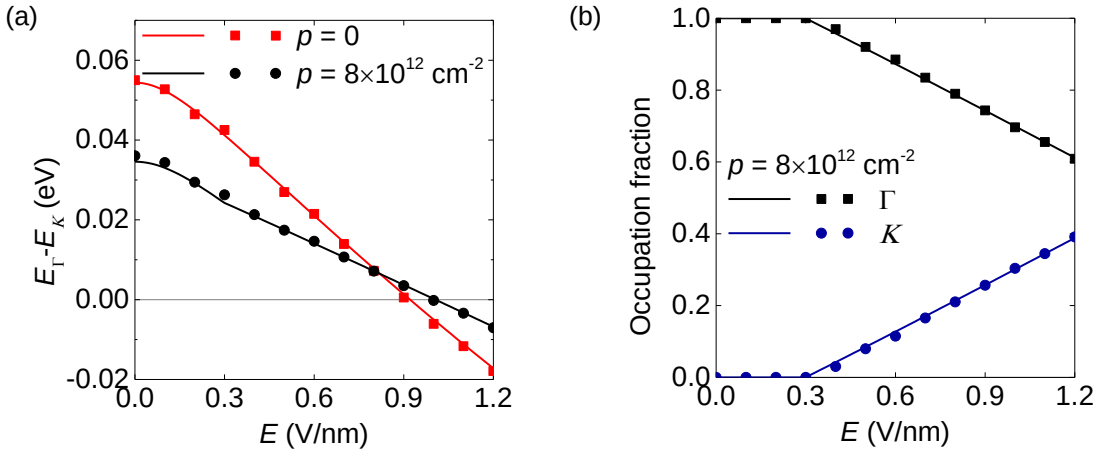

Figure 5.11: (a) E-field-dependence of $E_\Gamma - E_K$, at zero and a finite hole density, $p = 8\times10^{12}\ cm^{-2}$. (b) E-field-dependence of the relative occupation of the Γ and K valleys at fixed $p = 8\times10^{12}$ cm^{-2}. In panels (a) and (b), the symbols (lines) show results where the E-field is included via the DFT calculation ($\mathbf{k}\cdot\mathbf{p}$ model). Reproduced from Ref. [167].

From the DFT calculation at each E value, tightbinding and $\mathbf{k}\cdot\mathbf{p}$ models are constructed for states in the K and Γ valleys, defined on a basis of two states in each WSe_2

layer, capturing the six highest valence bands [186]. From the electric field dependence of the layer "on-site" energies, an effective dielectric constant of $\kappa_r^* = 7.87$ is extracted, comparable to the value of 7.2 observed in multilayer WSe_2 [60]. Using the value of κ_r^*, $\mathbf{k}\cdot\mathbf{p}$ models can be generated for any E from the $\mathbf{k}\cdot\mathbf{p}$ model at $E = 0$ by adding eEd/κ_r^* to the on-site energies for the top layer and $-eEd/\kappa_r^*$ to the on-site energies for the bottom layer; d is the transverse distance between the W atoms of two adjacent WSe_2 layers. The evolution of the difference in valence band maxima $E_\Gamma - E_K$ with E for $\mathbf{k}\cdot\mathbf{p}$ models obtained in this way is shown by the solid red line in Fig. 5.11(a).

The difference in the electric field response of the Γ and K bands is due to the differences in their orbital character. Figure 5.12(a) shows a schematic of the basis states of the layer-resolved $\mathbf{k}\cdot\mathbf{p}$ model at K and Γ.

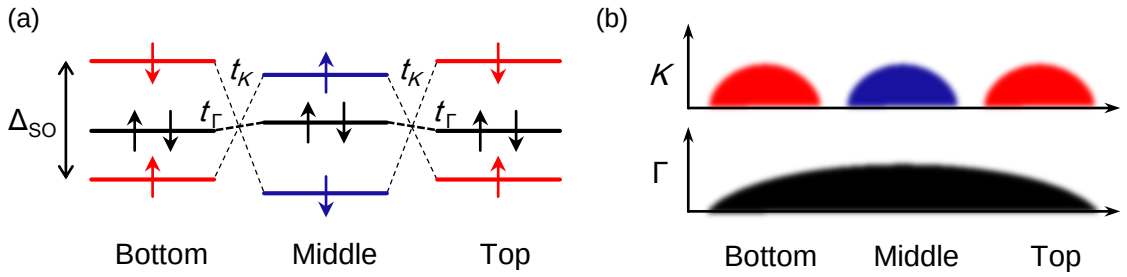

Figure 5.12: (a) Basis states on each layer of the layer-resolved $\mathbf{k}\cdot\mathbf{p}$ model. States at K are split by Δ_{SO}, with $l_z < 0$ states colored red and $l_z > 0$ states colored blue. States at Γ, with $l_z = 0$ are colored black. Reproduced from Ref. [167]. (b) Schematic of the spatial location of the wavefunctions making up the K and Γ bands among the three layers of trilayer WSe_2.

The valence band maximum states at K are made up of basis states having dominant d-orbital amplitudes with $|l_z = -2, \downarrow\rangle$ representations on the top and bottom layers, and a much smaller $|l_z = +2, \downarrow\rangle$ amplitude on the middle layer. Because of the change in sign of l_z, the on-site energy on the middle layer is shifted to lower energy by the spin–orbit interaction (Δ_{SO}). The opposite angular momenta and spin in outside and interior layers suppress the hybridization (t_K) between adjacent layers, leading to strong localization of subband wavefunctions on individual layers for $E \gtrsim 0.1$ V/nm, as shown in Fig. 5.12(b). At Γ, on the other hand, the eigenstate amplitudes include similar $l_z = 0$ representations on all layers, allowing for large effective interlayer coupling (t_Γ) and therefore, delocalization of the wavefunction across the three layers [Fig. 5.12(b)] and explaining a greatly reduced rate of change of the eigenstates and their energies with increasing electric field.

The theoretical Γ and K valley densities can be calculated using an effective mass parametrization of the highest valence bands. Holes are distributed among layers and valleys

accounting for screening self-consistently with a simple electrostatic model, considering a planar charge distribution at each W layer. The variation of $E_\Gamma - E_K$ with E is modified in the presence of holes, as shown by the black circles and line in Fig. 5.11(a) for $p = 8 \times 10^{12}$ cm^{-2}. The distribution of holes among the Γ and K valleys as a function of E is shown in Fig. 5.11(b), displaying a trend which is qualitatively consistent with the measured occupations of Fig. 5.9(a).

Hole effective masses of $m^*_\Gamma = 0.82m_e$ at Γ and $m^*_K = 0.35m_e$ at K are obtained from the effective mass parametrization of the bands. These effective mass values are smaller than the measured masses, but have a similar ratio. Considering the masses difference, the transfer of holes from Γ to K in the model is expected to begin at a smaller electric field and proceed more slowly with increasing E. The hole transfer rate, $dp_K/dE \propto m_K$, where p_K and m_K are the occupation fraction and effective mass of holes, respectively, in the K valley. The calculated hole transfer rate in Fig. 5.11(b) is 0.43 nm/V, a value nearly 50% smaller than the experimental hole transfer rate of 0.89 nm/V in Fig. 5.9(a).

The ~50% reduction of the calculated hole transfer rate by comparison to experiments is larger than the 30% reduction that would be expected due to the smaller calculated effective masses, i.e., $m^*_K/m^*_{K,\mathrm{SdH}} = 0.35m_e/0.5m_e = 0.7$, and the corresponding reduction in density of states; $m^*_{K,\mathrm{SdH}} = 0.5m_e$ is the measured K valley holes' effective mass. The remaining difference may be attributed to interaction effects beyond the Hartree level, and the simplicity of the screening model. In particular, exchange interactions are expected to further increase E_K as these orbitals become occupied, and to enhance the rate of change of $E_\Gamma - E_K$ with electric field.

The V_{TG} dependence of the FT peaks in Fig. 5.3(b) can be qualitatively explained in this framework as follows. At low $|V_{\mathrm{TG}}|$, i.e., low electric field, a majority of the holes reside in the Γ valley, thanks to a large $E_\Gamma - E_K$. Increasing $|V_{\mathrm{TG}}|$ and therefore, E, increases the density and simultaneously decreases $E_\Gamma - E_K$. While the effect of the density increase alone is to also increase the Γ density, the concomitant decrease of $E_\Gamma - E_K$ has a counteracting effect of transferring holes from Γ to K, resulting in a net Γ density that remains unchanged and a K density that increases with $|V_{\mathrm{TG}}|$.

Similarly in Fig. 5.4(b), a majority of the holes reside in the K valley at large V_{BG}, i.e., high electric field. Decreasing V_{BG} and therefore, E, increases both the total density and $E_\Gamma - E_K$, manifesting as a K density decrease as long as the Γ valley is empty, i.e., as long as $E_\Gamma - E_K$ is sufficiently small. Decreasing V_{BG} further causes preferential population of the Γ valley thanks to the supplemental effect of both increasing total density and $E_\Gamma - E_K$, whereas the two negate each other in the K valley, resulting in a net K density decrease.

The transverse electric field can therefore be used as an effective knob to populate holes selectively in the Γ or K valleys at a given total density in trilayer WSe_2. In practice, however, restrictions on V_{TG} in order to achieve reliable electrical contacts place a lower limit on the transverse electric field. The upper limit of the electric field, on the other hand, is a function of the dielectric breakdown strength of h-BN, which, thanks to its high value, permits unfettered access to relatively high electric fields and therefore, low hole densities. The next section focuses on magnetotransport measurements in trilayer WSe_2 at low-densities and high electric fields, where only the K valley is filled with holes.

5.7 Low-Density Magnetotransport Measurements

In light of the large effective g-factor enhancement in monolayer and bilayer WSe_2 with reducing hole density [Chapter 4], it is worthwhile to study magnetotransport in trilayer WSe_2 in the low-density regime. To further reduce impurity scattering and access lower densities, trilayer WSe_2 samples were fabricated with graphite top- and back-gates in place of metal gates [144]. The detailed fabrication process and techniques are described in Appendix B. The data presented in this section are from two trilayer WSe_2 samples with graphite gates, LD187 and LD205. Appendix A provides the samples' details.

Figure. 5.13(a) shows R_{xx} vs B in trilayer WSe_2 LD187 at various density values between $3.8-12.2\times10^{11}$ cm^{-2}, corresponding to E-fields of $1.65-1.50$ V/nm, at $T = 1.5$ K. In this range of E values, all the holes reside in the K valley. The R_{xx} data show well-defined SdH oscillations down to $p = 3.8 \times 10^{11}$ cm^{-2}, accompanied by a strong positive magnetoresistance at low magnetic fields. The positive magnetoresistance decreases with increasing density and disappears at $p = 12.2 \times 10^{11}$ cm^{-2}. This observation is similar to the positive magnetoresistance observed in Si [148], GaAs [149] and AlAs [124] 2DESs, and is associated with magnetic field induced spin-polarization.

At low magnetic fields, the Zeeman splitting induces a density imbalance between the spin-↑ and spin-↓ subbands and leads to a spin-polarization of the system. When this splitting exceeds the Fermi energy, the 2DES is fully spin-polarized. Assuming the effective g-factor is independent of the magnetic field, the Fermi energy ($\mathcal{E}_F$) at full spin-polarization can be written as

$$\mathcal{E}_F = |g^*|\mu_B B_p \tag{5.1}$$

where B_p is the magnetic field at full spin-polarization. Using the 2DES density of states at full spin-polarization, $D_p(E) = m^*/2\pi\hbar^2$, Eq. 5.1 can be written as

$$|g^*| = \frac{2h}{e}\frac{m_e}{m^*}\frac{p}{B_p} \tag{5.2}$$

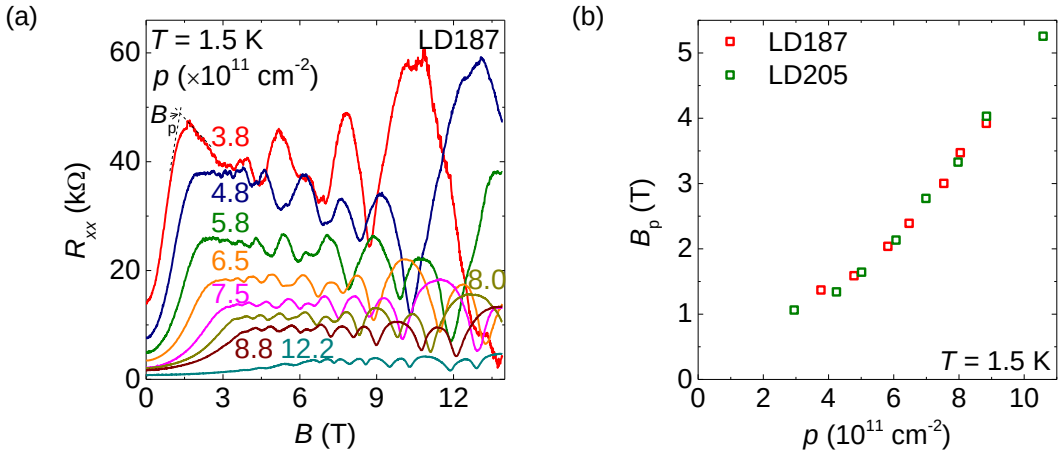

Figure 5.13: (a) R_{xx} vs B in trilayer WSe_2 LD187 at various density values (shown in units of 10^{11} cm^{-2}) and $T = 1.5$ K. The dashed lines for the trace at $p = 3.8 \times 10^{11}$ cm^{-2} mark the field B_p above which the holes are fully spin-polarized. (b) B_p vs p in two trilayer WSe_2 samples, LD187 and LD205, at $T = 1.5$ K.

Equation 5.2 provides a way to determine $|g^*|$ vs p from measurements of the polarization field. The positive magnetoresistance up to B_p is attributed to changes in the spin-↑ and spin-↓ subband populations and the resulting changes in mobility and intersubband scattering [187, 188]. The functional form of the magnetoresistance changes for $B > B_p$ where the spins are fully polarized [149]. A B_p value can therefore be assigned to each of the traces of Fig. 5.13(a) by linearly extrapolating the two regions of distinct magnetoresistance variation vs B, shown for example at $p = 3.8 \times 10^{11}$ cm^{-2}. Figure 5.13(b) shows the extracted B_p vs p for two trilayer samples, LD187 and LD205, at $T = 1.5$ K. The value of B_p decreases with reducing density.

Figure 5.14(a) shows $|g^*|$ vs r_s extracted from the B_p data of Fig. 5.13(b) using Eqs. 5.2 and 4.9.[1] For comparison, the quantum Monte Carlo (QMC) calculation for $g_b = 6.8$ in the two-fold degenerate Landau level model is shown as a solid line. It is noteworthy that the $|g^*|$ enhancement in trilayer WSe_2 closely follows the QMC calculation for the same g_b value extracted from the monolayer and bilayer WSe_2 data of Chapter 4 [Fig. 4.15]. Values of r_s up to 15 are achievable in trilayer WSe_2.

Theoretically, a ferromagnetic ground state, i.e., $B_p = 0$ is expected below a criti-

[1]The error bars in Fig. 5.14 correspond to an r_s uncertainty stemming from the uncertainty in the effective dielectric constant, κ, used to convert the density into r_s. The two extreme cases correspond to either the same dielectric constant used for bilayer WSe_2 from Chapter 4, i.e., $\kappa = [\kappa(h\text{-BN}, h\text{-BN}) + \kappa(h\text{-BN}, WSe_2)]/2$ or an h-BN top dielectric and WSe_2 bottom dielectric, i.e., $\kappa = \kappa(h\text{-BN}, WSe_2)$.

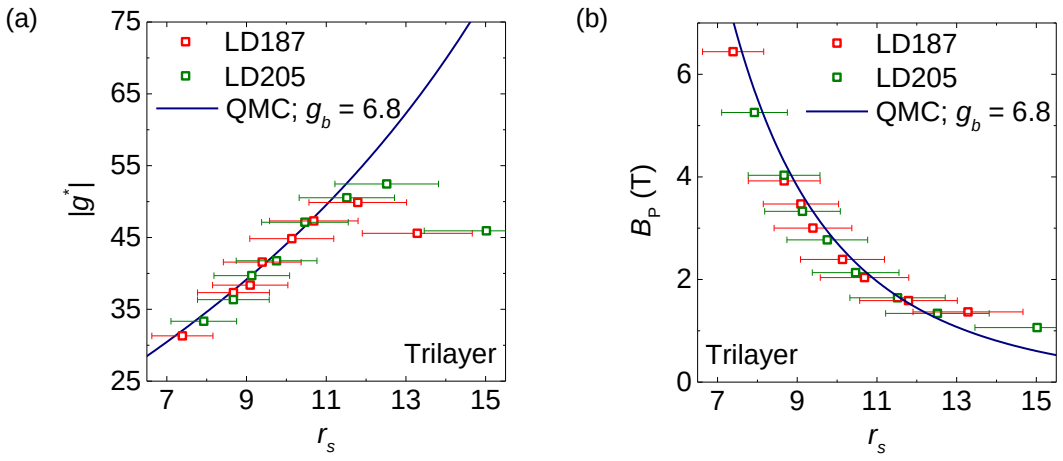

Figure 5.14: (a) $|g^*|$ vs r_s calculated from the B_p data of Fig. 5.13(b) assuming all the Landau levels are two-fold degenerate at low B-fields. The solid line shows the QMC calculation for $g_b = 6.8$. (b) B_p vs r_s corresponding to Fig. 5.13(b) data match well with the QMC calculation for $g_b = 6.8$. The error bars in panels (a) and (b) correspond to an r_s uncertainty stemming from the uncertainty in the dielectric constant used to convert the density into r_s.

cal density in a 2DES, driven by electron-electron interactions [17, Fig. 1.2]. The data of Fig. 5.13(b) show a trend of B_p starting to flatten with reducing density for $p < 5\times10^{11}$ cm^{-2}. The variation of B_p with density can be modeled by QMC calculations to determine the density at which the 2DES becomes ferromagnetic. The B_p value is determined by evaluating the magnetic field at which the total energy, including many-body exchange and correlation energies [21] of a spin-polarized 2DES is minimized, as described in Ref. [189].

Figure 5.14(b) shows B_p vs r_s corresponding to Fig. 5.13(b) data and the QMC calculation for $g_b = 6.8$. The data match closely with the QMC calculation, which predicts a ferromagnetic ground state at $r_s \simeq 26$, attained at a density value inaccessible in the current samples.

5.8 Summary

In summary, magnetotransport measurements of holes in trilayer WSe_2 reveal holes populating two subbands located in the Γ and K valleys, with different effective masses of $1.2m_e$ and $0.5m_e$, respectively. At a fixed hole density, an applied transverse electric field can transfer holes from the Γ to the K valley. This observation is substantiated by *ab initio* calculations of the bandstructure which show an electric field dependent $\Gamma - K$ valley-splitting, stemming from the different orbital characteristics of the Γ and K subbands.

At low-densities, the magnetoresistance data show a signature of magnetic field induced spin-polarization from which an interaction-enhanced, effective g-factor is extracted. Both the g-factor and polarization field data closely match quantum Monte Carlo predictions, underlining the ubiquity of electron-electron interactions in WSe_2.

Chapter 6

Conclusions

The WSe_2 magnetotransport data presented in this dissertation reveal several interesting electronic transport properties of holes in WSe_2. The key findings can be summarized as follows:

- Ohmic WSe_2 hole contacts down to 0.3 K using Pt bottom-electrodes [Chapter 2]
- Hole mobilities approaching 4000 cm^2/Vs at low-temperatures [Chapter 2]
- Two-fold degenerate Landau levels in monolayer and bilayer WSe_2 [Chapter 3]
- Hole effective mass of $0.45m_e$ in monolayer and bilayer WSe_2 [Chapter 3]
- Carrier localization in the constituent layers of bilayer WSe_2 [Chapter 3]
- Weak interlayer coupling < 3.4 meV in bilayer WSe_2 [Chapter 3]
- Negative compressibility of holes in the bottom layer of bilayer WSe_2 [Chapter 3]
- Density-dependent quantum Hall states in monolayer and bilayer WSe_2 [Chapter 4]
- Hole-spin-locking perpendicular to the monolayer and bilayer WSe_2 plane [Chapter 4]
- Transverse E-field independent QHS in monolayer and bilayer WSe_2 [Chapter 4]
- Interaction-enhancement of monolayer and bilayer WSe_2 hole g-factors [Chapter 4]
- Population of trilayer WSe_2 holes in both the Γ and K valleys [Chapter 5]
- Trilayer WSe_2 hole effective mass of $0.5m_e$ ($1.2m_e$) in the K (Γ) valley [Chapter 5]
- Transverse E-field-tunable $\Gamma - K$ valley populations in trilayer WSe_2 [Chapter 5]
- Trilayer WSe_2 holes in the Γ (K) valley at low (high) E-field values [Chapter 5]
- Interaction-enhancement of trilayer WSe_2 hole g-factor [Chapter 5]

A question to ask is what advantages these WSe_2 transport properties offer for discovering new quantum electronic phenomena, and in harnessing them for future electronic devices. The following sections outline the appeal of WSe_2, and semiconducting TMDs in general, as a platform for exploring electron-electron interaction effects, and finally provide possible directions for future work in the theme of this dissertation.

6.1 Appeal of TMDs for Exploring Interaction Effects

It is instructive to appraise the findings of this dissertation in the context of electron-electron interactions, and benchmark the TMD material system against existing 2DESs. At a given carrier density, the interaction parameter, r_s, which determines the strength of electron-electron interactions in a 2DES, depends only on the effective mass of carriers (m^*), and the effective dielectric constant (κ) of the medium surrounding the 2DES. These two parameters in the case of TMDs are (i) large carrier effective mass, and (ii) low effective dielectric constant of the h-BN dielectrics which are typically used to encapsulate them, which result in large r_s values even at moderate carrier density values. For comparison, Fig. 6.1 shows r_s vs carrier density for various 2DESs.

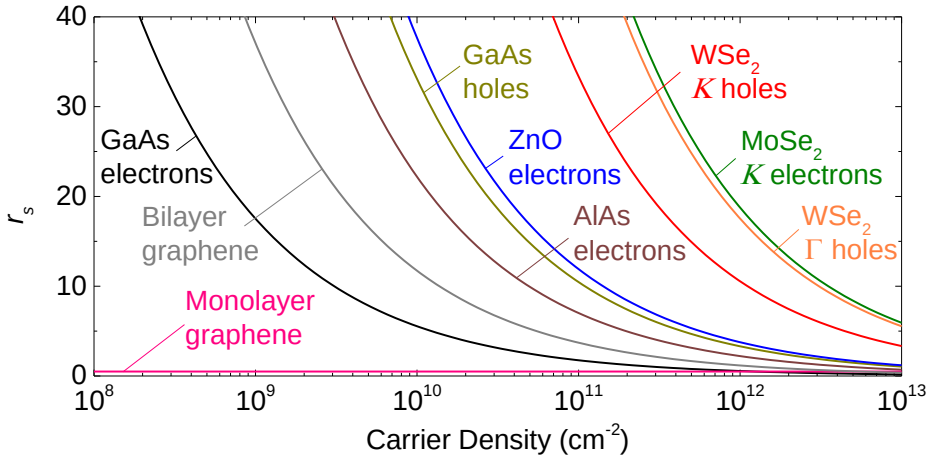

Figure 6.1: r_s vs carrier density for various 2DESs. The r_s values are calculated for GaAs electrons using $m^* = 0.067m_e$, $\kappa = 12.9$, GaAs holes using $m^* = 0.4m_e$, $\kappa = 12.9$, AlAs electrons using $m^* = 0.2m_e$, $\kappa = 10.1$ [157], ZnO electrons using $m^* = 0.3m_e$, $\kappa = 8.5$ [190], monolayer graphene using $v_F = 10^6$ m/s, $\kappa = 4.6$, bilayer graphene using $m^* = 0.05m_e$, $\kappa = 4.6$ [191], WSe_2 K valley holes using $m^* = 0.45m_e$, $\kappa = 4.6$ [Chapter 4], WSe_2 Γ valley holes using $m^* = 1.2m_e$, $\kappa = 7.3$ [Chapter 5], and $MoSe_2$ K valley electrons using $m^* = 0.8m_e$, $\kappa = 4.6$ [94].

Reaching the large r_s regime in the most commonly studied 2DES, GaAs electrons, requires access to very low densities due to the small electron effective mass, $m^* = 0.067m_e$. Larger effective mass 2DESs such as AlAs electrons with an $m^* = 0.2m_e$, and GaAs holes with an $m^* = 0.4m_e$ yield substantially larger r_s values in the same density range.[1] A

[1]Both AlAs electrons and GaAs holes can occupy one or more of multiple valleys, with the exact effective mass depending on the valley(s) occupied. The values used here are under the assumption that only one valley with the specified effective mass is populated.

more recent 2DES based on zinc oxide (ZnO) electrons with an $m^* = 0.3m_e$ also results in similar r_s values. A common feature of these 2DES host materials is their dielectric constant values, which lie in the range of $\kappa \sim 8 - 13$.

On the other hand, the low effective dielectric constant, $\kappa = 4.6$, for 2DESs based on TMD monolayers encapsulated in h-BN,[2] combined with their large carrier effective masses yield significantly larger r_s values at a given density compared to traditional 3D semiconductor 2DESs. Among WSe_2 K valley holes and $MoSe_2$ K valley electrons, the latter with an $m^* = 0.8m_e$ possess larger r_s values. Trilayer WSe_2 Γ valley holes with an $m^* = 1.2m_e$ are also attractive despite their higher effective dielectric constant, $\kappa = 7.3$, stemming from the 2DES residing in thicker WSe_2 with higher dielectric constants.[3]

Figure 6.1 also shows the r_s values for monolayer and bilayer graphene 2DESs encapsulated in h-BN. The case of monolayer graphene is peculiar due to its Dirac band-structure with massless quasiparticles which results in a constant $r_s = e^2/(2\kappa\epsilon_0 h v_F) \simeq 0.5$, independent of the density [4]; e is the electron charge, h is the Planck constant, and $v_F \simeq 10^6$ m/s is the Fermi velocity of graphene. Electron-electron interactions in monolayer graphene are therefore different, and weaker in comparison to conventional 2DESs with massive carriers. The electronic state in monolayer graphene close to the Dirac point, i.e., at low-densities, is a Dirac liquid as opposed to a Fermi liquid at a finite chemical potential, and in conventional 2DESs with massive quasiparticles [191].

Bilayer graphene, however, is analogous to conventional 2DESs due to its parabolic bandstructure and massive carriers with an $m^* = 0.05m_e$ [191], which result in an r_s which increases with decreasing density. The small m^* value, however, necessitates low-densities to access the large r_s regime. Few-layer graphene has been shown to be more conducive for obtaining large r_s values, thanks to its larger density of states, especially at low-densities [192].

In comparison to 2DESs based on large effective mass 3D semiconductors, the merit of TMDs lies in the ability to reduce their thicknesses down to a monolayer, and encapsulate the 2DES in a low dielectric constant environment such as h-BN. This advantage is however diminished if the TMD 2DES is several layers thick, in which case their large dielectric constants [193] would screen interactions, and lower the achievable r_s values. Therefore, monolayer or few-layer TMD 2DESs are best suited to harness the large effective mass advantage offered by TMDs.

[2]For a monolayer TMD encapsulated in h-BN, $\kappa = \kappa(h\text{-BN}, h\text{-BN}) = 4.6$ [Chapter 4].

[3]For trilayer WSe_2 Γ valley holes, a κ value of $\kappa = \kappa(h\text{-BN}, WSe_2) = 7.3$ is used [Chapter 4].

A more intricate difference between interaction effects in TMDs and large effective mass 2DESs such as AlAs electrons and GaAs holes has to do with the bandstructure anisotropies of the latter. It is believed that the effective electron-electron interactions in materials with anisotropic bandstructures are reduced [194, 195]. It has to be noted that TMDs are also expected to possess a certain degree of bandstructure anisotropy due to trigonal warping [196], which is however expected to be negligible, especially at low Fermi energies.

Disorder is an equally, if not more, important aspect which determines interaction effects in 2DESs. Manifestation of interaction effects requires low-disorder, otherwise the 2DES become insulating as the density is reduced due to carrier localization. The carrier mobility is the main metric of the degree of disorder, and therefore, of the potential for observing interaction effects in a 2DES. Figure 6.2 shows the low-temperature mobility vs carrier density for the 2DESs of Fig. 6.1. The mobility values for the TMDs are several orders of magnitude lower, and correspondingly, the lowest achievable densities several orders of magnitude higher than the state-of-the-art values for traditional 2DESs.

At low-temperatures, the mobility of a 2DES is predominantly determined by charged impurity scattering due to intrinsic defects and dopants, and/or extrinsic impurities in proximity of the 2DES. Charged impurity scattering is responsible for the trend of mobility decreasing with reducing density for nearly all the 2DESs in Fig. 6.2. The extremely high-mobilities in state-of-the-art GaAs, AlAs, and ZnO 2DESs can be attributed to the material quality, thanks to advances in the MBE techniques used for their growth [190, 198].

Graphene 2DESs also exhibit high intrinsic mobilities, thanks to the low defect densities in the natural graphite crystals from which the graphene flakes are isolated. In contrast, the substantially lower intrinsic mobilities in TMDs can be attributed to their high propensity for structural defects [204]. Improving the mobilities through refinements in synthesis techniques would provide access to lower densities where TMDs are very promising for exploring interaction effects.

6.2 Prospects for Future Work

There does not seem to be a dearth of research directions in the field of TMDs' electronic properties, in light of its recency. This section provides a few prospects for future work, in the context of this dissertation.

A straightforward direction for future research would be to study magnetotransport in higher quality samples, emulating the trajectory of research in GaAs 2DESs which led

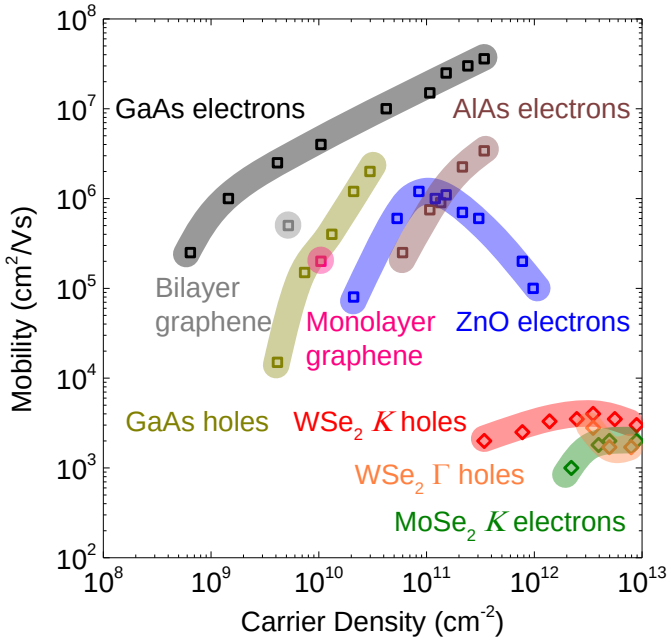

Figure 6.2: Low-temperature mobility vs carrier density for various 2DESs. The data points are sampled from Refs. [197, 198] for GaAs electrons, Ref. [199] for GaAs holes, Ref. [200] for AlAs electrons, Ref. [190] for ZnO electrons, Ref. [201] for monolayer graphene, Ref. [202] for bilayer graphene, Chapters 3, 5 data for WSe_2 K valley holes, Ref. [147] and Chapter 5 data for WSe_2 Γ valley holes, and Ref. [94] for $MoSe_2$ K valley holes. The shaded bands are a guide to the eye. Adapted, in part, from Ref. [203].

to the discovery of several interesting quantum electronic phenomena, thanks largely to improvements in sample quality [198]. The low-temperature hole mobilities in WSe_2 are believed to be limited by intrinsic point defects with a defect density of $\sim 10^{12}$ cm^{-2} in monolayer WSe_2 [65]. Synthesizing the bulk crystals using a flux growth technique [205] is expected to yield flakes with lower point defects than the commonly used chemical vapor transport method [206].

With access to higher quality material, the reduction of extrinsic disorder is required in parallel, in order to utilize the gains offered by lower intrinsic disorder. Cleaner sample fabrication techniques would ensure that the intrinsic mobility gains are preserved. One possibility is to suspend the WSe_2 layer, which can potentially eliminate extrinsic disorder, similar to the case of suspended graphene [207]. An added advantage of suspending the TMD layer is a reduction of the effective dielectric constant to its lowest possible value, $\kappa = 1$, and therefore, access to larger r_s values. However, suspended films have limits on the maximum attainable densities [207], which could severely limit the performance of TMDs'

electrical contacts.

A second direction could be to explore electronic phenomena which are unique to the TMD material system, for instance, the spin (valley) Hall effect. Figure 6.3(a) shows a schematic of the spin (valley) Hall effect in a TMD layer. When moving under the influence of an in-plane electric field, carriers in the K and K' valleys experience opposite magnetic moments which deflect them in opposite directions transverse to the current flow direction, leading to a spin (valley) polarization on the sample edges [143]. The valley magnetic moment arises due to the Berry curvature of the bandstructure, thanks to the large spin–orbit coupling and inversion symmetry breaking in monolayer TMDs [33].

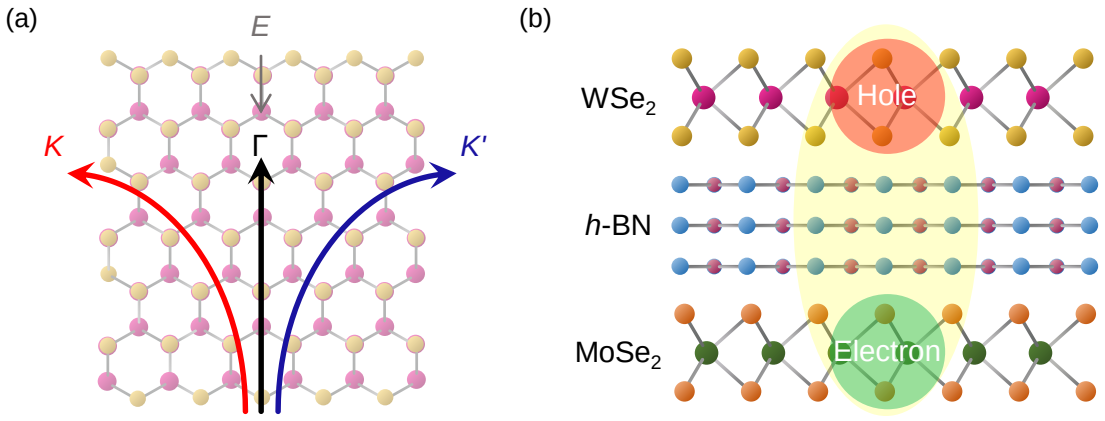

Figure 6.3: (a) Schematic of the spin (valley) Hall effect in a TMD. Carriers in the K and K' valleys experience opposite valley magnetic moments which leads to a spin (valley) polarization on the sample edges. Carriers in the Γ valley do not experience such an effect. Adapted, in part, from Ref. [143]. (b) Schematic of a TMD double layer heterostructure comprising hole-doped monolayer WSe_2 and electron-doped monolayer $MoSe_2$, separated by three monolayers of h-BN, which can host indirect excitons.

The spin (valley) Hall effect has been observed in monolayer MoS_2 using optical techniques to detect the spin (valley) accumulation along the sample edges [181]. Direct electrical detection of the spin (valley) Hall effect can be done using non-local resistance measurements [208], which can be performed using the device structure presented in this dissertation. Furthermore, the spin (valley) Hall effect is expected to be absent for carriers in the Γ valley [Fig. 6.3(a)] due to the vanishing Berry curvature at the Γ point [143]. Given the ability to transfer holes between the Γ and K valleys in trilayer WSe_2 using a transverse electric field, it can be used as an effective knob to tune the spin transport properties in trilayer WSe_2.

A third research direction could be to fabricate TMD heterostructure devices to study interactions between carriers residing in different layers, and how they impact electrical transport in the z-direction. Optical measurements of an MoS_2/WSe_2 double monolayer heterostructure have revealed signatures of strong coupling between the MoS_2 electrons and WSe_2 holes, which form indirect excitons [209]. Theory predicts that under certain conditions, such indirect excitons can form spontaneously without the need for optical excitation, and interestingly, can condense into a Bose–Einstein condensate (BEC) [210, 211]. Figure 6.3(b) shows the schematic of a TMD double layer structure comprising monolayer WSe_2 and monolayer $MoSe_2$, separated by three monolayers of h-BN, which can potentially host such a BEC.

Bose–Einstein condensates have been experimentally realized in double layer GaAs 2DESs, and form only at very low-temperatures and in high magnetic fields [212]. In comparison, theoretical calculations for TMD double layers predict BECs to form even in the absence of a magnetic field, and at temperatures up to room temperature [211]. The difference between the two systems can be attributed to the ability to bring the electron and hole layers in much closer proximity in TMD double layers than in GaAs, and the stronger interactions in TMDs, in general. A TMD double layer structure with independent layer contacts would be needed to experimentally investigate the existence of a BEC, typically through interlayer tunneling [213] or counterflow measurements [214, 215].

A device concept which utilizes the unique interlayer tunneling characteristics of such a double layer system for performing binary logic operations is the bilayer pseudospin field-effect transistor (BiSFET) [216], first proposed for a graphene double layer system. Although there is no experimental realization, to date, of a BiSFET operating at room temperature, recent experiments in double bilayer graphene heterostructures separated by a bilayer WSe_2 barrier have shown evidence of a BEC forming at low-temperatures [217].

6.3 Concluding Remarks

In conclusion, the findings of this dissertation shed some light on the electronic transport properties of holes in WSe_2. The nascence of the TMD material system combined with the rich assortment of TMDs leaves almost an entirety yet to be explored. It is hoped that the magnetotransport studies of WSe_2 holes presented in this dissertation prompt further experimental and theoretical studies to enrich the knowledge of the electronic properties of TMDs.

Appendices

Appendix A

Samples Catalog

Table A.1 lists the WSe_2 samples whose data is discussed in this dissertation. The capacitance values marked by a † are estimated based on the top-gate *h*-BN thickness, measured using atomic force microscopy, and an *h*-BN out-of-plane effective dielectric constant of 3.0 [Appendix C]. Values marked by a ‡ are estimated for a 300 nm SiO_2 back-gate dielectric, and an SiO_2 effective dielectric constant of 3.9 [82]. The unmarked capacitance values are obtained from gate-dependent SdH oscillations measurements, and/or Hall measurements.

Table A.1: List of WSe_2 samples whose data is discussed in this dissertation. The scale bars for the optical micrographs are 10 μm.

Name	WSe_2	Type	C_{TG} (nF/cm^2)	C_{BG} (nF/cm^2)	Optical micrograph	Chapter(s)
LD39	four-layer	Pd/*h*-BN top-gate; Si/SiO_2 back-gate	141†	11.5‡	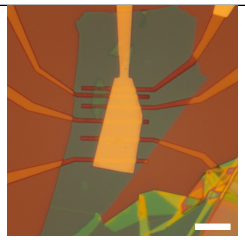	Chapter 2
LD55	trilayer	Pd/*h*-BN top-gate; Si/SiO_2 back-gate	134†	11.5‡	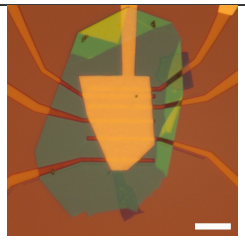	Chapter 2

Continued on next page

Table A.1 – *Continued from previous page*

Name	WSe_2	Type	C_{TG} (nF/cm^2)	C_{BG} (nF/cm^2)	Optical micrograph	Chapter(s)
LD56	four-layer	Pd/*h*-BN top-gate; Si/SiO_2 back-gate	150†	11.5‡	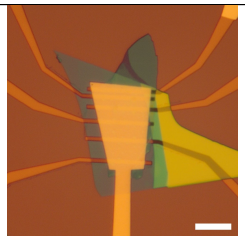	Chapter 2
LD63	bilayer	Pd/*h*-BN top-gate; Si/SiO_2/*h*-BN back-gate	188	10.1	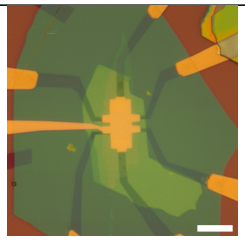	Chapter 3
LD65	trilayer	Pd/*h*-BN top-gate; Si/SiO_2/*h*-BN back-gate	210	11.0	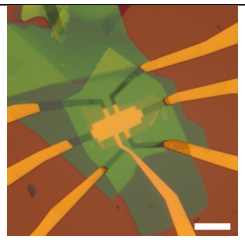	Chapter 5
LD71	mono-layer	Pd/*h*-BN top-gate; Si/SiO_2/*h*-BN back-gate	99.0	–[1]	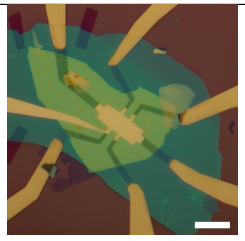	Chapter 3, Chapter 4
LD99B	bilayer	Pd/*h*-BN top-gate; Si/SiO_2/*h*-BN back-gate	202	10.8	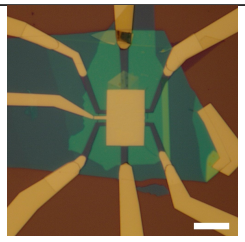	Chapter 3, Chapter 4

Continued on next page

[1] Non-functional back-gate

Table A.1 – *Continued from previous page*

Name	WSe_2	Type	C_{TG} (nF/cm^2)	C_{BG} (nF/cm^2)	Optical micrograph	Chapter(s)
LD103	mono-layer	Pd/*h*-BN top-gate; Si/SiO_2/ *h*-BN back-gate	238	10.9	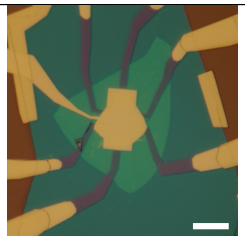	Chapter 3, Chapter 4
LD108	mono-layer	Pd/*h*-BN top-gate; Pt/*h*-BN back-gate	207	204	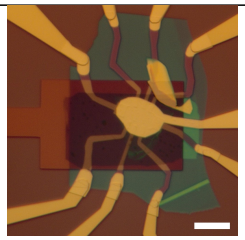	Chapter 4
LD123	bilayer	Au/*h*-BN top-gate; Pt/*h*-BN back-gate	233	139	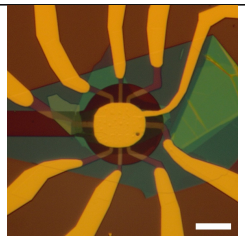	Chapter 4
LD133	mono-layer	Pd/*h*-BN top-gate; Si/SiO_2/ *h*-BN back-gate	231	10.8	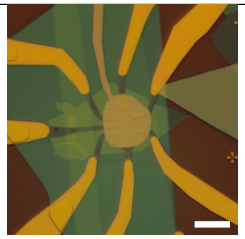	Chapter 4
LD163	bilayer	graphite/ *h*-BN top-gate; graphite/ *h*-BN back-gate	270	90.0	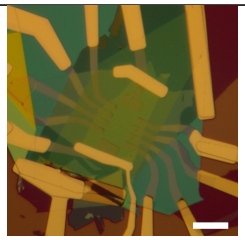	Chapter 3

Continued on next page

Table A.1 – *Continued from previous page*

Name	WSe_2	Type	C_{TG} (nF/cm^2)	C_{BG} (nF/cm^2)	Optical micrograph	Chapter(s)
LD187	trilayer	graphite/ *h*-BN top-gate; graphite/ *h*-BN back-gate	215	155	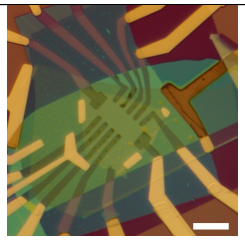	Chapter 5
LD189	trilayer	Pd/*h*-BN top-gate; Pt/*h*-BN back-gate	120	130	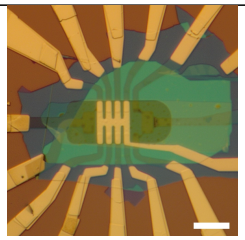	Chapter 5
LD201	bilayer	Pd/*h*-BN top-gate; Pt/*h*-BN back-gate	160	155	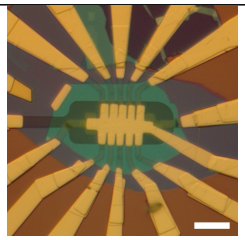	Chapter 3
LD205	trilayer	graphite/ *h*-BN top-gate; graphite/ *h*-BN back-gate	190	160	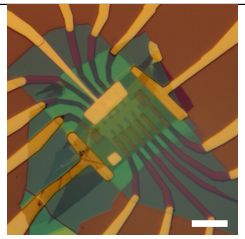	Chapter 5
WSe_2-04	bilayer	Pd/*h*-BN top-gate; Si/SiO_2/ *h*-BN back-gate	–[2]	–		Chapter 4

Continued on next page

[2]The density values were determined using the SdH oscillations' R_{xx} minima only at a few combinations of V_{TG} and V_{BG}. The C_{TG} and C_{BG} values are therefore unknown.

Table A.1 – *Continued from previous page*

Name	WSe_2	Type	C_{TG} (nF/cm^2)	C_{BG} (nF/cm^2)	Optical micrograph	Chapter(s)
WSe_2-06	mono-layer	Pd/*h*-BN top-gate; Si/SiO_2/ *h*-BN back-gate	174	–[3]	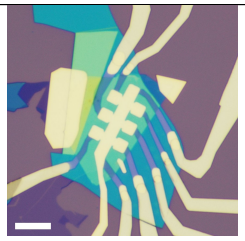	Chapter 2
WSe_2-07	bilayer	Pd/*h*-BN top-gate; Pt/*h*-BN back-gate	276	93.4	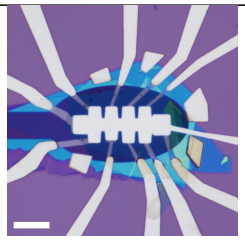	Chapter 2, Chapter 4
WSe_2-08	mono-layer	Pd/*h*-BN top-gate; Pt/*h*-BN back-gate	340	190	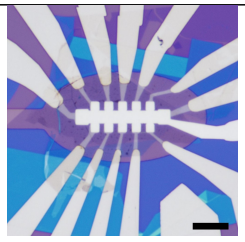	Chapter 2
WSe_2-09	bilayer	Pd/*h*-BN top-gate; Pt/*h*-BN back-gate	241	206	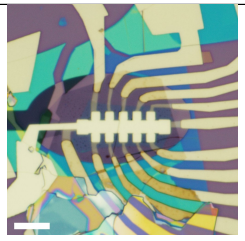	Chapter 2

[3]The back-gate was not used.

Appendix B

Fabrication Techniques

This Appendix describes the techniques used for fabrication of the WSe_2 devices whose data is discussed in this dissertation. The fabrication was performed at the Microelectronics Research Center in the University of Texas at Austin.

B.1 Micromechanical Cleavage

Micromechanical cleavage, or mechanical exfoliation is the technique used to obtain few-layer thick flakes of layered materials from their bulk crystal forms, famously demonstrated using Scotch™ Tape for synthesizing monolayer graphene from graphite [7]. A modified version of this technique was used for isolating the few-layer WSe_2 flakes and *h*-BN flakes used in this dissertation.

Figure B.1 shows the exfoliation process starting with bulk $2H$-WSe_2 crystals. The WSe_2 crystals purchased from HQ Graphene (www.hqgraphene.com) were synthesized using the chemical vapor transport technique [206] and appear as polycrystalline centimeter-sized chunks, $1-2$ mm thick, as shown in Fig. B.1(a). A $\sim$ 5 mm piece was cleaved from the bulk crystal using tweezers and placed on a piece of cleanroom tape (UltraTape® 1114/0114 from www.cleanroomtape.com). The tape was then repeatedly attached and peeled-off from the WSe_2 crystal until a substantial portion of the tape was covered in thinner WSe_2 cyrstals, as shown in Fig. B.1(b).

The tape was then placed face-down on a polydimethylsiloxane (PDMS) film in a Gel-Pak® box (Medium Tack Gel X4 from www.gelpak.com) and rapidly peeled-off to transfer some of the WSe_2 crystals onto the PDMS film, as shown in Fig. B.1(c). Subsequently, a 1 cm $\times$ 1 cm SiO_2/Si substrate with 300 nm of thermally grown SiO_2 was affixed onto the WSe_2 crystals on the PDMS film, as shown in Fig. B.1(d). The substrate was then rapidly peeled-off from the PDMS which resulted in a few WSe_2 flakes being transferred onto the SiO_2 surface, as shown in Fig. B.1(e). Using the intermediary step of transferring the WSe_2 flakes from the UltraTape® onto PDMS was found to increase the yield of few-layer WSe_2 flakes, as opposed to directly affixing the SiO_2/Si substrate on the tape like in Ref. [7].

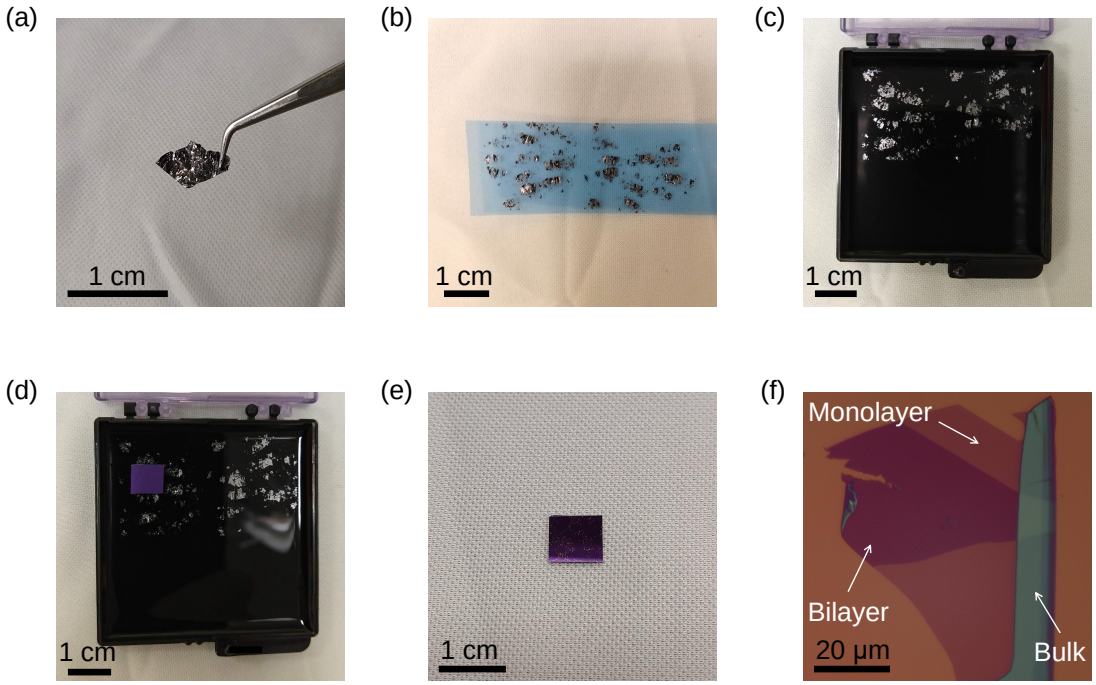

Figure B.1: (a) A typical bulk 2H-WSe_2 crystal. (b) Bulk WSe_2 crystals transferred onto UltraTape®. (c) Bulk WSe_2 crystals transferred from UltraTape® onto PDMS in a Gel-Pak® box. (d) A 300 nm SiO_2/Si substrate affixed on the WSe_2 crystals on PDMS. (e) The SiO_2/Si substrate from panel (d) after peeling-off from the PDMS. (f) A typical WSe_2 flake with monolayer, bilayer, and bulk regions.

The choice of substrates with a 300 nm SiO_2 layer on top is to maximize the optical contrast of few-layer flakes [218, 219], which enables their identification under an optical microscope. Figure B.1(f) shows the optical micrograph of a typical WSe_2 flake comprising monolayer, bilayer, and bulk (> 5 layers) regions, apparent by their distinct optical contrast with respect to the substrate. In addition to optical contrast and photoluminescence (PL) spectra which are a strong function of number-of-layers for few-layer flakes [Fig. 1.6(b)], the Raman spectra also show features dependent on the number-of-layers, which aid in their identification.

Figure B.2(a) shows the optical micrograph of a WSe_2 flake comprising monolayer to four-layer thick regions, and Fig. B.2(b) shows their corresponding room temperature Raman spectra obtained using 532 nm laser excitation. The peak near 250 cm^{-1} is called the A_{1g} peak and corresponds to the out-of-plane vibrations of the selenium (Se) atoms [220]. The peak adjacent to A_{1g} is labeled 2LA(M), whose position and intensity with respect to the A_{1g} peak vary strongly with the number-of-layers. The peak near 308 cm^{-1} is called the B^1_{2g} peak, and is present in all WSe_2 flakes except in monolayers [221]. The precise

positions, intensities, and presence or absence of these peaks, in combination with optical contrast and PL spectra enable unambiguous identification of the number-of-layers in the limit of monolayer to four-layer WSe_2. The peak at 520 cm^{-1} is from the Si substrate.

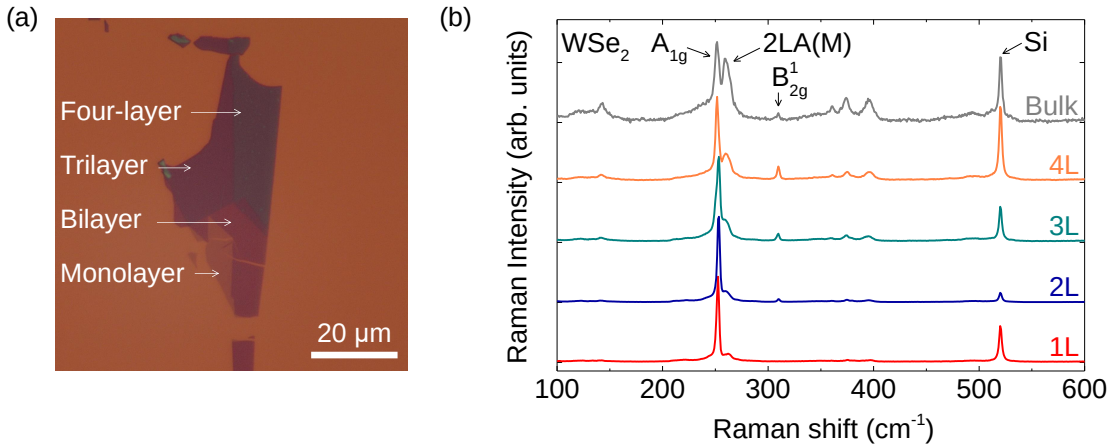

Figure B.2: (a) Optical micrograph of a WSe_2 flake comprising monolayer to four-layer thick regions. (b) Room temperature Raman spectra of WSe_2 flakes of various number-of-layers obtained using 532 nm laser excitation. The characteristic WSe_2 Raman peaks and the Si Raman peak are labeled. The individual spectra are normalized to the A_{1g} peak intensity and are offset for clarity.

The same exfoliation technique of Fig. B.1 was used to exfoliate the $10-30$ nm thick top-gate and bottom-gate *h*-BN dielectrics. The starting material was bulk *h*-BN crystallites provided by T. Taniguchi and K. Watanabe, synthesized using the growth method described in Ref. [222]. The *h*-BN flake thicknesses were measured using tapping mode atomic force microscopy (AFM) and flakes free from wrinkles and thickness non-uniformities were chosen. Figure B.3 shows optical micrographs of typical *h*-BN flakes of thicknesses ranging from $10-30$ nm.

B.2 "Pick and Place" Assembly

Deterministic flake transfer has been the mainstay behind fabrication of van der Waals (vdW) heterostructures and devices. Starting with early wet transfer techniques [223, 224], layered material transfer has evolved into cleaner and more versatile dry transfer techniques [37, 78, 79, 225]. The transfer technique used in this dissertation is based on the "pick and place" assembly technique of Refs. [78] and [79].

The transfer technique relies on the temperature-dependent adhesion of layered material flakes to thermoplastic polymers such as poly(propylene carbonate) (PPC). If the

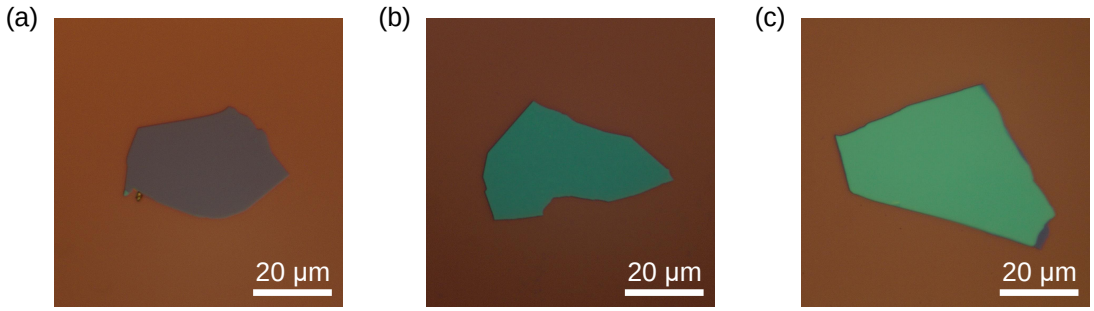

Figure B.3: Optical micrographs of typical exfoliated *h*-BN flakes on 300 nm SiO_2/Si substrates. The flake thicknesses are (a) 13 nm (b) 24 nm (c) 35 nm.

adhesion is tuned to be higher than the vdW attraction between the flake and the SiO_2 substrate, the flake gets "picked-up" by the polymer on making contact with the flake. This flake can then be used to sequentially pick up other flakes, thanks to the higher vdW attraction between layered material flakes compared to the flakes and SiO_2 [78]. Finally, the stack of flakes can be released, or "placed" on SiO_2 by heating the polymer to a temperature where its adhesion is lower than the adhesion between the flakes and SiO_2. Examples of such thermoplastic polymers include PPC [78], poly(bisphenol A carbonate) [226], and poly(methyl methacrylate) (PMMA) [227].

The polymer is typically coated onto a PDMS stamp which is attached to a glass coverslip for structural support. A modification of this "pick and place" technique, introduced by Ref. [79], was used to assemble the *h*-BN/WSe_2 stacks in this dissertation. It involved the addition of a hemispherical bulb-like PDMS handle on the planar PDMS stamp to constrain the contact area to only the handle, and enable selective flake "pick-up" with higher spatial resolution. Figure B.4(a) shows the schematics and corresponding optical micrographs of the modified "pick and place" process, demonstrated on an *h*-BN flake. Figure B.4(b) shows the PDMS hemispherical handle substrate on a glass coverslip. The "pick and place" process was performed on a probe station (Cascade Summit 11000 B) equipped with a temperature-controlled chuck and a micromanipulator retrofitted with a vacuum arm to hold the PDMS stamp, as shown in Fig. B.4(c).

The PDMS stamps were prepared from commercially available SYLGARD® 184 (www.sigmaaldrich.com) silicone elastomer which was cast into $1-3$ mm thick films and cut into 5×5 mm pieces. Each PDMS stamp was affixed onto a glass coverslip and the hemispherical handle drop-cast on the planar stamp using a liquid PMDS droplet from a syringe which was then rapidly cured at 180 °C for 5 min to minimize lateral diffusion of the droplet over the planar PDMS stamp. The PPC (molecular weight ~ 50000, Sigma Aldrich)

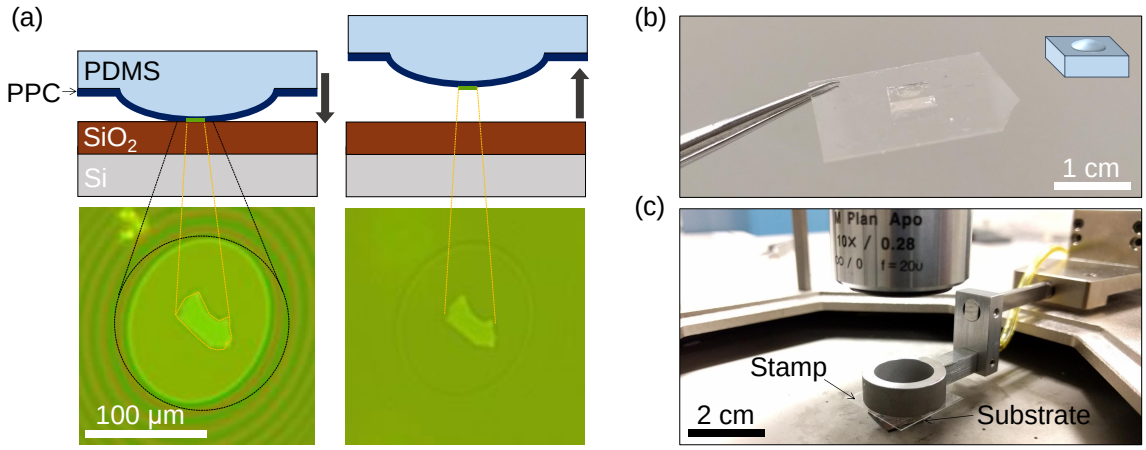

Figure B.4: (a) Schematics and corresponding optical micrographs of the PDMS/PPC hemispherical handle substrate and the flake "pick-up" process. Adapted from Ref. [79]. (b) A PDMS hemispherical handle substrate stamp supported on a glass coverslip. Inset: schematic of the PDMS hemispherical handle. (c) A retrofitted micromanipulator holding the PDMS/PPC stamp under an optical microscope on a probe station. The SiO_2/Si substrate is on a temperature-controlled chuck.

was dissolved in anisole to prepare a 15% wt/wt solution for spin-coating. The PPC solution was spin-coated at 3000 rpm for 1 min onto the PDMS stamps and subsequently baked at 180 °C for 3 min to remove the remaining solvent and improve the adhesion of the PPC layer to the PDMS stamp.

Figure B.5 shows the optical micrographs of a typical "pick and place" process for placing Flake 1 (monolayer MoS_2) [Fig. B.5(a)]on Flake 2 (monolayer WSe_2) [Fig. B.5(b)], which proceeds as follows. The SiO_2/Si substrate with Flake 1 is heated to 45 °C, and a PPC coated PDMS stamp brought into contact with Flake 1, and held for 15 s. The stamp is then rapidly raised from the substrate, which results in Flake 1 being attached to the PPC, as shown in Fig. B.5(c). The stamp is then aligned with Flake 2 by looking through the transparent PDMS/PPC stamp using the probe station microscope. The stamp is then lowered onto Flake 2 and the substrate heated to 90 °C which causes the PPC to lose its adhesion. After waiting for 1 min at 90 °C, the stamp is slowly raised, which causes Flake 1 to detach from the PPC and stay on Flake 2 on the SiO_2/Si substrate, as shown in Fig. B.5(d). The substrate is finally rinsed in acetone and isopropanol (IPA) to remove any remaining PPC residues. The PPC layer on the PDMS stamp is peeled off manually using tweezers and the stamp rinsed in acetone and IPA, after which it can be used again.

The "pick and place" process of Fig. B.5 is applicable to virtually all TMDs and *h*-BN flakes, and can be extended to assemble multiple flakes on top of each other before

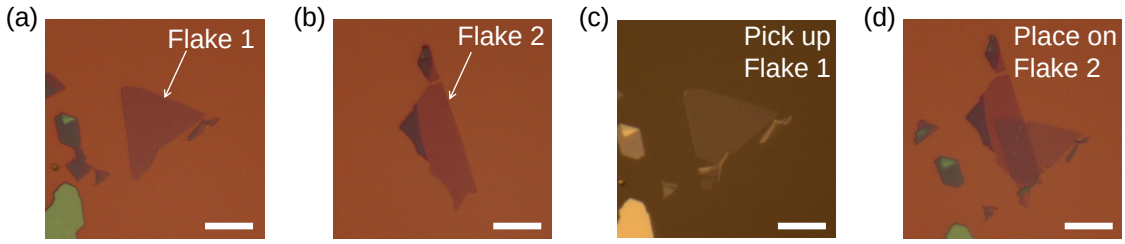

Figure B.5: Optical micrographs of a typical "pick and place" process where Flake 1 (monolayer MoS_2) is placed on Flake 2 (monolayer WSe_2). (a) Optical micrograph of Flake 1 and (b) Flake 2 on 300 nm SiO_2/Si substrates. (c) Flake 1 on PPC/PDMS after being "picked-up." (d) Flake 1 "placed" on Flake 2. The scale bars are 10 μm.

releasing the resulting heterostructure on the final substrate of choice. Annealing the flakes in vacuum (340 °C for 8 h at 10^{-7} Torr) prior to "pick-up" was found to increase the "pick-up" yield to nearly 100%. Annealing was also found to help reduce organic contaminants which get trapped between the flakes and result in contamination bubbles at the interfaces [228].

B.3 Microfabrication

This section describes the microfabrication techniques used to fabricate the WSe_2 devices of this dissertation. The process parameters are provided where applicable and can be adapted to suit equivalent process equipment as needed.

The starting Si wafers were degenerately-doped, 4″ n^+ wafers (<001>, < 0.005 Ω·cm, single side polished, from www.addisonengineering.com). The wafers were cleaned in a standard piranha bath and oxidized at 1050 °C in an oxygen ambient to grow a 300 nm SiO_2 layer. The wafers were then cleaved into 1×1 cm chips which were used for exfoliation and device fabrication. A piranha clean followed by a 180 °C, 2 min dehydration bake prior to exfoliation was found to increase the yield of few-layer flakes of both WSe_2 and *h*-BN.

Figure B.6 shows optical micrographs of the process flow used for fabricating the Si/SiO_2 back-gated, Pd/*h*-BN top-gated WSe_2 FET samples of Chapter 2. First, WSe_2 flakes were exfoliated and a suitable flake was chosen, as shown in Fig. B.6(a). On a separate SiO_2/Si substrate with prepatterned alignment markers[1], Pt bottom-electrodes

[1]The alignment markers are 200 μm apart in an *xy*-grid and are needed for alignment during electron-beam lithography. The alignment marker grid was patterned using optical lithography followed by electron-beam metal evaporation of 5 nm Cr/25 nm Pt, and lift-off.

were patterned using electron-beam lithography (EBL) and electron-beam metal evaporation (EBME) of Cr/Pt (2 nm/10 nm) electrodes, followed by lift-off [Fig. B.6(b)]. The substrate with Pt electrodes was then annealed in vacuum (340 °C for 8 h at 10^{-7} Torr) to remove EBL resist residues and other process contaminants, to create a clean surface for the subsequent flake transfer.

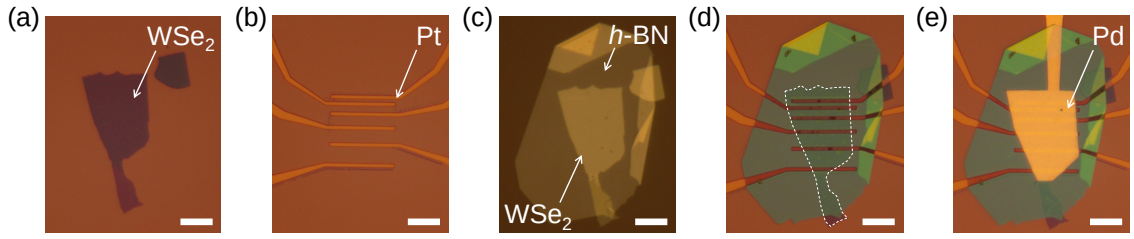

Figure B.6: Optical micrographs of the fabrication process flow for LD55, an Si/SiO_2 back-gated, Pd/*h*-BN top-gated WSe_2 FET sample. (a) Exfoliated trilayer WSe_2 flake. (b) Pt bottom-electrodes. (c) *h*-BN/WSe_2 stack on PDMS/PPC. (d) *h*-BN/WSe_2 transferred onto the Pt bottom-electrodes. The WSe_2 flake is outlined by a white dashed line. (e) Finished device with Pd top-gate electrode. The scale bars are 10 μm.

On a separate substrate, a suitable *h*-BN flake was exfoliated and "picked-up" using a PPC/PDMS stamp. The WSe_2 flake was then "picked-up" using the *h*-BN flake to result in an *h*-BN/WSe_2 stack on PPC/PDMS, as shown in Fig. B.6(c). The *h*-BN/WSe_2 stack was then aligned to the Pt bottom-electrodes and "placed" on them, as shown in Fig. B.6(d). The substrate was then annealed yet again (340 °C for 8 h at 10^{-7} Torr) to improve the physical contact between the Pt electrodes and WSe_2. It is to be noted that the annealing steps were not found to cause any measurable degradation in the WSe_2 electrical quality, whether it be exposed WSe_2, or covered with *h*-BN. A local Pd top-gate electrode was patterned to cover the WSe_2 flake area using EBL, EBME, and lift-off, as shown in Fig. B.6(e). Finally, the contact and gate electrodes were connected to bond pads (typically Cr/Au - 5 nm/50 – 100 nm) which were patterned using EBL, EBME, and lift-off.

The process steps for EBL were as follows:

1. Spin-coat the sample with PMMA (950PMMA 4% in anisole from www.microchem.com) at 3000 rpm for 45 s, and bake at 180 °C for 15 s.
2. Expose the pattern at a 20 kV electron-beam accelerating voltage and a dose of 350 – 380 $\mu C/cm^2$.
3. Develop in a 1 : 3 solution of methyl isobutyl ketone (MIBK) : IPA for 30 s followed by an IPA rinse for 30 s, and blow-dry.

The EBL exposures on top of, or in proximity of the WSe_2 channel were performed at the lowest possible electron-beam current (typically < 50 pA) in order to minimize electron-beam induced heating and damage to the WSe_2 channel [229]. The Cr/Pt deposition was done at a base pressure < 10^{-5} Torr and the deposition rate was kept below 0.5 Å/s to obtain smooth films. Care was taken to ensure that the chamber temperature stayed below 60 °C, in order to prevent PMMA reflow. Lift-off was performed in an acetone bath for $2-3$ h, and the residual metal films were detached from the substrate by gently spraying acetone from a squirt bottle when they did not delaminate by themselves.

The *h*-BN encapsulated WSe_2 Hall bar samples were fabricated using the same essential process steps described above, but with the following modifications. Figure B.7 shows select optical micrographs of the process flow used for fabricating the Si/SiO_2/*h*-BN back-gated, Pd/*h*-BN top-gated WSe_2 Hall bar samples. First, *h*-BN flakes were exfoliated and a suitable flake chosen as the substrate, as shown in Fig. B.7(a). Platinum bottom-electrodes were patterned in a Hall bar geometry on the *h*-BN flake using EBL, EBME, and lift-off, as shown in Fig. B.7(b). The substrate was then annealed and thick metal extensions (Cr/Ni/Pd - 5 nm/50 nm/10 nm) were patterned using EBL, EBME, and lift-off, as shown in Fig. B.7(c). The role of these extensions was twofold: to provide electrical continuity at the *h*-BN edge, where the Pt lines, being usually thinner than the *h*-BN flake, were usually disconnected, and to anchor the *h*-BN flake in place during further processing. The subsequent steps to finish device fabrication involved assembly of an *h*-BN/WSe_2 stack, placing it on the Pt electrodes, as shown in Fig. B.7(d), and finally patterning a top-gate electrode.

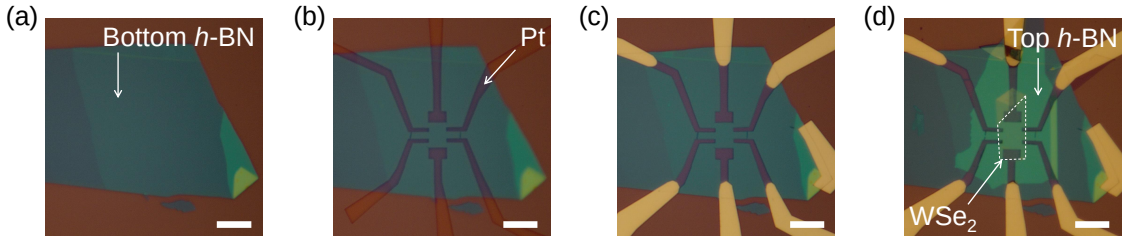

Figure B.7: Optical micrographs of the fabrication process flow for LD99B, an Si/SiO_2/*h*-BN back-gated, Pd/*h*-BN top-gated WSe_2 Hall bar sample. (a) Exfoliated bottom *h*-BN flake. (b) Pt electrodes on bottom *h*-BN. (c) Thick metal extensions to connect to the Pt electrodes, and also anchor the bottom *h*-BN in place during further processing. (d) Finished device before patterning the Pd top-gate. The WSe_2 flake is outlined by a white dashed line. The scale bars are 10 μm.

Thin cracks in the PMMA between exposed features close to each other were a common occurrence after developing in MIBK : IPA, which resulted in Pt slivers between

adjacent metal electrodes after EBME, e.g., between the adjacent Hall probes in Fig. B.7(b). These cracks were observed only for EBL on *h*-BN and are presumably due to electron-beam induced stress at the PMMA/*h*-BN interface [230]. A majority of the slivers were however found to break after subsequent anneals or transfers, e.g., Fig. B.7(d), and did not impact device functionality. Samples with metal extensions were annealed in forming gas (96% nitrogen + 4% hydrogen, 340 °C for 8 h at 1.5 Torr) to prevent agglomeration of the metal when annealed in vacuum.

In situations where the Pt electrodes were found to be broken underneath the top-gate *h*-BN, windows were etched in the *h*-BN to expose the Pt and deposit a second layer of thick metal connection to the corresponding metal extension. The *h*-BN etch was performed in a reactive-ion etching chamber using a tetrafluoromethane (CF_4, 40 sccm) + O_2 (10 sccm) plasma at a radio frequency power of 75 W and a chamber pressure of 50 mTorr. The typical *h*-BN etch rate was $\sim$ 3 nm/s.

In cases where the Pd top-gate electrode was shorted to the Pt electrodes or metal extensions due to EBL-induced cracks and consequent Pd slivers, or when the top-gate electrode needed rework, the affected part of the Pd metal was selectively etched away in potassium iodide + iodine (KI + I_2; TFA etchant from www.transene.com) using PMMA as the mask. The typical Pd etch rate was $\simeq$ 4 nm/s.

The next iteration of WSe_2 Hall bar samples used a Pt metal back-gate in place of the n^+ Si substrate. Figure B.8 shows select optical micrographs of the process flow used for fabricating the Pt/*h*-BN back-gated WSe_2 Hall bar samples. First, a Cr/Pt (2 nm/10 nm) back-gate electrode was patterned on an SiO_2/Si substrate using EBL, EBME, and lift-off, as shown in Fig. B.8(a). The substrate was annealed in vacuum, and a suitable *h*-BN flake was transferred on top of the Pt back-gate, as shown in Fig. B.8(b). Subsequently, similar to the process flow of Fig. B.6, Pt bottom-electrodes were patterned on the *h*-BN [Fig. B.8(c)], and a stack of *h*-BN/WSe_2 was transferred onto the Pt electrodes, as shown in Fig. B.8(d). Finally, a top-gate electrode and metal extensions were patterned to finish the device fabrication.[2]

The final iteration of WSe_2 Hall bar samples were fabricated using single crystal graphite flakes as both the top- and back-gates. The graphite flakes were exfoliated from natural graphite crystals (NGS Naturgraphit GmbH, www.graphit.de) using the same exfoliation technique described in Section B.1. Figure B.9 shows select optical micrographs of the process flow used for fabricating the graphite/*h*-BN back- and top-gated WSe_2 Hall bar samples. First, a 5 – 10 nm thick graphite flake was exfoliated on an SiO_2/Si substrate,

[2]In LD123, the top-gate electrode and metal extensions of Cr/Au (2 nm/70 nm) were patterned together.

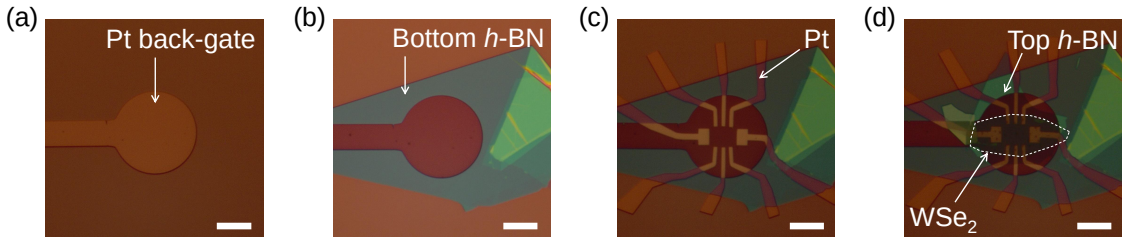

Figure B.8: Optical micrographs of the fabrication process flow for LD123, a Pt/*h*-BN back-gated, Au/*h*-BN top-gated WSe_2 Hall bar sample. (a) Pt back-gate electrode on an SiO_2/Si substrate. (b) Bottom *h*-BN transferred onto the Pt back-gate. (c) Pt electrodes on bottom *h*-BN. (d) Finished device before patterning the top-gate electrode and metal extensions. The WSe_2 flake is outlined by a white dashed line. The scale bars are 10 μm.

which serves as the back-gate electrode, as shown in Fig. B.9(a). A suitable bottom *h*-BN flake was identified [Fig. B.9(b)], and transferred onto the graphite flake, as shown in Fig. B.9(c). It was ensured that there were exposed regions of the graphite in order to make an electrical contact to the back-gate. Platinum bottom-electrodes and metal extensions were then patterned on the bottom *h*-BN substrate, as shown in Fig. B.9(d).

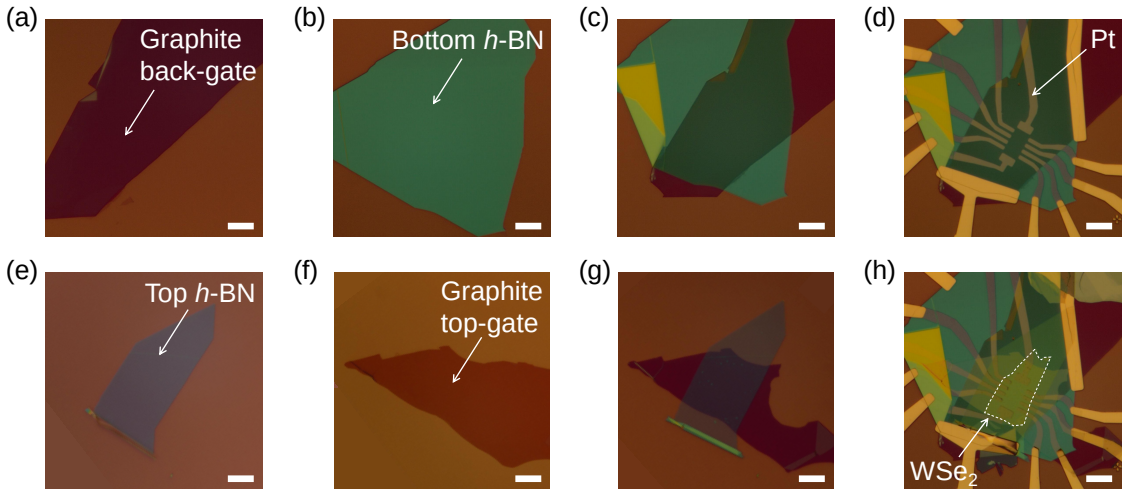

Figure B.9: Optical micrographs of the fabrication process flow for LD163, a graphite/*h*-BN back- and top-gated WSe_2 Hall bar sample. (a) Back-gate graphite flake on an SiO_2/Si substrate. (b) Bottom *h*-BN flake. (c) Bottom *h*-BN transferred onto the graphite back-gate. (d) Pt bottom-electrodes and metal extensions patterned on the *h*-BN/graphite. (e) Top *h*-BN flake. (f) Top-gate graphite flake. (g) Top-gate graphite transferred onto the top *h*-BN. (h) Finished device before connecting the top-gate graphite to its metal extension. The WSe_2 flake is outlined by a white dashed line. The scale bars are 10 μm.

On separate substrates, top *h*-BN and top-gate graphite flakes were identified, as shown in Figs. B.9(e) and B.9(f), respectively. The top-gate graphite was transferred onto the top *h*-BN, as shown in Fig. B.9(g).[3] The graphite/*h*-BN stack was then used to "pick-up" a suitable WSe_2 flake, and the entire stack was transferred onto the Pt bottom-contacts, as shown in Fig. B.9(e). Finally, the top-gate was connected to its metal extension. In situations where the top-gate graphite made contact with the Pt electrodes, the metal extensions, or the back-gate graphite, the affected regions were etched in an O_2 plasma (100 W, 18 sccm, 200 mTorr) using PMMA as the etch mask. The typical graphite etch rate was $\simeq$ 10 nm/min.

Apart from the aforementioned types of WSe_2 samples, LD201 and LD205 used WSe_2 flakes which were etched prior to device fabrication. The remainder of the fabrication process was unchanged. The WSe_2 was etched using the same chemistry used to etch *h*-BN, i.e., a CF_4 + O_2 plasma. A 5 s plasma was sufficient to etch up to four-layers of WSe_2.

[3]The "pick and place" technique of Section B.2 also works for graphite flakes.

Appendix C

Out-of-Plane Effective Dielectric Constant of *h*-BN

The out-of-plane effective dielectric constant of *h*-BN ($\kappa^{||}_{h\text{-BN}}$) was determined from the top-gate capacitance (C_{TG}) values obtained from gate-dependent SdH oscillations measurements, and/or Hall measurements in the WSe_2 Hall bar samples. The measured C_{TG} can be written as

$$C_{\text{TG}}^{-1} = \frac{t_{h\text{-BN}}}{\epsilon_0 \kappa^{||}_{h\text{-BN}}} + C_{\text{Q}}^{-1} + C_{\text{int}}^{-1} \tag{C.1}$$

where the first term is the geometric capacitance of the *h*-BN top-gate dielectric of thickness $t_{h\text{-BN}}$, C_{Q} is the quantum capacitance of WSe_2, and C_{int} is the interface capacitance due to the vdW gap between the WSe_2 and *h*-BN [60]. Therefore, the slope of C_{TG}^{-1} vs $t_{h\text{-BN}}$ can be used to extract $\kappa^{||}_{h\text{-BN}}$. Figure C.1 shows C_{TG}^{-1} vs $t_{h\text{-BN}}$ for various monolayer, bilayer, and trilayer WSe_2 samples. A linear fit to Fig. C.1 data yields $\kappa^{||}_{h\text{-BN}} = 3.0$.

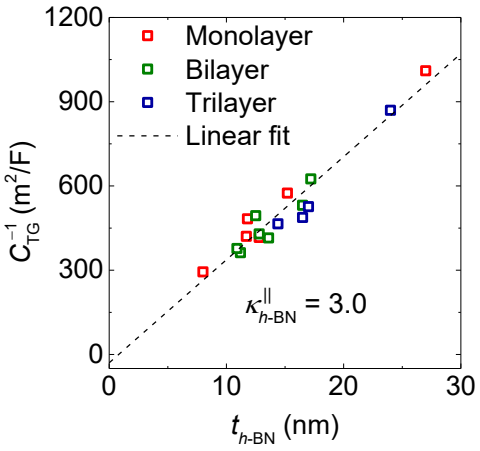

Figure C.1: C_{TG}^{-1} vs $t_{h\text{-BN}}$ for various monolayer, bilayer, and trilayer WSe_2 samples. The C_{TG} values were obtained from gate-dependent SdH oscillations measurements, and/or Hall measurements. A linear fit to the data yields $\kappa^{||}_{h\text{-BN}} = 3.0$.

Appendix D

List of Symbols

a	In-plane lattice constant of a TMD
a_{B}	Bohr radius
a^*_{B}	Effective Bohr radius
A	Cross sectional area of a Hall bar sample
$\hat{\mathbf{A}}, \boldsymbol{A}$	Magnetic vector potential
α	Valley Berry phase contribution to the valley g-factor in a TMD
B	Magnetic field
$\mathbf{B}$	Magnetic field vector
$B_{\|\|}$	Parallel component of the magnetic field
$B_{\perp}$	Perpendicular component of the magnetic field
B_{p}	Magnetic field at full spin-polarization
$\vec{B}_{\mathrm{SO}}$	Effective magnetic field due to spin–orbit interaction
c	Speed of light
C_{BG}	Back-gate capacitance
C_{int}	Interface capacitance due to the vdW gap between WSe_2 and h-BN
C_{Q}	Quantum capacitance of WSe_2
C_{TG}	Top-gate capacitance
d	Transverse distance between the W atoms of two adjacent WSe_2 layers
D_{LL}	Landau level degeneracy
D_s	Spin-degeneracy
D_v	Valley-degeneracy
$D(E)$	2D density of states
$D_{\mathrm{p}}(E)$	2D density of states at full spin-polarization

Δ	Measure of the monolayer TMD energy gap
Δ_{SO}	Spin–orbit interaction in WSe_2
Δ_V	Upper valence band energy of a monolayer TMD
Δg^*	Effective g-factor increment between consecutive QHS sequence transitions
ΔR_{xx}	Oscillatory part of the longitudinal resistance
ΔV	Voltage difference between voltage probes in a four-point measurement
e	Electron charge
E	Transverse electric field
$E_{\pm}$	Conduction (+) and valence (−) band energies of a monolayer TMD
E_c	Cyclotron energy
E_{cb}	Conduction band edge
E_{F}	Fermi level
E_g	Electronic bandgap
E_Γ	Energy of the valence band maximum at the Γ point in WSe_2
E_Γ^0	Energy of the valence band maximum at Γ at zero transverse electric field in trilayer WSe_2
E_K	Energy of the valence band maxima at K and K' in WSe_2
$E_{n_{\mathrm{LL}}}$	Landau level energies
$E_{n_{\mathrm{LL}},\pm}$	Conduction (+) and valence (−) band Landau levels of a monolayer TMD
$E_{n_{\mathrm{LL}},V}$	Upper valence band Landau levels without Zeeman splitting in a monolayer TMD
$E^{\tau s}_{n_{\mathrm{LL}},V}$	Upper valence band Landau levels with Zeeman splitting in a monolayer TMD
E_{vb}	Valence band edge
E_{Z}	Zeeman energy
E_{Z}^0	Zeeman energy at the highest probed density in monolayer and bilayer WSe_2
$E_{\mathrm{Z},v}$	Valley Zeeman contribution in a monolayer TMD
ϵ	Dielectric constant
ϵ_0	Vacuum permittivity
$\vec{\epsilon}_c$	Crystal electric field

$\mathcal{E}$	Eigenenergy
$\mathcal{E}_\mathrm{C}$	Average Coulomb energy per electron
$\mathcal{E}_\mathrm{F}$	Fermi energy
η	Proportionality constant in the temperature-dependent power-law for phonon limited mobility
f, f'	Characteristic SdH oscillations' peaks and/or their frequencies
F_e	Electrostatic force
$\mathbf{F}_\mathrm{L}$	Lorentz force vector
ϕ	Wavefunction component
ϕ_X	Workfunction of material X
Φ_SB	Schottky barrier height
g	Landé g-factor
g^*	Effective g-factor
g_0^*	Effective hole g-factor in WSe_2 at the highest density probed
g_b	Band g-factor
g_d	d-orbital contribution to the valley g-factor
g_s	Spin g-factor
g_v	Valley g-factor
G	Channel conductance
$G_\square$	Channel conductivity
G_2pt	Two-point conductance
G_4pt	Four-point conductance
G_c	Metal–insulator transition crossover conductivity
γ	Exponent in the temperature-dependent power-law for phonon limited mobility
Γ	Brillouin zone center
Γ_D	Impurity-scattering induced level broadening
h	Planck constant
$\hbar$	Reduced Planck constant
$\hat{H}$	Electron Hamiltonian

$\mathcal{H}$	Hamiltonian for a monolayer TMD
I	Current through the sample
I_{D}	Drain current
$\mathbf{k}$	Wavevector
k_{B}	Boltzmann constant
k_{F}	Fermi wavevector
k_y	Wavevector of a plane wave of y
K, K'	Hexagonal Brillouin zone corners
κ	Effective dielectric constant
κ_r^*	Effective out-of-plane dielectric constant of WSe_2 from DFT calculations
$\kappa_{\mathrm{X}}^{\perp}$	In-plane effective dielectric constant of material X
$\kappa_{\mathrm{X}}^{\parallel}$	Out-of-plane effective dielectric constant of material X
χ	Spin susceptibility
χ_0	Pauli susceptibility
$\chi_{\mathrm{WSe_2}}$	Electron affinity of WSe_2
l_B	Magnetic length
l_z	z-component of the angular momentum
L	Channel length or sample length
L_x, L_y	Sample dimensions in the x- and y-directions, respectively
λ	Measure of spin-splitting in a monolayer TMD
m^*	Effective mass
m_e^*	Electron effective mass
m_{Γ}^*	Hole effective mass at Γ in trilayer WSe_2 from DFT calculations
m_h^*	Hole effective mass
m_K^*	Hole effective mass at K in trilayer WSe_2 from DFT calculations
$m_{K,\mathrm{SdH}}^*$	Hole effective mass at K in trilayer WSe_2 measured from SdH oscillations
m_b	Band effective mass
m_e	Free electron mass
m_K	Hole effective mass at K in trilayer WSe_2

μ	Carrier mobility
$\mu_{2\text{pt}}$	Two-point field-effect mobility
$\mu_{4\text{pt}}$	Four-point field-effect mobility
μ_{B}	Bohr magneton
μ_c	Mobility at metal–insulator transition crossover
μ_{FE}	Field-effect mobility
μ_{Hall}	Hall mobility
μ_{imp}	Impurity scattering limited mobility
μ_{ph}	Phonon scattering limited mobility
μ_q	Quantum mobility
n	Areal density of electrons
n_{DOS}	Density of states in a Landau level
n_{LL}	Landau level index
N	Particle density per unit volume
$N_{\square}$	Number of squares in a sample
ν	Filling factor
p	Areal density of holes
$\hat{\mathbf{p}}, \boldsymbol{p}$	Canonical momentum operator
$p_{\uparrow}$	Density of spin-↑ holes
$p_{\downarrow}$	Density of spin-↓ holes
p_c	Metal–insulator transition crossover density
p_K	Occupation fraction of holes in the K valley in trilayer WSe_2
$\mathbf{r}$	Electron position
$\langle \mathbf{r} \rangle$	Average distance between electrons
r_s	Interaction parameter
R_0	Zero-field resistance of SdH oscillations' oscillatory component
$R_{4\text{pt}}$	Four-point resistance
R_{c}	Specific contact resistance
R_{xx}	Longitudinal resistance

R_{xy}	Transverse or Hall resistance
$R_{xy,B\pm}$	Hall resistance in positive (+) or negative (−) magnetic field
s	Monolayer TMD bandstructure spin index; spin-↑ ($s = +1$) or spin-↓ ($s = -1$)
$\boldsymbol{\sigma}$	Pauli matrices
ψ	Wavefunction
t	Sample thickness
t_Γ	Hopping integral between adjacent WSe_2 layers' Γ states
t_h	Effective in-plane hopping integral for a monolayer TMD
$t_{h\text{-BN}}$	Thickness of top-gate h-BN dielectric
t_K	Hopping integral between adjacent WSe_2 layers' K states
T	Temperature
T_{BG}	Bloch–Grüneisen temperature
T_c	Critical temperature at the transition between phonon scattering limited and impurity scattering limited mobility regimes
T_{D}	Dingle temperature
T_{F}	Fermi temperature
τ	Monolayer TMD bandstructure valley index; K ($\tau = +1$) and K' ($\tau = -1$)
τ_q	Quantum scattering lifetime
$\mathbf{v}$	Electron or hole velocity vector
v_d	Drift velocity
v_{F}	Fermi velocity
v_{ph}	Phonon velocity in WSe_2
V_{BG}	Back-gate bias
V_c	Top-gate voltage at the metal–insulator transition crossover
V_{D}	Drain bias
V_{g}	Gate voltage
V_{H}	Hall voltage
V_{S}	Source bias
V_{T}	Threshold voltage

V_{TG}	Top-gate bias
V_{xx}	Longitudinal voltage drop in a Hall bar sample
W	Channel width or sample width
ω_c	Cyclotron frequency
x	Cartesian x-coordinate or direction
x_0	Guiding center
ξ	Thermal damping factor coefficient of SdH oscillations
y	Cartesian y-coordinate or direction
z	Cartesian z-coordinate or direction

Appendix E

List of Acronyms

2D	Two-Dimensional
2DES	Two-Dimensional Electron System
3D	Three-Dimensional
AFM	Atomic Force Microscopy
ARPES	Angle-Resolved Photoemission Spectroscopy
BEC	Bose–Einstein Condensate
BiSFET	Bilayer PseudoSpin Field-Effect Transistor
BG	Back-Gate
DFT	Density Functional Theory
DOS	Density Of States
EBL	Electron-Beam Lithography
EBME	Electron-Beam Metal Evaporation
FET	Field-Effect Transistor
FF	Filling Factor
FT	Fourier Transform
***h*-BN**	Hexagonal Boron Nitride
IPA	Isopropanol
LL	Landau Level
MBE	Molecular Beam Epitaxy
MIBK	Methyl Isobutyl Ketone
MIT	Metal–Insulator Transition
MOSFET	Metal-Oxide-Semiconductor Field-Effect Transistor
NDR	Negative Differential Resistance

PDMS	Polydimethylsiloxane
PL	Photoluminescence
PMMA	Poly(methyl methacrylate)
PPC	Poly(propylene carbonate)
PPMS	Physical Properties Measurement System
QHE	Quantum Hall Effect
QHS	Quantum Hall States
QMC	Quantum Monte Carlo
RT	Room Temperature
SdH	Shubnikov–de Haas
SOC	Spin–Orbit Coupling
SS	Subthreshold Swing
STS	Scanning Tunneling Spectroscopy
TG	Top-Gate
TMD	Transition Metal Dichalcogenide
vdW	van der Waals

Bibliography

[1] K. v. Klitzing, G. Dorda, and M. Pepper, "New Method for High-Accuracy Determination of the Fine-Structure Constant Based on Quantized Hall Resistance," *Phys. Rev. Lett.*, vol. 45, no. 6, p. 494, 1980.

[2] E. Wigner, "On the Interaction of Electrons in Metals," *Phys. Rev.*, vol. 46, no. 11, p. 1002, 1934.

[3] S. D. Sarma and A. Pinczuk, *Perspectives in Quantum Hall Effects: Novel Quantum Liquids in Low-Dimensional Semiconductor Structures*. John Wiley & Sons, 2008.

[4] S. D. Sarma, S. Adam, E. H. Hwang, and E. Rossi, "Electronic Transport in Two-Dimensional Graphene," *Rev. Mod. Phys.*, vol. 83, no. 2, p. 407, 2011.

[5] M. Z. Hasan and C. L. Kane, "*Colloquium*: Topological Insulators," *Rev. Mod. Phys.*, vol. 82, no. 4, p. 3045, 2010.

[6] H. Y. Hwang, Y. Iwasa, M. Kawasaki, B. Keimer, N. Nagaosa, and Y. Tokura, "Emergent Phenomena at Oxide Interfaces," *Nat. Mater.*, vol. 11, no. 2, p. 103, 2012.

[7] K. S. Novoselov, A. K. Geim, S. V. Morozov, D. Jiang, Y. Zhang, S. V. Dubonos, I. V. Grigorieva, and A. A. Firsov, "Electric Field Effect in Atomically Thin Carbon Films," *Science*, vol. 306, no. 5696, p. 666, 2004.

[8] Q. H. Wang, K. Kalantar-Zadeh, A. Kis, J. N. Coleman, and M. S. Strano, "Electronics and Optoelectronics of Two-Dimensional Transition Metal Dichalcogenides," *Nat. Nanotechnol.*, vol. 7, no. 11, p. 699, 2012.

[9] F. Xia, H. Wang, and Y. Jia, "Rediscovering Black Phosphorus as an Anisotropic Layered Material for Optoelectronics and Electronics," *Nat. Commun.*, vol. 5, p. 4458, 2014.

[10] D. A. Bandurin, A. V. Tyurnina, L. Y. Geliang, A. Mishchenko, V. Zólyomi, S. V. Morozov, R. K. Kumar, R. V. Gorbachev, Z. R. Kudrynskyi, S. Pezzini *et al.*, "High Electron Mobility, Quantum Hall Effect and Anomalous Optical Response in Atomically Thin InSe," *Nat. Nanotechnol.*, vol. 12, no. 3, p. 223, 2017.

[11] L. D. Landau, "The Theory of a Fermi Liquid," *J. Exp. Theor. Phys.*, vol. 3, no. 6, p. 920, 1957.

[12] D. C. Tsui, H. L. Stormer, and A. C. Gossard, "Two-Dimensional Magnetotransport in the Extreme Quantum Limit," *Phys. Rev. Lett.*, vol. 48, no. 22, p. 1559, 1982.

[13] E. Y. Andrei, G. Deville, D. C. Glattli, F. I. B. Williams, E. Paris, and B. Etienne, "Observation of a Magnetically Induced Wigner Solid," *Phys. Rev. Lett.*, vol. 60, no. 26, p. 2765, 1988.

[14] R. L. Willett, H. L. Stormer, D. C. Tsui, L. N. Pfeiffer, K. W. West, and K. W. Baldwin, "Termination of the Series of Fractional Quantum Hall states at Small Filling Factors," *Phys. Rev. B*, vol. 38, no. 11, p. 7881, 1988.

[15] H. W. Jiang, R. L. Willett, H. L. Stormer, D. C. Tsui, L. N. Pfeiffer, and K. W. West, "Quantum Liquid versus Electron Solid Around ν= 1/5 Landau-Level Filling," *Phys. Rev. Lett.*, vol. 65, no. 5, p. 633, 1990.

[16] T. Ando, A. B. Fowler, and F. Stern, "Electronic Properties of Two-Dimensional Systems," *Rev. Mod. Phys.*, vol. 54, no. 2, p. 437, 1982.

[17] B. Tanatar and D. M. Ceperley, "Ground State of the Two-Dimensional Electron Gas," *Phys. Rev. B*, vol. 39, no. 8, p. 5005, 1989.

[18] M. Shayegan, E. P. De Poortere, O. Gunawan, Y. P. Shkolnikov, E. Tutuc, and K. Vakili, "Two-Dimensional Electrons Occupying Multiple Valleys in AlAs," *Phys. Status Solidi B*, vol. 243, no. 14, p. 3629, 2006.

[19] E. Abrahams, P. W. Anderson, D. C. Licciardello, and T. V. Ramakrishnan, "Scaling Theory of Localization: Absence of Quantum Diffusion in Two Dimensions," *Phys. Rev. Lett.*, vol. 42, no. 10, p. 673, 1979.

[20] S. V. Kravchenko and M. P. Sarachik, "Metal–Insulator Transition in Two-Dimensional Electron Systems," *Rep. Prog. Phys.*, vol. 67, no. 1, p. 1, 2003.

[21] C. Attaccalite, S. Moroni, P. Gori-Giorgi, and G. B. Bachelet, "Correlation Energy and Spin Polarization in the 2D Electron Gas," *Phys. Rev. Lett.*, vol. 88, no. 25, p. 256601, 2002.

[22] J. Yoon, C. C. Li, D. Shahar, D. C. Tsui, and M. Shayegan, "Wigner Crystallization and Metal-Insulator Transition of Two-Dimensional Holes in GaAs at $B = 0$," *Phys. Rev. Lett.*, vol. 82, no. 8, p. 1744, 1999.

[23] A. P. Mills Jr, A. P. Ramirez, L. N. Pfeiffer, and K. W. West, "Nonmonotonic Temperature-Dependent Resistance in Low Density 2D Hole Gases," *Phys. Rev. Lett.*, vol. 83, no. 14, p. 2805, 1999.

[24] E. Abrahams, S. V. Kravchenko, and M. P. Sarachik, "Metallic Behavior and Related Phenomena in Two Dimensions," *Rev. Mod. Phys.*, vol. 73, no. 2, p. 251, 2001.

[25] R. G. Dickinson and L. Pauling, "The Crystal Structure of Molybdenite," *J. Am. Chem. Soc.*, vol. 45, no. 6, p. 1466, 1923.

[26] R. Fivaz and E. Mooser, "Mobility of Charge Carriers in Semiconducting Layer Structures," *Phys. Rev.*, vol. 163, no. 3, p. 743, 1967.

[27] J. A. Wilson and A. D. Yoffe, "The Transition Metal Dichalcogenides Discussion and Interpretation of the Observed Optical, Electrical and Structural Properties," *Adv. Phys.*, vol. 18, no. 73, p. 193, 1969.

[28] K. F. Mak, C. Lee, J. Hone, J. Shan, and T. F. Heinz, "Atomically Thin MoS_2: a New Direct-Gap Semiconductor," *Phys. Rev. Lett.*, vol. 105, no. 13, p. 136805, 2010.

[29] A. K. Geim and I. V. Grigorieva, "Van der Waals Heterostructures," *Nature*, vol. 499, no. 7459, p. 419, 2013.

[30] K.-K. Kam, C.-L. Chang, and D. Lynch, "Fundamental Absorption Edges and Indirect Band Gaps in $W_{1-x}Mo_xSe_2$ ($0 \leq x \leq 1$)," *J. Phys. C: Solid State Phys.*, vol. 17, no. 22, p. 4031, 1984.

[31] D. Voß, P. Krüger, A. Mazur, and J. Pollmann, "Atomic and Electronic Structure of WSe_2 from *Ab Initio* Theory: Bulk Crystal and Thin Film Systems," *Phys. Rev. B*, vol. 60, no. 20, p. 14311, 1999.

[32] Z. Y. Zhu, Y. C. Cheng, and U. Schwingenschlögl, "Giant Spin-Orbit-Induced Spin Splitting in Two-Dimensional Transition-Metal Dichalcogenide Semiconductors," *Phys. Rev. B*, vol. 84, no. 15, p. 153402, 2011.

[33] D. Xiao, G.-B. Liu, W. Feng, X. Xu, and W. Yao, "Coupled Spin and Valley Physics in Monolayers of MoS_2 and Other Group-VI Dichalcogenides," *Phys. Rev. Lett.*, vol. 108, no. 19, p. 196802, 2012.

[34] A. Ramasubramaniam, "Large Excitonic Effects in Monolayers of Molybdenum and Tungsten Dichalcogenides," *Phys. Rev. B*, vol. 86, no. 11, p. 115409, 2012.

[35] W. Zhao, R. M. Ribeiro, M. Toh, A. Carvalho, C. Kloc, A. H. Castro Neto, and G. Eda, "Origin of Indirect Optical Transitions in Few-Layer MoS_2, WS_2, and WSe_2," *Nano Lett.*, vol. 13, no. 11, p. 5627, 2013.

[36] J. Chang, L. F. Register, and S. K. Banerjee, "Ballistic Performance Comparison of Monolayer Transition Metal Dichalcogenide MX_2 (M= Mo, W; X= S, Se, Te) Metal-Oxide-Semiconductor Field Effect Transistors," *J. Appl. Phys.*, vol. 115, no. 8, p. 084506, 2014.

[37] C. R. Dean, A. F. Young, I. Meric, C. Lee, L. Wang, S. Sorgenfrei, K. Watanabe, T. Taniguchi, P. Kim, K. L. Shepard *et al.*, "Boron Nitride Substrates for High-Quality Graphene Electronics," *Nat. Nanotechnol.*, vol. 5, no. 10, p. 722, 2010.

[38] R. Geick, C. H. Perry, and G. Rupprecht, "Normal Modes in Hexagonal Boron Nitride," *Phys. Rev.*, vol. 146, no. 2, p. 543, 1966.

[39] G. Cassabois, P. Valvin, and B. Gil, "Hexagonal Boron Nitride is an Indirect Bandgap Semiconductor," *Nat. Photonics*, vol. 10, no. 4, p. 262, 2016.

[40] L. Britnell, R. V. Gorbachev, R. Jalil, B. D. Belle, F. Schedin, M. I. Katsnelson, L. Eaves, S. V. Morozov, A. S. Mayorov, N. M. R. Peres *et al.*, "Electron Tunneling Through Ultrathin Boron Nitride Crystalline Barriers," *Nano Lett.*, vol. 12, no. 3, p. 1707, 2012.

[41] G. Moore, "Cramming More Components onto Integrated Circuits," *Electronics*, vol. 38, no. 8, p. 114, 1965.

[42] R. H. Dennard, F. H. Gaensslen, V. L. Rideout, E. Bassous, and A. R. LeBlanc, "Design of Ion-Implanted MOSFET's with Very Small Physical Dimensions," *IEEE J. Solid-State Circuits*, vol. 9, no. 5, p. 256, 1974.

[43] M. T. Bohr and I. A. Young, "CMOS Scaling Trends and Beyond," *IEEE Micro*, vol. 37, no. 6, p. 20, 2017.

[44] T. N. Theis and H.-S. P. Wong, "The End of Moore's Law: A New Beginning for Information Technology," *Comput. Sci. Eng.*, vol. 19, no. 2, p. 41, 2017.

[45] G. Fiori, F. Bonaccorso, G. Iannaccone, T. Palacios, D. Neumaier, A. Seabaugh, S. K. Banerjee, and L. Colombo, "Electronics Based on Two-Dimensional Materials," *Nat. Nanotechnol.*, vol. 9, no. 10, p. 768, 2014.

[46] H. C. P. Movva, A. Rai, S. Kang, K. Kim, B. Fallahazad, T. Taniguchi, K. Watanabe, E. Tutuc, and S. K. Banerjee, "High-Mobility Holes in Dual-Gated WSe_2 Field-Effect Transistors," *ACS Nano*, vol. 9, no. 10, p. 10402, 2015.

[47] V. Podzorov, M. E. Gershenson, C. Kloc, R. Zeis, and E. Bucher, "High-Mobility Field-Effect Transistors Based on Transition Metal Dichalcogenides," *Appl. Phys. Lett.*, vol. 84, no. 17, p. 3301, 2004.

[48] K. S. Novoselov, D. Jiang, F. Schedin, T. J. Booth, V. V. Khotkevich, S. V. Morozov, and A. K. Geim, "Two-Dimensional Atomic Crystals," *Proc. Natl. Acad. Sci. U.S.A.*, vol. 102, no. 30, p. 10451, 2005.

[49] A. Ayari, E. Cobas, O. Ogundadegbe, and M. S. Fuhrer, "Realization and Electrical Characterization of Ultrathin Crystals of Layered Transition-Metal Dichalcogenides," *J. Appl. Phys.*, vol. 101, no. 1, p. 014507, 2007.

[50] A. Allain, J. Kang, K. Banerjee, and A. Kis, "Electrical Contacts to Two-Dimensional Semiconductors," *Nat. Mater.*, vol. 14, no. 12, p. 1195, 2015.

[51] Y. Xu, C. Cheng, S. Du, J. Yang, B. Yu, J. Luo, W. Yin, E. Li, S. Dong, P. Ye *et al.*, "Contacts Between Two-and Three-Dimensional Materials: Ohmic, Schottky, and $p-n$ Heterojunctions," *ACS Nano*, vol. 10, no. 5, p. 4895, 2016.

[52] B. Radisavljevic, A. Radenovic, J. Brivio, V. Giacometti, and A. Kis, "Single-Layer MoS_2 Transistors," *Nat. Nanotechnol.*, vol. 6, no. 3, p. 147, 2011.

[53] S. Das, H.-Y. Chen, A. V. Penumatcha, and J. Appenzeller, "High Performance Multilayer MoS_2 Transistors with Scandium Contacts," *Nano Lett.*, vol. 13, no. 1, p. 100, 2012.

[54] J. Bardeen, "Surface States and Rectification at a Metal Semi-Conductor Contact," *Phys. Rev.*, vol. 71, no. 10, p. 717, 1947.

[55] S. M. Sze and K. K. Ng, *Physics of Semiconductor Devices*. John Wiley & Sons, 2006.

[56] Y. Guo, D. Liu, and J. Robertson, "Chalcogen Vacancies in Monolayer Transition Metal Dichalcogenides and Fermi Level Pinning at Contacts," *Appl. Phys. Lett.*, vol. 106, no. 17, p. 173106, 2015.

[57] S. Das and J. Appenzeller, "WSe_2 Field Effect Transistors with Enhanced Ambipolar Characteristics," *Appl. Phys. Lett.*, vol. 103, no. 10, p. 103501, 2013.

[58] D. Liu, Y. Guo, L. Fang, and J. Robertson, "Sulfur Vacancies in Monolayer MoS_2 and its Electrical Contacts," *Appl. Phys. Lett.*, vol. 103, no. 18, p. 183113, 2013.

[59] A. Prakash, H. Ilatikhameneh, P. Wu, and J. Appenzeller, "Understanding Contact Gating in Schottky Barrier Transistors From 2D Channels," *Sci. Rep.*, vol. 7, no. 1, p. 12596, 2017.

[60] K. Kim, S. Larentis, B. Fallahazad, K. Lee, J. Xue, D. C. Dillen, C. M. Corbet, and E. Tutuc, "Band Alignment in WSe_2–Graphene Heterostructures," *ACS Nano*, vol. 9, no. 4, p. 4527, 2015.

[61] H. Fang, S. Chuang, T. C. Chang, K. Takei, T. Takahashi, and A. Javey, "High-Performance Single Layered WSe_2 p-FETs with Chemically Doped Contacts," *Nano Lett.*, vol. 12, no. 7, p. 3788, 2012.

[62] G. N. Derry, M. E. Kern, and E. H. Worth, "Recommended Values of Clean Metal Surface Work Functions," *J. Vac. Sci. Technol., A*, vol. 33, no. 6, p. 060801, 2015.

[63] Y. Liu, J. Guo, E. Zhu, L. Liao, S.-J. Lee, M. Ding, I. Shakir, V. Gambin, Y. Huang, and X. Duan, "Approaching the Schottky–Mott Limit in van der Waals Metal–Semiconductor Junctions," *Nature*, vol. 557, no. 7707, p. 696, 2018.

[64] C. Zhang, Y. Chen, A. Johnson, M.-Y. Li, L.-J. Li, P. C. Mende, R. M. Feenstra, and C.-K. Shih, "Probing Critical Point Energies of Transition Metal Dichalcogenides: Surprising Indirect Gap of Single Layer WSe_2," *Nano Lett.*, vol. 15, no. 10, p. 6494, 2015.

[65] M. Yankowitz, D. McKenzie, and B. J. LeRoy, "Local Spectroscopic Characterization of Spin and Layer Polarization in WSe_2," *Phys. Rev. Lett.*, vol. 115, no. 13, p. 136803, 2015.

[66] A. Allain and A. Kis, "Electron and Hole Mobilities in Single-Layer WSe_2," *ACS Nano*, vol. 8, no. 7, p. 7180, 2014.

[67] H.-J. Chuang, X. Tan, N. J. Ghimire, M. M. Perera, B. Chamlagain, M. M.-C. Cheng, J. Yan, D. Mandrus, D. Tománek, and Z. Zhou, "High Mobility WSe_2 p- and n-Type Field-Effect Transistors Contacted by Highly Doped Graphene for Low-Resistance Contacts," *Nano Lett.*, vol. 14, no. 6, p. 3594, 2014.

[68] J. I.-J. Wang, Y. Yang, Y.-A. Chen, K. Watanabe, T. Taniguchi, H. O. H. Churchill, and P. Jarillo-Herrero, "Electronic Transport of Encapsulated Graphene and WSe_2

Devices Fabricated by Pick-Up of Prepatterned hBN," *Nano Lett.*, vol. 15, no. 3, p. 1898, 2015.

[69] H.-J. Chuang, B. Chamlagain, M. Koehler, M. M. Perera, J. Yan, D. Mandrus, D. Tománek, and Z. Zhou, "Low-Resistance 2D/2D Ohmic Contacts: A Universal Approach to High-Performance WSe_2, MoS_2, and $MoSe_2$ Transistors," *Nano Lett.*, vol. 16, no. 3, p. 1896, 2016.

[70] J. Guan, H.-J. Chuang, Z. Zhou, and D. Tománek, "Optimizing Charge Injection Across Transition Metal Dichalcogenide Heterojunctions: Theory and Experiment," *ACS Nano*, vol. 11, no. 4, p. 3904, 2017.

[71] Y. Sata, R. Moriya, S. Masubuchi, K. Watanabe, T. Taniguchi, and T. Machida, "N-and p-type Carrier Injections into WSe_2 with van der Waals Contacts of Two-Dimensional Materials," *Jpn. J. Appl. Phys.*, vol. 56, no. 4S, p. 04CK09, 2017.

[72] S. Chuang, C. Battaglia, A. Azcatl, S. McDonnell, J. S. Kang, X. Yin, M. Tosun, R. Kapadia, H. Fang, R. M. Wallace *et al.*, "MoS_2 p-type Transistors and Diodes Enabled by High Work Function MoO_x Contacts," *Nano Lett.*, vol. 14, no. 3, p. 1337, 2014.

[73] M. Yamamoto, S. Nakaharai, K. Ueno, and K. Tsukagoshi, "Self-Limiting Oxides on WSe_2 as Controlled Surface Acceptors and Low-Resistance Hole Contacts," *Nano Lett.*, vol. 16, no. 4, p. 2720, 2016.

[74] S. Xu, Z. Wu, H. Lu, Y. Han, G. Long, X. Chen, T. Han, W. Ye, Y. Wu, J. Lin *et al.*, "Universal Low-Temperature Ohmic Contacts for Quantum Transport in Transition Metal Dichalcogenides," *2D Mater.*, vol. 3, no. 2, p. 021007, 2016.

[75] X. Cui, G.-H. Lee, Y. D. Kim, G. Arefe, P. Y. Huang, C.-H. Lee, D. A. Chenet, X. Zhang, L. Wang, F. Ye *et al.*, "Multi-Terminal Transport Measurements of MoS_2 using a van der Waals Heterostructure Device Platform," *Nat. Nanotechnol.*, vol. 10, no. 6, p. 534, 2015.

[76] M. Salmerón, S. Ferrer, M. Jazzar, and G. A. Somorjai, "Photoelectron-Spectroscopy Study of the Electronic Structure of Au and Ag overlayers on Pt (100), Pt (111), and Pt (997) Surfaces," *Phys. Rev. B*, vol. 28, no. 12, p. 6758, 1983.

[77] G. N. Derry and Z. Ji-Zhong, "Work Function of Pt (111)," *Phys. Rev. B*, vol. 39, no. 3, p. 1940, 1989.

[78] L. Wang, I. Meric, P. Y. Huang, Q. Gao, Y. Gao, H. Tran, T. Taniguchi, K. Watanabe, L. M. Campos, D. A. Muller *et al.*, "One-Dimensional Electrical Contact to a Two-Dimensional Material," *Science*, vol. 342, no. 6158, p. 614, 2013.

[79] K. Kim, M. Yankowitz, B. Fallahazad, S. Kang, H. C. P. Movva, S. Huang, S. Larentis, C. M. Corbet, T. Taniguchi, K. Watanabe *et al.*, "van der Waals Heterostructures with High Accuracy Rotational Alignment," *Nano Lett.*, vol. 16, no. 3, p. 1989, 2016.

[80] Y. Wang, R. X. Yang, R. Quhe, H. Zhong, L. Cong, M. Ye, Z. Ni, Z. Song, J. Yang, J. Shi *et al.*, "Does p-type Ohmic Contact Exist in WSe_2–Metal Interfaces?" *Nanoscale*, vol. 8, no. 2, p. 1179, 2016.

[81] W. Liu, J. Kang, D. Sarkar, Y. Khatami, D. Jena, and K. Banerjee, "Role of Metal Contacts in Designing High-Performance Monolayer n-type WSe_2 Field Effect Transistors," *Nano Lett.*, vol. 13, no. 5, p. 1983, 2013.

[82] B. G. Streetman and S. K. Banerjee, *Solid State Electronic Devices*. Pearson Education, 2016.

[83] X. Li, L. Yang, M. Si, S. Li, M. Huang, P. Ye, and Y. Wu, "Performance Potential and Limit of MoS_2 Transistors," *Adv. Mater.*, vol. 27, no. 9, p. 1547, 2015.

[84] B. Radisavljevic and A. Kis, "Mobility Engineering and a Metal–Insulator Transition in Monolayer MoS_2," *Nat. Mater.*, vol. 12, no. 9, p. 815, 2013.

[85] B. W. H. Baugher, H. O. H. Churchill, Y. Yang, and P. Jarillo-Herrero, "Intrinsic Electronic Transport Properties of High-Quality Monolayer and Bilayer MoS_2," *Nano Lett.*, vol. 13, no. 9, p. 4212, 2013.

[86] S. D. Sarma and E. H. Hwang, "Two-Dimensional Metal-Insulator Transition as a Strong Localization Induced Crossover Phenomenon," *Phys. Rev. B*, vol. 89, no. 23, p. 235423, 2014.

[87] S. D. Sarma, E. H. Hwang, and Q. Li, "Two-Dimensional Metal-Insulator Transition as a Potential Fluctuation Driven Semiclassical Transport Phenomenon," *Phys. Rev. B*, vol. 88, no. 15, p. 155310, 2013.

[88] Z. Jin, X. Li, J. T. Mullen, and K. W. Kim, "Intrinsic Transport Properties of Electrons and Holes in Monolayer Transition-Metal Dichalcogenides," *Phys. Rev. B*, vol. 90, no. 4, p. 045422, 2014.

[89] K. Kaasbjerg, K. S. Thygesen, and K. W. Jacobsen, "Phonon-Limited Mobility in n-type Single-Layer MoS_2 From First Principles," *Phys. Rev. B*, vol. 85, no. 11, p. 115317, 2012.

[90] X. Chen, Z. Wu, S. Xu, L. Wang, R. Huang, Y. Han, W. Ye, W. Xiong, T. Han, G. Long *et al.*, "Probing the Electron States and Metal-Insulator Transition Mechanisms in Molybdenum Disulphide Vertical Heterostructures," *Nat. Commun.*, vol. 6, p. 6088, 2015.

[91] C. J. Adkins, "Threshold Conduction in Inversion Layers," *J. Phys. C: Solid State Phys*, vol. 11, no. 5, p. 851, 1978.

[92] K. Kaasbjerg, K. S. Thygesen, and A.-P. Jauho, "Acoustic Phonon Limited Mobility in Two-Dimensional Semiconductors: Deformation Potential and Piezoelectric Scattering in Monolayer MoS_2 from First Principles," *Phys. Rev. B*, vol. 87, no. 23, p. 235312, 2013.

[93] N. Ma and D. Jena, "Charge Scattering and Mobility in Atomically Thin Semiconductors," *Phys. Rev. X*, vol. 4, no. 1, p. 011043, 2014.

[94] S. Larentis, H. C. P. Movva, B. Fallahazad, K. Kim, A. Behroozi, T. Taniguchi, K. Watanabe, S. K. Banerjee, and E. Tutuc, "Large Effective Mass and Interaction-Enhanced Zeeman Splitting of K-Valley Electrons in $MoSe_2$," *Phys. Rev. B*, vol. 97, no. 20, p. 201407, 2018.

[95] R. Pisoni, A. Kormányos, M. Brooks, Z. Lei, P. Back, M. Eich, H. Overweg, Y. Lee, P. Rickhaus, K. Watanabe *et al.*, "Interactions and Magnetotransport Through Spin-Valley Coupled Landau Levels in Monolayer MoS_2," *arXiv preprint arXiv:1806.06402*, 2018. [Online]. Available: https://arxiv.org/abs/1806.06402

[96] B. Fallahazad, H. C. P. Movva, K. Kim, S. Larentis, T. Taniguchi, K. Watanabe, S. K. Banerjee, and E. Tutuc, "Shubnikov–de Haas Oscillations of High-Mobility Holes in Monolayer and Bilayer WSe_2: Landau Level Degeneracy, Effective Mass, and Negative Compressibility," *Phys. Rev. Lett.*, vol. 116, no. 8, p. 086601, 2016.

[97] A. B. Fowler, F. F. Fang, W. E. Howard, and P. J. Stiles, "Magneto-Oscillatory Conductance in Silicon Surfaces," *Phys. Rev. Lett.*, vol. 16, no. 20, p. 901, 1966.

[98] F. F. Fang and P. J. Stiles, "Effects of a Tilted Magnetic Field on a Two-Dimensional Electron Gas," *Phys. Rev.*, vol. 174, no. 3, p. 823, 1968.

[99] Y. Zhang, Y.-W. Tan, H. L. Stormer, and P. Kim, "Experimental Observation of the Quantum Hall Effect and Berry's Phase in Graphene," *Nature*, vol. 438, no. 7065, p. 201, 2005.

[100] K. S. Novoselov, A. K. Geim, S. V. Morozov, D. Jiang, M. I. Katsnelson, I. V. Grigorieva, S. V. Dubonos, and A. A. Firsov, "Two-Dimensional Gas of Massless Dirac Fermions in Graphene," *Nature*, vol. 438, no. 7065, p. 197, 2005.

[101] K. S. Novoselov, E. McCann, S. V. Morozov, V. I. Fal'ko, M. I. Katsnelson, U. Zeitler, D. Jiang, F. Schedin, and A. K. Geim, "Unconventional Quantum Hall effect and Berry's Phase of 2π in Bilayer Graphene," *Nat. Phys.*, vol. 2, no. 3, p. 177, 2006.

[102] K. I. Bolotin, F. Ghahari, M. D. Shulman, H. L. Stormer, and P. Kim, "Observation of the Fractional Quantum Hall Effect in Graphene," *Nature*, vol. 462, no. 7270, p. 196, 2009.

[103] E. H. Hall, "On a New Action of the Magnet on Electric Currents," *Am. J. Math.*, vol. 2, no. 3, p. 287, 1879.

[104] L. Shubnikov and W. J. de Haas, "Magnetische Widerstandsvergrösserung in Einkristallen von Wismut bei Tiefen Temperaturen," *Proc. R. Neth. Acad. Arts Sci.*, vol. 33, p. 130, 1930.

[105] C. R. Dean, "A Study of the Fractional Quantum Hall Energy Gap at Half Filling," Ph.D. dissertation, McGill University, 2008.

[106] R. B. Laughlin, "Quantized Hall Conductivity in Two Dimensions," *Phys. Rev. B*, vol. 23, no. 10, p. 5632, 1981.

[107] I. M. Lifschitz and A. M. Kosevich, "Theory of Magnetic Susceptibility in Metals at Low Temperatures," *J. Exp. Theor. Phys.*, vol. 2, p. 636, 1956.

[108] A. Isihara and L. Smrčka, "Density and Magnetic Field Dependences of the Conductivity of Two-Dimensional Electron Systems," *J. Phys. C: Solid State Phys.*, vol. 19, no. 34, p. 6777, 1986.

[109] R. B. Dingle, "Some Magnetic Properties of Metals II. The Influence of Collisions on the Magnetic Behaviour of Large Systems," *Proc. R. Soc. Lond. A*, vol. 211, no. 1107, p. 517, 1952.

[110] E. N. Adams and T. D. Holstein, "Quantum Theory of Transverse Galvano-Magnetic Phenomena," *J. Phys. Chem. Solids*, vol. 10, no. 4, p. 254, 1959.

[111] Y. Katayama, D. C. Tsui, H. C. Manoharan, S. Parihar, and M. Shayegan, "Charge Transfer at Double-Layer to Single-Layer Transition in Double-Quantum-Well Systems," *Phys. Rev. B*, vol. 52, no. 20, p. 14817, 1995.

[112] S. Larentis, J. R. Tolsma, B. Fallahazad, D. C. Dillen, K. Kim, A. H. MacDonald, and E. Tutuc, "Band Offset and Negative Compressibility in Graphene-MoS_2 Heterostructures," *Nano Lett.*, vol. 14, no. 4, p. 2039, 2014.

[113] J. P. Eisenstein, L. N. Pfeiffer, and K. W. West, "Compressibility of the Two-Dimensional Electron Gas: Measurements of the Zero-Field Exchange Energy and Fractional Quantum Hall Gap," *Phys. Rev. B*, vol. 50, no. 3, p. 1760, 1994.

[114] L. Li, C. Richter, S. Paetel, T. Kopp, J. Mannhart, and R. C. Ashoori, "Very Large Capacitance Enhancement in a Two-Dimensional Electron System," *Science*, vol. 332, no. 6031, p. 825, 2011.

[115] J. M. Riley, W. Meevasana, L. Bawden, M. Asakawa, T. Takayama, T. Eknapakul, T. K. Kim, M. Hoesch, S.-K. Mo, H. Takagi *et al.*, "Negative Electronic Compressibility and Tunable Spin Splitting in WSe_2," *Nat. Nanotechnol.*, vol. 10, no. 12, p. 1043, 2015.

[116] X. Li, F. Zhang, and Q. Niu, "Unconventional Quantum Hall Effect and Tunable Spin Hall Effect in Dirac Materials: Application to an Isolated MoS_2 Trilayer," *Phys. Rev. Lett.*, vol. 110, no. 6, p. 066803, 2013.

[117] H. Shi, H. Pan, Y.-W. Zhang, and B. I. Yakobson, "Quasiparticle Band Structures and Optical Properties of Strained Monolayer MoS_2 and WS_2," *Phys. Rev. B*, vol. 87, no. 15, p. 155304, 2013.

[118] A. Kormányos, G. Burkard, M. Gmitra, J. Fabian, V. Zólyomi, N. D. Drummond, and V. Fal'ko, "$\mathbf{k} \cdot \mathbf{p}$ Theory for Two-Dimensional Transition Metal Dichalcogenide Semiconductors," *2D Mater.*, vol. 2, no. 2, p. 022001, 2015.

[119] N. Zibouche, P. Philipsen, T. Heine, and A. Kuc, "Electron Transport in MoWSeS Monolayers in the Presence of an External Electric Field," *Phys. Chem. Chem. Phys.*, vol. 16, no. 23, p. 11251, 2014.

[120] S. Fang, R. K. Defo, S. N. Shirodkar, S. Lieu, G. A. Tritsaris, and E. Kaxiras, "*Ab Initio* Tight-Binding Hamiltonian for Transition Metal Dichalcogenides," *Phys. Rev. B*, vol. 92, no. 20, p. 205108, 2015.

[121] M. V. Gustafsson, M. Yankowitz, C. Forsythe, D. Rhodes, K. Watanabe, T. Taniguchi, J. Hone, X. Zhu, and C. R. Dean, "Ambipolar Landau Levels and Strong Band-Selective Carrier Interactions in Monolayer WSe_2," *Nat. Mater.*, vol. 17, no. 5, p. 411, 2018.

[122] J. L. Smith and P. J. Stiles, "Electron-Electron Interactions Continuously Variable in the Range $2.1 > r_s > 0.9$," *Phys. Rev. Lett.*, vol. 29, no. 2, p. 102, 1972.

[123] Y.-W. Tan, J. Zhu, H. L. Stormer, L. N. Pfeiffer, K. W. Baldwin, and K. W. West, "Measurements of the Density-Dependent Many-Body Electron Mass in Two Dimensional GaAs/AlGaAs Heterostructures," *Phys. Rev. Lett.*, vol. 94, no. 1, p. 016405, 2005.

[124] K. Vakili, Y. P. Shkolnikov, E. Tutuc, E. P. De Poortere, and M. Shayegan, "Spin Susceptibility of Two-Dimensional Electrons in Narrow AlAs Quantum Wells," *Phys. Rev. Lett.*, vol. 92, no. 22, p. 226401, 2004.

[125] P. T. Coleridge, M. Hayne, P. Zawadzki, and A. S. Sachrajda, "Effective Masses in High-Mobility 2D Electron Gas Structures," *Surf. Sci.*, vol. 361, p. 560, 1996.

[126] M. Padmanabhan, T. Gokmen, N. C. Bishop, and M. Shayegan, "Effective Mass Suppression in Dilute, Spin-Polarized Two-Dimensional Electron Systems," *Phys. Rev. Lett.*, vol. 101, no. 2, p. 026402, 2008.

[127] X. Ying, S. R. Parihar, H. C. Manoharan, and M. Shayegan, "Quantitative Determination of Many-Body-Induced Interlayer Charge Transfer in Bilayer Electron Systems via Shubnikov–de Haas Measurements," *Phys. Rev. B*, vol. 52, no. 16, p. R11611, 1995.

[128] Z. Gong, G.-B. Liu, H. Yu, D. Xiao, X. Cui, X. Xu, and W. Yao, "Magnetoelectric Effects and Valley-Controlled Spin Quantum Gates in Transition Metal Dichalcogenide Bilayers," *Nat. Commun.*, vol. 4, p. 2053, 2013.

[129] H. C. P. Movva, B. Fallahazad, K. Kim, S. Larentis, T. Taniguchi, K. Watanabe, S. K. Banerjee, and E. Tutuc, "Density-Dependent Quantum Hall States and Zeeman Splitting in Monolayer and Bilayer WSe_2," *Phys. Rev. Lett.*, vol. 118, no. 24, p. 247701, 2017.

[130] Y. Zhang, Z. Jiang, J. P. Small, M. S. Purewal, Y.-W. Tan, M. Fazlollahi, J. D. Chudow, J. A. Jaszczak, H. L. Stormer, and P. Kim, "Landau-Level Splitting in Graphene in High Magnetic Fields," *Phys. Rev. Lett.*, vol. 96, no. 13, p. 136806, 2006.

[131] B. E. Feldman, J. Martin, and A. Yacoby, "Broken-Symmetry States and Divergent Resistance in Suspended Bilayer Graphene," *Nat. Phys.*, vol. 5, no. 12, p. 889, 2009.

[132] A. F. Young, C. R. Dean, L. Wang, H. Ren, P. Cadden-Zimansky, K. Watanabe, T. Taniguchi, J. Hone, K. L. Shepard, and P. Kim, "Spin and Valley Quantum Hall Ferromagnetism in Graphene," *Nat. Phys.*, vol. 8, no. 7, p. 550, 2012.

[133] Y. Li, J. Ludwig, T. Low, A. Chernikov, X. Cui, G. Arefe, Y. D. Kim, A. M. van der Zande, A. Rigosi, H. M. Hill *et al.*, "Valley Splitting and Polarization by the Zeeman Effect in Monolayer $MoSe_2$," *Phys. Rev. Lett.*, vol. 113, no. 26, p. 266804, 2014.

[134] G. Aivazian, Z. Gong, A. M. Jones, R.-L. Chu, J. Yan, D. G. Mandrus, C. Zhang, D. Cobden, W. Yao, and X. Xu, "Magnetic Control of Valley Pseudospin in Monolayer WSe_2," *Nat. Phys.*, vol. 11, no. 2, p. 148, 2015.

[135] A. Srivastava, M. Sidler, A. V. Allain, D. S. Lembke, A. Kis, and A. Imamoğlu, "Valley Zeeman Effect in Elementary Optical Excitations of Monolayer WSe_2," *Nat. Phys.*, vol. 11, p. 141, 2015.

[136] D. MacNeill, C. Heikes, K. F. Mak, Z. Anderson, A. Kormányos, V. Zólyomi, J. Park, and D. C. Ralph, "Breaking of Valley Degeneracy by Magnetic Field in Monolayer $MoSe_2$," *Phys. Rev. Lett.*, vol. 114, no. 3, p. 037401, 2015.

[137] A. A. Mitioglu, P. Plochocka, Á. Granados del Aguila, P. C. M. Christianen, G. Deligeorgis, S. Anghel, L. Kulyuk, and D. K. Maude, "Optical Investigation of Monolayer and Bulk Tungsten Diselenide (WSe_2) in High Magnetic Fields," *Nano Lett.*, vol. 15, no. 7, p. 4387, 2015.

[138] G. Wang, L. Bouet, M. M. Glazov, T. Amand, E. L. Ivchenko, E. Palleau, X. Marie, and B. Urbaszek, "Magneto-Optics in Transition Metal Diselenide Monolayers," *2D Mater.*, vol. 2, no. 3, p. 034002, 2015.

[139] A. A. Shashkin, S. V. Kravchenko, V. T. Dolgopolov, and T. M. Klapwijk, "Indication of the Ferromagnetic Instability in a Dilute Two-Dimensional Electron System," *Phys. Rev. Lett.*, vol. 87, no. 8, p. 086801, 2001.

[140] J. Zhu, H. L. Stormer, L. N. Pfeiffer, K. W. Baldwin, and K. W. West, "Spin Susceptibility of an Ultra-Low-Density Two-Dimensional Electron System," *Phys. Rev. Lett.*, vol. 90, no. 5, p. 056805, 2003.

[141] G.-B. Liu, W.-Y. Shan, Y. Yao, W. Yao, and D. Xiao, "Three-Band Tight-Binding Model for Monolayers of Group-VIB Transition Metal Dichalcogenides," *Phys. Rev. B*, vol. 88, no. 8, p. 085433, 2013.

[142] A. Kormányos, V. Zólyomi, N. D. Drummond, and G. Burkard, "Spin-Orbit Coupling, Quantum Dots, and Qubits in Monolayer Transition Metal Dichalcogenides," *Phys. Rev. X*, vol. 4, no. 1, p. 011034, 2014.

[143] D. Xiao, W. Yao, and Q. Niu, "Valley-Contrasting Physics in Graphene: Magnetic Moment and Topological Transport," *Phys. Rev. Lett.*, vol. 99, no. 23, p. 236809, 2007.

[144] L. A. Ponomarenko, A. K. Geim, A. A. Zhukov, R. Jalil, S. V. Morozov, K. S. Novoselov, I. Grigorieva, E. H. Hill, V. V. Cheianov, V. I. Fal'ko *et al.*, "Tunable Metal–Insulator Transition in Double-Layer Graphene Heterostructures," *Nat. Phys.*, vol. 7, no. 12, p. 958, 2011.

[145] F. Rose, M. O. Goerbig, and F. Piéchon, "Spin- and Valley-Dependent Magneto-Optical Properties of MoS_2," *Phys. Rev. B*, vol. 88, no. 12, p. 125438, 2013.

[146] L. Li, F. Yang, G. J. Ye, Z. Zhang, Z. Zhu, W. Lou, X. Zhou, L. Li, K. Watanabe, T. Taniguchi *et al.*, "Quantum Hall Effect in Black Phosphorus Two-Dimensional Electron System," *Nat. Nanotechnol.*, vol. 11, no. 7, p. 593, 2016.

[147] S. Xu, J. Shen, G. Long, Z. Wu, Z.-Q. Bao, C.-C. Liu, X. Xiao, T. Han, J. Lin, Y. Wu *et al.*, "Odd-Integer Quantum Hall States and Giant Spin Susceptibility in *p*-Type Few-Layer WSe_2," *Phys. Rev. Lett.*, vol. 118, no. 6, p. 067702, 2017.

[148] T. Okamoto, K. Hosoya, S. Kawaji, and A. Yagi, "Spin Degree of Freedom in a Two-Dimensional Electron Liquid," *Phys. Rev. Lett.*, vol. 82, no. 19, p. 3875, 1999.

[149] E. Tutuc, E. P. De Poortere, S. J. Papadakis, and M. Shayegan, "In-Plane Magnetic Field-Induced Spin Polarization and Transition to Insulating Behavior in Two-Dimensional Hole Systems," *Phys. Rev. Lett.*, vol. 86, no. 13, p. 2858, 2001.

[150] X. Xi, Z. Wang, W. Zhao, J.-H. Park, K. T. Law, H. Berger, L. Forró, J. Shan, and K. F. Mak, "Ising Pairing in Superconducting $NbSe_2$ Atomic Layers," *Nat. Phys.*, vol. 12, no. 2, p. 139, 2016.

[151] J. M. Lu, O. Zheliuk, I. Leermakers, N. F. Q. Yuan, U. Zeitler, K. T. Law, and J. T. Ye, "Evidence for Two-Dimensional Ising Superconductivity in Gated MoS_2," *Science*, vol. 350, no. 6266, p. 1353, 2015.

[152] Y. A. Bychkov and E. I. Rashba, "Oscillatory Effects and the Magnetic Susceptibility of Carriers in Inversion Layers," *J. Phys. C: Solid State Phys.*, vol. 17, no. 33, p. 6039, 1984.

[153] H. Yuan, M. S. Bahramy, K. Morimoto, S. Wu, K. Nomura, B.-J. Yang, H. Shimotani, R. Suzuki, M. Toh, C. Kloc *et al.*, "Zeeman-Type Spin Splitting Controlled by an Electric Field," *Nat. Phys.*, vol. 9, no. 9, p. 563, 2013.

[154] J. Nitta, T. Akazaki, H. Takayanagi, and T. Enoki, "Gate Control of Spin-Orbit Interaction in an Inverted $In_{0.53}Ga_{0.47}As/In_{0.52}Al_{0.48}As$ Heterostructure," *Phys. Rev. Lett.*, vol. 78, no. 7, p. 1335, 1997.

[155] J. P. Lu, J.-B. Yau, S. Shukla, M. Shayegan, L. Wissinger, U. Rössler, and R. Winkler, "Tunable Spin-Splitting and Spin-Resolved Ballistic Transport in GaAs/AlGaAs Two-Dimensional Holes," *Phys. Rev. Lett.*, vol. 81, no. 6, p. 1282, 1998.

[156] R. Winkler, E. Tutuc, S. J. Papadakis, S. Melinte, M. Shayegan, D. Wasserman, and S. A. Lyon, "Anomalous Spin Polarization of GaAs Two-Dimensional Hole Systems," *Phys. Rev. B*, vol. 72, no. 19, p. 195321, 2005.

[157] R. Winkler, *Spin–Orbit Coupling in Two-Dimensional Electron and Hole Systems*. Springer, 2003, vol. 41.

[158] S. Yarlagadda and G. F. Giuliani, "Spin Susceptibility in a Two-Dimensional Electron Gas," *Phys. Rev. B*, vol. 40, no. 8, p. 5432, 1989.

[159] S. De Palo, M. Botti, S. Moroni, and G. Senatore, "Effects of Thickness on the Spin Susceptibility of the Two Dimensional Electron Gas," *Phys. Rev. Lett.*, vol. 94, no. 22, p. 226405, 2005.

[160] Z. Wang, J. Shan, and K. F. Mak, "Valley-and Spin-Polarized Landau Levels in Monolayer WSe_2," *Nat. Nanotechnol.*, vol. 12, no. 2, p. 144, 2017.

[161] Y. Li, A. Chernikov, X. Zhang, A. Rigosi, H. M. Hill, A. M. van der Zande, D. A. Chenet, E.-M. Shih, J. Hone, and T. F. Heinz, "Measurement of the Optical Dielectric Function of Monolayer Transition-Metal Dichalcogenides: MoS_2, $MoSe_2$, WS_2, and WSe_2," *Phys. Rev. B*, vol. 90, no. 20, p. 205422, 2014.

[162] O. Gunawan, Y. P. Shkolnikov, K. Vakili, T. Gokmen, E. P. De Poortere, and M. Shayegan, "Valley Susceptibility of an Interacting Two-Dimensional Electron System," *Phys. Rev. Lett.*, vol. 97, no. 18, p. 186404, 2006.

[163] Y. P. Shkolnikov, K. Vakili, E. P. De Poortere, and M. Shayegan, "Dependence of Spin Susceptibility of a Two-Dimensional Electron System on the Valley Degree of Freedom," *Phys. Rev. Lett.*, vol. 92, no. 24, p. 246804, 2004.

[164] S. D. Sarma, E. Hwang, and Q. Li, "Valley-Dependent Many-Body Effects in Two-Dimensional Semiconductors," *Phys. Rev. B*, vol. 80, no. 12, p. 121303, 2009.

[165] A. Kormányos, P. Rakyta, and G. Burkard, "Landau Levels and Shubnikov–de Haas Oscillations in Monolayer Transition Metal Dichalcogenide Semiconductors," *New J. Phys.*, vol. 17, no. 10, p. 103006, 2015.

[166] D. V. Rybkovskiy, I. C. Gerber, and M. V. Durnev, "Atomically Inspired k· p Approach and Valley Zeeman Effect in Transition Metal Dichalcogenide Monolayers," *Phys. Rev. B*, vol. 95, no. 15, p. 155406, 2017.

[167] H. C. P. Movva, T. Lovorn, B. Fallahazad, S. Larentis, K. Kim, T. Taniguchi, K. Watanabe, S. K. Banerjee, A. H. MacDonald, and E. Tutuc, "Tunable $\Gamma - K$ Valley Populations in Hole-Doped Trilayer WSe_2," *Phys. Rev. Lett.*, vol. 120, p. 107703, 2018.

[168] A. Splendiani, L. Sun, Y. Zhang, T. Li, J. Kim, C.-Y. Chim, G. Galli, and F. Wang, "Emerging Photoluminescence in Monolayer MoS_2," *Nano Lett.*, vol. 10, no. 4, p. 1271, 2010.

[169] W. Zhao, Z. Ghorannevis, L. Chu, M. Toh, C. Kloc, P.-H. Tan, and G. Eda, "Evolution of Electronic Structure in Atomically Thin Sheets of WS_2 and WSe_2," *ACS Nano*, vol. 7, no. 1, p. 791, 2012.

[170] P.-C. Yeh, W. Jin, N. Zaki, D. Zhang, J. T. Liou, J. T. Sadowski, A. Al-Mahboob, J. I. Dadap, I. P. Herman, P. Sutter *et al.*, "Layer-Dependent Electronic Structure of an Atomically Heavy Two-Dimensional Dichalcogenide," *Phys. Rev. B*, vol. 91, no. 4, p. 041407, 2015.

[171] Y. Zhang, M. M. Ugeda, C. Jin, S.-F. Shi, A. J. Bradley, A. Martín-Recio, H. Ryu, J. Kim, S. Tang, Y. Kim *et al.*, "Electronic Structure, Surface Doping, and Optical Response in Epitaxial WSe_2 Thin Films," *Nano Lett.*, vol. 16, no. 4, p. 2485, 2016.

[172] E. V. Castro, K. S. Novoselov, S. V. Morozov, N. M. R. Peres, J. M. B. L. Dos Santos, J. Nilsson, F. Guinea, A. K. Geim, and A. H. Castro Neto, "Biased Bilayer Graphene: Semiconductor With a Gap Tunable by the Electric Field Effect," *Phys. Rev. Lett.*, vol. 99, no. 21, p. 216802, 2007.

[173] Y. Zhang, T.-T. Tang, C. Girit, Z. Hao, M. C. Martin, A. Zettl, M. F. Crommie, Y. R. Shen, and F. Wang, "Direct Observation of a Widely Tunable Bandgap in Bilayer Graphene," *Nature*, vol. 459, no. 7248, p. 820, 2009.

[174] A. Ramasubramaniam, D. Naveh, and E. Towe, "Tunable Band Gaps in Bilayer Transition-Metal Dichalcogenides," *Phys. Rev. B*, vol. 84, no. 20, p. 205325, 2011.

[175] T. Chu, H. Ilatikhameneh, G. Klimeck, R. Rahman, and Z. Chen, "Electrically Tunable Bandgaps in Bilayer MoS_2," *Nano Lett.*, vol. 15, no. 12, p. 8000, 2015.

[176] J. Klein, J. Wierzbowski, A. Regler, J. Becker, F. Heimbach, K. Möller, M. Kaniber, and J. J. Finley, "Stark Effect Spectroscopy of Mono-and Few-Layer MoS_2," *Nano Lett.*, vol. 16, no. 3, p. 1554, 2016.

[177] A. Kumar and P. K. Ahluwalia, "Electronic Structure of Transition Metal Dichalcogenides Monolayers 1H-MX_2 (M= Mo, W; X= S, Se, Te) from Ab-Initio Theory: New Direct Band Gap Semiconductors," *Eur. Phys. J. B*, vol. 85, no. 6, p. 186, 2012.

[178] W. S. Yun, S. W. Han, S. C. Hong, I. G. Kim, and J. D. Lee, "Thickness and Strain Effects on Electronic Structures of Transition Metal Dichalcogenides: 2H-MX_2 Semiconductors (M= Mo, W; X= S, Se, Te)," *Phys. Rev. B*, vol. 85, no. 3, p. 033305, 2012.

[179] H. Zeng, G.-B. Liu, J. Dai, Y. Yan, B. Zhu, R. He, L. Xie, S. Xu, X. Chen, W. Yao *et al.*, "Optical Signature of Symmetry Variations and Spin-Valley Coupling in Atomically Thin Tungsten Dichalcogenides," *Sci. Rep.*, vol. 3, p. 1608, 2013.

[180] W. Huang, X. Luo, C. K. Gan, S. Y. Quek, and G. Liang, "Theoretical Study of Thermoelectric Properties of Few-Layer MoS_2 and WSe_2," *Phys. Chem. Chem. Phys.*, vol. 16, no. 22, p. 10866, 2014.

[181] K. F. Mak, K. L. McGill, J. Park, and P. L. McEuen, "The Valley Hall Effect in MoS_2 Transistors," *Science*, vol. 344, no. 6191, p. 1489, 2014.

[182] J. Lee, K. F. Mak, and J. Shan, "Electrical Control of the Valley Hall Effect in Bilayer MoS_2 Transistors," *Nat. Nanotechnol.*, vol. 11, no. 5, p. 421, 2016.

[183] J. P. Perdew and A. Zunger, "Self-Interaction Correction to Density-Functional Approximations for Many-Electron Systems," *Phys. Rev. B*, vol. 23, p. 5048, 1981.

[184] P. Giannozzi, S. Baroni, N. Bonini, M. Calandra, R. Car, C. Cavazzoni, D. Ceresoli, G. L. Chiarotti, M. Cococcioni, I. Dabo *et al.*, "QUANTUM ESPRESSO: A Modular and Open-Source Software Project for Quantum Simulations of Materials," *J. Phys. Condens. Matter*, vol. 21, no. 39, p. 395502, 2009.

[185] T. Lovorn, H. C. P. Movva, B. Fallahazad, S. Larentis, K. Kim, T. Taniguchi, K. Watanabe, S. K. Banerjee, E. Tutuc, and A. H. MacDonald, "Theory Dataset for "Tunable $\Gamma - K$ Valley Populations in Trilayer WSe_2"," Zenodo, Jan 2018.

[186] A. A. Mostofi, J. R. Yates, Y.-S. Lee, I. Souza, D. Vanderbilt, and N. Marzari, "An Updated Version of WANNIER90: A Tool for Obtaining Maximally-Localised Wannier Functions," *Comput. Phys. Commun.*, vol. 185, no. 8, p. 2309, 2014.

[187] S. J. Papadakis, E. P. De Poortere, M. Shayegan, and R. Winkler, "Anisotropic Magnetoresistance of Two-Dimensional Holes in GaAs," *Phys. Rev. Lett.*, vol. 84, no. 24, p. 5592, 2000.

[188] V. T. Dolgopolov and A. Gold, "Magnetoresistance of a Two-Dimensional Electron Gas in a Parallel Magnetic Field," *J. Exp. Theor. Phys. Lett.*, vol. 71, no. 1, p. 27, 2000.

[189] A. Subaşi and B. Tanatar, "Effects of a Parallel Magnetic Field on the Ground-State Magnetic Properties of a Two-Dimensional Electron Gas," *Phys. Rev. B*, vol. 78, no. 15, p. 155304, 2008.

[190] J. Falson and M. Kawasaki, "A Review of the Quantum Hall Effects in MgZnO/ZnO Heterostructures," *Rep. Prog. Phys.*, vol. 81, no. 5, p. 056501, 2018.

[191] V. N. Kotov, B. Uchoa, V. M. Pereira, F. Guinea, and A. H. Castro Neto, "Electron-Electron Interactions in Graphene: Current Status and Perspectives," *Rev. Mod. Phys.*, vol. 84, no. 3, p. 1067, 2012.

[192] M. Zarenia, A. Perali, D. Neilson, and F. M. Peeters, "Enhancement of Electron-Hole Superfluidity in Double Few-Layer Graphene," *Sci. Rep.*, vol. 4, p. 7319, 2014.

[193] A. Laturia, M. L. Van de Put, and W. G. Vandenberghe, "Dielectric Properties of Hexagonal Boron Nitride and Transition Metal Dichalcogenides: from Monolayer to Bulk," *npj 2D Mater. Appl.*, vol. 2, no. 1, p. 6, 2018.

[194] V. M. Pudalov, M. Gershenson, and H. Kojima, "On the Electron-Electron Interactions in Two Dimensions," in *Fundamental Problems of Mesoscopic Physics*, I. V. Lerner, B. L. Altshuler, and Y. Gefen, Eds. Springer, 2004, p. 309.

[195] T. Gokmen, M. Padmanabhan, E. Tutuc, M. Shayegan, S. De Palo, S. Moroni, and G. Senatore, "Spin Susceptibility of Interacting Two-Dimensional Electrons with Anisotropic Effective Mass," *Phys. Rev. B*, vol. 76, no. 23, p. 233301, 2007.

[196] A. Kormányos, V. Zólyomi, N. D. Drummond, P. Rakyta, G. Burkard, and V. I. Fal'ko, "Monolayer MoS_2: Trigonal Warping, the Γ Valley, and Spin-Orbit Coupling Effects," *Phys. Rev. B*, vol. 88, no. 4, p. 045416, 2013.

[197] V. Umansky, M. Heiblum, Y. Levinson, J. Smet, J. Nübler, and M. Dolev, "MBE Growth of Ultra-Low Disorder 2DEG with Mobility Exceeding 35×10^6 cm^2/Vs," *J. Cryst. Growth*, vol. 311, no. 7, p. 1658, 2009.

[198] L. Pfeiffer and K. W. West, "The Role of MBE in Recent Quantum Hall Effect Physics Discoveries," *Phys. E (Amsterdam, Neth.)*, vol. 20, no. 1-2, p. 57, 2003.

[199] M. J. Manfra, E. H. Hwang, S. D. Sarma, L. N. Pfeiffer, K. W. West, and A. M. Sergent, "Transport and Percolation in a Low-Density High-Mobility Two-Dimensional Hole System," *Phys. Rev. Lett.*, vol. 99, no. 23, p. 236402, 2007.

[200] Y. J. Chung, K. A. Villegas Rosales, H. Deng, K. W. Baldwin, K. W. West, M. Shayegan, and L. N. Pfeiffer, "Multivalley Two-Dimensional Electron System in an AlAs Quantum Well with Mobility Exceeding 2×10^6 $cm^2V^{-1}s^{-1}$," *Phys. Rev. Mater.*, vol. 2, p. 071001, 2018.

[201] Y. Zeng, J. I. A. Li, S. A. Dietrich, O. M. Ghosh, K. Watanabe, T. Taniguchi, J. Hone, and C. R. Dean, "Ultra-High Quality Magnetotransport in Graphene Using the Edge-Free Corbino Geometry," *arXiv preprint arXiv:1805.04904*, 2018. [Online]. Available: https://arxiv.org/abs/1805.04904

[202] D.-K. Ki, V. I. Fal'ko, D. A. Abanin, and A. F. Morpurgo, "Observation of Even Denominator Fractional Quantum Hall Effect in Suspended Bilayer Graphene," *Nano Lett.*, vol. 14, no. 4, p. 2135, 2014.

[203] D. Zhang, "Probing the Liquid and Solid Phases in Closely Spaced Two-Dimensional Systems," Ph.D. dissertation, Universität Stuttgart, 2014.

[204] Z. Lin, B. R. Carvalho, E. Kahn, R. Lv, R. Rao, H. Terrones, M. A. Pimenta, and M. Terrones, "Defect Engineering of Two-Dimensional Transition Metal Dichalcogenides," *2D Mater.*, vol. 3, no. 2, p. 022002, 2016.

[205] W. K. Hofmann, "Molybdenum and Tungsten Diselenide from High Temperature Solutions," *J. Cryst. Growth*, vol. 76, no. 1, p. 93, 1986, Also personal communication with Keiji Ueno.

[206] K. Ueno, "Introduction to the Growth of Bulk Single Crystals of Two-Dimensional Transition-Metal Dichalcogenides," *J. Phys. Soc. Jpn.*, vol. 84, no. 12, p. 121015, 2015.

[207] K. I. Bolotin, K. J. Sikes, Z. Jiang, M. Klima, G. Fudenberg, J. Hone, P. Kim, and H. L. Stormer, "Ultrahigh Electron Mobility in Suspended Graphene," *Solid State Commun.*, vol. 146, no. 9-10, p. 351, 2008.

[208] E. M. Hankiewicz, L. W. Molenkamp, T. Jungwirth, and J. Sinova, "Manifestation of the Spin Hall Effect Through Charge-Transport in the Mesoscopic Regime," *Phys. Rev. B*, vol. 70, no. 24, p. 241301, 2004.

[209] H. Fang, C. Battaglia, C. Carraro, S. Nemsak, B. Ozdol, J. S. Kang, H. A. Bechtel, S. B. Desai, F. Kronast, A. A. Unal *et al.*, "Strong Interlayer Coupling in van der Waals Heterostructures Built from Single-Layer Chalcogenides," *Proc. Natl. Acad. Sci. U.S.A.*, vol. 111, no. 17, p. 6198, 2014.

[210] M. M. Fogler, L. V. Butov, and K. S. Novoselov, "High-Temperature Superfluidity with Indirect Excitons in van der Waals Heterostructures," *Nat. Commun.*, vol. 5, p. 4555, 2014.

[211] F.-C. Wu, F. Xue, and A. H. MacDonald, "Theory of Two-Dimensional Spatially Indirect Equilibrium Exciton Condensates," *Phys. Rev. B*, vol. 92, no. 16, p. 165121, 2015.

[212] J. P. Eisenstein and A. H. MacDonald, "Bose–Einstein Condensation of Excitons in Bilayer Electron Systems," *Nature*, vol. 432, no. 7018, p. 691, 2004.

[213] I. B. Spielman, J. P. Eisenstein, L. N. Pfeiffer, and K. W. West, "Resonantly Enhanced Tunneling in a Double Layer Quantum Hall Ferromagnet," *Phys. Rev. Lett.*, vol. 84, no. 25, p. 5808, 2000.

[214] M. Kellogg, J. P. Eisenstein, L. N. Pfeiffer, and K. W. West, "Vanishing Hall Resistance at High Magnetic Field in a Double-Layer Two-Dimensional Electron System," *Phys. Rev. Lett.*, vol. 93, no. 3, p. 036801, 2004.

[215] E. Tutuc, M. Shayegan, and D. A. Huse, "Counterflow Measurements in Strongly Correlated GaAs Hole Bilayers: Evidence for Electron-Hole Pairing," *Phys. Rev. Lett.*, vol. 93, no. 3, p. 036802, 2004.

[216] S. K. Banerjee, L. F. Register, E. Tutuc, D. Reddy, and A. H. MacDonald, "Bilayer PseudoSpin Field-Effect Transistor (BiSFET): A Proposed New Logic Device," *IEEE Electron Device Lett.*, vol. 30, no. 2, p. 158, 2009.

[217] G. W. Burg, N. Prasad, K. Kim, T. Taniguchi, K. Watanabe, A. H. MacDonald, L. F. Register, and E. Tutuc, "Strongly Enhanced Tunneling at Total Charge Neutrality in Double-Bilayer Graphene-WSe_2 Heterostructures," *Phys. Rev. Lett.*, vol. 120, no. 17, p. 177702, 2018.

[218] P. Blake, E. W. Hill, A. H. Castro Neto, K. S. Novoselov, D. Jiang, R. Yang, T. J. Booth, and A. K. Geim, "Making Graphene Visible," *Appl. Phys. Lett.*, vol. 91, no. 6, p. 063124, 2007.

[219] M. M. Benameur, B. Radisavljevic, J. S. Héron, S. Sahoo, H. Berger, and A. Kis, "Visibility of Dichalcogenide Nanolayers," *Nanotechnology*, vol. 22, no. 12, p. 125706, 2011.

[220] W. Zhao, Z. Ghorannevis, K. K. Amara, J. R. Pang, M. Toh, X. Zhang, C. Kloc, P. H. Tan, and G. Eda, "Lattice Dynamics in Mono-and Few-Layer Sheets of WS_2 and WSe_2," *Nanoscale*, vol. 5, no. 20, p. 9677, 2013.

[221] X. Luo, Y. Zhao, J. Zhang, M. Toh, C. Kloc, Q. Xiong, and S. Y. Quek, "Effects of Lower Symmetry and Dimensionality on Raman Spectra in Two-Dimensional WSe_2," *Phys. Rev. B*, vol. 88, no. 19, p. 195313, 2013.

[222] T. Taniguchi and K. Watanabe, "Synthesis of High-Purity Boron Nitride Single Crystals Under High Pressure by Using Ba–BN Solvent," *J. Cryst. Growth*, vol. 303, no. 2, p. 525, 2007.

[223] A. Reina, X. Jia, J. Ho, D. Nezich, H. Son, V. Bulovic, M. S. Dresselhaus, and J. Kong, "Large Area, Few-Layer Graphene Films on Arbitrary Substrates by Chemical Vapor Deposition," *Nano Lett.*, vol. 9, no. 1, p. 30, 2008.

[224] X. Li, W. Cai, J. An, S. Kim, J. Nah, D. Yang, R. Piner, A. Velamakanni, I. Jung, E. Tutuc *et al.*, "Large-Area Synthesis of High-Quality and Uniform Graphene Films on Copper Foils," *Science*, vol. 324, no. 5932, p. 1312, 2009.

[225] R. Frisenda, E. Navarro-Moratalla, P. Gant, D. P. De Lara, P. Jarillo-Herrero, R. V. Gorbachev, and A. Castellanos-Gomez, "Recent Progress in the Assembly of Nanodevices and van der Waals Heterostructures by Deterministic Placement of 2D Materials," *Chem. Soc. Rev.*, vol. 47, no. 1, p. 53, 2018.

[226] P. J. Zomer, M. H. D. Guimarães, J. C. Brant, N. Tombros, and B. J. van Wees, "Fast Pick Up Technique for High Quality Heterostructures of Bilayer Graphene and Hexagonal Boron Nitride," *Appl. Phys. Lett.*, vol. 105, no. 1, p. 013101, 2014.

[227] A. V. Kretinin, Y. Cao, J. S. Tu, G. L. Yu, R. Jalil, K. S. Novoselov, S. J. Haigh, A. Gholinia, A. Mishchenko, M. Lozada *et al.*, "Electronic Properties of Graphene Encapsulated with Different Two-Dimensional Atomic Crystals," *Nano Lett.*, vol. 14, no. 6, p. 3270, 2014.

[228] S. J. Haigh, A. Gholinia, R. Jalil, S. Romani, L. Britnell, D. C. Elias, K. S. Novoselov, L. A. Ponomarenko, A. K. Geim, and R. Gorbachev, "Cross-Sectional Imaging of Individual Layers and Buried Interfaces of Graphene-Based Heterostructures and Superlattices," *Nat. Mater.*, vol. 11, no. 9, p. 764, 2012.

[229] S. Kang, H. C. P. Movva, A. Sanne, A. Rai, and S. K. Banerjee, "Influence of Electron-Beam Lithography Exposure Current Level on the Transport Characteristics of Graphene Field Effect Transistors," *J. Appl. Phys.*, vol. 119, no. 12, p. 124502, 2016.

[230] M. J. Rooks, E. Kratschmer, R. Viswanathan, J. Katine, R. E. Fontana Jr., and S. A. MacDonald, "Low Stress Development of Poly(methylmethacrylate) for High Aspect Ratio Structures," *J. Vac. Sci. Technol., B*, vol. 20, no. 6, p. 2937, 2002.